Anthracenylporphyrin based building blocks for the bottom-up fabrication of nitrogen-doped graphene nanostructures

Joffrey Pijeat

NNT : 2019SACLS346

Anthracenylporphyrin-based building blocks for the bottom-up fabrication of nitrogen-doped graphene nanostructures

Thèse de doctorat de l'Université Paris-Saclay
préparée à l'Université Paris-Sud

École doctorale n°571 Sciences chimiques : molécules, matériaux, instrumentation et biosystèmes (2MIB)
Spécialité de doctorat: Chimie

Thèse présentée et soutenue à Saint-Aubin, le 11/10/2019, par

M. Joffrey PIJEAT

Composition du Jury :

Prof. Anna Chrostowska Professeur, Université de Pau et des pays de l'Adour (IPREM)	Rapporteur
Dr. Jennifer Wytko Chargé de recherche, CNRS (CLAC)	Rapporteur
Prof. Laurence Masson Professeur, Aix Marseille Université (CINaM)	Examinateur
Prof. Jean-Pierre Mahy Professeur, Université Paris-Sud (ICMMO)	Président
Dr. Stéphane Campidelli Chercheur, CEA (NIMBE)	Directeur de thèse

Thèse de doctorat

Remerciements

Je souhaite en premier lieu, remercier les membres de mon jury : Prof. Anna Chrostowska, Dr. Jennifer Wytko, Prof. Laurence Masson et Prof. Jean-Pierre Mahy pour avoir accepté de juger ce travail de thèse.

Je remercie mon directeur de thèse Stéphane Campidelli, pour m'avoir offert cette opportunité de thèse, m'avoir supervisé et formé au cours de ces 3 ans tout en me laissant développer mon aspect critique et mes idées qui font le chercheur que je suis devenu aujourd'hui.

Je tiens également à remercier Vincent Dericke pour sa disponibilité, ses conseils avisés et ses réponses didactiques quand à toutes mes interrogations de physique. Concernant notre équipe de chimistes, je souhaite saluer mon compagnon de thèse, Julien Lavie, aujourd'hui Docteur, avec qui nous avons beaucoup échangé sur nos projets respectifs. Je remercie Léo Chaussy pour son superbe travail de stage de Master 2 lié à ce projet et je souhaite à Manel Hanana et Hanine Kamaleddine, une bonne continuation pour leur 3e année de thèse. Je remercie chaleureusement Philippe Surugue, mon dessinateur préféré, pour m'avoir fait rire si souvent avec ses blagues au café, sa bonne humeur et sa gentillesse à toutes épreuves. J'adresse un grand merci à Julie Machado et Thomas Petenzi pour leur amitié, leur convivialité et pour les petits moments de détente en pause-café. Je souhaite à Julie beaucoup de succès dans sa future carrière et à Thomas toute la réussite qu'il mérite pour la suite de sa thèse ! Enfin, je remercie les membres du LCMCE avec qui j'ai beaucoup échangé durant ces 3 ans et avec qui j'ai particulièrement aimé discuter de chimie organique ; et tous les membres du LICSEN pour leur bonne humeur, leurs qualités humaines et je pense particulièrement aux rires de certaines personnes qui me manqueront !

Concernant les différentes collaborations de cette thèse, j'adresse mes remerciements à Vincent Guérineau et Nicolas Ellie de l'ICSN ainsi qu'à Solène Legand du LAMBE pour leurs disponibilités et la qualité des analyses de spectrométrie de masse. Je remercie Sylvain Clair, Laurence Masson et leurs équipes respectives de l'IM2NP et du CINaM, pour les études et les belles images STM présentées dans cet écrit. Enfin, je remercie Anna Chrostowska et son équipe de l'IPREM pour les premières études de pyrolyse flash sous vide qui j'espère se poursuivront à la suite de cette thèse.

Finalement, je souhaite remercier mes amis, Maximilien, Erwan, Alexandre, Michaël, Tom, Antoine, qui ont toujours étés imaginatifs et présents pour permettre aux uns et aux autres de décompresser, et ce depuis les années lycée !

Je tiens tout particulièrement à remercier mes parents Françoise et Claude, mes sœurs Christine et Marjorie, mon frère Stéphane ainsi que ma belle-famille Brigitte, Cléa, Laurie, Philippe, Antoine et Thierry, qui ont été chaque jour, une source de réconfort et d'encouragement.

Enfin, j'adresse un remerciement spécial à ma compagne Céline, qui a toujours été là, à m'apporter son soutien dans les moments de doutes, sa patience et son amour tout au long de cette thèse. Je reste persuadé que cette thèse n'aurait pas été la même sans elle.

Briques de construction à base d'anthracénylporphyrines pour la fabrication bottom-up de nanostructures de graphène dopées à l'azote

Les porphyrines sont des molécules présentent à l'état naturelles dans l'environnement biologique. Etant un composant essentiel de l'hémoglobine, elles sont souvent attribuées à la couleur rouge du sang et sont aussi présentes sous une forme dérivée dans la chlorophylle, responsable de la photosynthèse et de la couleur verte des plantes. Dans le domaine des nanosciences, les porphyrines sont étudiées depuis plusieurs décennies pour leurs propriétés optiques et électroniques à la fois par les physiciens et les chimistes. Parmi ces études, il a été montré que les propriétés d'absorptions et d'émissions optiques des porphyrines peuvent être considérablement modifiées par la fusion d'Hydrocarbures Aromatiques Polycycliques (HAPs) substitués sur leurs positions *méso via* la réaction de Scholl conduisant à la formation de porphyrines π-étendues. Ces porphyrines π-étendues présentent de nouvelles propriétés d'absorption et d'émissions par déplacement bathochrome avec possiblement des bandes optiques dans l'infrarouge proche. D'un point de vue chimique, les porphyrines sont des molécules robustes pouvant être substituées à leurs périphéries par une grande variété de fonctions ou groupes directionnels et ont été largement étudiées comme blocs de construction pour la conception d'édifices supramoléculaires. La fabrication et le contrôle du taux de dopants dans les nanostructures de graphène tels que les quantum dots (GQDs), les nanorubans (GNRs) et les nanomèches (GNM) représentent d'importants enjeux en recherche car les structures de ces nanomatériaux doivent être contrôlés avec une précision atomique afin de pouvoir contrôler en retour l'ouverture d'une bande interdite et leurs propriétés optoélectroniques. L'approche bottom-up est une méthode de synthèse basée sur la fabrication de nanomatériaux à partir de l'assemblage de petites molécules utilisées comme bloc de construction permettant potentiellement de former des structures avec une précision atomique. Bien que de nombreux GQDs et GNRs ont été obtenus par approche bottom-up, aucun GNM n'a encore été formé par cette approche à ce jour. Dans ce contexte, les dérivés de porphyrine à teneur contrôlée en azote sont des composés attrayants pouvant être utilisés soit comme éléments de base pour la fabrication bottom-up sur surface catalytiques de GNRs et GNMs dopés à l'azote, soit comme GQDs dopés à l'azote sous forme de porphyrines π-étendues. Au cours de cette thèse, nous avons développé une série de blocs de construction à base d'anthracénylporphyrines halogénées et avons étudié leurs assemblages sur surfaces. Nous avons également étudié la fusion d'anthracényle, de pyrényle et de naphtylporphyrines *méso*-substituées *via* une méthode de pyrolyse flash pour former des porphyrines π-étendues alternativement à la réaction de Scholl trop restrictive en solution.

Dans le chapitre II, nous avons reporté la synthèse de blocs de construction à base d'anthracenylporphyrins halogénées que nous avons nommés **BrTAP**, **ClTAP**, **ITAP BrDTAP** et **BrBAP**. Bien que **BrTAP**, **ClTAP** et **BrBAP** ont été synthétisés et caractérisées par les techniques analytiques usuelles, il a été déterminé que **ITAP** était instable dans les conditions ambiantes. La synthèse de **BrDTAP** a été réalisé avec succès et sa caractérisation par RMN proton est toujours en cours au laboratoire. Nous avons étudié le dépôt de **BrTAP** sur différentes surfaces et suivi visuellement son assemblage sur surface par microscopy à effet tunnel (STM). Dans la plupart des cas, une forte interaction par π-stacking entre les anthracenes a conduit à des organisation 1D avec une configuration de porphyrines adsorbées sur le côté (edge-on configuration) empêchant la polymérisation et la formation de réseau nécessaire à la formation de GNM. Seul le dépôt de **BrTAP** sur Pd (111) a conduit à la formation d'une organisation 2D de porphyrines adsorbées à plat. Cependant, lors de l'étape de polymérisation induite par recuit de la surface, la phase fut modifiée et un retour à la configuration edge-on a été observé. Ces résultats ont permis de mieux comprendre le comportement sur surface des tétra-anthracénylporphyrines et d'envisager des alternatives pour la suite de ces travaux.

Pour l'avenir, nous sommes convaincus que l'étude du dépôt de **BrDTAP** sur surface pourrait conduire à un assemblage complètement différent en raison de la perturbation de l'interaction intermoléculaire due au rang supplémentaire d'anthracènes sur le bloc de construction et conduire à la formation de GNM. En effet, selon des études théoriques sur la structure de **BrDTAP,** les deux rangs d'anthracène sont presque perpendiculaires entre eux ce qui pourrait fortement perturber l'interaction de π-stacking. D'autre part, le deuxième rang d'anthracène est presque parallèle au plan macrocyclique de la porphyrine et pourrait favoriser une absorption à plat avec les substrats permettant la polymérisation dans les deux dimensions du plan de la surface.

D'autre part, considérant qu'aucune étude liée à la cyclodéhydrogénation sur surface des HAPs sur des porphyrines n'a été reportée jusqu'à présent, il serait intéressant d'étudier le dépôt de **ClTAP** sur Pd (111) afin d'étudier la réaction de cyclodéhydrogénation entre anthracènes et porphyrines en inversant les températures d'activation des réactions de cyclodéhydrogénation et de polymérisation par déhalogenation. En effet, en remplaçant le brome par le chlore, Jacobse et ses collaborateurs ont constaté que la cyclodéhydrogénation intramoléculaire du 10,10'-dichloro-9,9'-bianthryle (**DCBA**) se produisait à une température inférieure à celle requise pour la polymérisation par déhalogénation et conduisait à la formation de polybisanthracène désordonné. Puis-ce que nous avons observé une adsorption à plat de **BrTAP** sur Pd (111), nous pensons fortement que la **ClTAP** sera adsorbée de manière similaire sur Pd (111) et l'étude de son dépôt pourrait permettre d'examiner la réaction de cyclodéhydrogénation entre anthracènes et porphyrines si la cyclodéhydrogénation a lieu avant la réaction de polymérisation sur surface.

L'étude des dépôts de **BrBAP** sur Cu (110) et Cu (111) à température ambiante n'a pas conduit à une adsorption stable des précurseurs et le dépôt à 250 ° C et à 400 ° C a conduit à la formation d'assemblages d'orientation indéterminée. Nous avons expliqué les résultats par une faible interaction molécule-substrat des surfaces de Cu à température ambiante et par la forte réactivité à haute température ne permettant pas un contrôle séquentiel des réactions assistées sur surface empêchant la formation contrôlée de GNR.

A l'avenir, il serait intéressant d'étudier le dépôt de **BrBAP** à température ambiante sur Pd (111) pour obtenir la formation de GNR sur surface. En effet, la haute réactivité de la surface de Pd (111) devrait renforcer l'interaction entre les molécules de **BrBAP** et le substrat et pourrait potentiellement conduire à une adsorption stable des précurseurs à température ambiante. Un recuit ultérieur de la surface permettrait l'activation séquentielle de réactions assistées sur surface conduisant à la formation de structures contrôlées.

Dans le chapitre III, une série de porphyrines substituées en position *meso* avec du naphthalene (**ZnSNP**), du pyrène (**ZnSPP** et **ZnTPyP**) et de l'anthracène (**ZnSAP**, **ZnBAP** et **ZnTAP**) ont été synthétisées et utilisées comme précurseurs pour l'étude de la formation de porphyrines π-étendue *via* la méthode de pyrolyse flash. Un montage expérimental a été mis au point et validé par reproduction de la réaction de fusion de la **ZnTPyP** reporté dans la littérature. A partir des expériences de pyrolyse de **ZnBAP** et **ZnTAP**, nous avons déduit que la fusion de multiple anthracene était difficilement contrôlable et faisait face à des problèmes de non-liquéfaction, sublimation et de sévère dégradation des précurseurs. Nous avons réussi la fusion à 515°C des sous unités anthracene, pyrene et naphthalene des molécules de **ZnSAP**, **ZnSPP** et **SNP** respectivement et prouvé l'efficacité de notre méthode de pyrolyse flash. Les produits fusionnés nommés **fused ZnSAP**, **fused ZnSPP** ont été correctement isolés et la purification de la **fused ZnSNP** est toujours à l'étude. De plus, nous avons montré que le zinc pouvait être retiré de la cavité de la molécule **fused ZnSPP** par traitement acide conduisant à la formation d'une porphyrine π-étendue sans présence de métaux nommée **fused SPP**.

Dans le chapitre IV, nous avons montré que les quatre anthracenes à la périphérie de la molécule de **BrTAP** pouvait être fonctionnalisés par le couplage de Suzuki-Miyaura en réaction avec des acides phenyl-, tolyl-, p-methoxyphenyl-, napthyl- and pyrenylboronic et générer une série de nouvelles molécules à base de tétra-anthracénylporphyrines nommées **TPAP**, **TTAP**, **TMPAP**, **TNAP**, **TPyAP**. Les caractérisations optiques des dérivés de tétra-anthracényl porphyrines avec les phényles (**TPAP**), les naphtyles (**TNAP**) et les sous-unités pyrényle (**TPyAP**) ont été étudiées. Nous avons constaté que les spectres d'émission de **TPAP**, **TNAP** et **TPyAP** montraient presque exclusivement la fluorescence du noyau de porphyrine dans la région visible avec l'extinction de la fluorescence des HAPs dans les régions UV ou visibles, à l'exception de la **TPyAP** dans laquelle l'émission de pyrène exciplex était discernable. Les arguments concernant l'extinction de la luminescence des HAPs, les

chevauchements d'absorption et d'émission, la reconnaissance des signatures optiques de chaque sous unité par excitation de la photoluminescence (PLE) et les calculs par Density Functional Theory (DFT) sont en accord avec l'hypothèse d'un transfert d'énergie des HAPs externes vers le noyau de porphyrine. Cependant, seule une spectroscopie d'absorption / émission transitoire confirmerait définitivement cette hypothèse. Enfin, nous avons montré que la molécule de **BrTAP** pouvait être utilisée comme un dérivé fonctionnel pouvant ouvrir la voie à l'utilisation de tétra-anthracénylporphyrines comme élément de base pour la construction de structures plus complexes.

À Céline

THESIS SUMMARY

ABBREVIATION

2D	Two dimensional
A	Absorbance
n-BuLi	*n*-Butyllithium
CNT	Carbon NanoTube
CVD	Chemical Vapor Deposition
DBBA	10,10'-dibromo-9,9'-bianthracene
DCM	Dichloromethane
DDQ	2,3-dichloro-5,6-dicyano-*p*-benzoquinone
DFT	Density Funtional Thoery
DMF	Dimethylformamide
ε	Extinction coefficient
eq	Equivalent number
eV	Electron Volt
FET	Field-effect transistor
GNM	Graphene NanoMesh
GNR	Graphene NanoRibbon
GQD	Graphene Quantum Dot
HBC	Hexa-peri-benzocoronene
HREELS	High-resolution Electron Energy Loss Spectroscopy
HRMS	High Resolution Mass Spectrometry
IR	InfraRed
MALDI	Matrix Assisted Laser Desorption Ionisation
Me	Methyl
MS	Mass Spectrometry
NEXAFS	Near Edge X-ray Absorption Fine Structure
NIR	Near InfraRed
nm	nanometer
NMR	Nuclear Magnetic Resonance spectrocopy
PAH	Polycyclic Aromatic Hydrocarbon
PDT	PhotoDynamic Therapy
ppm	Parts per million
r.t	room temperature
Ref	Reference

SEC	Size Exclusion Chromatography
SPhos	2-dicyclohexylphosphino-2',6'-dimethoxybiphenyl
STM	Scanning Tunneling Microscopy
T	Temperature
TCE	Tetrachloroethane
TFA	TriFluoroAcetic acid
TGA	ThermoGravimetry Analysis
THF	Tetrahydrofuran
TLC	Thin Layer Chromatography
TOF	Time Of Flight
μ	Micro
UHV	Ultra High Vacuum
UV	UltraViolet
Vis	Visible
VT-NMR	Variable Temperature Nuclear Magnetic Resonance spectroscopy
XPS	X-Ray Photoemission Spectroscopy
XRD	X-Ray Diffraction
λ	Wavelength

Chapter I. Introduction

I. 1. Porphyrins

I. 1.1. Generalities

The origin of the term *porphyrin* derived from the word *porphura* for purple in Greek as a reminder of the intense violet colour of most of porphyrins. From a chemical point of view, a porphyrin is a macrocycle constituted by four pyrrolic units connected with methines bridges. Crystallographic studies revealed that this macrocycle is flat and allows an important electronic delocalization of the 18 electrons constituting its π-conjugated system as illustrated in **Fig. I-1**.

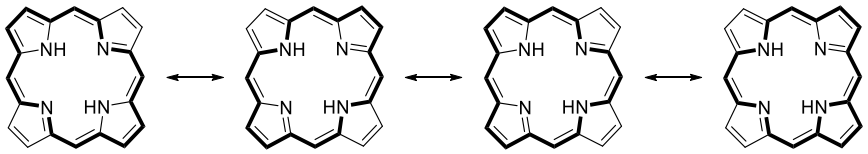

Fig. I-1 Representation of the electronic delocalization of the 18 π-conjugated electrons within a macrocycle of porphyrin.

A nomenclature proper to porphyrin was developed to describe the variety of the chemical substitutions on the α, β, *meso* positions or on nitrogen atoms present in the cavity (**Fig. I-2**).

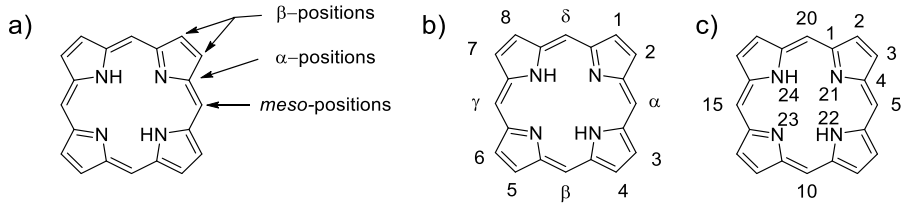

Fig. I-2 a) Chemical structure of porphyrin with specific positions annotated; b) first system of nomenclature of porphyrin proposed by Fisher in the 1930s; c) actual IUPAC nomenclature adopted since 1987

The first system of nomenclature of porphyrin was proposed by Fisher in the 1930s. β-pyrrolic carbons were numbered from 1 to 8 while carbons on *meso* positions were represented by symbols α, β, γ and δ (**Fig. I-2**, b).[1,2] Since 1987, with the development of porphyrins and because of the increase of complexity of chemical structures, the actual IUPAC system has been adopted.[3] According to the IUPAC system, carbons at α and β pyrrolic positions are respectively numbered 1, 4, 6, 9, 11, 14, 16, 19 and 2, 3, 7, 8, 12, 13, 17, 18; *meso* positions are numbered 5, 10, 15, 20; and nitrogens from 21 to 24 (**Fig. I-2**, c).

The properties of porphyrins can be modulated by chemical substitutions over the macrocycle which affect the planarity and thus the global electronic of the system. A non-substituted macrocycle is called porphin whereas the usual name porphyrin is dedicated to a macrocycle with substitutions. The substituents are generally observed on pyrroles (β positions) in natural porphyrins while most of the synthetic porphyrins are substituted on their methine bridges (*meso* positions). The variety of *meso*-

substituted porphyrins can be divided into seven categories abbreviated as A_4, A_3B, *trans*-A_2B_2, *cis*-A_2B_2, *cis*-A_2BC, *trans*-AB_2C, ABCD depending on the nature and positions of the substituents (**Fig. I-3**).

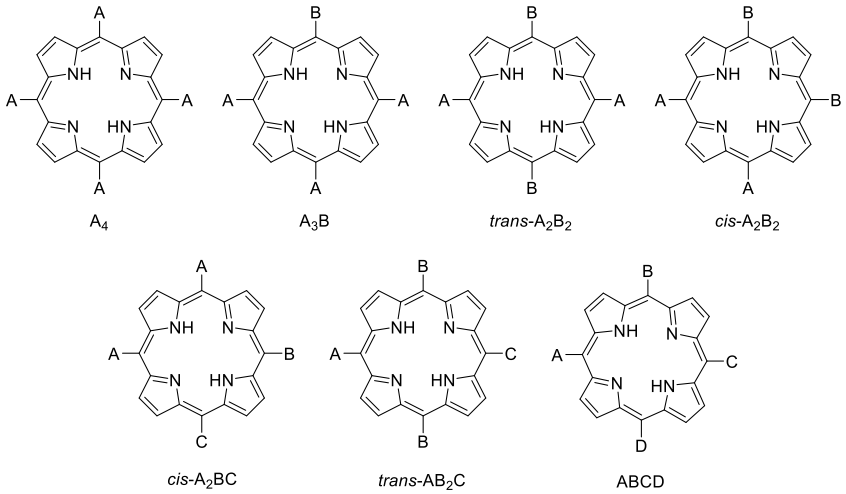

Fig. I-3 Representation of the seven categories of *meso*-substituted porphyrins

Moreover, the cavity of free-base porphyrins, with a size between 18 to 22 angstroms, is able to chelate most of metals from the periodic table and form metalloporphyrins (**Fig. I-4**). The coordination of a metal M is stabilized by the bonds with the four nitrogens within the macrocycle. Most of these metals are able to complete their coordination spheres with other relatively labile axial ligands (L). In addition to chemical substitutions, the presence and nature of the metal in the cavity also allows modulation of the optical and electronic properties of porphyrins with a visible effect on the UV-visible absorption spectra.

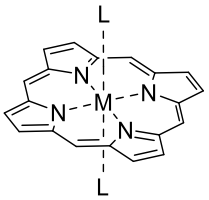

Fig. I-4 Coordination of a metal M in the cavity of a porphyrin macrocycle. Axial labile ligands L are susceptible to complete the sphere of coordination of the inserted metal.

I. 1.1.1. Natural porphyrins

Porphyrin and its derivatives constitute a class of compounds particularly present in biological systems. Historically, the discovery of porphyrin is related to the first investigation in biology of chlorophyll. Chlorophyll is a central element in natural photosynthesis. Its structure is based on an analogue of porphyrin called chlorin in which two carbon atoms of a pyrrole ring are sp^3 hybridised; the macrocycle contains a Mg^{2+} cation (**Fig. I-5**).[4] The chlorin core is also responsible for the intense green colour of leaves.

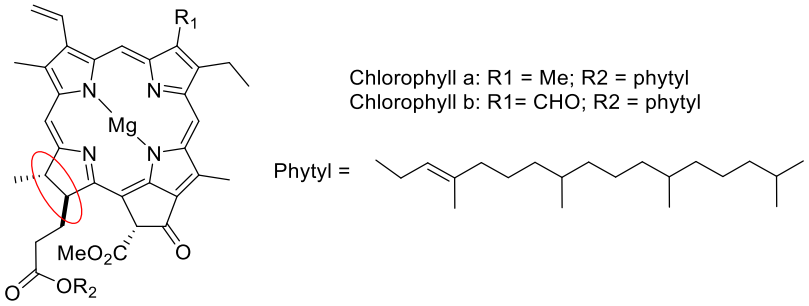

Fig. I-5 Chemical structure of chlorophyll

In 1884, F. Verdeil suggested that the green pigment of leaves should have the same origin as the red colour of blood. Indeed, the origin of the apparent red colour of blood is due to a strong absorbance of haemoglobin, a metalloprotein known to ensure the function of transport of oxygen in most living organisms.[5] Haemoglobin (**Fig. I-6**, a) is composed of four subunits, each containing an iron-porphyrin called heme. In biology, the term heme is used to describe the active centres of proteins based on iron-porphyrins. Nowadays, different types of hemes have been discovered and classified, the most abundant is the heme b (**Fig. I-6**, b).

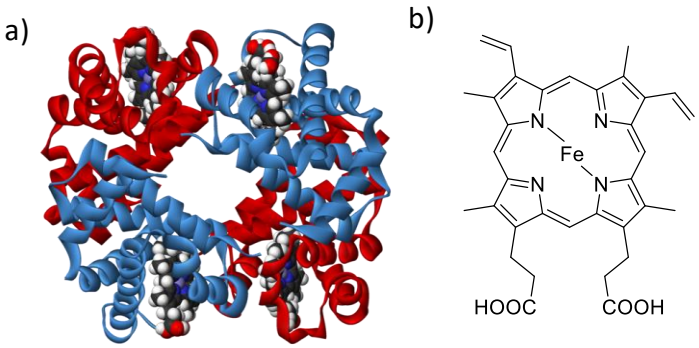

Fig. I-6 a) 3D structure of haemoglobin; b) chemical structure of heme b.

I. 1.1.2. Synthetic strategies

Rothemund reported in 1935 the first method to synthesise symmetric *meso*-substituted porphyrins.[6] This method consisted in the condensation of pyrrole and aldehyde in a closed tube with pyridine under an inert atmosphere. The tube was heated at different temperatures from 140°C to 220°C for 24h - 48h and led to porphyrins in 5-10% yields. However, the harsh conditions used for the synthesis limited the choice of starting materials and thus the development of this method. In 1964, an alternative method was reported by Adler and Longo who performed the condensation reaction in air with propionic acid instead of pyridine at reflux (**Fig. I-7**).[7] This method usually yields 20% of *meso*-substituted tetra-aryl porphyrin in approximatively 30 min and is still applied nowadays for the gram scale preparation of porphyrins.

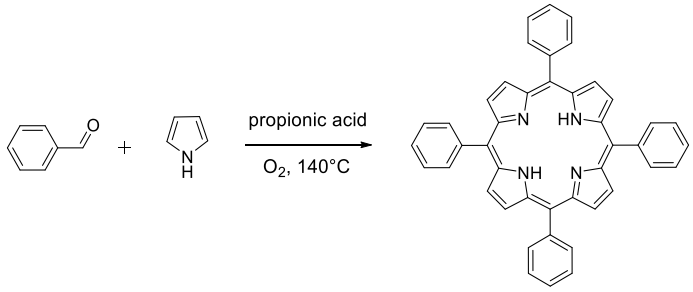

Fig. I-7 Synthesis of a 5,10,15,20-tetraphenylporphyrin (**TPP**) under the method developed by Adler and Longo.

By adapting the protocol of Adler and Longo, Little *et al.*[8] developed a method called "mixed aldehydes" to synthetise asymmetric *meso*-substituted porphyrins by adjusting the number of equivalents of different aldehydes. However, this method often leads to a complex mixture of isomers difficult to separate. In 1986, Lindsey developed a strategy to synthesise porphyrins giving up to 50% yield under mild conditions.[9] In this method, the reaction was performed at room temperature (r.t) under an inert atmosphere of nitrogen (N_2) or argon (Ar). A first step of polycondensation was initiated by addition of catalytic amount of Lewis acid (TFA or BF_3OEt_2) to form the porphyrinogen. In a second step, the porphyrinogen was oxidized with DDQ (2,3-dichloro-5,6-dicyano-1,4-benzoquinone) or *p*-chloranil (**Fig. I-8**) to afford the corresponding porphyrin.

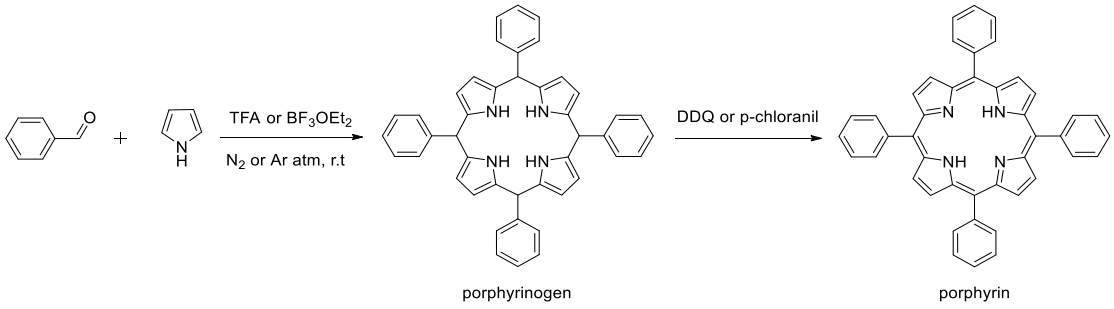

Fig. I-8 Synthesis of a 5,10,15,20-tetraphenylporphyrin (**TPP**) under the method developed by Lindsey.

To understand the strategy developed by Lindsey, the mechanism of the formation of porphyrin is displayed in **Fig. I-9**. The amount of the resulting porphyrin directly depends on the concentration of porphyrinogen formed by the cyclocondensation reaction which is in competition with the reaction of linear polymerisation. Therefore, to enhance the yield of the formation of porphyrin, it is necessary to increase the preliminary formation of porphyrinogen species. In the previous methods developed by Rothemund and Adler/Longo, the porphyrinogen was immediately oxidized after its formation by surrounding oxygen and the porphyrin product was thus kinetically formed. Knowingly that the formation of a macrocycle is thermodynamically favourable, the idea of Lindsey was to introduce an equilibrium in the reaction to increase the formation of thermodynamic species. Therefore, to avoid an irreversible oxidation of polymers, the condensation reaction is protected from oxygen and conducted under inert atmosphere. In a second time and only after reaching the equilibrium, the porphyrinogen is irreversibly transformed into porphyrin by oxidation.

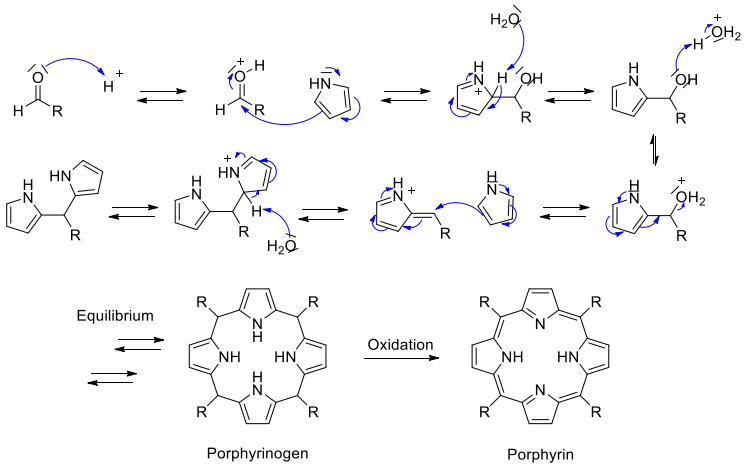

Fig. I-9 Mechanism of formation of the tetrapyrrolic macrocycle of porphyrin.

In the early 1960's, MacDonald described the synthesis of *trans*-A_2B_2 porphyrins with a protocol that involved a first step of acid catalysed condensation between a dipyrromethane (containing the group A) and an aldehyde (containing the group B) that led to the formation of a porphodimethene intermediate. A second oxidation step afforded the corresponding A_2B_2 porphyrin (**Fig. I-10**).[10]

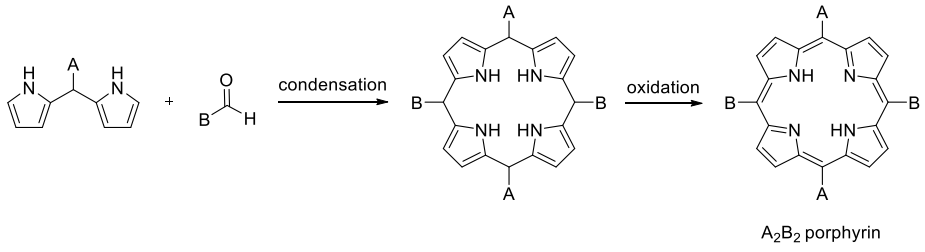

Fig. I-10 MacDonald-type 2+2 condensation for the synthesis of asymmetric A_2B_2 porphyrin.

In addition to the formation of challenging A_2B_2 porphyrins, the authors demonstrated that dipyrromethanes were species stable enough to be isolated as intermediates.

The major issue in this method was the possible rearrangement of substituents during the condensation reaction known as "scrambling" that could lead to a complex mixture of isomeric porphyrins.[11] In 1998, the group of Lindsey reported optimal synthetic conditions to form *trans*-A_2B_2 porphyrin with a minimal scrambling as a function of concentration of acid and reactants.[12] Last but not least, other methods exist for the formation of A_3B porphyrins based on 3+1 condensation.[13–15]

I. 1.1.3. Optical properties of porphyrins

The characteristic absorption spectrum (**Fig. I-11**, deep blue) of a free-base porphyrin is composed of an intense absorption band around 420 nm called "Soret" and less intense bands between 500-700 nm called "Q bands". Four Q bands are expected for free-base porphyrins and two Q bands for metallated ones. The emission spectrum of a porphyrin exhibits two bands located between 650 nm and 720 nm (**Fig. I-11**, light blue).

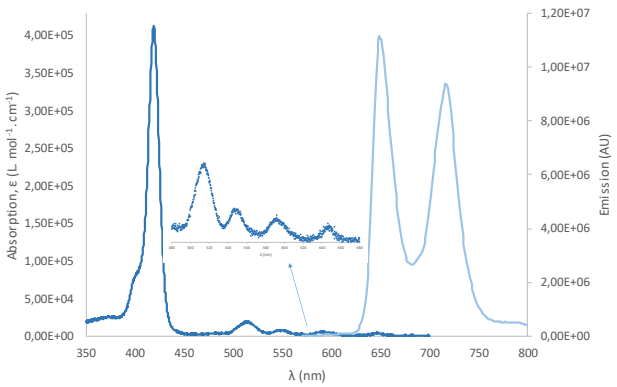

Fig. I-11 Absorption (deep blue) and emission (light blue) spectra of a 5,10,15,20-tetraphenylporphyrin.[16]

I. 1.1.4. NMR spectroscopy of porphyrins

The ^{1}H NMR spectrum of a porphyrin displays three characteristic signals:

- β-pyrrolic protons are located around 8-9 ppm. The multiplicity and chemical shift of these signals depend on the symmetry of porphyrins and vary as a function of the substituents present at *meso* positions.
- Protons in *meso* position are located around 10 ppm.
- In free-base porphyrins, the protons of the nitrogen atoms in the cavity of the macrocycle are observed around -2 ppm with a broad signal characteristic of their labile nature.

The chemical shifts of the signals is due to an anisotropic magnetic cone in the macrocycle that strongly shields protons of the nitrogens in its cavity and deshields the protons in *meso* positions.[17]

I. 1.2. Optoelectronic and redox properties of porphyrins

As mentioned previously, a chelate effect due to the four nitrogens within the cavity of the macrocycle of porphyrins allows the formation of stable complexes with metals. Metallo-porphyrins exhibit redox properties that can be modulated by the nature of metals. The systems can be used as sensitizers to activate photo-induced oxidations like epoxidation,[18–20] sulfoxidation,[21–23] hydroxylation,[24,25] oxidation of alcohols[26,27] or to activate redox processes with oxygen.[28,29] In addition to the nature of metals, the variety of substitutions of porphyrins allows chemists to both control the symmetry and modulate the optoelectronic properties of porphyrins. Therefore, porphyrins constitute an appealing and convenient material for applications in energy conversion,[30–33] molecular sensing,[34–36] and non-linear optics.[37–39] On the other hand, the development of materials with optical properties in Near Infra-Red region (NIR) is of great interest in biology. Particularly, the research in diagnosis and photodynamic therapy (PDT) requires the use of NIR dyes in excitation or in emission because of the relative transparency of biological tissues in the NIR region.[40–43] In this context, a red-shift of the properties of porphyrins is attractive to promote NIR dyes. A red-shift of the optical properties of a material can be achieved by an extension of its electronic system that leads to a decrease of the HOMO-LUMO bandgap. Because porphyrins intrinsically strongly absorb in the visible region, the development of NIR dyes based on π-extended porphyrins has emerged as a hot topic of research.

I. 1.3. π-extended porphyrins

π-extended porphyrins can be seen as porphyrins with extended skeletons that are able to participate to the delocalization of electrons and exhibit structures, electronic and optical properties that are significantly different from those of porphyrins. The β-fusion of porphyrins with Polycyclic Aromatic Hydrocarbons (PAHs) is a popular method to form π-extended porphyrins with a red-shift of the optical absorption and emission.[44] The general term of "fusion" describes the set of reactions able to connect molecular fragments to the porphyrin core by at least two bonds that prevent the free rotation between subunits, flatten the molecular assemblies and afford fully conjugated systems. The fusion of PAHs on porphyrins are achieved by cyclodehydrogenation or oxidative ring closure reactions that are not dissociated in the literature and often referred to a single term as Scholl reaction (**Fig. I-12**, b).[45]

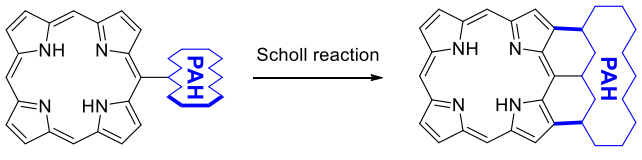

Fig. I-12 Illustration of the Scholl reaction used to achieve the β-fusion of the PAH substituted in *meso*-

position of the porphyrin macrocycle and form a flat and conjugated π-extended porphyrin.

However, the cyclodehydrogenation reaction on PAH-porphyrins succeeds only under very specific conditions. Indeed, Yamane *et al.*[46] reported in 2004 the fusion of pyrene on porphyrins and suggested that the fusion of PAHs should occur only when porphyrins were metallated with nickel and when PAHs contained ether or ester activating groups. Subsequently, the group of Osuka reported in 2006 the fusion of Ni-porphyrins substituted in *meso*-positions with azulene moieties containing esters. The quadruply azulene-fused porphyrins exhibited two major bands on the absorption spectrum at λ = 684 and 1136 nm.[47] In 2011, the group of Anderson reported the fusion of four anthracenes on the core of a porphyrin and the resulting fused product exhibited strong absorption properties in the NIR region until 1417 nm (**Fig. I-13**).[48] Recently, the groups of Müllen and Narita reported the fusion of hexabenzocoronene derivatives on Ni-porphyrins and the products of fusion exhibited intense absorption bands in NIR region up to 1176 nm.[49]

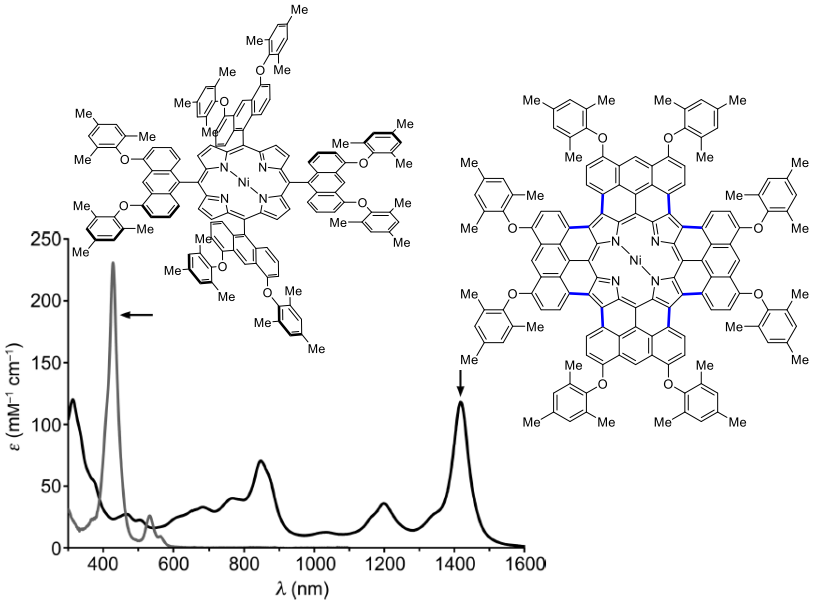

Fig. I-13 Absorption spectra and chemical structures of unfused- (left, grey) and fused- (right, black) [5,10,15,20-tetrakis(4,5-bis(mesityloxy)anthracen-9-yl)porphyrinato]Ni(II). Due to the fusion with the four anthracenes on the macrocycle, an important change of the optical properties was observed with a maximal absorption band in NIR region at 1417 nm.[48]

Unfortunately, the metalation of porphyrin with nickel causes a fast deactivation of the porphyrin excited states while the substitution with donor groups drastically limits tuning the periphery of the molecule. In 2012, the group of Thompson proposed a method of pyrolysis to activate the reaction of fusion of PAHs to *meso*-substituted Zn-porphyrins.[50] This method does not require the presence of Ni in the porphyrin neither the presence of activating groups on PAHs and the efficiency of the method was demonstrated with porphyrins containing naphthalene, pyrene, perylene and coronene derivatives. The solubility and processibility of the fused compounds were conserved but mixtures of

syn/anti isomers were reported due to the asymmetry of the PAHs studied, as illustrated with the thermal fusion of [5,15-bis(pyren-1-yl)porphyrinato]Zn(II) (**Fig. I-14**).

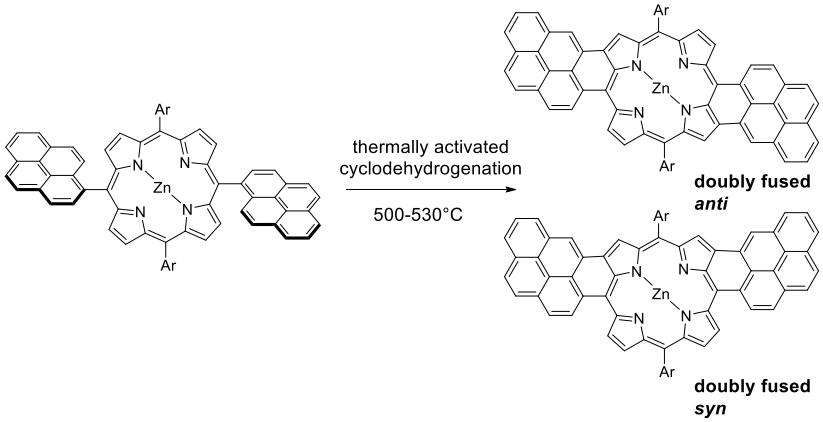

Fig. I-14 Thermal activation of cyclodehydrogenation reaction of a [5,15-bis(pyren-1-yl)porphyrinato]Zn(II) leading to a mixture of isomers due to the free rotation of the pyrene moieties in the starting material.[50]

I. 1.4. Porphyrin-based building blocks

Considering the robustness of the core of porphyrin and the easy access to a large variety of topologies, porphyrins are particularly suitable as building blocks for the formation of molecular materials. Indeed, the control of the number, positions and nature of the chemical substitutions with directional connecting groups allow the design of linear-, right-angled- or cross-shaped porphyrins. Drain and Lehn reported in 1994 a series of pyridylporphyrin building blocks for the formation of supramolecular dimers or square structures that self-assembled by coordination of *trans* or *cis* complexes of Pt(II) or Pd (II) (**Fig. I-15**).[51]

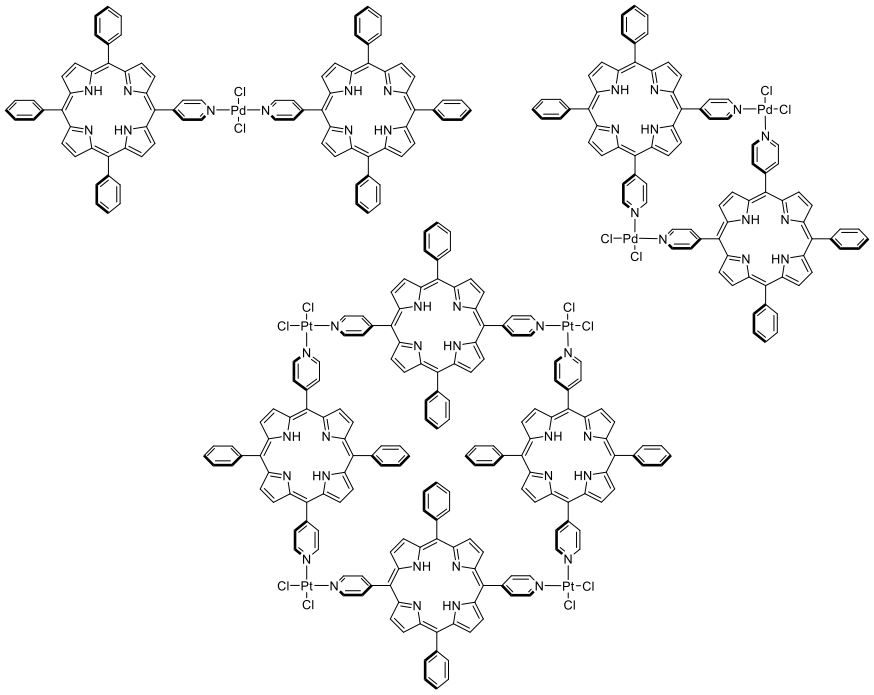

Fig. I-15 Supramolecular structures reported by Drain and Lehn. Pyridylporphyrin building blocks used to form different supramolecular architectures by coordination with *trans*-, *cis*- complexes of Pt(II) or Pd(II).[51]

The formations of supramolecular structures were monitored by UV-Visible spectroscopy; the spectra exhibited a red-shift of the Soret band and a change of the intensity of absorbance. Further evidence came from the chemical shifts on the ^{1}H NMR spectra and the presence of unique compounds with Pt were confirmed by the observation of a single resonance on the ^{195}Pt NMR spectra.

A large collection of examples incorporating porphyrin-based building blocks with variety of topologies can be found in the literature; these supramolecular architectures usually find applications in host-guest chemistry, artificial light-harvesting, catalysis and molecular photonics.[52–58]

I. 1.5. Porphyrin-based polymers

In the context of porphyrin-based materials, porphyrins can be used as monomeric species to form polymers.[59,60] One of the most impressive examples is the synthesis of a giant polymer with micro-meter length based on *meso–meso* linked porphyrins reported by the group of Osuka in 2005 (**Fig. I-16**).[61] This polymer containing up to 1024 monomers was formed by iterative synthesis *via* the coupling of zinc porphyrins in the presence of $AgPF_6$.

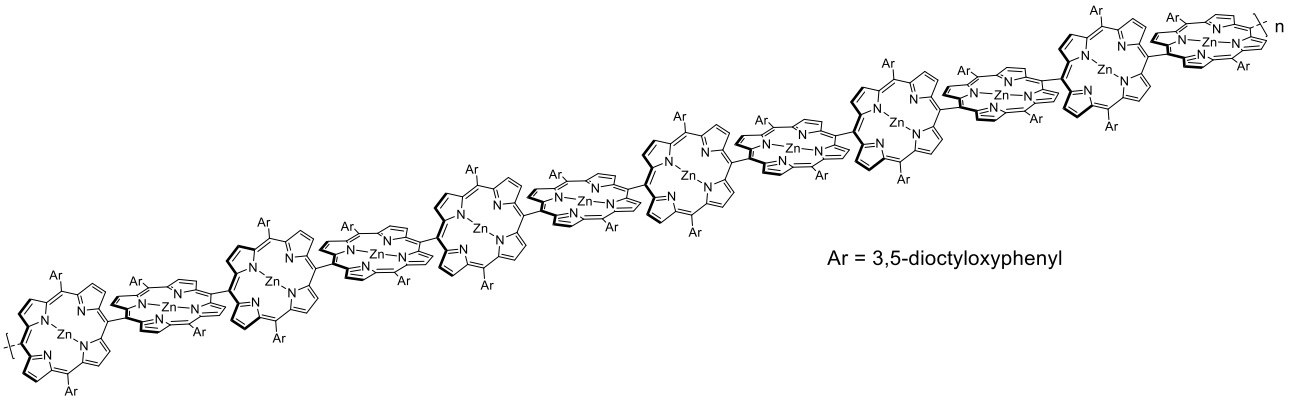

Fig. I-16 Chemical structure of the giant polymer containing up to 1024 units of porphyrin reported by the group of Osuka.[61]

Porphyrins have been also widely used for the fabrication of 2D or 3D Metal Organic Frameworks (MOFs) (**Fig. I-17**).[62,63] These networks were self-assembled by coordination of porphyrins with metal complexes and the structure of the final assemblies were directly programmed by a careful choice of shape, size, positions and number of coordinated groups of the building blocks.

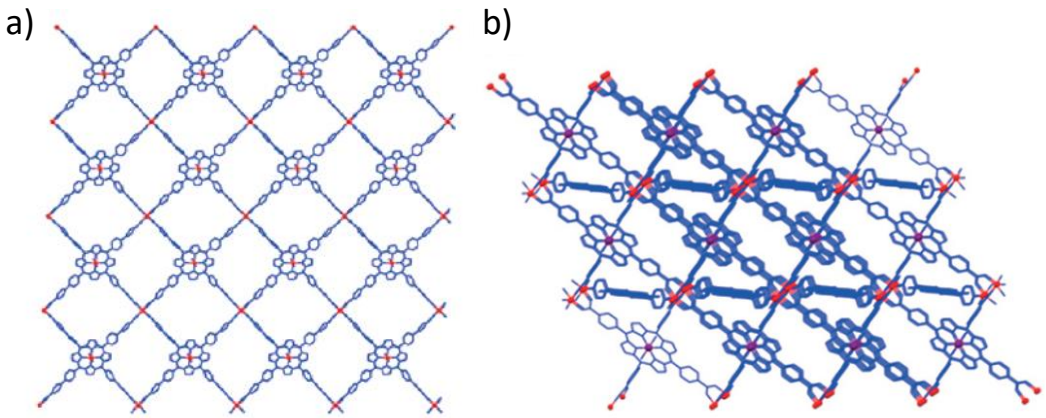

Fig. I-17 Examples of a) 2D; and b) 3D-MOFs structures.

I. 1.6. π-conjugated polymers of porphyrin

In the context of molecular electronics,[64–67] π-conjugated polymers based on porphyrins have inspired scientists.[68] Because the electronic interaction depends on the nature and the positions of the bridge between the moieties, several strategies to interconnect monomeric species and form π-conjugated polymers of porphyrins emerged.[69,70] These strategies are summarized in three categories:

- Strategy A: monomeric porphyrins are connected with a single bond by using a π-conjugated bridge allowing the free rotation of macrocycles between *meso*-positions as, for example, with ethyne[71–73] or ethene groups (**Fig. I-18**, a).[74–76]
- Strategy B: monomeric porphyrins are connected by fusing π-conjugated bridges at β-positions. For example, Crossley *et al.*[77–79] used a polycondensation reaction between tetracyanophenyls and carbonyl groups at β-positions of porphyrins to form the fused polymer represented in **Fig. I-18**, b.
- Strategy C: monomeric porphyrins are connected through multiple bonds, by fusing porphyrin subunits at β,β-positions and *meso*,*meso*-positions. For example, the group of Osuka reported the structures of fully aromatic tapes of porphyrins consisted in flat 1D and 2D polymers of porphyrins as represented in **Fig. I-18**, c.[80–82] The 1D extended polymer exhibited an exceptional red-shifted absorption band up to 2800 nm.

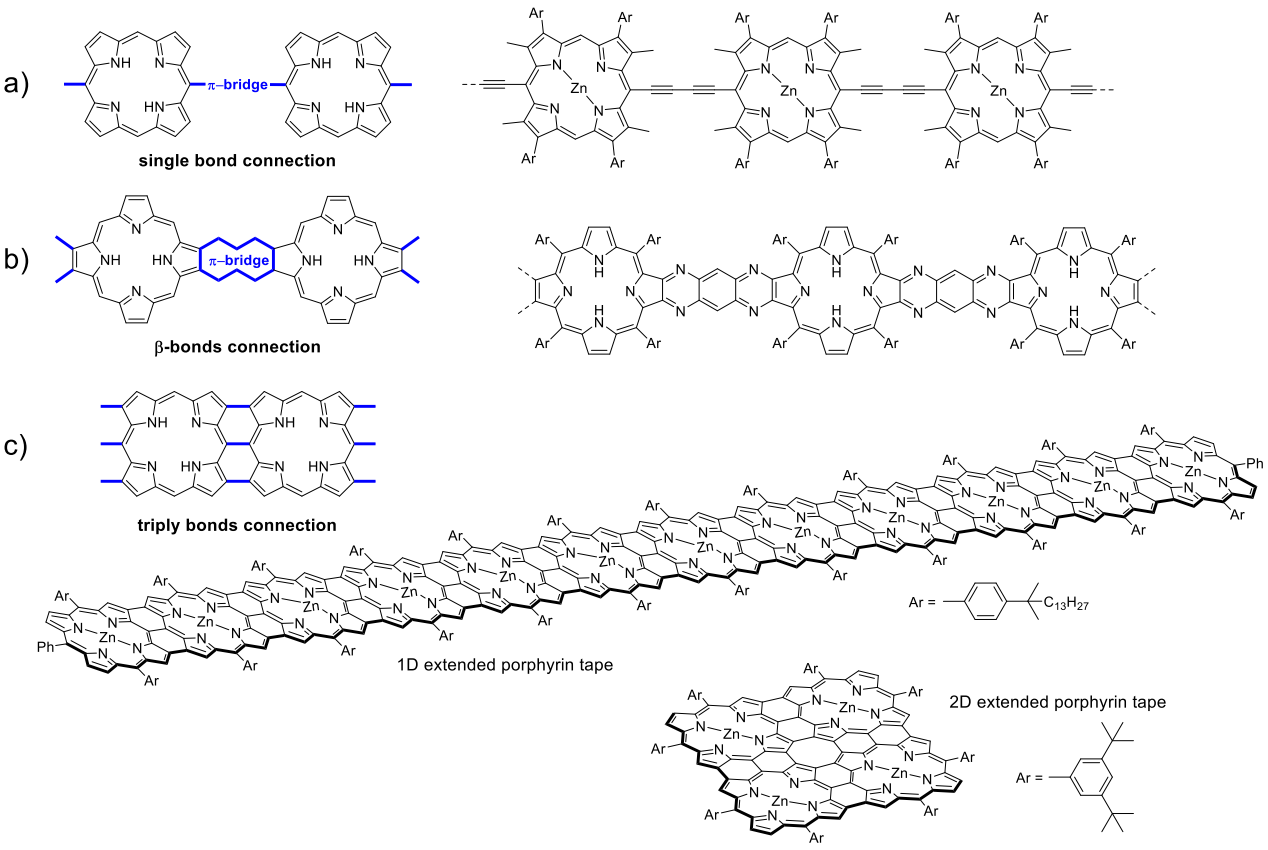

Fig. I-18 Illustration of the three main strategies applied to form fully π-conjugated polymers of porphyrin with corresponding examples from the literature. Porphyrin subunits can be connected by a) π-conjugated bridge between *meso*-positions; b) β-bonds; c) three bonds connecting β-, and *meso*-positions.

It is worth mentioning that in solution, these strategies give a limited degree of polymerisation because of the decrease of solubility over the polymerisation process. Strategies of on-surface synthesis have been developed to overcome the limitation of solutions and achieve the formation of expanded assemblies of porphyrins. The assemblies are built-up from molecular precursors deposed on substrates (*in situ* in the chamber of a scanning tunnelling microscope) and the supramolecular assemblies are imaged *via* Scanning Tunneling Microscopy (STM).

I. 2. Synthesis on surface

I. 2.1. STM Operating principle

Scanning Tunneling Microscopy (STM) is an analytical tool that allows imaging of the surfaces and adsorbed species with atomic resolution. The simplified operating concept of a scanning tunneling microscope shown in **Fig. I-19**, is based on a dependence of the tunnelling current with the distance separating a conductive tip ending with a single atom (probe) and a conductive surface (sample).[83,84] The sensitivity of the STM technique is derived from the exponential dependence of the tunnelling current that makes possible the detection of small variations of distance between the probe and the

surface. To keep a constant value of the tunnelling current while scanning horizontally the plane of a surface with the tip (x, y positions), the position of the probe along the z axis has to vary as a function of the morphology of the surface. Consequently, the morphology of a surface can be imaged by combining the data positions on the plane (scanning surface along x, y axes) and out of the plane (along z). An example of an image of the topographic scan of a surface of graphite by STM is shown in **Fig. I-19**.

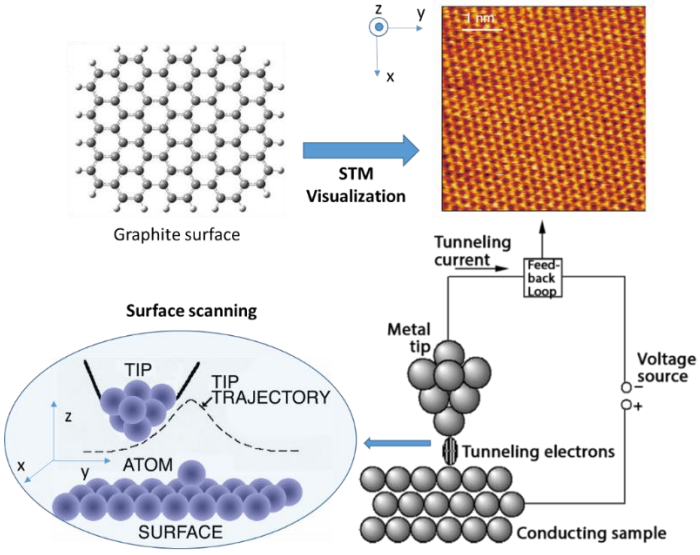

Fig. I-19 Illustration of the operating principle of a STM.

STM can operate either in solution at ambient pressure and room temperature (r.t) or under ultra-high vacuum (UHV) conditions. STM at the solid-liquid interface simplifies the maintenance and the preparation of samples but the substrates are exposed to the surrounding environment, which can modify the surface of sensitive substrates. In contrast, STM under UHV conditions drastically limits the access to samples and usually implies the preparation of the sample *in-situ*. However, oxygen-sensitive surfaces are preserved from the external environment that allows the use of catalytic substrates and chemical reactions required to form covalent assemblies on surface. Therefore, STM under UHV conditions have been widely used as a powerful analytical tool to explore the structures of covalent nanomaterials prepared by "on-surface" synthesis.[85–87]

I. 2.2. Covalent assemblies of porphyrins on surface

Although few examples were reported in the literature in 90s,[88,89] the "on-surface" synthesis have truly emerged as a promising strategy for the bottom-up fabrication of well-defined molecular assemblies since 2007. Grill *et al.*[90] reported the formation of dimers, linear chains and 2D networks of porphyrins from the polymerisation of variety of *para*-substituted bromotetraphenylporphyrins *via* surface-assisted Ullmann coupling on Au (111) (**Fig. I-20**). Although STM was used as an analytical

tool to visualize the assemblies on the surface, this technique probes low-energy electronic states and cannot be related to the bonding structures. Therefore, STM images were supported with theoretical calculations to provide a reliable interpretation of the structures.

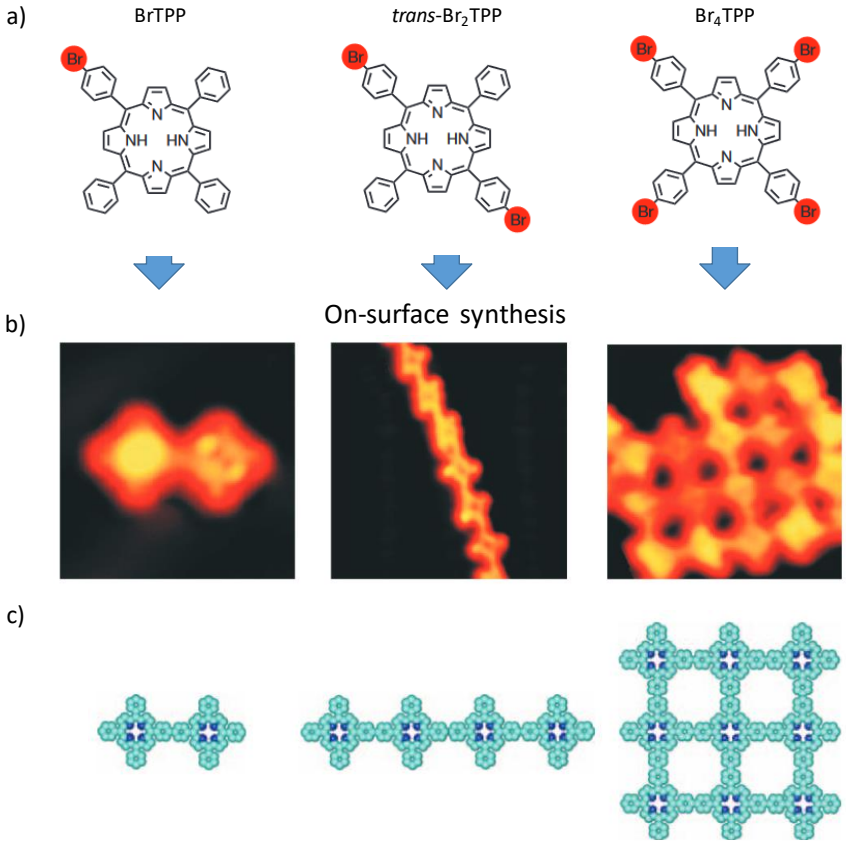

Fig. I-20 a) Chemical structures of the designed building blocks based on *para*-substituted tetraphenylporphyrins with bromines; b) STM images of the corresponding controlled assemblies after on-surface polymerisation of the precursors leading to dimers, linear chains and 2D networks; c) chemical structures of the corresponding nanostructures.[90]

Hierarchical strategies by means of control of the order of activation of surface-assisted reactions have been investigated by Lafferentz *et al.*[91] with the deposition of 5,15-bis(4-bromophenyl)-10,20-bis(4-iodophenyl)porphyrins on Au (111). Annealing the surface at T1 (393K) induced a first polymerisation with the activation of iodines that led to the formation of linear chains. Additional annealing the surface at T2 (523K) induced lateral polymerisation between chains by activation of bromines that led to the desired formation of networks of porphyrins (**Fig. I-21**).[92] This work demonstrated the difference of temperature of activation of the Ullmann coupling depending on the nature of the halogens that allowed the selective control of the direction of growth and the structure of the nanomaterial on the surface.

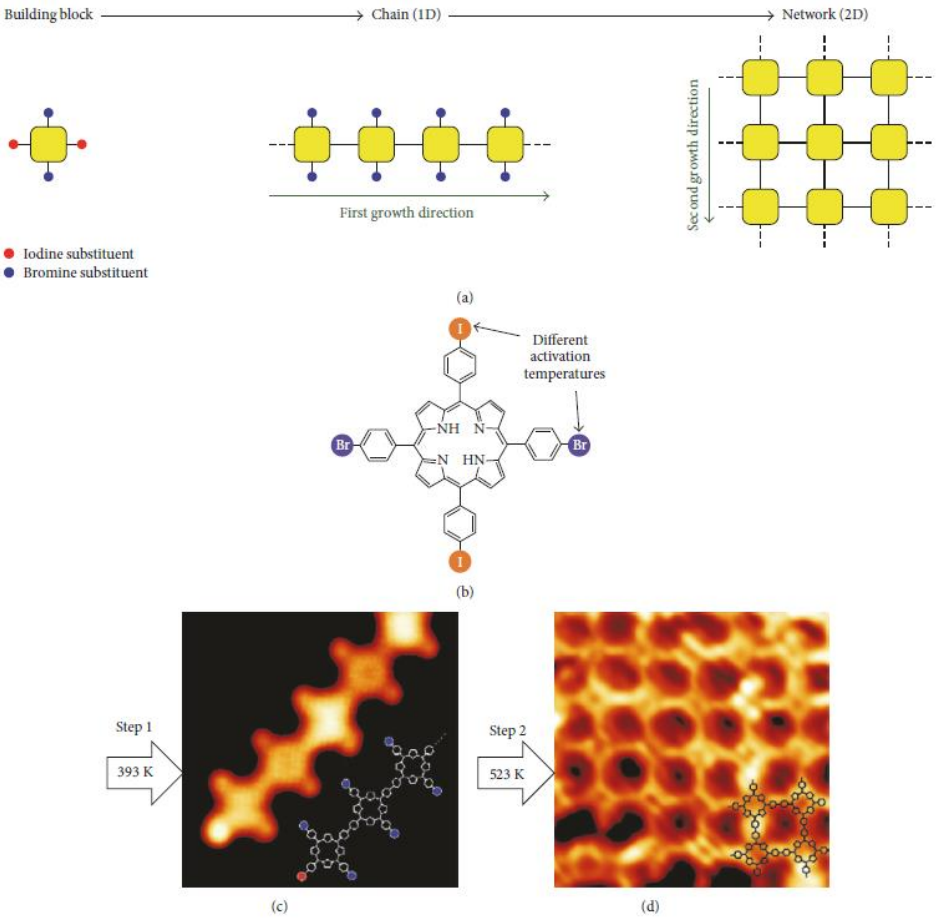

Fig. I-21 a) Illustration the hierarchical Ullmann-coupling strategy. b) Chemical structure of 5,15-bis(4-bromophenyl)-10,20-bis(4-iodophenyl)porphyrin and STM images of c) the linear chains formed by iodines activation after annealing the surface at T1 (393K); d) the network of porphyrin afforded by bromines activation after annealing the surface at T2 (323K).[91,92]

As an alternative to the Ullmann-coupling, Sonogashira-type[93]and Heck-type[94] coupling reactions have also been reported with porphyrins on a surface. In addition, Wiengarten *et al.*[95] reported the polymerisation of porphine *via* surface-assisted dehydrogenative homocoupling *via* direct CH activation. From STM, Near-edge X-ray Absorption Fine Structure (NEXAFS) and theoretical calculations, three distinct motifs of coupling were comprehensively distinguished (**Fig. I-22**). Consequently, the control of the direction of polymerisation without the use of halogens on precursors seemed to be more difficult and led to the formation of various kinked structures.[96–98]

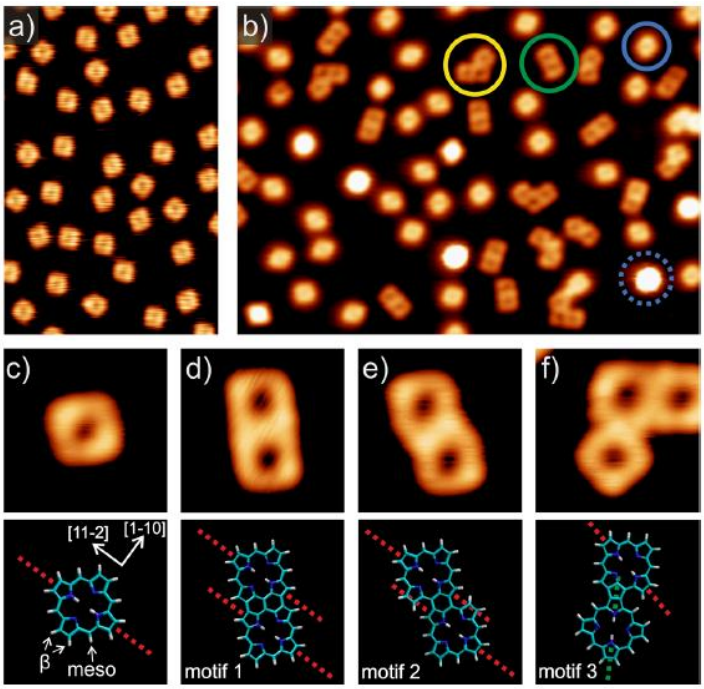

Fig. I-22 STM images on Ag (111) of a) free-base porphines and; b) products on surface after annealing at 573K with presence of monomers (blue), dimers (green), trimers (yellow) and porphines interacting with Ag adatoms (dashed blue circle); c) single porphine monomer with theoretical model; (d−f) Three motifs of coupling identified with corresponding structural models.[95]

Beyond the coupling reactions, the first suspicions of surface-assisted cyclodehydrogenation were reported by Di Santo *et al.*[99] in 2011 and Xiao *et al.*[100] in 2012 from the study of the insertion of metal atoms from the surface into the cavity of a free-base **TPP**. Chemical and structural changes were tracked by XPS and STM and suggested the presence of cyclodehydrogenated species, but no structures of fused species were proposed. Further insights on the structures of fused products of **TPP** were provided by Wiengarten *et al.*[101] on Ag (111). After annealing the surface at 520K and cooling to 6K, structures of partially fused products (spots with bright lobes due to upstanding configuration of phenyl rings, **Fig. I-23**, a-d) and isomers of tetrafused **TPP** (flat spots, **Fig. I-23**, A-D) were identified in STM images in agreement with theoretical studies. The authors demonstrated that the cyclodehydrogenation of the phenyl moieties of **TPP** could be achieved on the surface and suggested that the reaction occurred in multiple steps.

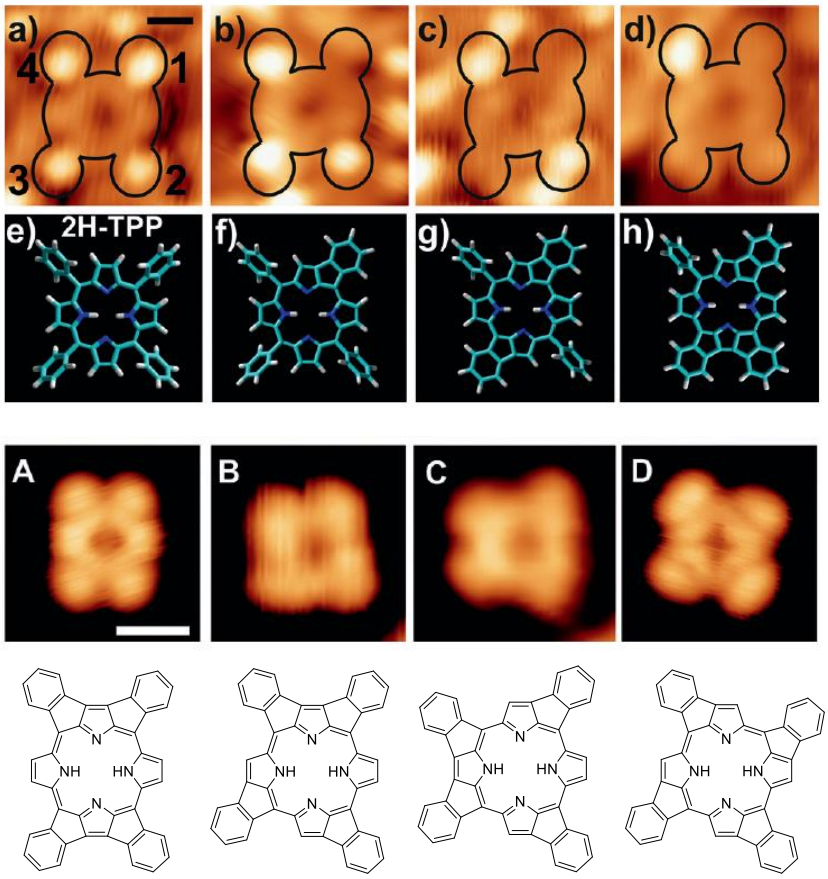

Fig. I-23 a-d) STM images on Ag (111) and e-h) theoretical models of a free-base **TPP** with its corresponding fused products from the dehydrogenation of one, two, three phenyls respectively; A-D) STM images and corresponding chemical structures of isomers of tetrafused phenyls of **TPP**.

Although the fusion of phenylporphyrins can be found in the literature (see **I. 1.3**),[101–104] no studies related to the on-surface cyclodehydrogenation of PAHs to porphyrins have been reported so far. However, the surface-assisted cyclodehydrogenation of PAH-porphyrins would constitute a convenient strategy to generate π-extended porphyrins by a method other than the Scholl reaction developed in solution. Porphyrins have been also investigated on surface to modify the properties of graphene. The group of Barth reported the functionalization of the edges of graphene with porphines[105] and the group of Pascual reported a hierarchical strategy to form hybrid systems based on the combination of **TPP** and graphene nanoribbons (GNRs) (**Fig. I-24**, b).[106] The second example of incorporation of porphyrins into GNRs was reported by Perkins and Fischer *via* solution-mediated synthesis to investigate the original optical properties of the material (**Fig. I-24**, a).[107]

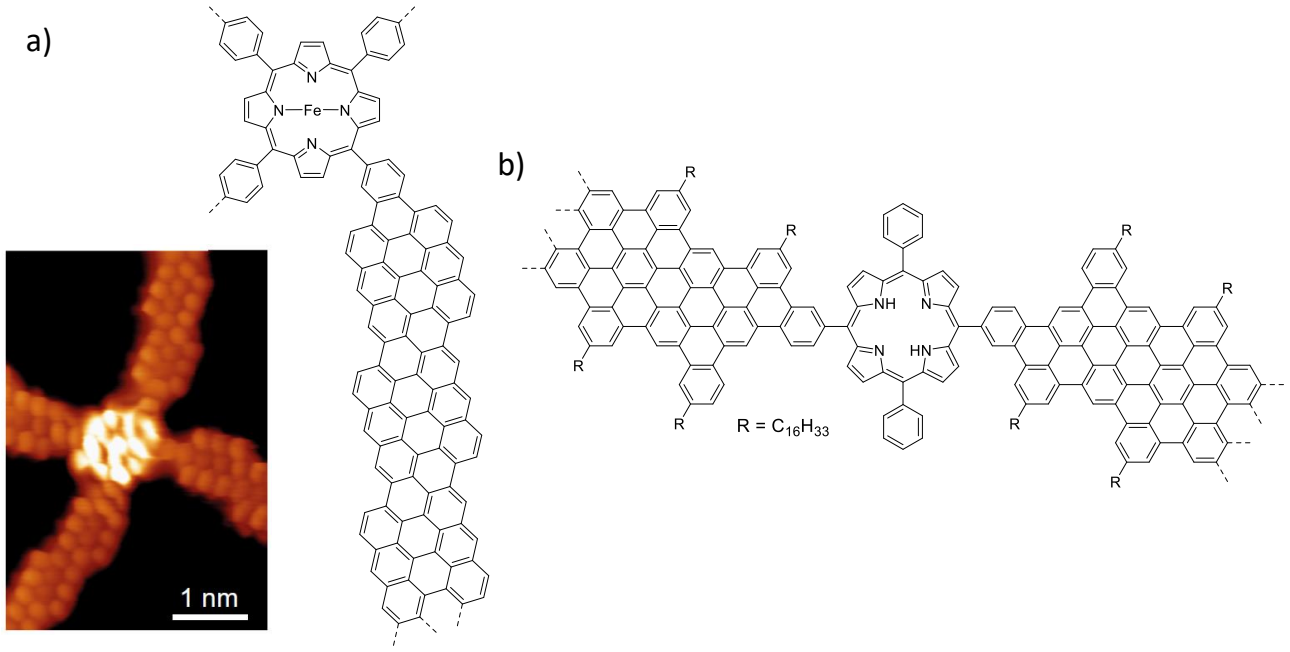

Fig. I-24 Chemical structures of a) the hybrid system based on Fe-TPP-GNRs with the corresponding nc-STM image and; b) graphene incorporating a porphyrin molecule.[106,107]

Finally, the chemical structures of porphyrin assemblies synthetised in solution or on a surface exhibit important structural similarities with graphene structures. Particularly, the tape-like polymers of porphyrins reported by the group of Osuka in solution (**Fig. I-18**, c) strongly resemble the structure of GNRs[108] and can be regarded as nitrogen-doped GNRs. In the next section, I will introduce graphene and graphene related-materials like GNRs and I will show that the control of doping of graphene with nitrogen is a hot topic of research that aims to control the electronic properties. In this context, the contribution of porphyrins with a controlled nitrogen content is an attractive subject of research.

I. 3. Graphene and graphene related nanostructures

I. 3.1. Generalities

Graphene is an atomic thick monolayer of carbon sp^2 arranged in a 2D honeycomb lattice (**Fig. I-25**, a). This atomic plane derives from the structure of graphite in which thousands of sheets of graphene are sustained by strong π-stacking interactions (**Fig. I-25**, b).

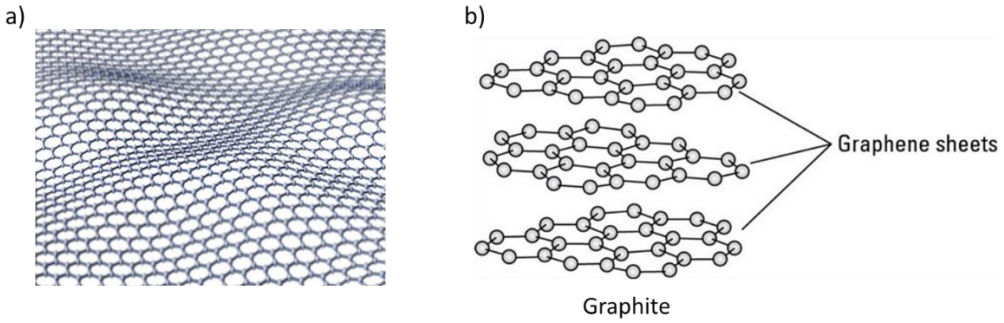

Fig. I-25 Representation of a) monolayer of graphene; b) crystallographic structure of graphite

Although it was postulated for decades and theoretically expected to be unstable, the existence of graphene was experimentally demonstrated in 2004 by Geim and Novoselov, who obtained the Nobel Prize in Physics in 2010 for the isolation and their experiments on a single layer of graphene.[109,110] The preparation of high quality graphene was achieved by a simple method based on the mechanical exfoliation of a crystal of graphite with scotch tape.[111]

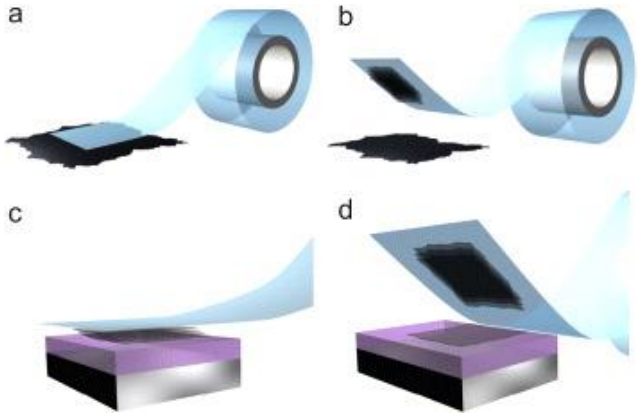

Fig. I-26 Illustration of mechanical exfoliation of graphite. a) Adhesive tape is pressed against a surface of graphite; b) A few layers of graphene are peeled off and attached on the tape; c) the tape with layers of graphene is pressed against the surface of a new substrate; d) by peeling off, only layers at the bottom are deposed on the surface of the substrate.[111]

The simplicity of this method has inspired the community of scientists to investigate the properties of graphene and a new topic of research for graphene and 2D materials emerged.[112–115] Graphene shows a high electronic mobility of about 200 000 $cm^2\ V^{-1}\ s^{-1}$ for suspending graphene[116] (150 times greater than silicon), an important thermal conductivity of about 5300 $W\ m^{-1}\ K^{-1}$ (10 times higher

than copper),[117,118] and a quantum Hall effect even at room temperature.[119–121] Regarding its mechanical properties, graphene is very robust and possesses a Young's modulus of ~ 1TPa and a tensile strength of ~ 130 GPa.[122] In addition, graphene is transparent and flexible, which is particularly suitable for flexible electronic applications.[123,124]

Although the modulation of its electronic properties is sensitive to its environment,[125,126] graphene became a very promising material for a wide range of applications, from electronics,[127–130] energy conversion and storage,[131–133] catalysis[134,135] and sensing[136,137] to photonics.[138–140]

Nevertheless, the valence and the conduction bands of graphene are cone-shaped and both meet at the Dirac point where the density of state is zero, meaning that graphene is a semi-metal with an electronic bandgap equal to zero (**Fig. I-27**).[112] Therefore, the current in a graphene-based transistor cannot be switched off properly, which drastically hinders the integration of graphene in Field Effect Transistor (FET) devices.[141] In order to broaden the range of applications in semi-conductors, a great challenge in fundamental research is to open a bandgap in the electronic structure of graphene.

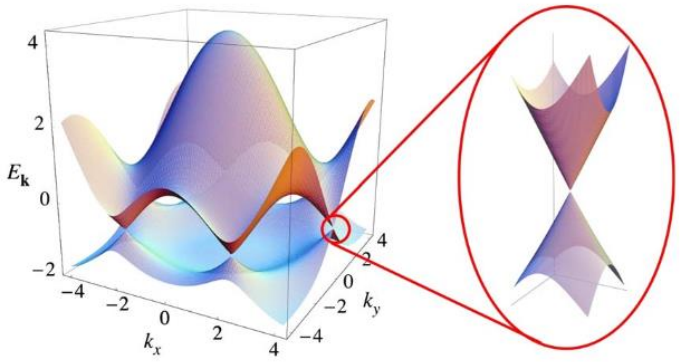

Fig. I-27 Partial representation of the band structure of graphene with an enlargement of the energy bands close to one of the Dirac points.[112]

I. 3.2. Bandgap opening

Theoretical and experimental studies suggested that a sizeable bandgap can be opened in graphene by nanostructuration. The method that has been widely reported in the literature, consists in the structural confinement of graphene and the fabrication of nanostructures with at least one dimension at the nanoscale.[142,143]

I. 3.3. Nanostructures of graphene

It is well known that matter reduced to its nanometer scale exhibits completely different properties than the bulk material. For example, CdS or CdSe Quantum Dots (QD) possess semi-conducting and high luminescence properties that only exist at the nanoscale and can be modulated by the size and the shape of the particles.[144,145] Likewise, by reducing the size of graphene down to the nanoscale, an

important modification of the electronic properties is expected and a sizeable bandgap can be opened.[146]

The nanoscale reduction of two dimensions of graphene leads to Graphene Quantum Dots (GQDs) with optical bandgaps that depend on the size and the shape of the particles (**Fig. I-28**, a).[147] GQDs are potentially interesting for biology because of the chemical inertness of carbon materials, their generally low cytotoxicity and high biocompatibility.[148–151]

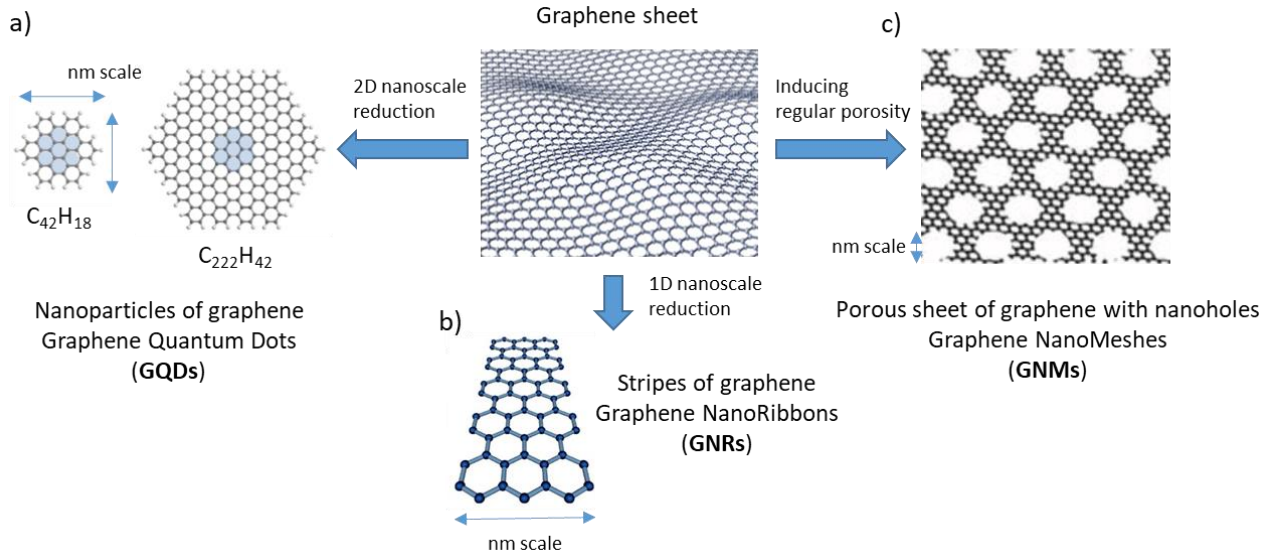

Fig. I-28. Representation of the structural confinement of graphene to afford a) nanoparticles of graphene called GQDs; b) stripes of graphene called GNRs; and c) porous sheets of graphene with regularly patterned nanoholes called GNMs. All of these nanostructures of graphene exhibit opened bandgaps.

The nanoscale reduction of one dimension of graphene leads to Graphene NanoRibbons (GNRs) that structurally consist in stripes of graphene with nanometer widths that govern the value of the bandgaps (**Fig. I-28**, b).[152–155] For example, armchair-type GNRs (A-GNR)[156] are predicted to exhibit semiconducting behaviours, whereas zig-zag types (Z-GNRs)[157] are predicted to exhibit interesting magnetic properties because of the strongly localized charge density of the edge state at the zigzag sites (**Fig. I-29**).

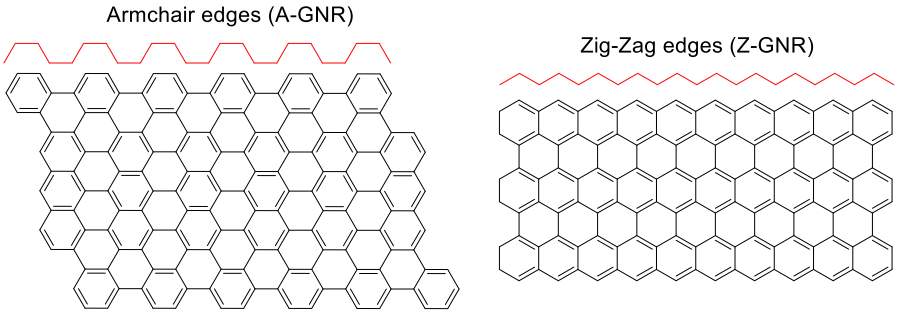

Fig. I-29 Variation of the edge states of GNRs.

As an alternative to reducing dimensionality, Graphene NanoMeshes (GNMs) are porous graphene sheets with regularly patterned nano-holes (**Fig. I-28**, c). It was predicted in 2008 that GNMs should exhibit bandgaps[158] and this was experimentally confirmed in 2010.[159] Several structural parameters have to be precisely controlled to tailor the electronic properties of GNMs with accuracy.[160–162] As illustrated in **Fig. I-30**, these parameters are intrinsically due to the control of the patterned nanoholes like the neck, the periodicity, the form, the size, the variation of the edge states that can be even multiple in a single hole etc.

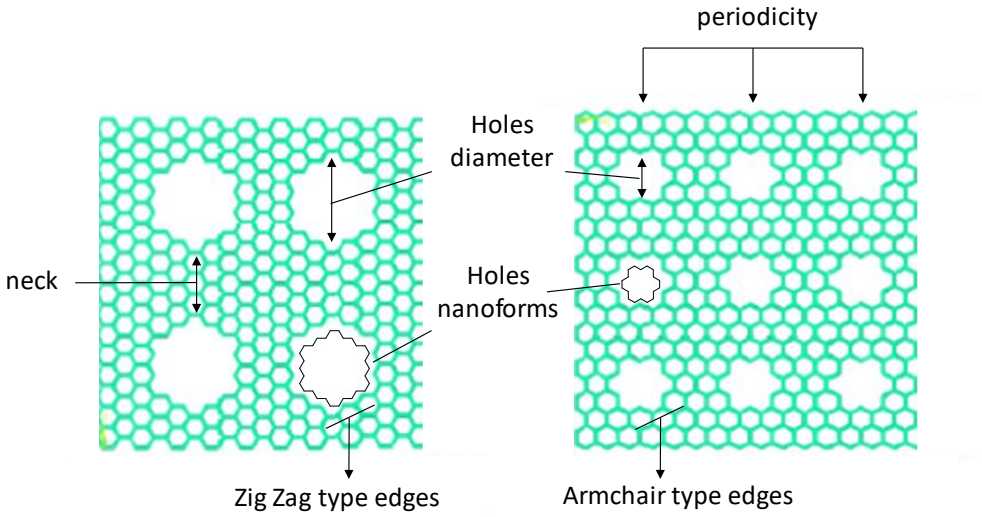

Fig. I-30 Illustration of the range of structural parameters that affect the electronic properties of GNMs.

Two methods can be used to produce gaped graphene materials:

The first one is the top-down approach, it is based on a strategy that physically carves the desired structure of nanoscopic materials from the bulk graphene or graphite.

The second is the bottom-up approach, based on the controlled assembly of small entities used as building blocks for the creation of larger and structurally well-defined nanomaterials. These two approach are described in the following sections.

I. 3.4. Top-down approach

I. 3.4.1. Top-down preparation of Graphene Quantum Dots

The principal method for the top-down preparation of GQDs is based on a chemical ablation of graphite (**Fig. I-31**).[163] This sequential method requires a first step of oxidation of graphite by the method of Hummers[164] to form graphene oxide. The second step consists in the oxidation and sonication of the graphene oxide flakes to break them into nanometer pieces. A last step of chemical reduction affords GQDs.

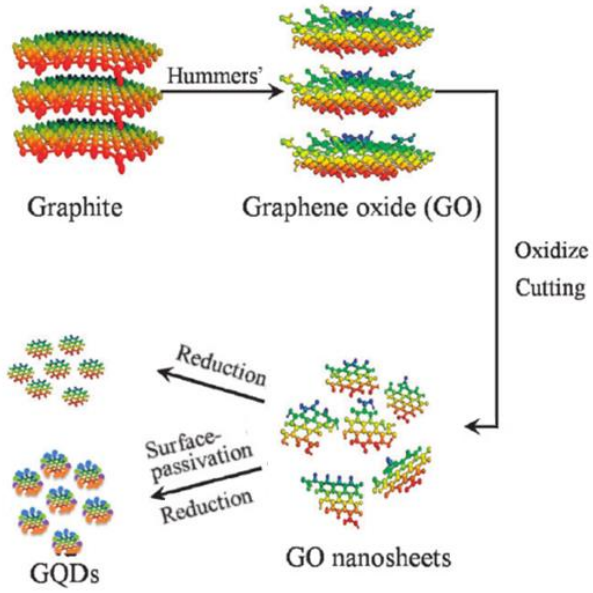

Fig. I-31 Chemical ablation method commonly used for the top-down preparation of GQDs from graphite.[163]

Although this method allows a mass production, the low control of the size, the shape, the edges and the oxidative states of the resulting GQDs constitute important limitations that render impossible a control of the opto-electronic properties of the nanomaterial. Other top-down methods have been reported in the literature for the fabrication of GQDs including the chemical or electrochemical oxidation/exfoliation,[165] the solvothermal techniques[166] or the oxygen plasma treatments.[167] All of these methods lead to a distribution of particle sizes with broad optical absorption or emission from the visible to the NIR region.

I. 3.4.2. Top-down preparation of Graphene Nanoribbons

The first method of preparation of GNRs was described from expanded graphite. GNRs were afforded by a rapid thermal annealing followed by dispersion using poly(m-phenylenevinylene-co-2,5-dioctoxy-p-phenylenevinylene) (PmPV) in 1,2-dichloroethane (DCE).[168] The resulting GNRs were obtained with a poor yield and a broad width distribution (from less than 10 nm to 100 nm). Subsequently, alternative methods based on the etching of carbon nanotubes (CNTs) were developed.[169,170] In the first method, multi-wall carbon nanotubes (MWCNTs) were deposited on a silicon substrate and embedded in poly(methyl methacrylate) (PMMA). The PMMA-MWCNT film was exposed to an argon plasma to selectively etch the upper part of the tubes. Depending on the etching time, single layer GNRs could be isolated with widths from 10 to 20 nm (**Fig. I-32**, a).[169]
The second method was based on chemical unzipping to produce well-defined GNRs (**Fig. I-32**, b) and the resulting GNRs exhibited widths from 20 to 100 nm with a yield of up to 100% depending on the oxidation conditions.[170]

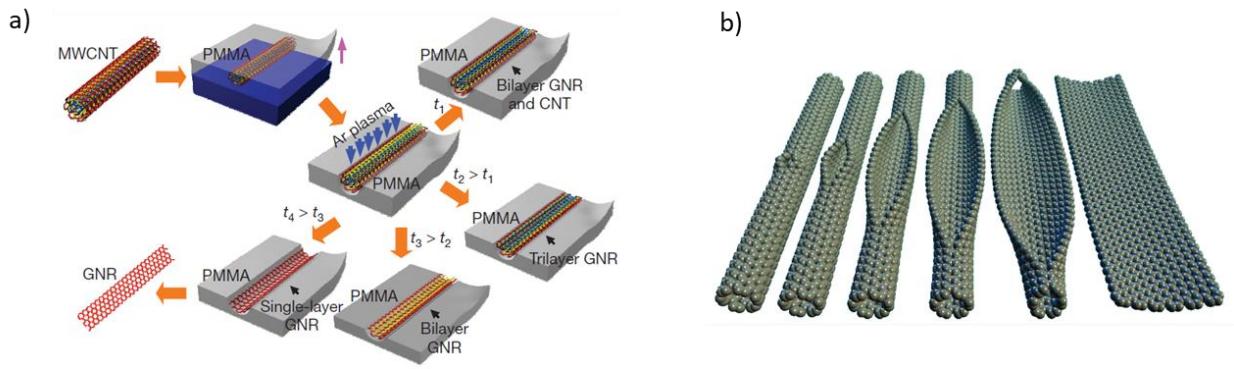

Fig. I-32 Top-down methods for the preparation of GNRs by a) Argon plasma etching from MWCNTs; and b) Unzipping of MWCNTs by chemical oxidation.

I. 3.4.3. Top-down preparation of Graphene Nanomeshes

The main strategy to prepare GNMs is to drill regular and periodic holes in a graphene sheet. The first attempts for the fabrication of GNMs were based on the electron and ion-beam lithography techniques.[171,172] The structural parameters like the position, shape and size of the pores were controlled by the positioning and the movement of the beam. The technique was time consuming and not appropriated for the conception of regularly patterned networks of holes.

From 2010, a series of methods based on nanolithography with etching techniques have been developed.[159,173–175] A famous example of nanolithography through a template-mask based on co-polymer was reported by Bai *et al.*[159] (**Fig. I-33**). A graphene sheet was covered with a thin layer of evaporated SiO_x and a thin film of polystyrene/polymethylmethacryalte (PS/PMMA) block copolymer. The copolymer was annealed and developed to selectively remove PMMA leaving a porous PS template. Fluoride-based reactive ion etching (RIE) was used to etch the exposed SiO_x and oxygen plasma was used to remove the remaining PS film that formed the holes in graphene. Finally, the SiO_x layer was removed with HF treatment leading to the desired graphene nanomesh.[159] Although a bandgap of about 0.1 eV was determined by electrical transport measurements, an atomically control of structural parameters like the periodicity, the size, the form and the multi-edges states of holes could not be attained with the method, which did not allow a predictable control of the bandgaps of GNMs.

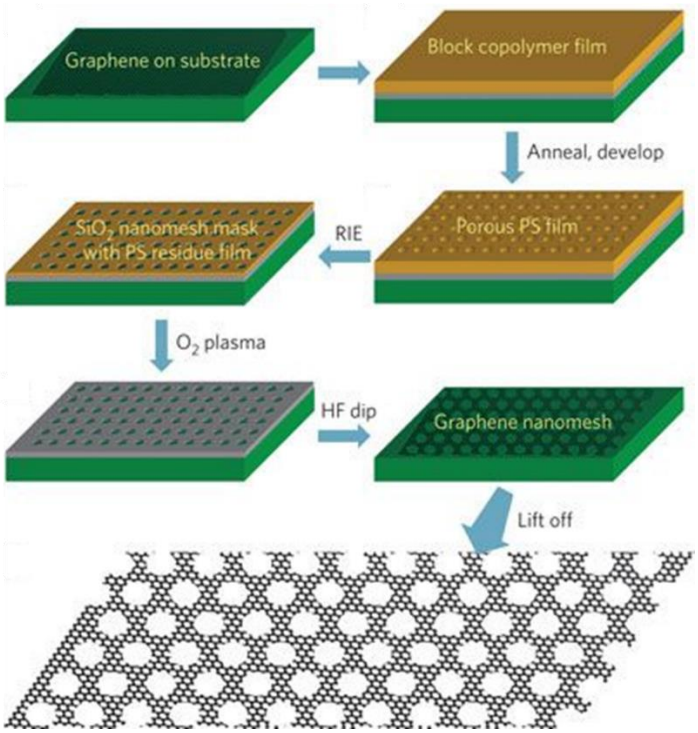

Fig. I-33 Nanolitography method with etching process for the preparation of GNMs. A graphene sheet was covered with a thin layer of evaporated SiO_x and a thin film of polystyrene/polymethylmethacryalte (PS/PMMA) block copolymer. PMMA was selectively removed by annealing leaving a porous PS template. Fluoride-based reactive ion etching (RIE) removed the exposed SiO_x layer and oxygen plasma was used to remove the remaining PS film and form the holes in graphene. Finally, the SiO_x layer was removed with HF treatment leading to the desired graphene nanomesh.[159]

Although other methods based on local catalytic hydrogenation of carbon by Cu nanoparticles[176] or local photodegradation of graphene oxide sheets with ZnO nanorods followed by reduction[177] have also been reported, these methods do not offer a better control of structures of GNMs than the nanolithography techniques described above.

To sum-up, the top-down approaches allow the formation of large amount of materials but the lack of control of structures represents an important drawback that has to be tackled to tailor precisely the bandgap of nanomaterials.

I. 3.5. Bottom-up approach

Applying the bottom-up approach for the fabrication of GQDs, GNRs and GNMs potentially allows the control at the atomic level of both the morphology (edges state, defects, size…) and the chemical composition of materials. In particular, this method permits control of doping parameters, such as ratio, type and position of dopants. Because the structure of graphene can be seen as multiple fused benzene rings forming a flat and electronically delocalized polymer, the bottom-up approach is usually decomposed into two-steps. First, the formation of a 0D-, 1D- or 2D- species that constitutes the molecular skeleton of the final structure and a second step of cyclodehydrogenation that induces

the aromatization of the system leading to the final conjugated structure. These two-steps can be achieved in solution or on-surface.

I. 3.5.1. Bottom-up preparation of Graphene Quantum Dots

A general procedure for the synthesis of GQDs is illustrated in **Fig. I-34** by the typical examples of synthesis in solution of "supernapthalene and supertriphenylene" developed by the group of K. Mullen in the 199s.[178] Polyphenylene precursors were formed in the first step by a Diels-Alder reaction and then oxidised in a second step by the Scholl reaction to afford the corresponding GQDs.

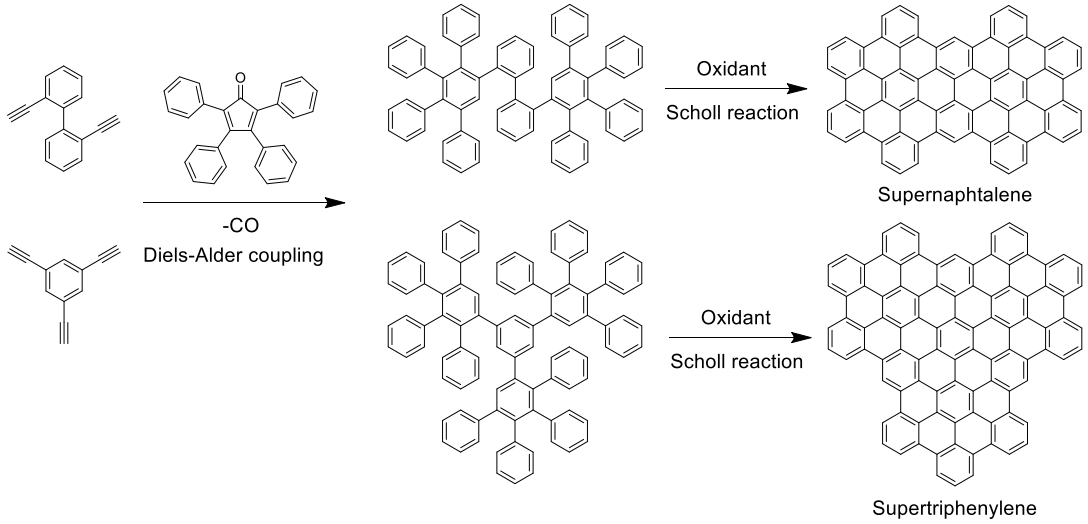

Fig. I-34 General procedure for the synthesis of GQDs with the example of synthesis of "supernapthalene" and "supertriphenylene".[178]

Since then, several structures with different shapes were synthesised and investigated for their electronic, absorption and photoluminescence properties.[179–183] The biggest structure synthetised so far contained 474 carbons; unfortunately, it was not possible to fully dehydrogenate the compound *via* the Scholl reaction and only propeller-shaped molecules were obtained.[184] In order to improve the solubility of GQDs, the periphery of the molecules can be functionnalized with alkyl chains[185,186] or with chlorine atoms.[187]

Despite the large variety of GQDs synthesised so far, examples of nitrogen-doped structures remain limited because the cyclodehydrogenation of molecules containing pyridyl moieties cannot be achieved in solution.[188,189] The difference of activation between pyridyl groups and benzene-like rings can be related to an electronic deactivation of C–H bonds of the 4-pyridyl groups and a non-stabilization of radicals required to achieve the cyclodehydrogenative coupling at specific positions.[45]

As an alternative to solution-based processes, GQDs can be prepared *in situ* on surfaces by deposition of precursors on catalytic substrates followed by cyclodehydrogenation, as demonstrated by Fasel and collaborators in 2010 on a triangular PAH.[190,191]

Using a similar strategy, Pinardi *et al.*[189] succeeded in the complete cyclodehydrogenation of pyridyl-disubstituted dibenzo-helicene on Pt (111) that could not be achieved in solution. The authors demonstrated the difference of energy required to fuse benzene- and azabenzene rings by the sequential activation of the reactions of cyclodehydrogenation on surface at 450K and 650K (**Fig. I-35**). Although most GQDs are synthetised in solution, the last example demonstrated the potential of "on-surface" synthesis that can be applied as an alternative method for the preparation of GQDs.

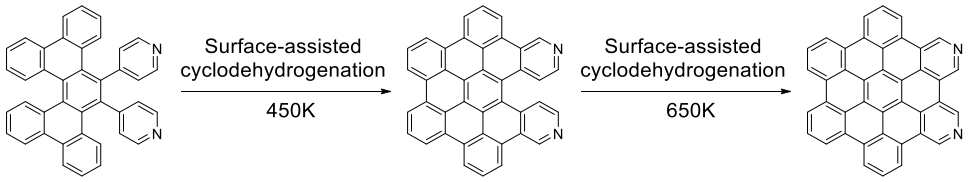

Fig. I-35 Surface-assisted cyclodehydrogenation on a pyridyl-disubstituted dibenzo-helicene.[189]

I. 3.5.2. Bottom-up preparation of Graphene Nanoribbons

The fabrication of GNRs was first achieved in solution using different synthetic strategies mainly based on Diels-Alder,[192–194] Suzuki-Miyaura[195–197] or Yamamoto coupling reactions,[198–200] followed by cyclodehydrogenation (**Fig. I-36**). These strategies led to a variety of well-defined GNRs with atomically precise edges, lateral functionalities or structural features such as gulf-type edges (**Fig. I-36**, a),[193] armchair-edges (**Fig. I-36**, b),[195] chevron-type structures (**Fig. I-36**, c).[199]

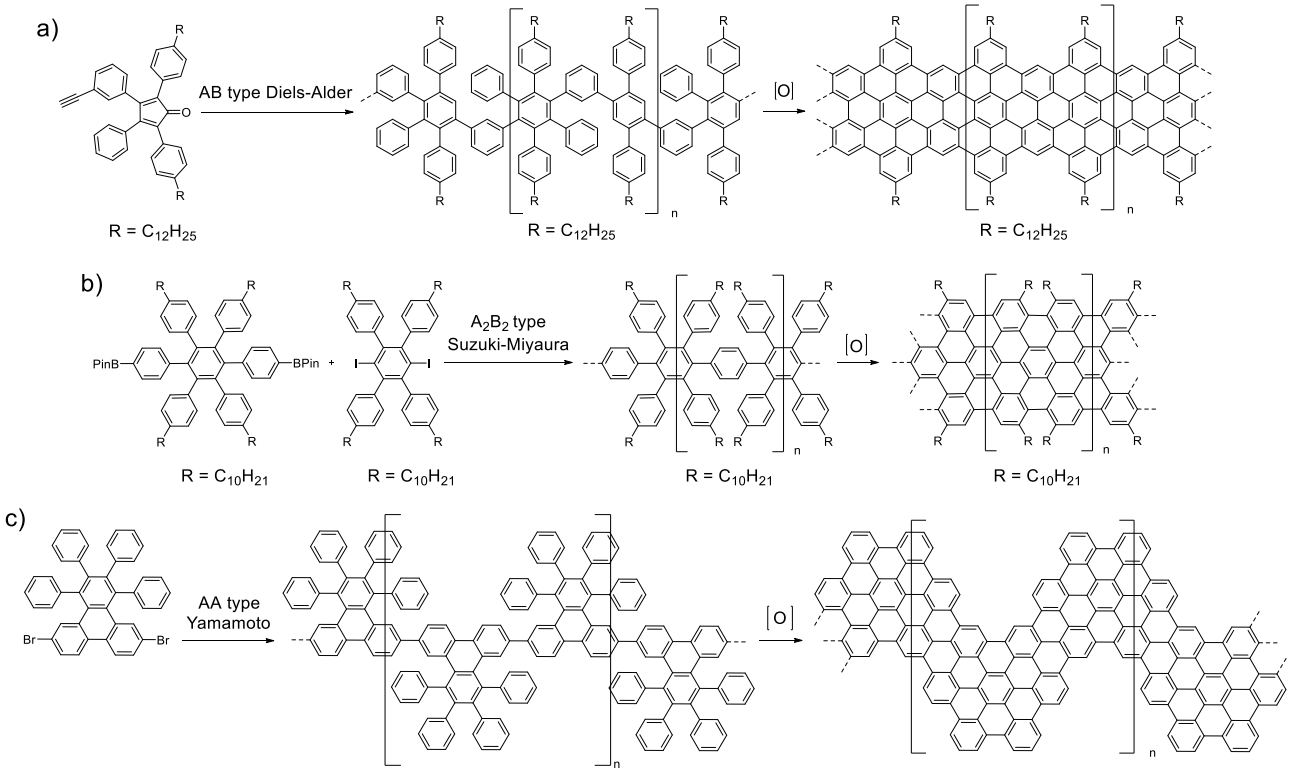

Fig. I-36 Main synthetic strategies developed in solution for the synthesis of GNRs *via* a) AB type Diels-Alder polymerisation;[193] b) A_2B_2 type Suzuki-Miyaura polymerisation;[195] c) AA type Yamamoto polymerisation.[199]

Beyond the modifications of morphology like width and edges, bandgaps of GNRs can be also modulated by doping with heteroelements. The bottom-up approach allows the control of doping parameters like the positions of dopants and the doping ratio in the structures. For example, Vo *et al.*[201] reported the formation of a nitrogen-doped c-GNR from 5-(6,11-dibromo-1,3,4-triphenyltriphenylen-2-yl)pyrimidine monomer (**Fig. I-37**). Considering the partial cyclodehydrogenation reported with the example of pyridyl-disubstituted dibenzo-helicene in solution (**Fig. I-35**), we can wonder if the nitrogen-doped c-GNR reported in this work was fully conjugated. Only the resolution of its bonding structure with non-contact STM[202,203] would definitely prove the authenticity of the fully conjugated nitrogen-doped c-GNR reported.

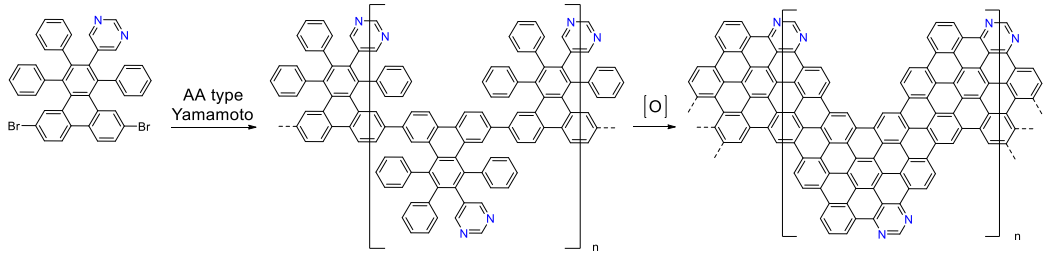

Fig. I-37 Example of c-GNR doped with nitrogens. By the use of a bottom-up approach , doping parameters like positions of dopants and doping ratio are perfectly controlled and defined.[201]

In 2010, Fasel and Müllen developed a surface-assisted protocol for the formation of A-GNR and c-GNR.[108] The protocol depends on a hierarchical strategy based on a first step of dehalogenative coupling at T_1 (around 200°C) and a second step of cyclodehydrogenation to afford the corresponding GNR at T_2 (around 400°C).

For the last nine years, inspired by the work of Müllen and Fasel, many GNR structures and GNRs containing heterojunctions have been reported and studied in order to understand the impact of the structural parameters and the role of doping on the optical and electronic properties of ribbons.[204]

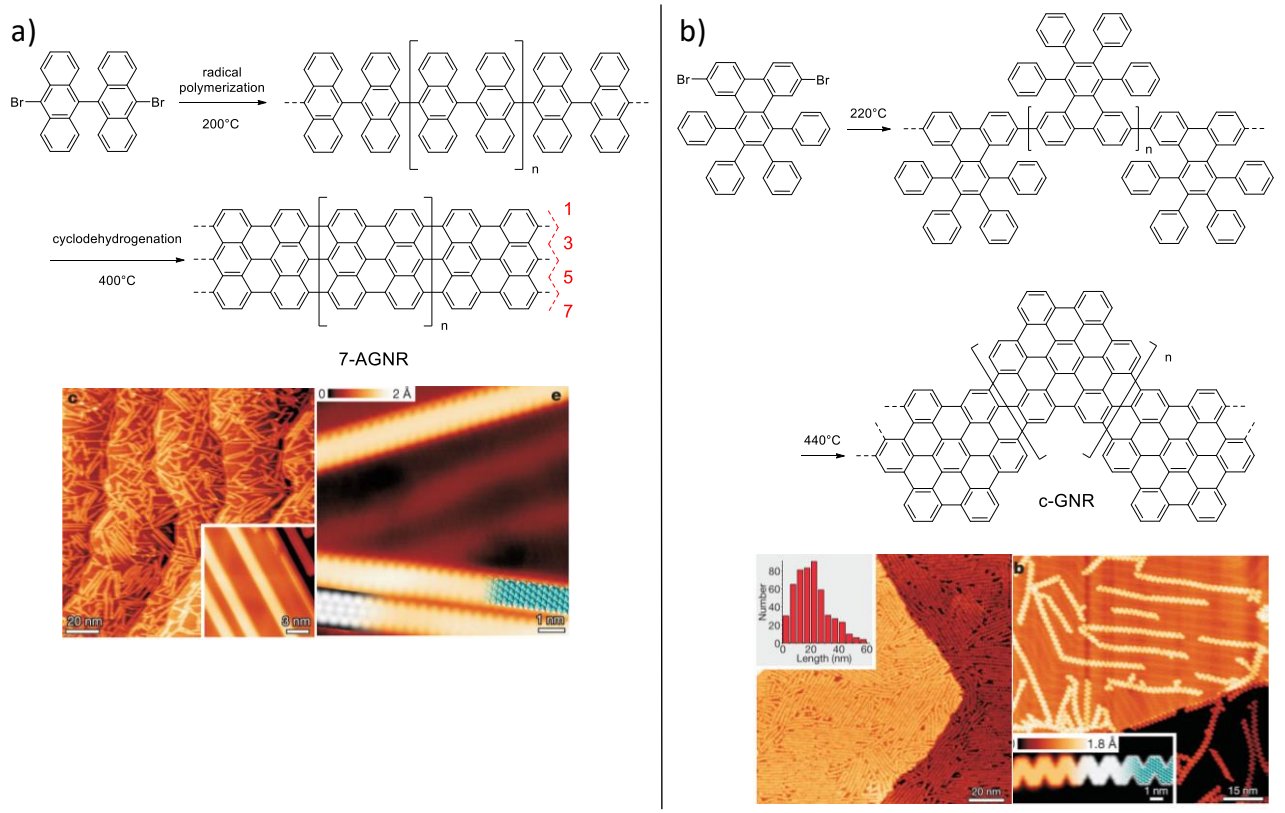

Fig. I-38 Surface-assisted protocol developed by Müllen and Fasel for the fabrication of a) straight A-GNR and b) c-GNR with corresponding STM images on Au (111) superimposed with calculated models in blue.[108]

A variety of armchair-GNRs (A-GNRs) have been reported and were classified into three families depending of their distinct properties:[146,153]

- The N = 3*p* and N = 3*p*+1 families (*p* is an integer and N the number of carbon rows forming GNRs, see **Fig. I-39**) exhibit wide bandgaps inversely proportional to the width of ribbons.
- The N = 3*p*+2 family which is supposed to be nearly metallic with a very small bandgap.

The group of Liljeroth reported the structure of the thinnest GNR of the N=3*p*+2 family with a width corresponding to N=5 (**Fig. I-39**, a). A very narrow bandgap of 0.1 eV was determined by Scanning Tunneling Spectroscopy (STS).[205] Concerning the N=3*p* and N=3*p*+1 families, in 2017 the group of Fasel reported the structure of 9-GNR (N=9) (**Fig. I-39**, b)[206] which can be seen as a larger version of the 7-GNR reported by the same group in 2010 (**Fig. I-38**, a). While a bandgap of 2.4-2.7 eV was previously found for the 7-GNR,[207,208] a lower bandgap of 1.7 eV was determined for the 9-GNR by STS. Finally, the groups of Crommie and Fischer reported the fabrication of a larger 13-GNR on Au (111)[156] and STS characterization again exhibited a smaller gap (around 1.4 eV) compared to the 9-GNR. These experimental results clearly illustrated the dependence between the widths and the bandgaps of GNRs.

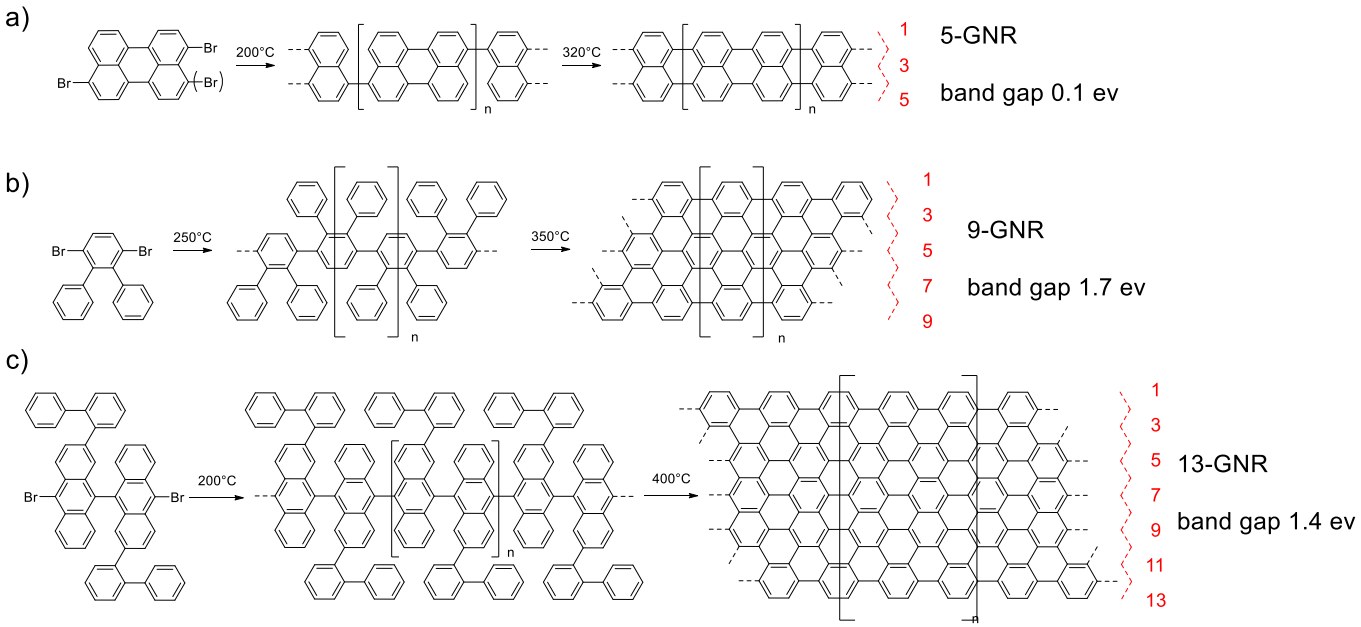

Fig. I-39 On surface synthesis on Au (111) of straight A-GNRs with different widths: a) N = 5;[205] b) N = 9[206] and c) N = 13.[156]

Zig-zag GNRs (z-GNRs) are expected to possess magnetic properties due to their spin polarized edge states and might be promising for spintronic applications.[209] Intrinsically, a ferromagnetic coupling is expected along the edges while an antiferromagnetic comportment is expected between the edges.[143] The experimental visualization of these spin polarized edge states required highly uniform structures exhibiting an atomic precision that cannot be achieved with the classical top-down methods. The formation of z-GNRs was first achieved on surface by Ruffieux *et al.*[157] in 2016. Chemical structures, STM and non-contact AFM images of these GNRs are displayed in **Fig. I-40**. Despite the high structural quality, these z-GNRs did not yet confirm the predicted magnetism.

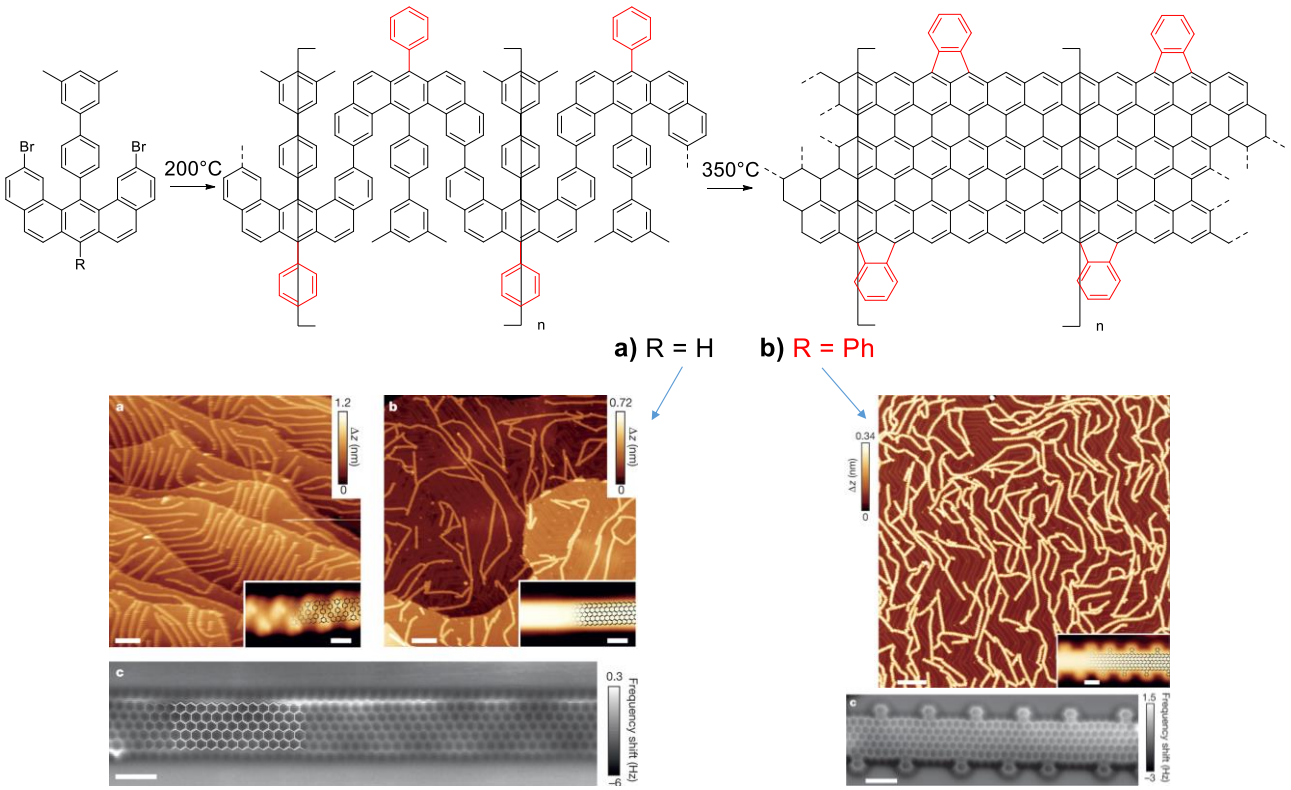

Fig. I-40 Synthetic route of z-GNRs synthesised by on-surface protocol (top) and their corresponding nc-STM and nc-AFM images on Au (111).[157]

Finally, the effect of concentration of dopant on the band structures of GNRs has been investigated by Bronner *et al.*[210] In this work, two nitrogen-doped c-GNRs were synthesised from different monomers containing either one or two pyridine rings (**Fig. I-41**, a-b) and compared to the nitrogen-free c-GNR developed by Mullen and Fasel in 2010 (**Fig. I-38**, b). The characterization of these GNRs by ultraviolet photoelectron spectroscopy (UPS) and angle-resolved high-resolution electron energy loss spectroscopy (HREELS) demonstrated that although the bandgaps were unaffected by the presence of nitrogen in the GNRs, the entire band structure shifted to lower energy as a function of the concentration of dopants. Vo *et al.*[211] reported another example of a nitrogen-doped structure with an increase of the nitrogen content (**Fig. I-41**, c). According to STS studies, the comparison between the nitrogen-doped GNR and its nitrogen-free version revealed similar bandgap close to 2 eV, and confirmed the results of Bronner *et al.* concerning the band alignments that can be achieved independently of the difference in energy between the valence and the conduction bands.

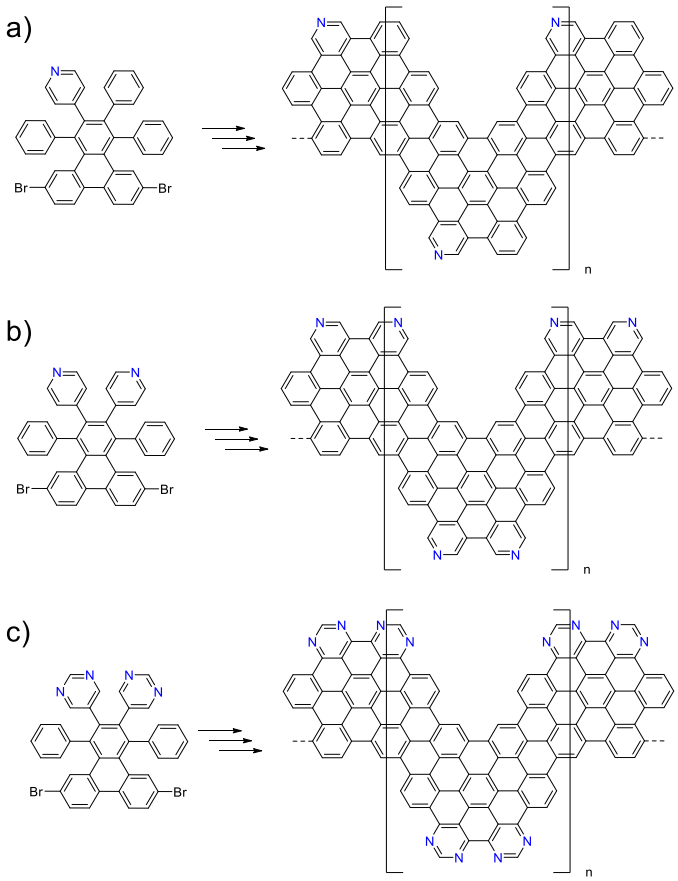

Fig. I-41 Structures of nitrogen-doped GNRs with variable nitrogen contents synthesised on Au (111) reported by a-b) Bronner *et al.*;[210] and c) Vo *et al.*[211]

Incorporation of sulphur in the structure of a GNR was reported by the groups of Crommie and Fischer and because of the small difference of electronegativity between carbon and sulphur atoms, the authors concluded that doping with sulphur did not strongly affect the position of the conduction band (**Fig. I-42**, a).[212] The p-type doping of GNRs with boron has been investigated simultaneously by Cloke *et al.*[213] and Kawai *et al.*[214] and the electronic structure of a boron-doped 7-GNR was investigated by both DFT calculations and STS (**Fig. I-42**, b). Although DFT calculations suggested that doping with boron introduced acceptor bands at energies within the gap, reducing the latter from 2.1 to 0.8 eV, comparable bandgaps of 2.4 eV were experimentally estimated by STS between the boron-doped GNR and its 7-GNR analogue on Au (111) leaving the overall electronic structure unchanged. Finally, it turns out that several factors, like the morphology of the ribbon, the position of the dopants in the backbone and the doping ratio, need to be considered to understand the effect of nitrogen, sulphur or boron dopants on the electronic structure.

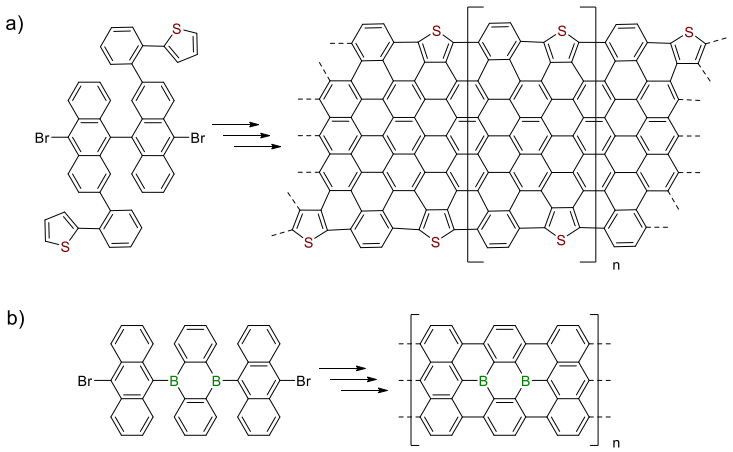

Fig. I-42 Structures a) sulphur doped-;[212] and b) boron-doped GNRs[213,214] synthetised on Au (111).

I. 3.5.3. Bottom-up preparation of Graphene Nanomeshes

The bottom-up synthesis of network structures requires the deposition on a surface of organic precursors containing at least three connecting groups to afford a 2D polymerisation. For example, the synthesis of polyphenylene networks known as Porous Aromatic Frameworks (PAFs) were initially performed in solution[215–217] and investigated for their high stabilities, low densities and large surface areas that are promising for applications in gas and energy storage,[218,219] catalysis,[220] sensing.[221] Later on, their on surface-synthesis were investigated by the group of Lackinger starting from a tris-phenylbenzene (**Fig. I-43**, a)[222] and by the groups of Müllen and Fasel starting from a hexaiodo-substituted cyclohexa-*m*-phenylene (**Fig. I-43**, b).[223] However, the network reported by the group of Lackinger produced irregular structures with by the formation of penta-, hexa- and heptagons. A less-defective network was obtained *via* Ullman coupling of the preformed macrocycle in the work of Müllen and Fasel.

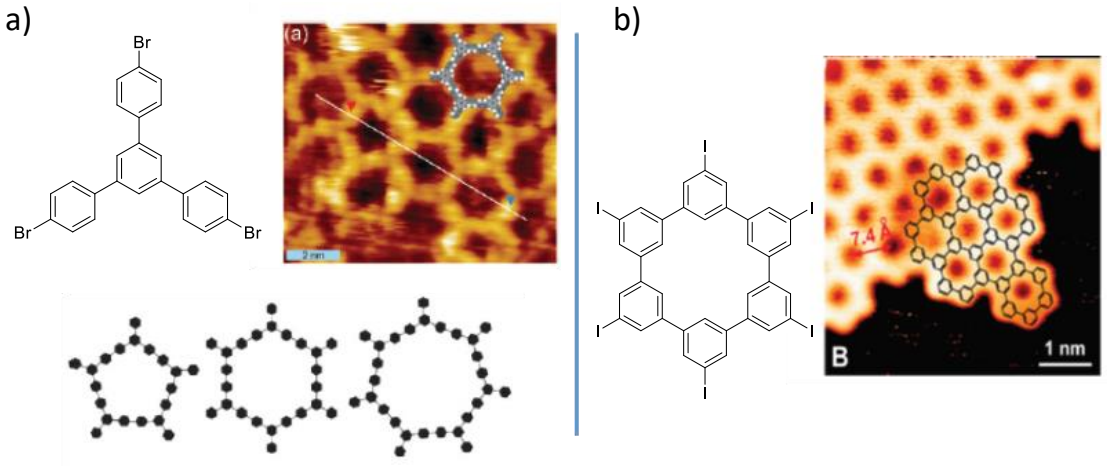

Fig. I-43 Chemical structures and STM images of 2D networks of polyphenylenes from: a) 1,3,5-tris-(4'-bromophenyl)benzene[222] b) cyclohexa-*m*-phenylene.[223]

Examples of on-surface synthesis of networks containing sulphur and nitrogen have been reported in the literature. Cardenas et *al.*[224] reported the formation of a sulphur-doped network on Ag (111) from tetrabromotetrathienoanthracene (**TBTTA)** (**Fig. I-44**, a) and Liu et *al.*[225] reported the structure of nitrogen-doped networks on Au (111) from tetrabromodibenzo[a,c]dibenzo[5,6:7,8]quinoxalino-[2,3-i]phenazine (**TBQP**, **Fig. I-44**, b). However, some irregularities were still observed in these resulting networks due to the rotational disorder of the precursors. The use of rigid precursors like methylene-bridged triphenylamine (**DTPA, Fig. I-44**, c) or carbonyl-bridged triphenylamines (**CTPA, Fig. I-44**, d) allowed the formation of less-defective network as reported by Bieri *et al.*[226] on Ag (111) and Steiner *et al.*[227] on Au (111) respectively. In 2011, Abel *et al.*[228] and Nardi *et al.*[229] reported another strategy for the conception of nitrogen-doped 2D network on Au (111) or Ag (111) based on the *in-situ* creation of phthalocyanine macrocycles formed *via* cyclotetramerization from precursors containing tetracarbonitrile groups (**Fig. I-44**, e).

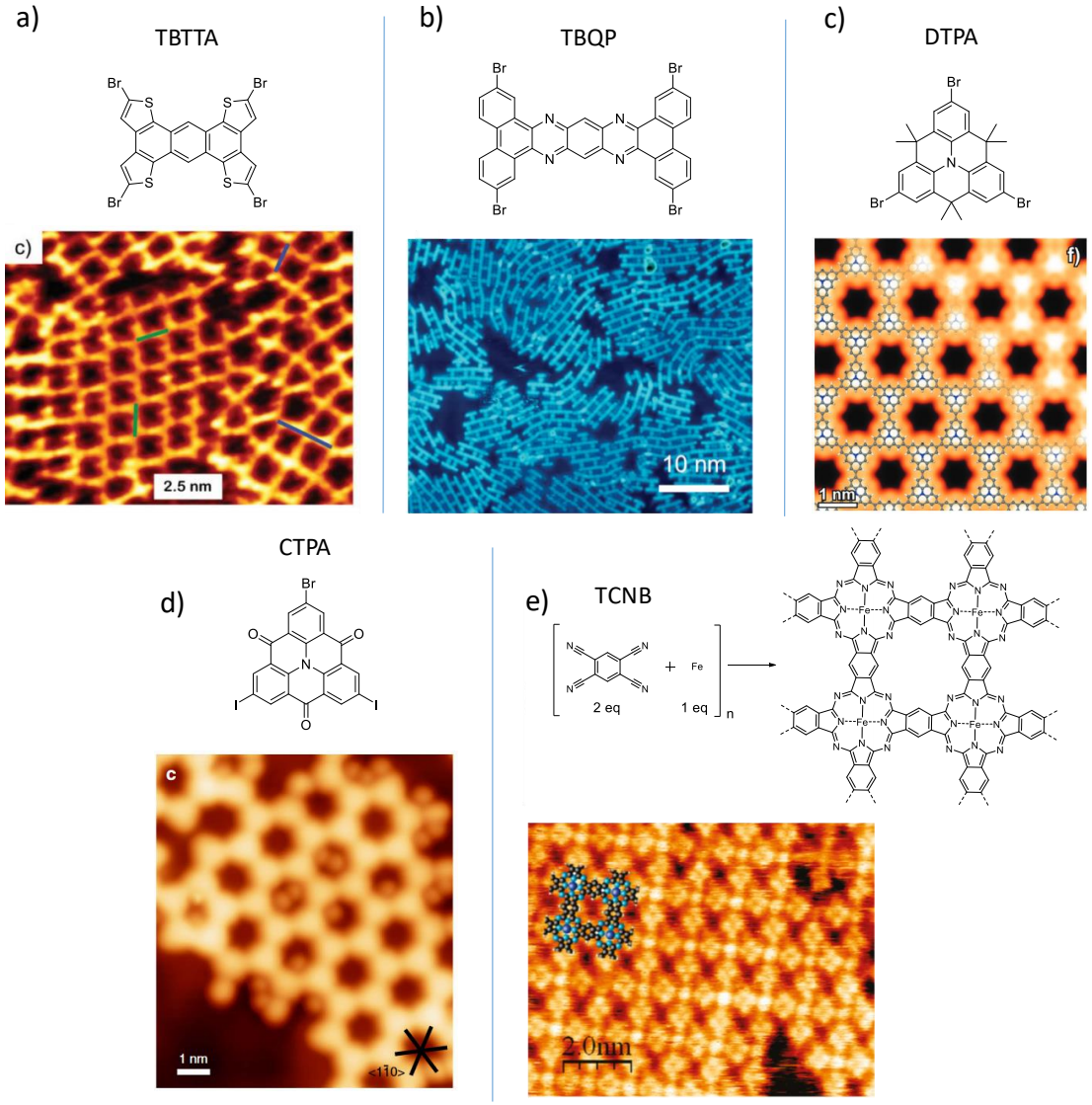

Fig. I-44 Chemical structures and corresponding STM images of heteroatomically-doped networks.[224–228]

Although these 2D covalent networks can in some aspects be related to GNMs; in most cases, the "graphene necks" are constituted by a single C-C bond between phenyl rings. Because of the free rotation along the single bond and the steric hindrance between the hydrogen atoms in position *ortho* to the C-C bond, the phenyl rings are not coplanar, which significantly reduces the delocalization of electrons and decreases the conductivity. To increase the conductivity, it is necessary to develop new precursors that could lead to structures with larger "graphene necks". According to our knowledge, no example of bottom-up synthesis of networks with such large necks corresponding to the definition of GNMs have been reported in the literature.

I. 4. Aim of the thesis

For the last decades, π-extended porphyrins have been actively explored for their electronic, optical and electrochemical properties. In some aspects, these π-extended porphyrins can be seen as nitrogen-doped GQDs with promising NIR properties. However, the cyclodehydrogenation reaction required to induce aromatisation occurred only under very specific conditions as shown in the works of the groups of Yamane, Osuka and Anderson (section **I. 1.3**). The pyrolysis technique reported by the group of Thompson was proven to activate the β-fusion of *meso*-substituted PAH-porphyrins containing zinc and could represent an alternative method to the Scholl reaction. Therefore, we would like to investigate the technique of pyrolysis to achieve the fusion of various *meso*-substituted porphyrins with symmetric PAHs to prevent the formation of isomers and afford nitrogen-doped GQD-based on porphyrins. On the other hand, the properties of porphyrins used as building blocks for the fabrication of supramolecular assemblies have been widely investigated both in solution and on surfaces and could be applied for the bottom-up fabrication of atomically defined nitrogen-doped GNRs and GNMs. Consequently, for symmetry and electronic reasons, we chose to design and develop the synthesis of building blocks based on halogenated anthracenylporphyrins. Our objective is to use these precursors for the fabrication of controlled structures of nitrogen-doped GNRs and GNMs on surface.

The second chapter of this thesis is dedicated to the synthesis of halogenated anthracenylporphyrin-based building blocks and to the investigation of their assemblies on-surface with Scanning Tunneling Microscopy (STM). Several porphyrins with variation of structures and halogens have been imagined to trigger on surface either a linear polymerisation to form nitrogen-doped GNRs or a 2D polymerisation to form nitrogen-doped GNMs as illustrated in **Fig. I-45**.

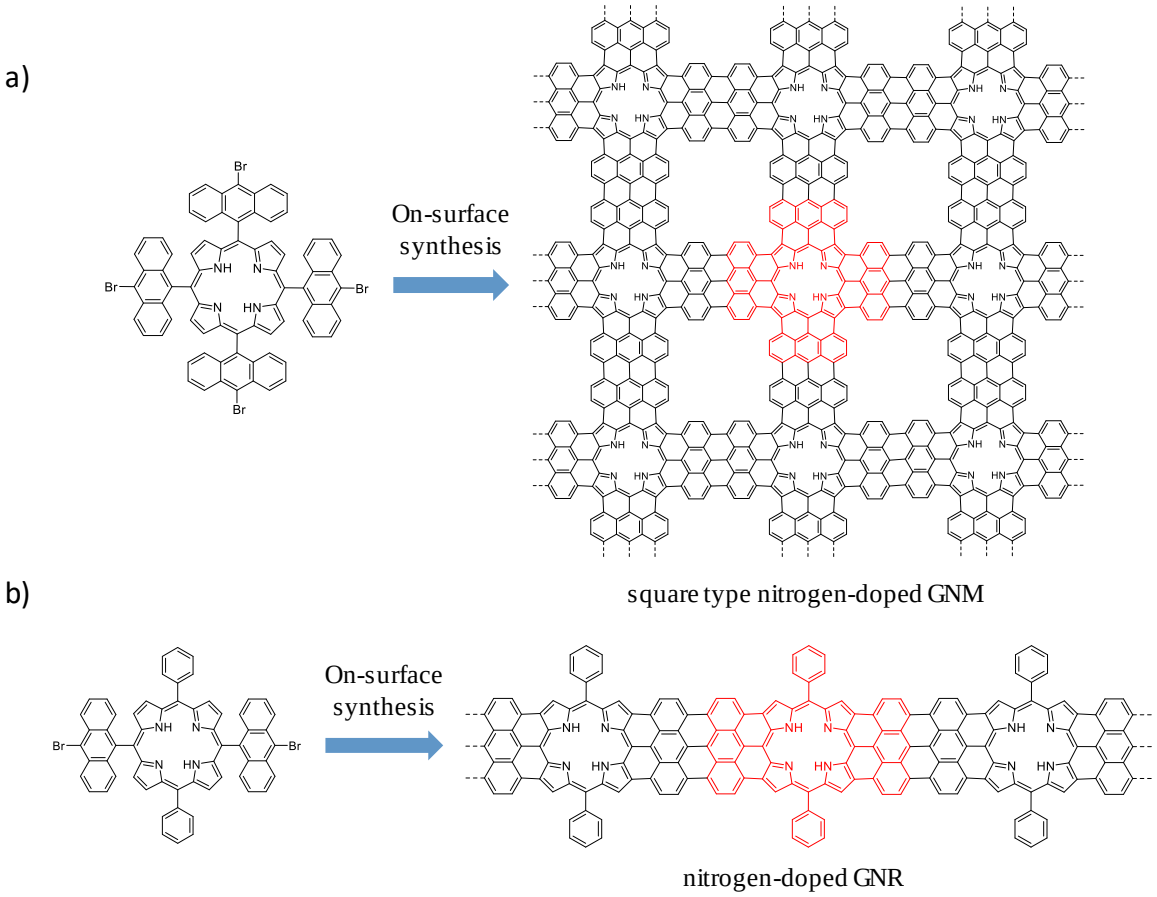

Fig. I-45 Target structures of atomically defined nitrogen-doped GNR and GNM from a) tetra- and b) bis-bromoanthracenylporphyrins.

The third chapter is dedicated to the study of formation of π-extended porphyrins *via* a method of pyrolysis able to activate the reaction of fusion of *meso*-substituted Znporphyrins with PAHs. A series of experiments were conducted on various *meso*-substituted porphyrins with anthracene, pyrene or naphthalene derivatives (**Fig. I-46**).

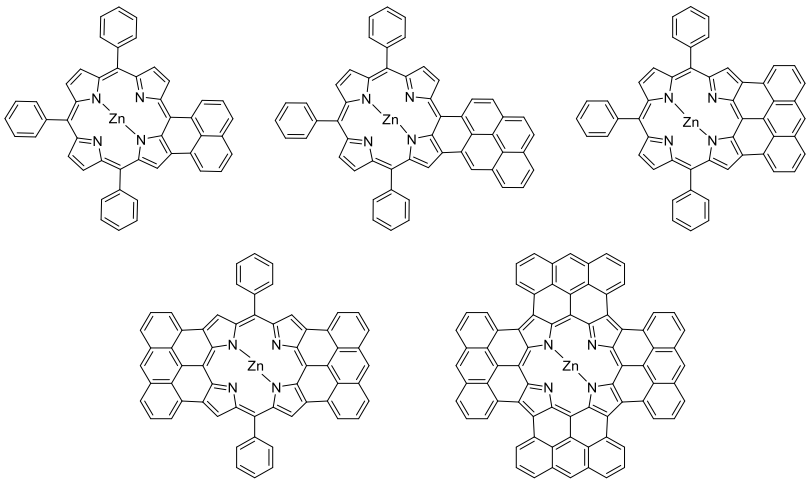

Fig. I-46 Target structures of π-extended porphyrins we aim to form *via* thermal activation of the cyclodehydrogenation reaction from *meso*-substituted Znporphyrin with naphthalene, pyrene and anthracene derivatives.

Finally, the chapter IV is dedicated to the post synthetic modification of a tetrabromoanthracenylporphyrin with additional PAHs at its periphery *via* Suzuki-Miyaura coupling reaction (**Fig. I-47**). Absorption and fluorescence measurements were conducted to characterize the optical properties of these original anthracenylporphyrin-based molecules.

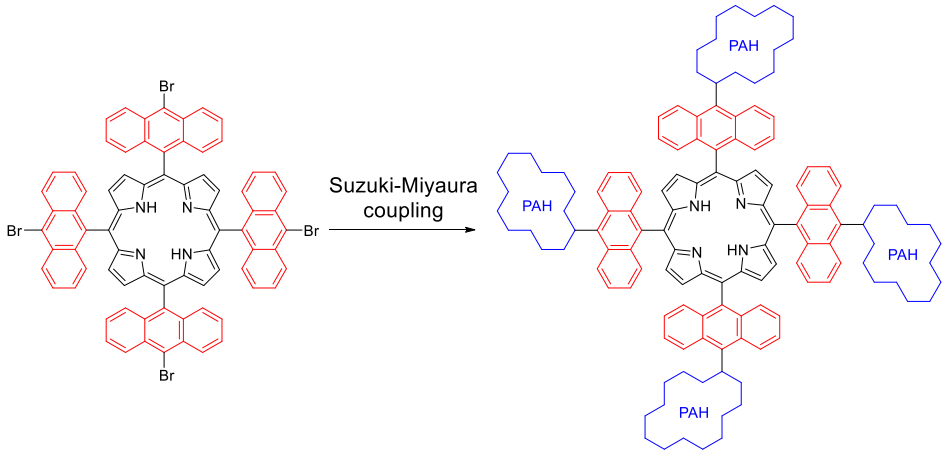

Fig. I-47 Illustration of the Suzuki-Miyaura coupling for the post synthetic modification of a tetrabromoanthracenylporphyrin with additional PAHs.

I. 5. References

(1) Fischer, H.; Orth, H. Die Chemie Des Pyrrols. *Akademische Verlagsgesellschaft, Leipzig* **1937**, *11.1*.

(2) Fischer, H.; Orth, H. Die Chemie Des Pyrrols. *Akademische Verlagsgesellschaft, Leipzig* **1940**, *11.2*.

(3) Moss, G. P. Nomenclature of Tetrapyrroles. *Eur. J. Biochem.* **1988**, *178*, 277–328.

(4) Krause, G. H.; Weis, E. Chlorophyll Fluorescence and Photosynthesis: The Basics. *Annu. Rev. Plant Physiol. Plant Mol. Biol.* **1991**, *42*, 313–349.

(5) Baldwin, J. M. Structure and Function of Haemoglobin. *Prog. Biophys. Mol. Biol.* **1976**, *29*, 225–320.

(6) Rothemund, P. Formation of Porphyrins from Pyrrole and Aldehydes. *J. Am. Chem. Soc.* **1935**, *57*, 2010–2011.

(7) Adler, A. D.; Longo, F. R.; Shergalis, W. Mechanistic Investigations of Porphyrin Syntheses. I. Preliminary Studies on Ms-Tetraphenylporphin. *J. Am. Chem. Soc.* **1964**, *86*, 3145–3149.

(8) Little, R. G.; Anton, J. A.; Loach, P. A.; Ibers, J. A. The Synthesis of Some Substituted Tetraarylporphyrins. *J. Heterocycl. Chem.* **1975**, *12*, 343–349.

(9) Lindsey, J. S.; Hsu, H. C.; Schreiman, I. C. Synthesis of Tetraphenylporphyrins under Very Mild Conditions. *Tetrahedron Lett.* **1986**, *27*, 4969–4970.

(10) Arsenault, G. P.; Bullock, E.; MacDonald, S. F. Pyrromethanes and Porphyrins Therefrom. *J. Am. Chem. Soc.* **1960**, *82*, 4384–4389.

(11) Kooriyaden, F. R.; Sujatha, S.; Arunkumar, C. Study of Scrambling in Porphyrin Forming Reactions: Synthesis, Structure, Photophysical, Electrochemical and Antimicrobial Studies. *Polyhedron* **2017**, *128*, 85–94.

(12) Littler, B. J.; Ciringh, Y.; Lindsey, J. S. Investigation of Conditions Giving Minimal Scrambling in the Synthesis of Trans -Porphyrins from Dipyrromethanes and Aldehydes. *J. Org. Chem.* **1999**, *64*, 2864–2872.

(13) Okujima, T.; Mack, J.; Nakamura, J.; Kubheka, G.; Nyokong, T.; Zhu, H.; Komobuchi, N.; Ono, N.; Yamada, H.; Uno, H.; et al. Synthesis, Characterization, and Electronic Structures of Porphyrins Fused with Polycyclic Aromatic Ring Systems. *Chem. Eur. J.* **2016**, *22*, 14730–14738.

(14) Boudif, A.; Momenteau, M. A New Convergent Method for Porphyrin Synthesis Based on a '3 + l' Condensation. *J. Chem. Soc. Perkin Trans. 1* **1996**, *0*, 1235–1242.

(15) Arlegui, A.; El-Hachemi, Z.; Crusats, J.; Moyano, A. 5-Phenyl-10,15,20-Tris(4-Sulfonatophenyl)Porphyrin: Synthesis, Catalysis, and Structural Studies. *Molecules* **2018**, *23*, 3363.

(16) Lindsey, J. S.; Du, H.; Fuh, R.-C. A.; Li, J.; Corkan, L. A.; Dixon, J. M.; Taniguchi, M. PhotochemCAD. 2018.

(17) Arnold, D. P. Aromatic Ring Currents Illustrated-NMR Spectra of Tin(IV) Porphyrin Complexes. *J. Chem. Ed.* **1988**, *65*, 1111–1112.

(18) Rose, E.; Andrioletti, B.; Zrig, S.; Quelquejeu-Ethève, M. Enantioselective Epoxidation of Olefins with Chiral Metalloporphyrin Catalysts. *Chem. Soc. Rev.* **2005**, *34*, 573–583.

(19) Srour, H.; Maux, P. Le; Simonneaux, G. Enantioselective Manganese-Porphyrin-Catalyzed Epoxidation and C-H Hydroxylation with Hydrogen Peroxide in Water/Methanol Solutions. *Inorg. Chem.* **2012**, *51*, 5850–5856.

(20) Zhang, J.-L.; Zhou, H.-B.; Huang, J.-S.; Che, C.-M. Dendritic Ruthenium Porphyrins: A New Class of Highly Selective Catalysts for Alkene Epoxidation and Cyclopropanation. *Chem. Eur. J.* **2002**, *8*, 1554–1562.

(21) Mori, T.; Santa, T.; Higuchi, T.; Mashino, T.; Hirobe, M. Oxygen Activation by Iron(III)-Porphyrin/NaBH4/Me4N.OH System as Cytochrome P-450 Model. Oxygenation of Olefin, N-Dealkylation of Tertiary Amine, Oxidation of Sulfide, and Oxidative Cleavage of Ether Bond. *Chem. Pharm. Bull.* **1993**, *41*, 292–295.

(22) Baciocchi, E.; Gerini, M. F.; Lapi, A. Synthesis of Sulfoxides by the Hydrogen Peroxide Induced Oxidation of Sulfides Catalyzed by Iron Tetrakis(Pentafluorophenyl)Porphyrin: Scope and Chemoselectivity. *J. Org. Chem.* **2004**, *69*, 3586–3589.

(23) Oae, S.; Watanabe, Y.; Fujimori, K. Biomimetic Oxidation of Organic Sulfides with TPPFe(III)Cl/Imidazole/Hydrogen Peroxide. *Tetrahedron Lett.* **1982**, *23*, 1189–1192.

(24) Iida, T.; Ogawa, S.; Hosoi, K.; Makino, M.; Fujimoto, Y.; Goto, T.; Mano, N.; Goto, J.; Hofmann, A. F. Regioselective Oxyfunctionalization of Unactivated Carbons in Steroids by a Model of Cytochrome P-450: Osmiumporphyrin Complex/Tert-Butyl Hydroperoxide System. *J. Org. Chem.* **2007**, *72*, 823–830.

(25) Ogawa, S.; Wakatsuki, Y.; Makino, M.; Fujimoto, Y.; Yasukawa, K.; Kikuchi, T.; Ukiya, M.; Akihisa, T.; Iida, T. Oxyfunctionalization of Unactivated C-H Bonds in Triterpenoids with Tert-Butylhydroperoxide Catalyzed by Meso-5,10,15,20-Tetramesitylporphyrinate Osmium(II) Carbonyl Complex. *Chem. Phys. Lipids* **2010**, *163*, 165–171.

(26) Ren, Q. G.; Chen, S. Y.; Zhou, X. T.; Ji, H. B. Highly Efficient Controllable Oxidation of Alcohols to Aldehydes and Acids with Sodium Periodate Catalyzed by Water-Soluble Metalloporphyrins as Biomimetic Catalyst. *Bioorganic Med. Chem.* **2010**, *18*, 8144–8149.

(27) Ji, H. B.; Yuan, Q. L.; Zhou, X. T.; Pei, L. X.; Wang, L. F. Highly Efficient Selective Oxidation of Alcohols to Carbonyl Compounds Catalyzed by Ruthenium (III) Meso-Tetraphenylporphyrin Chloride in the Presence of Molecular Oxygen. *Bioorganic Med. Chem. Lett.* **2007**, *17*, 6364–6368.

(28) Morozan, A.; Campidelli, S.; Filoramo, A.; Jousselme, B.; Palacin, S. Catalytic Activity of Cobalt and Iron Phthalocyanines or Porphyrins Supported on Different Carbon Nanotubes towards Oxygen Reduction Reaction. *Carbon* **2011**, *49*, 4839–4847.

(29) Zhang, W.; Lai, W.; Cao, R. Energy-Related Small Molecule Activation Reactions: Oxygen Reduction and Hydrogen and Oxygen Evolution Reactions Catalyzed by Porphyrin- and Corrole-Based Systems. *Chem. Rev.* **2017**, *117*, 3717–3797.

(30) Yella, A.; Lee, H.-W.; Tsao, H. N.; Yi, C.; Chandiran, K. A.; Nazeeruddin, M. K.; Diau, E. W.; Yeh, C.-Y.; Zakeeruddin, S. M.; Grätzel, M. Porphyrin-Sensitized Solar Cells with Cobalt (II/III)-Based Redox Electrolyte Exceed 12 Percent Efficiency. *Science* **2011**, *334*, 629–633.

(31) Mathew, S.; Yella, A.; Gao, P.; Humphry-Baker, R.; Curchod, B. F. E.; Ashari-Astani, N.; Tavernelli, I.; Rothlisberger, U.; Nazeeruddin, M. K.; Grätzel, M. Dye-Sensitized Solar Cells with 13% Efficiency Achieved through the Molecular Engineering of Porphyrin Sensitizers. *Nat. Chem.* **2014**, *6*, 242–247.

(32) Bottari, G.; de la Torre, G.; Guldi, D. M.; Torres, T. Covalent and Noncovalent Phthalocyanine-Carbon Nanostructure Systems: Synthesis, Photoinduced Electron Transfer, and Application to Molecular Photovoltaics. *Chem. Rev.* **2010**, *110*, 6768–6816.

(33) Imahori, H.; Umeyama, T.; Ito, S. Large π-Aromatic Molecules as Potential Sensitizers for Highly Efficient Dye-Sensitized Solar Cells. *Acc. Chem. Res.* **2009**, *42*, 1809–1818.

(34) Gai, F.; Zhou, T.; Zhang, L.; Li, X.; Hou, W.; Yang, X.; Li, Y.; Zhao, X.; Xu, D.; Liu, Y.; et al. Silica Cross-Linked Nanoparticles Encapsulating Fluorescent Conjugated Dyes for Energy Transfer-Based White Light Emission and Porphyrin Sensing. *Nanoscale* **2012**, *4*, 6041–6049.

(35) Ding, Y.; Zhu, W. H.; Xie, Y. Development of Ion Chemosensors Based on Porphyrin Analogues. *Chem. Rev.* **2017**, *117*, 2203–2256.

(36) Paolesse, R.; Nardis, S.; Monti, D.; Stefanelli, M.; Di Natale, C. Porphyrinoids for Chemical Sensor

Applications. *Chem. Rev.* **2017**, *117*, 2517–2583.

(37) Dini, D.; Calvete, M. J. F.; Hanack, M. Nonlinear Optical Materials for the Smart Filtering of Optical Radiation. *Chem. Rev.* **2016**, *116*, 13043–13233.

(38) Senge, M. O.; Fazekas, M.; Notaras, E. G. A.; Blau, W. J.; Zawadzka, M.; Locos, O. B.; Ni Mhuircheartaigh, E. M. Nonlinear Optical Properties of Porphyrins. *Adv. Mater.* **2007**, *19*, 2737–2774.

(39) Bhyrappa, P. Recent Advances in Mixed β-Pyrrole Substituted Meso-Tetraphenylporphyrins. *Tetrahedron Lett.* **2016**, *57*, 5150–5167.

(40) Vargas, A.; Pegaz, B.; Debefve, E.; Konan-Kouakou, Y.; Lange, N.; Ballini, J. P.; Van Den Bergh, H.; Gurny, R.; Delie, F. Improved Photodynamic Activity of Porphyrin Loaded into Nanoparticles: An in Vivo Evaluation Using Chick Embryos. *Int. J. Pharm.* **2004**, *286*, 131–145.

(41) Kolarova, H.; Nevrelova, P.; Tomankova, K.; Kolar, P.; Bajgar, R.; Mosinger, J. Production of Reactive Oxygen Species after Photodynamic Therapy by Porphyrin Sensitizers. *Gen. Physiol. Biophys.* **2008**, *27*, 101–105.

(42) Ethirajan, M.; Chen, Y.; Joshi, P.; Pandey, R. K. The Role of Porphyrin Chemistry in Tumor Imaging and Photodynamic Therapy. *Chem. Soc. Rev.* **2011**, *40*, 340–362.

(43) Singh, S.; Aggarwal, A.; Bhupathiraju, N. V. S. D. K.; Arianna, G.; Tiwari, K.; Drain, C. M. Glycosylated Porphyrins, Phthalocyanines, and Other Porphyrinoids for Diagnostics and Therapeutics. *Chem. Rev.* **2015**, *115*, 10261–10306.

(44) Lewtak, J. P.; Gryko, D. T. Synthesis of π-Extended Porphyrins via Intramolecular Oxidative Coupling. *Chem. Commun.* **2012**, *48*, 10069–10086.

(45) Grzybowski, M.; Skonieczny, K.; Butenschön, H.; Gryko, D. T. Comparison of Oxidative Aromatic Coupling and the Scholl Reaction. *Angew. Chem. Int. Ed.* **2013**, *52*, 9900–9930.

(46) Yamane, O.; Sugiura, K.; Miyasaka, H.; Nakamura, K.; Fujimoto, T.; Nakamura, K.; Kaneda, T.; Sakata, Y.; Yamashita, M. Pyrene-Fused Porphyrins: Annulation Reactions of Meso-Pyrenylporphyrins. *Chem. Lett.* **2004**, *33*, 40–41.

(47) Kurotobi, K.; Kim, K. S.; Noh, S. B.; Kim, D.; Osuka, A. A Quadruply Azulene-Fused Porphyrin with Intense near-IR Absorption and a Large Two-Photon Absorption Cross Section. *Angew. Chem. Int. Ed.* **2006**, *45*, 3944–3947.

(48) Davis, N. K. S.; Thompson, A. L.; Anderson, H. L. A Porphyrin Fused to Four Anthracenes. *J. Am. Chem. Soc.* **2011**, *133*, 30–31.

(49) Chen, Q.; Brambilla, L.; Daukiya, L.; Mali, K. S.; De Feyter, S.; Tommasini, M.; Müllen, K.; Narita, A. Synthesis of Triply Fused Porphyrin-Nanographene Conjugates. *Angew. Chem. Int. Ed.* **2018**, *57*, 11233–11237.

(50) Diev, V. V.; Schlenker, C. W.; Hanson, K.; Zhong, Q.; Zimmerman, J. D.; Forrest, S. R.; Thompson, M. E. Porphyrins Fused with Unactivated Polycyclic Aromatic Hydrocarbons. *J. Org. Chem.* **2012**, *77*, 143–159.

(51) Drain, C. M.; Lehn, J. Self-Assembly of Square Multiporphyrin Arrays by Metal Ion Coordination. *J. Chem. Soc. Chem. Commun.* **1994**, 2313.

(52) Otsuki, J. Supramolecular Approach towards Light-Harvesting Materials Based on Porphyrins and Chlorophylls. *J. Mater. Chem. A* **2018**, *6*, 6710–6753.

(53) Cen, T.-Y.; Wang, S.-P.; Zhang, Z.; Wu, J.; Li, S. Flexible Porphyrin Cages and Nanorings. *J. Porphyr. Phthalocyanines* **2018**, *22*, 726–738.

(54) Wang, S.-P.; Shen, Y.-F.; Zhu, B.-Y.; Wu, J.; Li, S. Recent Advances in the Template-Directed Synthesis of Porphyrin Nanorings. *Chem. Commun.* **2016**, *52*, 10205–10216.

(55) Haino, T. Designer Supramolecular Polymers with Specific Molecular Recognitions. *Polym. J.* **2019**, *51*, 303–318.

(56) Li, J.; Ambroise, A.; Yang, S. I.; Diers, J. R.; Seth, J.; Wack, C. R.; Bocian, D. F.; Holten, D.; Lindsey, J. S. Template-Directed Synthesis , Excited-State Photodynamics , and Electronic Communication in a Hexameric Wheel of Porphyrins. *J. Am. Chem. Soc.* **1999**, *121*, 8927–8940.

(57) Prathapan, S.; Johnson, T. E.; Lindsey, J. S. Building-Block Synthesis of Porphyrin Light-Harvesting Arrays. *J. Am. Chem. Soc.* **1993**, *115*, 7519–7520.

(58) Wytko, J. A.; Ruppert, R.; Jeandon, C.; Weiss, J. Metal-Mediated Linear Self-Assembly of Porphyrins. *Chem. Commun.* **2018**, *54*, 1550–1558.

(59) Aratani, N.; Osuka, A. Monodisperse Giant Porphyrin Arrays. *Macromol. Rapid Commun.* **2001**, *22*, 725–740.

(60) Day, N. U.; Wamser, C. C.; Walter, M. G. Porphyrin Polymers and Organic Frameworks. *Polym. Int.* **2015**, *64*, 833–857.

(61) Aratani, N.; Takagi, A.; Yanagawa, Y.; Matsumoto, T.; Kawai, T.; Yoon, Z. S.; Kim, D.; Osuka, A. Giant Meso-Meso-Linked Porphyrin Arrays of Micrometer Molecular Length and Their Fabrication. *Chem. Eur. J.* **2005**, *11*, 3389–3404.

(62) Huh, S.; Kim, S.-J.; Kim, Y. Porphyrinic Metal–Organic Frameworks from Custom-Designed Porphyrins. *CrystEngComm* **2016**, *18*, 345–368.

(63) Pereira, C.; Simões, M.; Tomé, J.; Almeida Paz, F. Porphyrin-Based Metal-Organic Frameworks as Heterogeneous Catalysts in Oxidation Reactions. *Molecules* **2016**, *21*, 1348.

(64) Song, H. Electrostatic Gate Control in Molecular Transistors. *Top. Curr. Chem.* **2018**, *376*, 37.

(65) Aviram, A.; Ratner, M. A. Molecular Rectifiers. *Chem. Phys. Lett.* **1974**, *29*, 277–283.

(66) Lo, W. Y.; Zhang, N.; Cai, Z.; Li, L.; Yu, L. Beyond Molecular Wires: Design Molecular Electronic Functions Based on Dipolar Effect. *Acc. Chem. Res.* **2016**, *49*, 1852–1863.

(67) Carroll, R. L.; Gorman, C. B. The Genesis of Molecular Electronics. *Angew. Chem. Int. Ed.* **2002**, *41*, 4379–4400.

(68) Susumu, K.; Maruyama, H.; Kobayashi, H.; Tanaka, K. Theoretical Approach to the Design of Supramolecular Conjugated Porphyrin Polymers. *J. Mater. Chem.* **2001**, *11*, 2262–2270.

(69) Tanaka, T.; Osuka, A. Conjugated Porphyrin Arrays: Synthesis, Properties and Applications for Functional Materials. *Chem. Soc. Rev.* **2015**, *44*, 943–969.

(70) Burrell, A. K.; Officer, D. L.; Plieger, P. G.; Reid, D. C. W. Synthetic Routes to Multiporphyrin Arrays. *Chem. Rev.* **2001**, *101*, 2751–2796.

(71) Anderson, H. L. Building Molecular Wires from the Colours of Life: Conjugated Porphyrin Oligomers. *Chem. Commun.* **1999**, 2323–2330.

(72) Taylor, P. N.; Anderson, H. L. Cooperative Self-Assembly of Double-Strand Conjugated Porphyrin Ladders. *J. Am. Chem. Soc.* **1999**, *121*, 11538–11545.

(73) Anderson, H. L.; Martin, S. J.; Bradley, D. D. C. Synthesis and Third-Order Nonlinear Optical Properties of a Conjugated Porphyrin Polymer. *Angew. Chem. Int. Ed. Engl.* **1994**, *33*, 655–657.

(74) Higuchi, H.; Shimizu, K.; Ojima, J.; Sugiura, K.; Sakata, Y. Synthesis and Properties of Etheno-Bridged Porphyrin Trimers. *Tetrahedron Lett.* **1995**, *36*, 5359–5362.

(75) Higuchi, H.; Shimizu, K.; Takeuchi, M.; Ojima, J.; Sugiura, K.; Sakata, Y. Synthesis and Properties of Tris(Octaethylporphyrin)s Connected with Vinylene Groups. *Bull. Chem. Soc. Jpn.* **1997**, *70*, 1923–1933.

(76) Bonfantini, E. E.; Officer, D. L. The Synthesis of Butadiene-Bridged Porphyrin Dimers and Styryl Porphyrins Using a Porphyrin-Derived Wittig Reagent. *Tetrahedron Lett.* **1993**, *34*, 8531–8534.

(77) Crossley, M. J.; Govenlock, L. J.; Prashar, J. K. Synthesis of Porphyrin-2,3,12,13- and -2,3,7,8-Tetraones: Building Blocks for the Synthesis of Extended Porphyrin Arrays. *Chem. Commun.* **1995**, 2379–2380.

(78) Crossley, M. J.; Burn, P. L. Rigid, Laterally-Bridged Bis-Porphyrin Systems. *Chem. Commun.* **1987**, 39–40.

(79) Crossley, M. J.; Burn, P. L. An Approach to Porphyrin-Based Molecular Wires: Synthesis of a Bis(Porphyrin)Tetraone and Its Conversion to a Linearly Conjugated Tetrakisporphyrin System. *Chem. Commun.* **1991**, 1569–1571.

(80) Ikeda, T.; Aratani, N.; Osuka, A. Synthesis of Extremely Pi -Extended Porphyrin Tapes from Hybrid Meso-Meso Linked Porphyrin Arrays : An Approach Towards the Conjugation Length. *Chem. Asian. J.* **2009**, *4*, 1248–1256.

(81) Nakamura, Y.; Aratani, N.; Shinokubo, H.; Takagi, A.; Kawai, T.; Matsumoto, T.; Seok, Z. S.; Kim, D. Y.; Ahn, T. K.; Kim, D.; et al. A Directly Fused Tetrameric Porphyrin Sheet and Its Anomalous Electronic Properties That Arise from The Planar Cyclooctatetraene Core. *J. Am. Chem. Soc.* **2006**, *128*, 4119–4127.

(82) Tsuda, A.; Furuta, H.; Osuka, A. Completely Fused Diporphyrins and Triporphyrin. *Angew. Chem. Int. Ed.* **2000**, *39*, 2549–2552.

(83) Binnig, G.; Rohrer, H.; Gerber, C.; Weibel, E. Surface Studies by Scanning Tunneling Microscopy. *Phys. Rev. Lett.* **1982**, *49*, 57–61.

(84) Binnig, G.; Rohrer, H. Scanning Tunneling Microscopy. *Surf. Sci.* **1983**, *126*, 236–244.

(85) Clair, S.; de Oteyza, D. G. Controlling a Chemical Coupling Reaction on a Surface: Tools and Strategies for On-Surface Synthesis. *Chem. Rev.* **2019**, *119*, 4717–4776.

(86) Pigot, C.; Dumur, F. Recent Advances of Hierarchical and Sequential Growth of Macromolecular Organic Structures on Surface. *Materials (Basel).* **2019**, *12*, 662.

(87) Auwärter, W.; Écija, D.; Klappenberger, F.; Barth, J. V. Porphyrins at Interfaces. *Nat. Chem.* **2015**, *7*, 105–120.

(88) Xi, M.; Bent, B. E. Mechanisms of the Ullmann Coupling Reaction in Adsorbed Monolayers. *J. Am. Chem. Soc.* **1993**, *115*, 7426–7433.

(89) Grim, P. C. M.; De Feyter, S.; Gesquière, A.; Vanoppen, P.; Rüker, M.; Valiyaveettil, S.; Moessner, G.; Müllen, K.; De Schryver, F. C. Submolecularly Resolved Polymerisation of Diacetylene Molecules on the Graphite Surface Observed with Scanning Tunneling Microscopy. *Angew. Chem. Int. Ed. Engl.* **1997**, *36*, 2601–2603.

(90) Grill, L.; Dyer, M.; Lafferentz, L.; Persson, M.; Peters, M. V; Hecht, S. Nano-Architectures by Covalent Assembly of Molecular Building Blocks. *Nat. Nanotechnol.* **2007**, *2*, 687–691.

(91) Lafferentz, L.; Eberhardt, V.; Dri, C.; Africh, C.; Comelli, G.; Esch, F.; Hecht, S.; Grill, L. Controlling On-Surface Polymerisation by Hierarchical and Substrate-Directed Growth. *Nat. Chem.* **2012**, *4*, 215–220.

(92) Hu, J.; Liang, Z.; Shen, K.; Sun, H.; Jiang, Z.; Song, F. Recent Progress in the Fabrication of Low Dimensional Nanostructures via Surface-Assisted Transforming and Coupling. *J. Nanomater.* **2017**, *2017*, 1–17.

(93) Zhang, R.; Lyu, G.; Li, D. Y.; Liu, P. N.; Lin, N. Template-Controlled Sonogashira Cross-Coupling Reactions on a Au(111) Surface. *Chem. Commun.* **2017**, *53*, 1731–1734.

(94) Shi, K.-J.; Shu, C.-H.; Wang, C.-X.; Wu, X.-Y.; Tian, H.; Liu, P.-N. On-Surface Heck Reaction of Aryl Bromides with Alkene on Au(111) with Palladium as Catalyst. *Org. Lett.* **2017**, *19*, 2801–2804.

(95) Wiengarten, A.; Seufert, K.; Auwärter, W.; Ecija, D.; Diller, K.; Allegretti, F.; Bischoff, F.; Fischer, S.; Duncan, D. A.; Papageorgiou, A. C.; et al. Surface-Assisted Dehydrogenative Homocoupling of Porphine Molecules. *J. Am. Chem. Soc.* **2014**, *136*, 9346–9354.

(96) In't Veld, M.; Iavicoli, P.; Haq, S.; Amabilino, D. B.; Raval, R. Unique Intermolecular Reaction of Simple Porphyrins at a Metal Surface Gives Covalent Nanostructures. *Chem. Commun.* **2008**, 1536.

(97) Haq, S.; Hanke, F.; Dyer, M. S.; Persson, M.; Iavicoli, P.; Amabilino, D. B.; Raval, R. Clean Coupling of Unfunctionalized Porphyrins at Surfaces To Give Highly Oriented Organometallic Oligomers. *J. Am. Chem. Soc.* **2011**, *133*, 12031–12039.

(98) Smykalla, L.; Shukrynau, P.; Korb, M.; Lang, H.; Hietschold, M. Surface-Confined 2D Polymerisation of a Brominated Copper-Tetraphenylporphyrin on Au(111). *Nanoscale* **2015**, *7*, 4234–4241.

(99) Di Santo, G.; Blankenburg, S.; Castellarin-Cudia, C.; Fanetti, M.; Borghetti, P.; Sangaletti, L.; Floreano, L.; Verdini, A.; Magnano, E.; Bondino, F.; et al. Supramolecular Engineering through Temperature-Induced Chemical Modification of 2H-Tetraphenylporphyrin on Ag(111): Flat Phenyl Conformation and Possible Dehydrogenation Reactions. *Chem. Eur. J.* **2011**, *17*, 14354–14359.

(100) Xiao, J.; Ditze, S.; Chen, M.; Buchner, F.; Stark, M.; Drost, M.; Steinrück, H.-P.; Gottfried, J. M.; Marbach, H. Temperature-Dependent Chemical and Structural Transformations from 2H-Tetraphenylporphyrin to Copper(II)-Tetraphenylporphyrin on Cu(111). *J. Phys. Chem. C* **2012**, *116*, 12275–12282.

(101) Wiengarten, A.; Lloyd, J. A.; Seufert, K.; Reichert, J.; Auwärter, W.; Han, R.; Duncan, D. A.; Allegretti, F.; Fischer, S.; Oh, S. C.; et al. Surface-Assisted Cyclodehydrogenation; Break the Symmetry, Enhance the Selectivity. *Chem. Eur. J.* **2015**, *21*, 12285–12290.

(102) Ruggieri, C.; Rangan, S.; Bartynski, R. A.; Galoppini, E. Zinc(II) Tetraphenylporphyrin on Ag(100) and Ag(111): Multilayer Desorption and Dehydrogenation. *J. Phys. Chem. C* **2016**, *120*, 7575–7585.

(103) Xiang, F.; Gemeinhardt, A.; Schneider, M. A. Competition between Dehydrogenative Organometallic Bonding and Covalent Coupling of an Unfunctionalized Porphyrin on Cu(111). *ACS Nano* **2018**, *12*, 1203–1210.

(104) Röckert, M.; Franke, M.; Tariq, Q.; Ditze, S.; Stark, M.; Uffinger, P.; Wechsler, D.; Singh, U.; Xiao, J.; Marbach, H.; et al. Coverage- and Temperature-Dependent Metalation and Dehydrogenation of Tetraphenylporphyrin on Cu(111). *Chem. Eur. J.* **2014**, *20*, 8948–8953.

(105) He, Y.; Garnica, M.; Bischoff, F.; Ducke, J.; Bocquet, M. L.; Batzill, M.; Auwärter, W.; Barth, J. V. Fusing Tetrapyrroles to Graphene Edges by Surface-Assisted Covalent Coupling. *Nat. Chem.* **2017**, *9*, 33–38.

(106) Li, J.; Merino-Díez, N.; Carbonell-Sanromà, E.; Vilas-Varela, M.; de Oteyza, D. G.; Peña, D.; Corso, M.; Pascual, J. I. Survival of Spin State in Magnetic Porphyrins Contacted by Graphene Nanoribbons. *Sci. Adv.* **2018**, *4*, eaaq0582.

(107) Perkins, W.; Fischer, F. R. Inserting Porphyrin Quantum Dots in Bottom-Up Synthesised Graphene Nanoribbons. *Chem. – A Eur. J.* **2017**, *23*, 17687–17691.

(108) Cai, J.; Ruffieux, P.; Jaafar, R.; Bieri, M.; Braun, T.; Blankenburg, S.; Muoth, M.; Seitsonen, A. P.; Saleh, M.; Feng, X.; et al. Atomically Precise Bottom-up Fabrication of Graphene Nanoribbons. *Nature* **2010**, *466*, 470–473.

(109) Novoselov, K. S.; Geim, A. K.; Morozov, S. V.; Jiang, D.; Zhang, Y.; Dubonos, S. V.; Grigorieva, I. V.; Firsov, A. A. Electric Field Effect in Atomically Thin Carbon Films. *Science* **2004**, *306*, 666–669.

(110) Geim, A. K.; Novoselov, K. S. The Rise of Graphene. *Nat. Mater.* **2007**, *6*, 183–191.

(111) Novoselov, K. S.; Castro Neto, A. H. Two-Dimensional Crystals-Based Heterostructures: Materials with

Tailored Properties. *Phys. Scr.* **2012**, *T146*, 014006.

(112) Castro Neto, A. H.; Guinea, F.; Peres, N. M. R.; Novoselov, K. S.; Geim, A. K. The Electronic Properties of Graphene. *Rev. Mod. Phys.* **2009**, *81*, 109–162.

(113) Jariwala, D.; Sangwan, V. K.; Lauhon, L. J.; Marks, T. J.; Hersam, M. C. Emerging Device Applications for Semiconducting Two-Dimensional Transition Metal Dichalcogenides. *ACS Nano* **2014**, *8*, 1102–1120.

(114) Novoselov, K. S.; Mishchenko, A.; Carvalho, A.; Castro Neto, A. H. 2D Materials and van Der Waals Heterostructures. *Science* **2016**, *353*, 461–472.

(115) Butler, S. Z.; Hollen, S. M.; Cao, L.; Cui, Y.; Gupta, J. A.; Gutiérrez, H. R.; Heinz, T. F.; Hong, S. S.; Huang, J.; Ismach, A. F.; et al. Progress, Challenges, and Opportunities in Two-Dimensional Materials Beyond Graphene. *ACS Nano* **2013**, *7*, 2898–2926.

(116) Bolotin, K. I.; Sikes, K. J.; Jiang, Z.; Klima, M.; Fudenberg, G.; Hone, J.; Kim, P.; Stormer, H. L. Ultrahigh Electron Mobility in Suspended Graphene. *Solid State Commun.* **2008**, *146*, 351–355.

(117) Saito, K.; Nakamura, J.; Natori, A. Ballistic Thermal Conductance of a Graphene Sheet. *Phys. Rev. B* **2007**, *76*, 115409.

(118) Peres, N. M. R.; Lopes dos Santos, J. M. B.; Stauber, T. Phenomenological Study of the Electronic Transport Coefficients of Graphene. *Phys. Rev. B* **2007**, *76*, 073412.

(119) Peres, N. M. R.; Guinea, F.; Castro Neto, A. H. Electronic Properties of Two-Dimensional Carbon. *Ann. Phys.* **2006**, *321*, 1559–1567.

(120) Gusynin, V. P.; Sharapov, S. G. Unconventional Integer Quantum Hall Effect in Graphene. *Phys. Rev. Lett.* **2005**, *95*, 146801.

(121) Zheng, Y.; Ando, T. Hall Conductivity of a Two-Dimensional Graphite System. *Phys. Rev. B* **2002**, *65*, 245420.

(122) Lee, C.; Wei, X.; Kysar, J. W.; Hone, J. Measurement of the Elastic Properties of Intrinsic Strengh of Monolayer Graphene. *Science* **2008**, *321*, 385–388.

(123) Nair, R. R.; Blake, P.; Grigorenko, A. N.; Novoselov, K. S.; Booth, T. J.; Stauber, T.; Peres, N. M. R.; Geim, A. K. Fine Structure Constant Defines Visual Transparency of Graphene. *Science* **2008**, *320*, 1308–1308.

(124) Wassei, J. K.; Kaner, R. B. Graphene, a Promising Transparent Conductor. *Mater. Today* **2010**, *13*, 52–59.

(125) Docherty, C. J.; Lin, C. Te; Joyce, H. J.; Nicholas, R. J.; Herz, L. M.; Li, L. J.; Johnston, M. B. Extreme Sensitivity of Graphene Photoconductivity to Environmental Gases. *Nat. Commun.* **2012**, *3*, 1226–1228.

(126) Berashevich, J.; Chakraborty, T. Tunable Bandgap and Magnetic Ordering by Adsorption of Molecules on Graphene. *Phys. Rev. B* **2009**, *80*, 033404.

(127) Novoselov, K. S.; Fal'Ko, V. I.; Colombo, L.; Gellert, P. R.; Schwab, M. G.; Kim, K. A Roadmap for Graphene. *Nature* **2012**, *490*, 192–200.

(128) Das, T.; Sharma, B. K.; Katiyar, A. K.; Ahn, J.-H. Graphene-Based Flexible and Wearable Electronics. *J. Semicond.* **2018**, *39*, 011007.

(129) Wang, C.; Xia, K.; Wang, H.; Liang, X.; Yin, Z.; Zhang, Y. Advanced Carbon for Flexible and Wearable Electronics. *Adv. Mater.* **2019**, *31*, 1801072.

(130) Westervelt, R. M. Graphene Nanoelectronics. *Science* **2008**, *320*, 324–325.

(131) Yang, X.; Cheng, C.; Wang, Y.; Qiu, L.; Li, D. Liquid-Mediated Dense Integration of Graphene Materials for Compact Capacitive Energy Storage. *Science* **2013**, *341*, 534–538.

(132) Pumera, M. Graphene-Based Nanomaterials for Energy Storage. *Energy Environ. Sci.* **2011**, *4*, 668–674.

(133) Sun, Y.; Wu, Q.; Shi, G. Graphene Based New Energy Materials. *Energy Environ. Sci.* **2011**, *4*, 1113–1132.

(134) Dreyer, D. R.; Bielawski, C. W. Carbocatalysis: Heterogeneous Carbons Finding Utility in Synthetic Chemistry. *Chem. Sci.* **2011**, *2*, 1233–1240.

(135) Scheuermann, G. M.; Rumi, L.; Steurer, P.; Bannwarth, W.; Mülhaupt, R. Palladium Nanoparticles on Graphite Oxide and Its Functionalized Graphene Derivatives as Highly Active Catalysts for the Suzuki-Miyaura Coupling Reaction. *J. Am. Chem. Soc.* **2009**, *131*, 8262–8270.

(136) Schedin, F.; Geim, A. K.; Morozov, S. V.; Hill, E. W.; Blake, P.; Katsnelson, M. I.; Novoselov, K. S. Detection of Individual Gas Molecules Adsorbed on Graphene. *Nat. Mater.* **2007**, *6*, 652–655.

(137) Dua, V.; Surwade, S. P.; Ammu, S.; Agnihotra, S. R.; Jain, S.; Roberts, K. E.; Park, S.; Ruoff, R. S.; Manohar, S. K. All-Organic Vapor Sensor Using Inkjet-Printed Reduced Graphene Oxide. *Angew. Chem. Int. Ed.* **2010**, *49*, 2154–2157.

(138) Bonaccorso, F.; Sun, Z.; Hasan, T.; Ferrari, A. C. Graphene Photonics and Optoelectronics. *Nat. Photonics* **2010**, *4*, 611–622.

(139) Oztas, Z.; Yuce, C. Spontaneously Broken Particle-Hole Symmetry in Photonic Graphene with Gain and Loss. *Phys. Rev. A* **2018**, *98*, 042104.

(140) Guo, C.; Zhang, J.; Xu, W.; Liu, K.; Yuan, X.; Qin, S.; Zhu, Z. Graphene-Based Perfect Absorption Structures in the Visible to Terahertz Band and Their Optoelectronics Applications. *Nanomaterials* **2018**, *8*, 1033.

(141) Schwierz, F. Graphene Transistors. *Nat. Nanotechnol.* **2010**, *5*, 487–496.

(142) Dvorak, M.; Oswald, W.; Wu, Z. Bandgap Opening by Patterning Graphene. *Sci. Rep.* **2013**, *3*, 2289.

(143) Nakada, K.; Fujita, M.; Dresselhaus, G.; Dresselhaus, M. S. Edge State in Graphene Ribbons: Nanometer Size Effect and Edge Shape Dependence. *Phys. Rev. B* **1996**, *54*, 17954–17961.

(144) Pietryga, J. M.; Park, Y.; Lim, J.; Fidler, A. F.; Bae, W. K.; Brovelli, S.; Klimov, V. I. Spectroscopic and Device Aspects of Nanocrystal Quantum Dots. *Chem. Rev.* **2016**, *116*, 10513–10622.

(145) Hildebrandt, N.; Spillmann, C. M.; Algar, W. R.; Pons, T.; Stewart, M. H.; Oh, E.; Susumu, K.; Díaz, S. A.; Delehanty, J. B.; Medintz, I. L. Energy Transfer with Semiconductor Quantum Dot Bioconjugates: A Versatile Platform for Biosensing, Energy Harvesting, and Other Developing Applications. *Chem. Rev.* **2017**, *117*, 536–711.

(146) Brey, L.; Fertig, H. A. Electronic States of Graphene Nanoribbons Studied with the Dirac Equation. *Phys. Rev. B* **2006**, *73*, 235411.

(147) Cocchi, C.; Prezzi, D.; Ruini, A.; Caldas, M. J.; Molinari, E. Anisotropy and Size E Ff Ects on the Optical Spectra of Polycyclic Aromatic Hydrocarbons. *J. Phys. Chem. A* **2014**, *118*, 6507–6513.

(148) Zhao, S.; Lavie, J.; Rondin, L.; Orcin-Chaix, L.; Diederichs, C.; Roussignol, P.; Chassagneux, Y.; Voisin, C.; Müllen, K.; Narita, A.; et al. Single Photon Emission from Graphene Quantum Dots at Room Temperature. *Nat. Commun.* **2018**, *9*, 3470.

(149) Hasan, M. T.; Gonzalez-Rodriguez, R.; Ryan, C.; Pota, K.; Green, K.; Coffer, J. L.; Naumov, A. V. Nitrogen-Doped Graphene Quantum Dots: Optical Properties Modification and Photovoltaic Applications. *Nano Res.* **2019**, *12*, 1041–1047.

(150) Ge, J.; Lan, M.; Zhou, B.; Liu, W.; Guo, L.; Wang, H.; Jia, Q.; Niu, G.; Huang, X.; Zhou, H.; et al. A Graphene Quantum Dot Photodynamic Therapy Agent with High Singlet Oxygen Generation. *Nat. Commun.* **2014**, *5*, 4596.

(151) Thakur, M.; Kumawat, M. K.; Srivastava, R. Multifunctional Graphene Quantum Dots for Combined Photothermal and Photodynamic Therapy Coupled with Cancer Cell Tracking Applications. *RSC Adv.* **2017**, *7*,

5251–5261.

(152) Han, M. Y.; Özyilmaz, B.; Zhang, Y.; Kim, P. Energy Band-Gap Engineering of Graphene Nanoribbons. *Phys. Rev. Lett.* **2007**, *98*, 206805.

(153) Yang, L.; Park, C. H.; Son, Y. W.; Cohen, M. L.; Louie, S. G. Quasiparticle Energies and Bandgaps in Graphene Nanoribbons. *Phys. Rev. Lett.* **2007**, *99*, 186801.

(154) Barone, V.; Hod, O.; Scuseria, G. E. Electronic Structure and Stability of Semiconducting Graphene Nanoribbons. *Nano Lett.* **2006**, *6*, 2748–2754.

(155) Son, Y.-W.; Cohen, M. L.; Louie, S. G. Energy Gaps in Graphene Nanoribbons. *Phys. Rev. Lett.* **2006**, *97*, 216803.

(156) Chen, Y. C.; De Oteyza, D. G.; Pedramrazi, Z.; Chen, C.; Fischer, F. R.; Crommie, M. F. Tuning the Bandgap of Graphene Nanoribbons Synthesised from Molecular Precursors. *ACS Nano* **2013**, *7*, 6123–6128.

(157) Ruffieux, P.; Wang, S.; Yang, B.; Sanchez-Sanchez, C.; Liu, J.; Dienel, T.; Talirz, L.; Shinde, P.; Pignedoli, C. A.; Passerone, D.; et al. On-Surface Synthesis of Graphene Nanoribbons with Zigzag Edge Topology. *Nature* **2016**, *531*, 489–492.

(158) Pedersen, T. G.; Flindt, C.; Pedersen, J.; Mortensen, N. A.; Jauho, A.; Pedersen, K. Graphene Antidot Lattices: Designed Defects and Spin Qubits. *Phys. Rev. Lett.* **2008**, *100*, 136804.

(159) Bai, J.; Zhong, X.; Jiang, S.; Huang, Y.; Duan, X. Graphene Nanomesh. *Nat. Nanotechnol.* **2010**, *5*, 190–194.

(160) Hung Nguyen, V.; Chung Nguyen, M.; Nguyen, H.-V.; Dollfus, P. Disorder Effects on Electronic Bandgap and Transport in Graphene-Nanomesh-Based Structures. *J. Appl. Phys.* **2013**, *113*, 013702.

(161) Power, S. R.; Jauho, A.-P. Electronic Transport in Disordered Graphene Antidot Lattice Devices. *Phys. Rev. B* **2014**, *90*, 115408.

(162) Ji, X.; Zhang, J.; Wang, Y.; Qian, H.; Yu, Z. Influence of Edge Imperfections on the Transport Behavior of Graphene Nanomeshes. *Nanoscale* **2013**, *5*, 2527.

(163) Shen, J.; Zhu, Y.; Yang, X.; Li, C. Graphene Quantum Dots: Emergent Nanolights for Bioimaging, Sensors, Catalysis and Photovoltaic Devices. *Chem. Commun.* **2012**, *48*, 3686.

(164) Hummers, W. S.; Offeman, R. E. Preparation of Graphitic Oxide. *J. Am. Chem. Soc.* **1958**, *80*, 1339–1339.

(165) Sun, X.; Liu, Z.; Welsher, K.; Robinson, J. T.; Goodwin, A.; Zaric, S.; Dai, H. Nano-Graphene Oxide for Cellular Imaging and Drug Delivery. *Nano Res.* **2008**, *1*, 203–212.

(166) Li, L.; Ji, J.; Fei, R.; Wang, C.; Lu, Q.; Zhang, J.; Jiang, L.-P.; Zhu, J.-J. A Facile Microwave Avenue to Electrochemiluminescent Two-Color Graphene Quantum Dots. *Adv. Funct. Mater.* **2012**, *22*, 2971–2979.

(167) Liu, D.; Chen, X.; Hu, Y.; Sun, T.; Song, Z.; Zheng, Y.; Cao, Y.; Cai, Z.; Cao, M.; Peng, L.; et al. Raman Enhancement on Ultra-Clean Graphene Quantum Dots Produced by Quasi-Equilibrium Plasma-Enhanced Chemical Vapor Deposition. *Nat. Commun.* **2018**, *9*, 193.

(168) Li, X.; Wang, X.; Zhang, L.; Lee, S.; Dai, H. Chemically Derived Ultramooth Graphene Nanoribbon Semiconductors. *Science* **2008**, *319*, 1229–1232.

(169) Jiao, L.; Zhang, L.; Wang, X.; Diankov, G.; Dai, H. Narrow Graphene Nanoribbons from Carbon Nanotubes. *Nature* **2009**, *458*, 877–880.

(170) Kosynkin, D. V.; Higginbotham, A. L.; Sinitskii, A.; Lomeda, J. R.; Dimiev, A.; Price, B. K.; Tour, J. M. Longitudinal Unzipping of Carbon Nanotubes to Form Graphene Nanoribbons. *Nature* **2009**, *458*, 872–876.

(171) Fischbein, M. D.; Drndić, M. Electron Beam Nanosculpting of Suspended Graphene Sheets. *Appl. Phys. Lett.* **2008**, *93*, 113107.

(172) Standop, S.; Lehtinen, O.; Herbig, C.; Lewes-Malandrakis, G.; Craes, F.; Kotakoski, J.; Michely, T.; Krasheninnikov, A. V.; Busse, C. Ion Impacts on Graphene/Ir(111): Interface Channeling, Vacancy Funnels, and a Nanomesh. *Nano Lett.* **2013**, *13*, 1948–1955.

(173) Sinitskii, A.; Tour, J. M. Patterning Graphene through the Self-Assembled Templates: Toward Periodic Two-Dimensional Graphene Nanostructures with Semiconductor Properties. *J. Am. Chem. Soc.* **2010**, *132*, 14730–14732.

(174) Zeng, Z.; Huang, X.; Yin, Z.; Li, H.; Chen, Y.; Li, H.; Zhang, Q.; Ma, J.; Boey, F.; Zhang, H. Fabrication of Graphene Nanomesh by Using an Anodic Aluminum Oxide Membrane as a Template. *Adv. Mater.* **2012**, *24*, 4138–4142.

(175) Liang, X.; Jung, Y.-S.; Wu, S.; Ismach, A.; Olynick, D. L.; Cabrini, S.; Bokor, J. Formation of Bandgap and Subbands in Graphene Nanomeshes with Sub-10 Nm Ribbon Width Fabricated via Nanoimprint Lithography. *Nano Lett.* **2010**, *10*, 2454–2460.

(176) Liu, J.; Cai, H.; Yu, X.; Zhang, K.; Li, X.; Li, J.; Pan, N.; Shi, Q.; Luo, Y.; Wang, X. Fabrication of Graphene Nanomesh and Improved Chemical Enhancement for Raman Spectroscopy. *J. Phys. Chem. C* **2012**, *116*, 15741–15746.

(177) Akhavan, O. Graphene Nanomesh by ZnO Nanorod Photocatalysts. *ACS Nano* **2010**, *4*, 4174–4180.

(178) Iyer, V. S.; Wehmeier, M.; Brand, J. D.; Keegstra, M. A.; Müllen, K. From Hexa-Peri-Hexabenzocoronene to “Superacenes". *Angew. Chem. Int. Ed. Engl.* **1997**, *36*, 1604–1607.

(179) Wu, J.; Tomović, Ž.; Enkelmann, V.; Müllen, K. From Branched Hydrocarbon Propellers to C 3 -Symmetric Graphite Disks. *J. Org. Chem.* **2004**, *69*, 5179–5186.

(180) Böhme, T.; Simpson, C. D.; Müllen, K.; Rabe, J. P. Current–Voltage Characteristics of a Homologous Series of Polycyclic Aromatic Hydrocarbons. *Chem. Eur. J.* **2007**, *13*, 7349–7357.

(181) Feng, X.; Wu, J.; Ai, M.; Pisula, W.; Zhi, L.; Rabe, J. P.; Müllen, K. Triangle-Shaped Polycyclic Aromatic Hydrocarbons. *Angew. Chem. Int. Ed.* **2007**, *46*, 3033–3036.

(182) Simpson, C. D.; Brand, J. D.; Berresheim, A. J.; Przybilla, L.; Räder, H. J.; Müllen, K. Synthesis of a Giant 222 Carbon Graphite Sheet. *Chem. Eur. J.* **2002**, *8*, 1424–1429.

(183) Beser, U.; Kastler, M.; Maghsoumi, A.; Wagner, M.; Castiglioni, C.; Tommasini, M.; Narita, A.; Feng, X.; Müllen, K. A C216-Nanographene Molecule with Defined Cavity as Extended Coronoid. *J. Am. Chem. Soc.* **2016**, *138*, 4322–4325.

(184) Simpson, C. D.; Mattersteig, G.; Martin, K.; Gherghel, L.; Bauer, R. E.; Räder, H. J.; Müllen, K. Nanosized Molecular Propellers by Cyclodehydrogenation of Polyphenylene Dendrimers. *J. Am. Chem. Soc.* **2004**, *126*, 3139–3147.

(185) Simpson, C. D.; Wu, J.; Watson, M. D.; Müllen, K. From Graphite Molecules to Columnar Superstructures – an Exercise in Nanoscience. *J. Mater. Chem.* **2004**, *14*, 494–504.

(186) Yan, X.; Li, B.; Li, L. Colloidal Graphene Quantum Dots with Well-Defined Structures. *Acc. Chem. Res.* **2013**, *46*, 2254–2262.

(187) Tan, Y.-Z.; Yang, B.; Parvez, K.; Narita, A.; Osella, S.; Beljonne, D.; Feng, X.; Müllen, K. Atomically Precise Edge Chlorination of Nanographenes and Its Application in Graphene Nanoribbons. *Nat. Commun.* **2013**, *4*, 2646.

(188) Narita, A.; Wang, X.-Y.; Feng, X.; Müllen, K. New Advances in Nanographene Chemistry. *Chem. Soc. Rev.* **2015**, *44*, 6616–6643.

(189) Pinardi, A. L.; Martínez, J. I.; Jančařík, A.; Stará, I. G.; Starý, I.; López, M. F.; Méndez, J.; Martín-Gago, J. Á. Sequential Formation of N-Doped Nanohelicenes, Nanographenes and Nanodomes by Surface-Assisted Chemical (Cyclo)Dehydrogenation of Heteroaromatics. *Chem. Commun.* **2014**, *50*, 1555.

(190) Treier, M.; Pignedoli, C. A.; Laino, T.; Rieger, R.; Müllen, K.; Passerone, D.; Fasel, R. Surface-Assisted Cyclodehydrogenation Provides a Synthetic Route towards Easily Processable and Chemically Tailored Nanographenes. *Nat. Chem.* **2011**, *3*, 61–67.

(191) Sun, Q.; Zhang, R.; Qiu, J.; Liu, R.; Xu, W. On-Surface Synthesis of Carbon Nanostructures. *Adv. Mater.* **2018**, *30*, 1705630.

(192) Fogel, Y.; Zhi, L.; Rouhanipour, A.; Andrienko, D.; Räder, H. J.; Müllen, K. Graphitic Nanoribbons with Dibenzo[e,l]Pyrene Repeat Units: Synthesis and Self-Assembly. *Macromolecules* **2009**, *42*, 6878–6884.

(193) Narita, A.; Feng, X.; Hernandez, Y.; Jensen, S. A.; Bonn, M.; Yang, H.; Verzhbitskiy, I. A.; Casiraghi, C.; Hansen, M. R.; Koch, A. H. R.; et al. Synthesis of Structurally Well-Defined and Liquid-Phase-Processable Graphene Nanoribbons. *Nat. Chem.* **2014**, *6*, 126–132.

(194) Narita, A.; Verzhbitskiy, I. A.; Frederickx, W.; Mali, K. S.; Jensen, S. A.; Hansen, M. R.; Bonn, M.; De Feyter, S.; Casiraghi, C.; Feng, X.; et al. Bottom-up Synthesis of Liquid-Phase-Processable Graphene Nanoribbons with near-Infrared Absorption. *ACS Nano* **2014**, *8*, 11622–11630.

(195) Yang, X.; Dou, X.; Rouhanipour, A.; Zhi, L.; Räder, H. J.; Müllen, K. Two-Dimensional Graphene Nanoribbons. *J. Am. Chem. Soc.* **2008**, *130*, 4216–4217.

(196) Li, G.; Yoon, K. Y.; Zhong, X.; Zhu, X.; Dong, G. Efficient Bottom-Up Preparation of Graphene Nanoribbons by Mild Suzuki–Miyaura Polymerisation of Simple Triaryl Monomers. *Chem. Eur. J.* **2016**, *22*, 9116–9120.

(197) Dössel, L.; Gherghel, L.; Feng, X.; Müllen, K. Graphene Nanoribbons by Chemists : Nanometer-Sized , Soluble , and Defect-Free. *Angew. Chem. Int. Ed.* **2011**, *50*, 2540–2543.

(198) Schwab, M. G.; Narita, A.; Hernandez, Y.; Balandina, T.; Mali, K. S.; De Feyter, S.; Feng, X.; Müllen, K. Structurally Defined Graphene Nanoribbons with High Lateral Extension. *J. Am. Chem. Soc.* **2012**, *134*, 18169–18172.

(199) Vo, T. H.; Shekhirev, M.; Kunkel, D. A.; Morton, M. D.; Berglund, E.; Kong, L.; Wilson, P. M.; Dowben, P. A.; Enders, A.; Sinitskii, A. Large-Scale Solution Synthesis of Narrow Graphene Nanoribbons. *Nat. Commun.* **2014**, *5*, 3189.

(200) Mehdi Pour, M.; Lashkov, A.; Radocea, A.; Liu, X.; Sun, T.; Lipatov, A.; Korlacki, R. A.; Shekhirev, M.; Aluru, N. R.; Lyding, J. W.; et al. Laterally Extended Atomically Precise Graphene Nanoribbons with Improved Electrical Conductivity for Efficient Gas Sensing. *Nat. Commun.* **2017**, *8*, 820.

(201) Vo, T. H.; Shekhirev, M.; Kunkel, D. A.; Orange, F.; Guinel, M. J. F.; Enders, A.; Sinitskii, A. Bottom-up Solution Synthesis of Narrow Nitrogen-Doped Graphene Nanoribbons. *Chem. Commun.* **2014**, *50*, 4172–4174.

(202) Hieulle, J.; Carbonell-Sanromà, E.; Vilas-Varela, M.; Garcia-Lekue, A.; Guitián, E.; Peña, D.; Pascual, J. I. On-Surface Route for Producing Planar Nanographenes with Azulene Moieties. *Nano Lett.* **2018**, *18*, 418–423.

(203) Colazzo, L.; Mohammed, M. S. G.; Dorel, R.; Nita, P.; García Fernández, C.; Abufager, P.; Lorente, N.; Echavarren, A. M.; de Oteyza, D. G. On-Surface Synthesis of Heptacene on Ag(001) from Brominated and Non-Brominated Tetrahydroheptacene Precursors. *Chem. Commun.* **2018**, *54*, 10260–10263.

(204) Pijeat, J.; Lauret, J.-S.; Campidelli, S. *Bottom-up Approach for the Synthesis of Graphene Nanoribbons*; Tejeda, A., Brey, L., Seneor, P., Eds.; IOP Publishing Ltd. In press.

(205) Kimouche, A.; Ervasti, M. M.; Drost, R.; Halonen, S.; Harju, A.; Joensuu, P. M.; Sainio, J.; Liljeroth, P. Ultra-

Narrow Metallic Armchair Graphene Nanoribbons. *Nat. Commun.* **2015**, *6*, 10177.

(206) Talirz, L.; Söde, H.; Dumslaff, T.; Wang, S.; Sanchez-Valencia, J. R.; Liu, J.; Shinde, P.; Pignedoli, C. A.; Liang, L.; Meunier, V.; et al. On-Surface Synthesis and Characterization of 9-Atom Wide Armchair Graphene Nanoribbons. *ACS Nano* **2017**, *11*, 1380–1388.

(207) Ruffieux, P.; Cai, J.; Plumb, N. C.; Patthey, L.; Prezzi, D.; Ferretti, A.; Molinari, E.; Feng, X.; Müllen, K.; Pignedoli, C. A.; et al. Electronic Structure of Atomically Precise Graphene Nanoribbons. *ACS Nano* **2012**, *6*, 6930–6935.

(208) Koch, M.; Ample, F.; Joachim, C.; Grill, L. Voltage-Dependent Conductance of a Single Graphene Nanoribbon. *Nat. Nanotechnol.* **2012**, *7*, 713–717.

(209) Cummings, A. W.; Valenzuela, S. O.; Ortmann, F.; Roche, S. Graphene Spintronics. *2D Mater. Prop. Devices* **2017**, *9*, 197–218.

(210) Bronner, C.; Stremlau, S.; Gille, M.; Braußе, F.; Haase, A.; Hecht, S.; Tegeder, P. Aligning the Bandgap of Graphene Nanoribbons by Monomer Doping. *Angew. Chem. Int. Ed.* **2013**, *52*, 4422–4425.

(211) Vo, T. H.; Perera, U. G. E.; Shekhirev, M.; Mehdi Pour, M.; Kunkel, D. A.; Lu, H.; Gruverman, A.; Sutter, E.; Cotlet, M.; Nykypanchuk, D.; et al. Nitrogen-Doping Induced Self-Assembly of Graphene Nanoribbon-Based Two-Dimensional and Three-Dimensional Metamaterials. *Nano Lett.* **2015**, *15*, 5770–5777.

(212) Nguyen, G. D.; Toma, F. M.; Cao, T.; Pedramrazi, Z.; Chen, C.; Rizzo, D. J.; Joshi, T.; Bronner, C.; Chen, Y. C.; Favaro, M.; et al. Bottom-Up Synthesis of N=13 Sulfur-Doped Graphene Nanoribbons. *J. Phys. Chem. C* **2016**, *120*, 2684–2687.

(213) Cloke, R. R.; Marangoni, T.; Nguyen, G. D.; Joshi, T.; Rizzo, D. J.; Bronner, C.; Cao, T.; Louie, S. G.; Crommie, M. F.; Fischer, F. R. Site-Specific Substitutional Boron Doping of Semiconducting Armchair Graphene Nanoribbons. *J. Am. Chem. Soc.* **2015**, *137*, 8872–8875.

(214) Kawai, S.; Saito, S.; Osumi, S.; Yamaguchi, S.; Foster, A. S.; Spijker, P.; Meyer, E. Atomically Controlled Substitutional Boron-Doping of Graphene Nanoribbons. *Nat. Commun.* **2015**, *6*, 8098.

(215) Ben, T.; Ren, H.; Ma, S.; Cao, D.; Lan, J.; Jing, X.; Wang, W.; Xu, J.; Deng, F.; Simmons, J. M.; et al. Targeted Synthesis of a Porous Aromatic Framework with High Stability and Exceptionally High Surface Area. *Angew. Chem. Int. Ed.* **2009**, *48*, 9457–9460.

(216) Xiang, Z.; Cao, D. Synthesis of Luminescent Covalent-Organic Polymers for Detecting Nitroaromatic Explosives and Small Organic Molecules. *Macromol. Rapid Commun.* **2012**, *33*, 1184–1190.

(217) Goesten, M. G.; Szécsényi, À.; de Lange, M. F.; Bavykina, A. V.; Gupta, K. B. S. S.; Kapteijn, F.; Gascon, J. Sulfonated Porous Aromatic Frameworks as Solid Acid Catalysts. *ChemCatChem* **2016**, *8*, 961–967.

(218) Yuan, D.; Lu, W.; Zhao, D.; Zhou, H.-C. Highly Stable Porous Polymer Networks with Exceptionally High Gas-Uptake Capacities. *Adv. Mater.* **2011**, *23*, 3723–3725.

(219) Sakaushi, K.; Hosono, E.; Nickerl, G.; Zhou, H.; Kaskel, S.; Eckert, J. Bipolar Porous Polymeric Frameworks for Low-Cost, High-Power, Long-Life All-Organic Energy Storage Devices. *J. Power Sources* **2014**, *245*, 553–556.

(220) Chen, L.; Yang, Y.; Guo, Z.; Jiang, D. Highly Efficient Activation of Molecular Oxygen with Nanoporous Metalloporphyrin Frameworks in Heterogeneous Systems. *Adv. Mater.* **2011**, *23*, 3149–3154.

(221) Rao, K. V.; Mohapatra, S.; Maji, T. K.; George, S. J. Guest-Responsive Reversible Swelling and Enhanced Fluorescence in a Super-Absorbent, Dynamic Microporous Polymer. *Chem. Eur. J.* **2012**, *18*, 4505–4509.

(222) Gutzler, R.; Walch, H.; Eder, G.; Kloft, S.; Heckl, W. M.; Lackinger, M. Surface Mediated Synthesis of 2D

Covalent Organic Frameworks: 1,3,5-Tris(4-Bromophenyl)Benzene on Graphite(001), Cu(111), and Ag(110). *Chem. Commun.* **2009**, 4456.

(223) Bieri, M.; Treier, M.; Cai, J.; Aït-Mansour, K.; Ruffieux, P.; Gröning, O.; Gröning, P.; Kastler, M.; Rieger, R.; Feng, X.; et al. Porous Graphenes: Two-Dimensional Polymer Synthesis with Atomic Precision. *Chem. Commun.* **2009**, 6919–6921.

(224) Cardenas, L.; Gutzler, R.; Lipton-Duffin, J.; Fu, C.; Brusso, J. L.; Dinca, L. E.; Vondráček, M.; Fagot-Revurat, Y.; Malterre, D.; Rosei, F.; et al. Synthesis and Electronic Structure of a Two Dimensional π-Conjugated Polythiophene. *Chem. Sci.* **2013**, *4*, 3263–3268.

(225) Liu, W.; Luo, X.; Bao, Y.; Liu, Y. P.; Ning, G.-H.; Abdelwahab, I.; Li, L.; Nai, C. T.; Hu, Z. G.; Zhao, D.; et al. A Two-Dimensional Conjugated Aromatic Polymer via C–C Coupling Reaction. *Nat. Chem.* **2017**, *9*, 563–570.

(226) Bieri, M.; Blankenburg, S.; Kivala, M.; Pignedoli, C. A.; Ruffieux, P.; Müllen, K.; Fasel, R. Surface-Supported 2D Heterotriangulene Polymers. *Chem. Commun.* **2011**, *47*, 10239.

(227) Steiner, C.; Gebhardt, J.; Ammon, M.; Yang, Z.; Heidenreich, A.; Hammer, N.; Görling, A.; Kivala, M.; Maier, S. Hierarchical On-Surface Synthesis and Electronic Structure of Carbonyl-Functionalized One- and Two-Dimensional Covalent Nanoarchitectures. *Nat. Commun.* **2017**, *8*, 14765.

(228) Abel, M.; Clair, S.; Ourdjini, O.; Mossoyan, M.; Porte, L. Single Layer of Polymeric Fe-Phthalocyanine: An Organometallic Sheet on Metal and Thin Insulating Film. *J. Am. Chem. Soc.* **2011**, *133*, 1203–1205.

(229) Nardi, E.; Chen, L.; Clair, S.; Koudia, M.; Giovanelli, L.; Feng, X.; Müllen, K.; Abel, M. On-Surface Reaction between Tetracarbonitrile-Functionalized Molecules and Copper Atoms. *J. Phys. Chem. C* **2014**, *118*, 27549–27553.

Chapter II. Anthracenylporphyrin-based building blocks

Chapter II. Anthracenylporphyrin-based building blocks

This chapter is dedicated to the design and synthesis of a series of anthracenylporphyrins that will be used as molecular building blocks for the “on surface” bottom-up fabrication of atomically defined nitrogen-doped GNRs and GNMs.

In a first part, the structures and the synthesis of different halogenated anthracenylporphyrins will be presented. We especially designed porphyrins with various topology, size, nature and number of halogens to target specific 1D and 2D assemblies on surface.

In the last part, the investigation on surface of two of these anthracenylporphyrin-based building blocks will be presented on different substrates with different orientations to modulate the molecule-substrate interactions. The assemblies observed by STM will be discussed and compared with computational models.

II. 1. Tetra-anthracenylporphyrins in the literature

Among the large collection of porphyrinic structures, anthracenylporphyrin derivatives still lack of reporting due to important synthetic challenges.[1–3] Historically, tetra-anthracenylporphyrin (**TAP)** was studied for its particular *bis*-facially blocked geometry because of perpendicular anthracenyl groups and was tested as a catalyst for the reversible coordination of oxygen,[4] the oxidation of PAHs,[5] or as an active molecule against HIV infection.[6] (**Fig. II-1**).

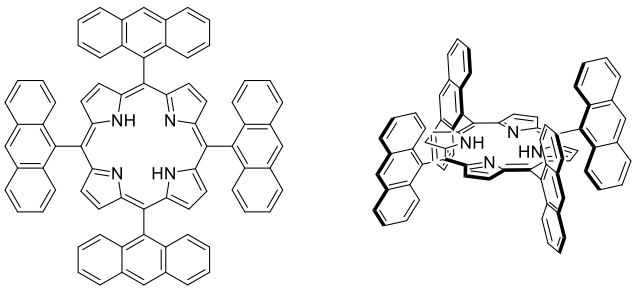

Fig. II-1 Chemical structures of a 5,10,15,20-tetra(anthracen-9-yl)porphyrin (**TAP**).

TAP was first synthetised *via* conventional synthetic methods of porphyrin chemistry by Cense *et al.*[4] in 1979 who isolated the porphyrin in 0.2% yield following the method developed by Adler and Longo.[7] Thereafter, attempts to synthesise **TAP** using the Lindsey strategy[8] or the reaction in inorganic acid[9] were carried out, but yields barely reached 3%. (**Fig. II-2**).

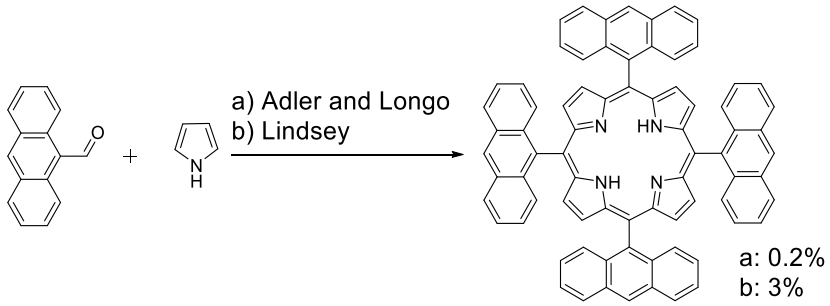

Fig. II-2 Conventional synthesis of **TAP** by a) the method of Adler and Longo in propionic acid at 125°C that gives 0.2% yield;[4] b) the method of Lindsey with BF_3OEt_2 and DDQ under argon that gives 3% yield.[8]

Lindsey *et al.*[10] reported in 1989 that the major limitation in the formation of porphyrinogen from 9-anthracenaldehyde was due to an important steric repulsion between a hydrogen on the methine bridge of the porphyrinogen and the hydrogen in position 1 of the anthracene moieties (**Fig. II-3**, a). In comparison, the authors mentioned that no problem of formation of porphyrinogen was encountered from the use of 1-naphthalaldehyde because the previous steric repulsion was avoided by rotation of the naphthalene moieties (**Fig. II-3**, b).

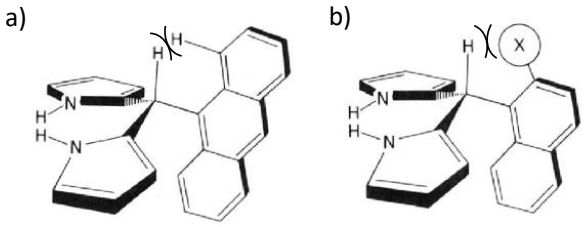

Fig. II-3 a) Representation of the steric repulsion between a hydrogen in methine bridge of porphyrinogens and the hydrogen in position 1 of the anthracene moieties; b) Representation of the twisted naphthalene moiety on porphyrinogen that avoided an important steric repulsion.[10]

In 1985, Volz and Schaeffer reported a new synthetic method based on the formation of a pyrrole-carbinol intermediate, which cyclo-tetramerised in propionic acid to form **TAP** in 6% yield.[11] In 2015, the yield of the synthesis was increased of up to 15% by Filatov *et al.*[12] starting from a phenylbromoanthracene to form tetraphenylanthracenyl porphyrin (**TPAP**). The strategy of Volz and Schaeffer was applied by the group of Anderson in 2010 to synthetise a tetra-dimesityloxyanthracenylporphyrin that permitted the fusion of the anthracenes on the core of the porphyrin giving rise to π-extended porphyrin exhibiting a maximum absorption around 1400 nm.[13] The first objective of this thesis was to design and synthetise halogenated-**TAP** that could polymerise on surface *via* dehalogenative coupling reaction and form the 1D or 2D skeletons of GNRs and GNMs.

II. 2. Synthesis of tetra-anthracenylporphyrin-based building blocks

II. 2.1. Tetra-bromoanthracenylporphyrin

At first, we imagined the structure of a 5,10,15,20-tetrakis(10-bromoanthracen-9-yl)porphyrin (**BrTAP**) to induce on surface a 2D polymerisation and afford the corresponding square type nitrogen-doped **GNM-1** with a nitrogen content of 5.7% per repeat unit (**Fig. II-4**).

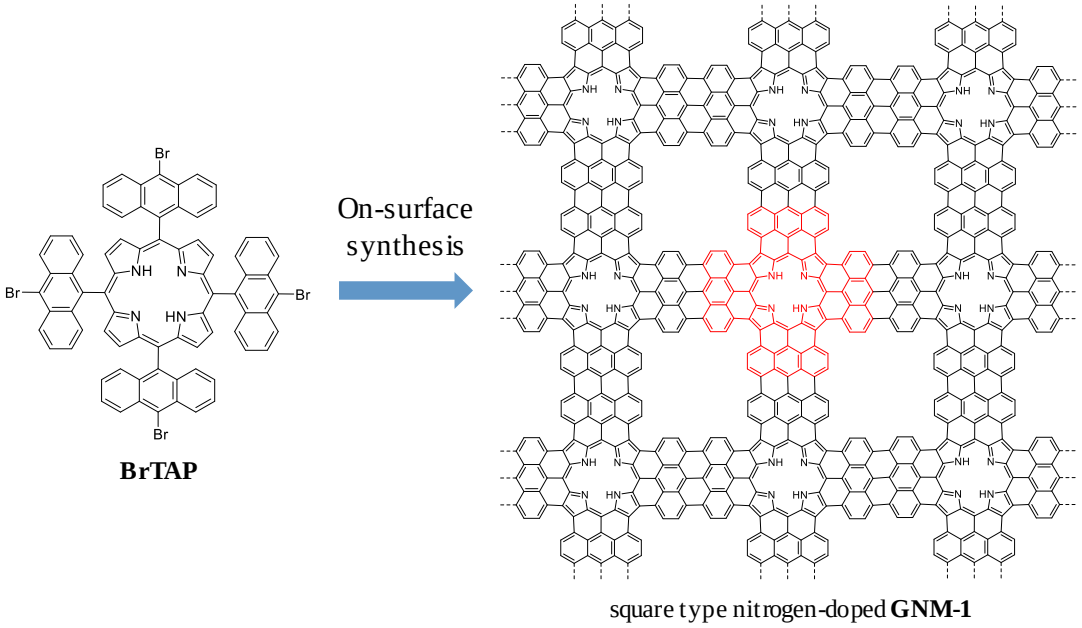

Fig. II-4 Target structure of square type nitrogen-doped **GNM-1** (right) from on-surface synthesis of 5,10,15,20-tetrakis(10-bromoanthracen-9-yl)porphyrin (**BrTAP**, left).

a) Synthesis

We chose to apply the Volz and Schaeffer strategy to synthesise **BrTAP** (**Fig. II-5**). A mixture of 9,10-dibromoanthracene in dry diethylether was first treated with 1 equivalent of *n*-BuLi at room temperature (r.t). The formation of lithium monobromoanthracene **2** was confirmed by the observation of the dissolution of the 9,10-dibromoanthracene and the formation of an orange-red solution that quickly reprecipitated. By addition of pyrrole-2-carboxaldehyde, the precipitate disappeared and a green solution was observed. This mixture turned deep red after 1h of stirring, indicating the formation of the alcohol intermediate **3** (not isolated). **3** was then introduced in hot propionic acid and refluxed overnight. After purification, the target **BrTAP** was isolated with 15% yield.[14]

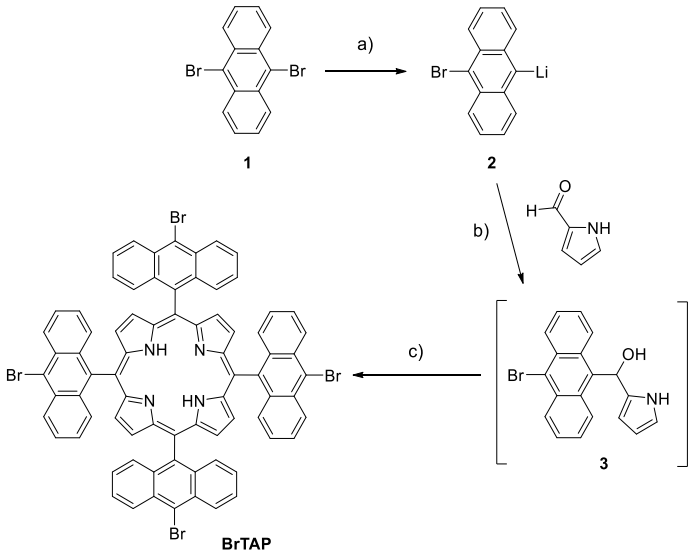

Fig. II-5 Synthetic route of **BrTAP**: a) *n*-BuLi (2 mol/L in hexane, 2.04 eq), diethylether, 30 min, r.t.; b) 1h, r.t (intermediate not isolated); c) propionic acid, 3h, 140°C, 15%.

Before reaching the optimized conditions, we have tested different reaction conditions by variating the solvent and the temperature to enhance the formation of **2**. No change of colour was observed during lithium-halogen exchange for the reaction temperatures at -78°C or 0°C supporting the fact that the organolithium **2** did not form at these temperatures, probably because of the low reactivity of the C−Br bond in the anthracene. The formation of **2** seemed to be limited in anhydrous THF because of the potential reaction between THF and *n*-BuLi at room temperature and under this condition only few amounts of **BrTAP** were collected. Finally, the best yield was obtained with freshly distilled Et_2O, at room temperature, under strictly inert atmosphere of dry argon and *n*-BuLi had to be added in once. **BrTAP** was successfully characterized by ^{1}H and ^{13}C NMRs, High Resolution Mass Spectrometry (HRMS), absorption/fluorescence spectroscopies and X-Ray Diffraction (XRD).

b) NMRs

The ^{1}H NMR spectrum of **BrTAP** was recorded in deuterated 1,1,2,2-tetrachloroethane ($C_2D_2Cl_4$) at 400 MHz and the aromatic region is shown **Fig. II-6**. The chemical shifts at δ 8.11 and -1.77 ppm (not shown) were respectively attributed to the eight hydrogens at β-pyrrolic positions that appeared as singlet because of the symmetry of the porphyrin, and to the two hydrogens in the cavity of the free-base porphyrin. The other signals at δ (ppm): 8.80-8.77 (m, 8H, 4,5-anthracenyls), 7.60-7.57 (m, 8H, 3,6-anthracenyls), 7.30-7.28 (m, 8H, 1,8-anthracenyls), 7.12-7.08 (m, 8H, 2,7-anthracenyls) were attributed to the hydrogens in the anthracene moieties in comparison to anthracenylporphyrins described in the literature.[2,13]

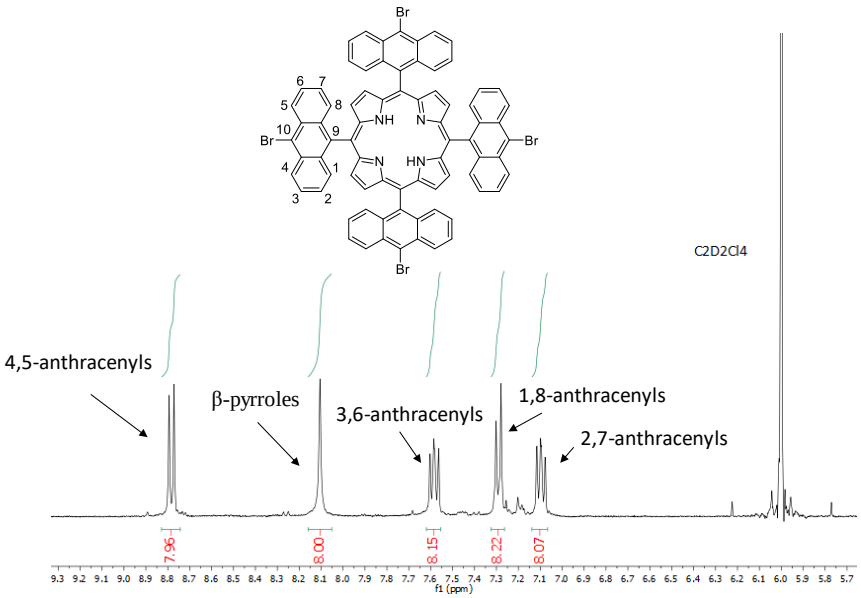

Fig. II-6 ^{1}H NMR spectrum of **BrTAP** (400 MHz, $C_2D_2Cl_4$, 298K).

Although ^{1}H NMR of **BrTAP** was successfully recorded at r.t, we were not able to reach a high signal/noise ratio for the ^{13}C NMR spectrum under ambient conditions. In order to enhance the solubility of the compound, we performed ^{13}C NMR at 333K in $C_2D_2Cl_4$ (boiling point 420K) and we finally recorded a comprehensive spectrum (**Fig. II-7**). The NMR characterizations of our synthetic anthracenylporphyrins were recorded in $C_2D_2Cl_4$ in order to perform NMR at high temperature when necessary.

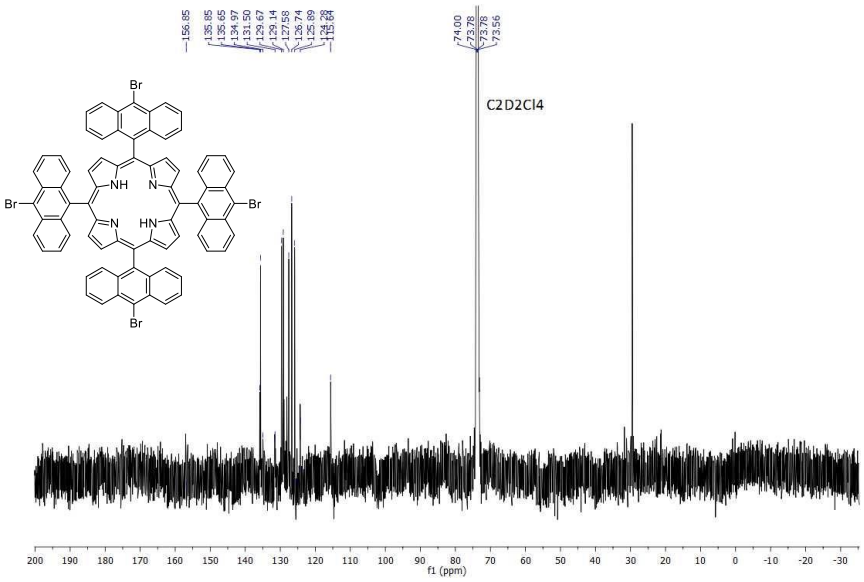

Fig. II-7 ^{13}C NMR spectrum of **BrTAP** (125 MHz, $C_2D_2Cl_4$, 333K).

c) HRMS

The HRMS spectrum of **BrTAP** is shown **Fig. II-8**. An exact mass of 1326.0137 was calculated from $C_{76}H_{42}Br_4N_4$ corresponding to the brut formula of **BrTAP** and an exact mass of 1326.0136 was experimentally determined for M^+. An error of 0.0893 ppm was estimated that definitively confirmed the presence of the target porphyrin.

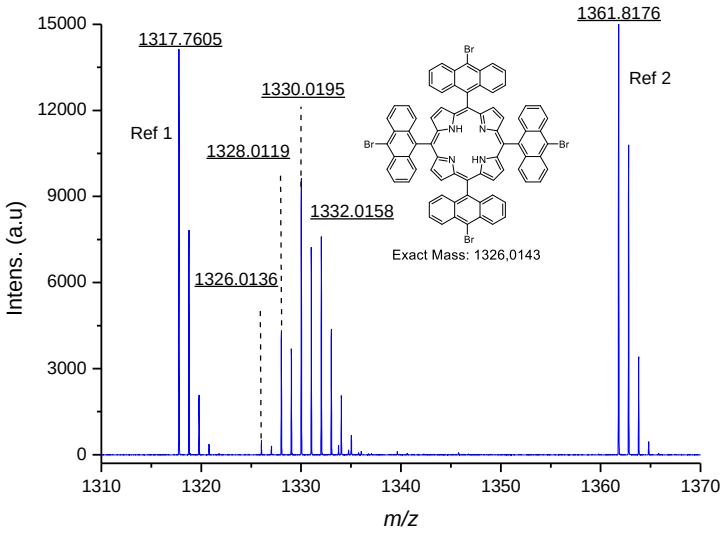

Fig. II-8 HRMS, MALDI-TOF spectrum of **BrTAP**

d) Absorption / fluorescence spectroscopies

The absorption spectra of **BrTAP** (**Fig. II-9**, black solid line) showed the typical absorption features of the porphyrins with a Soret band at 429 nm followed by four Q-bands at 519, 549, 591 and 658 nm and additional bands at 252, 366 and 380 nm arising from the presence of the anthracene units. The emission spectrum of **BrTAP** is shown in **Fig. II-9** (dash line). Both the excitation of the anthracene at λ_{max} = 250 nm and of the Soret band of the porphyrin at λ_{max} = 429 nm led to the typical emission of the porphyrins at 650 and 720 nm without any fluorescence of anthracene in the UV or visible region. The latter phenomena is due to an intramolecular energy transfer, it will be detailed in the Chapter IV of this thesis.

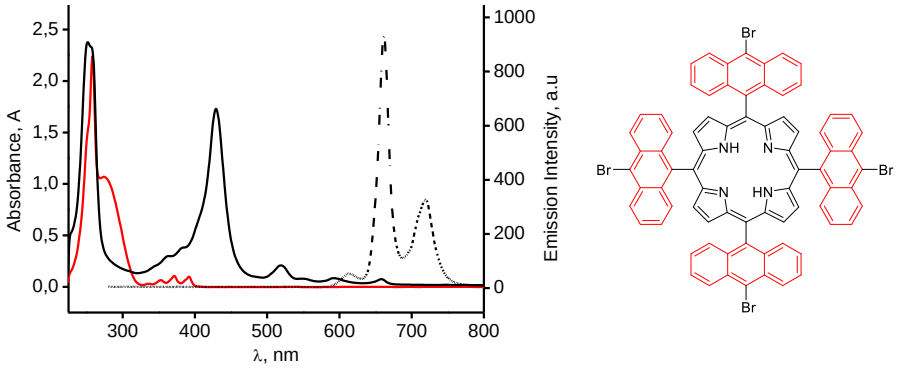

Fig. II-9 Absorption and fluorescence spectra in DCM of **BrTAP** (respectively black solid and dash lines) superimposed with the absorption spectrum of 9-bromoanthracene (red solid line).

e) XRD

The growth of monocrystals was facilitated by insertion of zinc into the cavity of **BrTAP.** Zinc insertion was achieved by modification of literature procedure[15] and afforded **ZnBrTAP** in 76% yield after purification. Crystals of [**ZnBrTAP**(pyridine)] were grown by slow evaporation of a solution in toluene/pyridine (9:1) and the structure was determined by single-crystal X-ray diffraction (**Fig. II-10**, a). The zinc(II) cation is bound to the four nitrogen atoms of [**ZnBrTAP**(pyridine)], with a Zn–N bond length of 2.066 Å, in agreement with the average value of 2.06 Å for the zinc(II) complexes with porphyrins reported in the Cambridge Structural Database (CSD, version 5.39),[16] and to the pyridine molecule, with a bond length of 2.160 Å (average value 2.10 Å from the CSD). The zinc atom is slightly displaced, by 0.309 Å, from the N4 plane, on the same side as the pyridine molecule. The bromoanthracenyl group makes a dihedral angle of 74.33° with the N_4 plane. The molecules are arranged in layers parallel to (001) successive layers along the *c* axis being translated from one another by (½ ½ ½) (**Fig. II-10**, b).

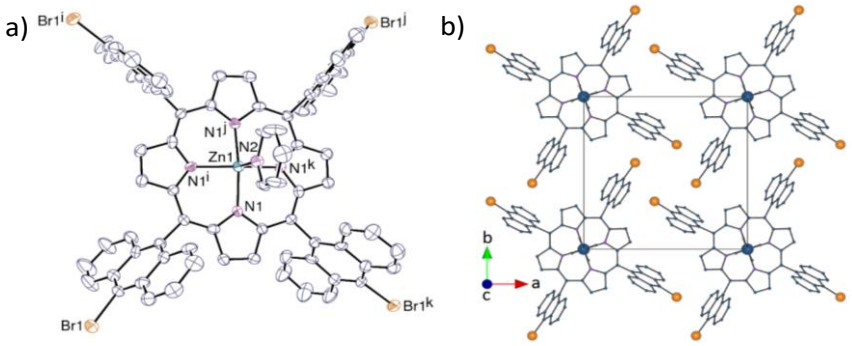

Fig. II-10 a) Molecular structure of [**ZnBrTAP**(pyridine)] with hydrogen atoms omitted; b) arrangement of the molecules within one layer parallel to (001).

II. 2.2. Halogens variation on tetra-anthracenylporphyrins

To investigate the difference of behaviour on surface depending on the nature of halogens, we decided to synthetise the iodinated and chlorinated versions of **BrTAP** and respectively named these compounds **ITAP** (**Fig. II-11**, a) and **ClTAP** (**Fig. II-11**, b)**.**

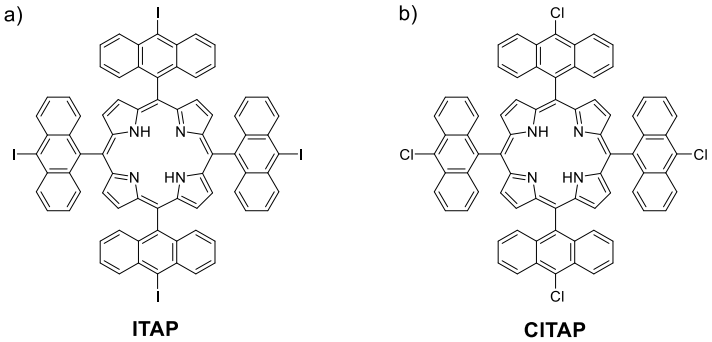

Fig. II-11 Chemical structures of a) 5,10,15,20-tetrakis(10-iodoanthracen-9-yl)porphyrin (**ITAP);** and b) 5,10,15,20-tetrakis(10-chloroanthracen-9-yl)porphyrin (**ClTAP)**.

a) Synthesis

For the synthesis of **ITAP**, the 9,10-diiodoanthracene (**5**) precursor was prepared following literature procedure by lithiation of its brominated analogue **3** followed by iodination of the organolithium compound **6**.[17] Recrystallisation from CCl_4 afforded yellow needles corresponding to compound **5** in 47% yield (**Fig. II-12**).

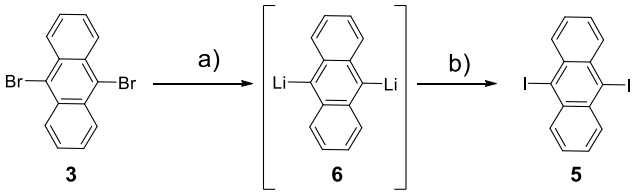

Fig. II-12 Synthetic route of 9,10-diiodoanthracene **5**, a) *n*-BuLi, (2.05 eq), dry diethylether, 15 min, r.t; b) I_2, dry diethylether, 30 min, r.t, 47%.

For the synthesis of **ClTAP**, the 9-bromo-10-chloroanthracene precursor (**8**) was prepared by bromination of 9-chloroanthracene **7** with Br_2 following literature procedure.[18] Recrystallisation from CCl_4 afforded yellow needles corresponding to target compound **8** isolated in 33% yield (**Fig. II-13**).

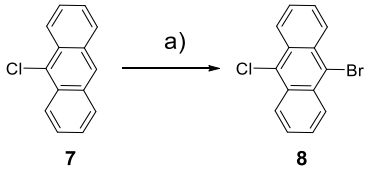

Fig. II-13 Bromination of 9-bromo-10-chloroanthracene **8,** a) Br_2, dry DCM, 8h, r.t, 33%.

We applied the Volz and Schaeffer strategy to synthetise **ITAP** and **ClTAP** from pyrrole-2-carboxaldehyde and the corresponding anthracene precursors **5** and **8** (**Fig. II-14**).

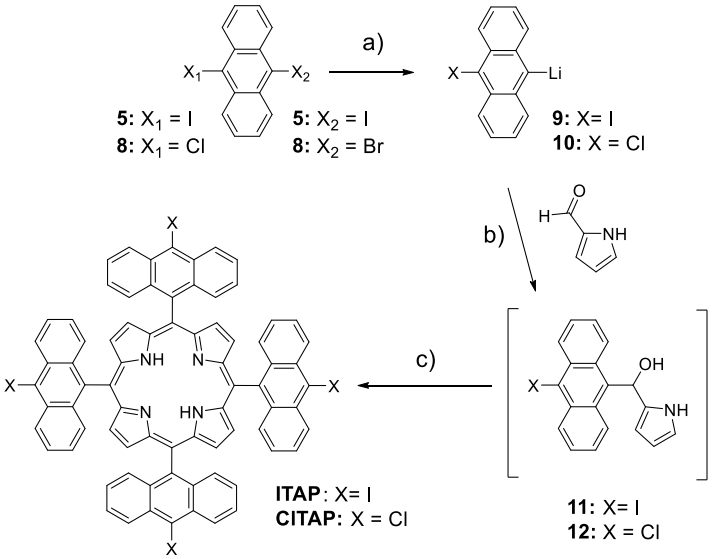

Fig. II-14 Synthetic routes of **ITAP** and **ClTAP**, a) *n*-BuLi (2.04 eq), diethylether, 30 min, r.t.; b) 1h, r.t, intermediate not isolated; c) propionic acid, 3h, 140°C, less than 1% (**ITAP**) 7% (**ClTAP**).

Similarly to the synthesis of **BrTAP**, the same changes of colour were observed by addition of *n*-BuLi and pyrrole-2-carboxaldehyde at r.t to the mixtures of **5** or **8** in Et_2O. After treatments, the resulting mixtures were introduced in hot propionic acid, refluxed overnight and purified by filtration on filter paper with a large amount of MeOH until the elution of a clear solution. The collected precipitates were poured into MeOH (500 mL), sonicated for 2 min and filtered again. This process was repeated twice to remove the major part of polymeric side products. After purification on a silica column eluted with toluene/heptane (1:1, v/v) and precipitation in MeOH, **ITAP** an **ClTAP** were afforded in less than 1% yield and 7% yield respectively (with respect to pyrrole-2-carboxaldehyde). The identities of **ITAP** and **ClTAP** were confirmed by HRMS and the absorption and ^{1}H NMR spectra were recorded. Only **ClTAP** was characterized by ^{13}C NMR (see Experimental section).

b) MS

The presence of **ITAP** was detected by MS analysis with an isotopic signature at *m/z* 1517.96 but we also detected the presence of other derivatives. In particular, an intense peak of iodopentamer was detected in the MS spectrum with an isotopic distribution at *m/z* 1915.03 (**Fig. II-15**, a). The presence of **ClTAP** was detected by MS analysis with an isotopic signature at *m/z* 1150.21 and importantly no pentamer seemed to form in the synthesis of **ClTAP** because no peak corresponding to the chloropentamer at *m/z* 1455.3 was detected in the MS spectrum (**Fig. II-15**, b).

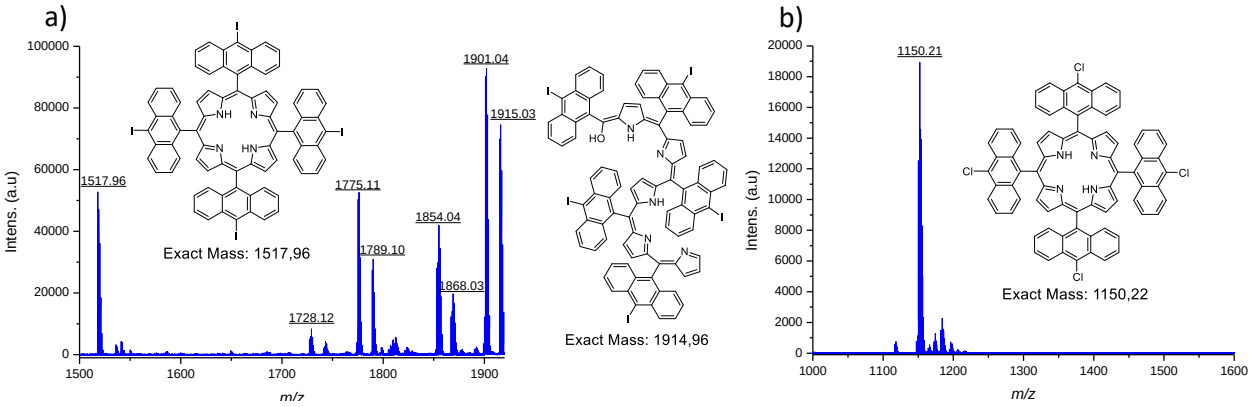

Fig. II-15 Mass spectra with chemical structures of a) **ITAP** and iodopentamer**;** b) **ClTAP**.

To limit the formation of pentamer in the synthesis of **ITAP**, we tried to template the formation of the macrocycle of **ITAP** by insertion of Cu(II) that unfortunately led to similar results. The formation of pentamers was observed in the synthesis of **BrTAP** but was insignificant and we suspected that the enhancement of the side reaction was due to the enhanced reactivity of C-I bonds compared to C-Br and C-Cl bonds. It is worth mentioning that the isolation of **ITAP** from the mixture containing the iodopentamer was achieved by size exclusion chromatography (SEC) using THF before recording the absorption and ^{1}H NMR spectra.

c) ^{1}H NMRs

The ^{1}H NMR spectrum of **ClTAP** was recorded in $C_2D_2Cl_4$ at 400 MHz and the aromatic region of the spectrum is shown in **Fig. II-16.** The chemical shifts at δ 8.11 ppm and -1.77 ppm (not shown) were respectively attributed to the eight hydrogens at β-pyrrolic positions the two hydrogens of the free-base porphyrin. The other signals at δ (ppm) 8.84-8.70 (m, 8H, 4,5-anthracenyls), 7.64-7.54 (m, 8H, 3,6-anthracenyls), 7.35-7.25 (m, 8H, 1,8-anthracenyls), 7.16-7.06 (m, 8H, 2,7-anthracenyls) were attributed to the hydrogens in the anthracene moieties in comparison to anthracenylporphyrins described in the literature.[2,13]

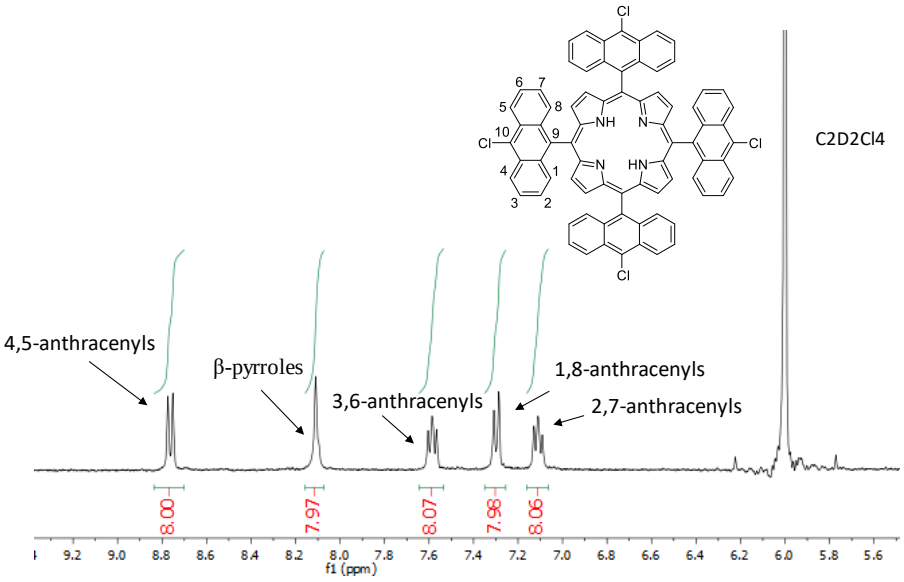

Fig. II-16 ^{1}H NMR spectra of **ClTAP** (400 MHz, $C_2D_2Cl_4$, 298K).

Although, a low signal/noise ratio was afforded on the ^{1}H NMR spectrum of **ITAP,** we observed the presence of duplicated signals with different intensities and a chemical shift at 8.85 ppm that corresponded to signals of hydrogens in position 10 of anthracenes. We thus thought of the presence of deiodinated porphyrins that could come from either lithiation of the two iodines during the synthesis or from a thermal degradation already strong at r.t. To investigate the ageing, we warmed a powder of **ITAP** at 50°C for 2h under vacuum and recorded again the NMR. Because we observed an increase of number of duplicated signals, we thus came to the conclusion that **ITAP** was not stable at r.t. and decided to stop the development of **ITAP** due to its instability over thermal treatment incompatible with on-surface synthesis. Therefore, we explained the low yield of formation of **ITAP** by a strong thermal degradation and/or the important formation of polymers during the synthesis.

II. 2.3. Tetra-bromobisanthracenylporphyrins

We imagined the structure of 5,10,15,20-tetrakis(10'-bromo-[9,9'-bianthracen]-10-yl)porphyrin (**BrDTAP**) that can be seen as an extended version of **BrTAP** with an additional row of anthracenes along the periphery of the molecule (**Fig. II-17**). The objective of this extension is to form on surface a square type nitrogen-doped **GNM-2** with a decrease of nitrogen content (3.3% per repeating units), larger pores and longer necks compared to the structure of **GNM-1.** The ultimate goal of this project is to compare the electronic properties of these two GNMs to propose a reliable comprehension of the impact of these structural and chemical variations.

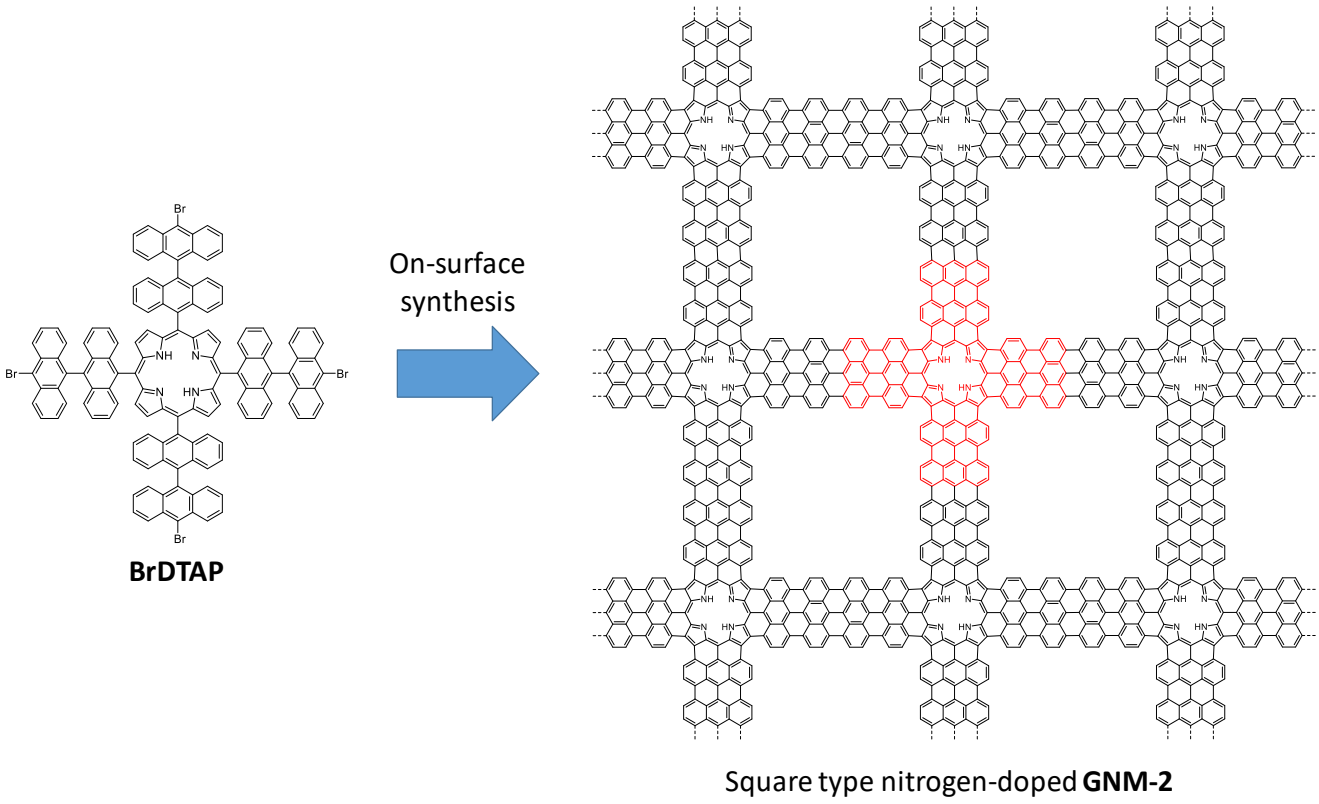

Fig. II-17 Target structure of square type nitrogen-doped **GNM-2** (right) after on-surface synthesis from 5,10,15,20-tetrakis(10'-bromo-[9,9'-bianthracen]-10-yl)porphyrin (**BrDTAP**, left).

a) Synthesis

We applied the strategy of Volz and Schaeffer to synthetise **BrDTAP** from **DBBA** (**Fig. II-18**). The lithiation of **DBBA** was initially performed in Et_2O at r.t with *n*-BuLi (2.05 eq) but we observed neither the dissolution of **DBBA** nor the formation of an orange-red solution. No further change occurred by addition of pyrrole-2-carboxaldehyde even after 1h of stirring and no absorption bands of porphyrin were detected by UV-visible after the reaction in propionic acid. Therefore, we supposed that the organolithium species **15** did not or barely formed and we explored a variety of synthetic conditions that are summarised in **Table II-1** to enable the lithiation and afford the target **BrDTAP**.

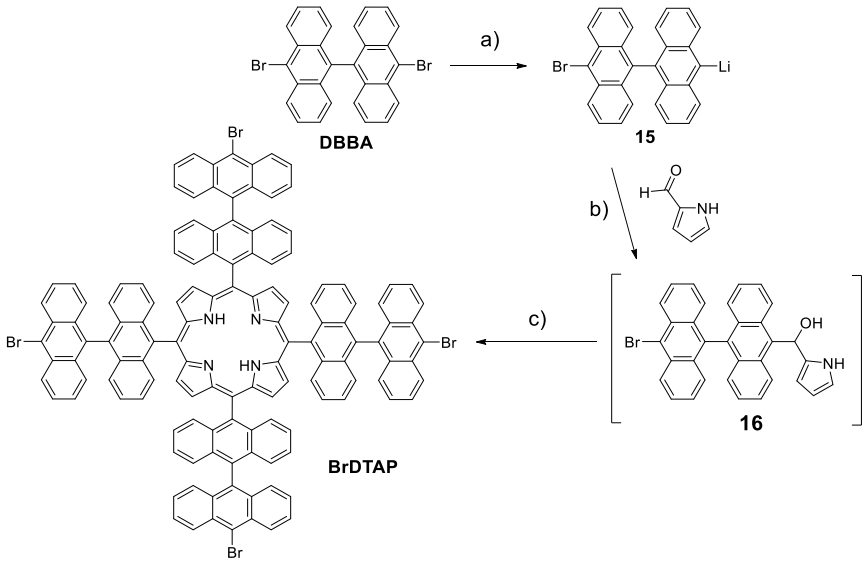

Fig. II-18 Synthetic route of **BrDTAP**; a) *n*-BuLi (2.04 eq), diethylether, 30 min, r.t.; b) 1h, r.t, intermediate not isolated; c) propionic acid, 3h, 140°C.

Entry	Solvent(s) (ratio)	Organolithium reagent	Lithiation temperature (°C)	Observation
1	Et_2O	*t*-BuLi	r.t	Starting material insoluble, no formation of porphyrin
2	Et_2O/THF 1:1	*t*-BuLi	r.t	No formation of porphyrin
3	THF	*n*-BuLi	r.t	No formation of porphyrin
4	THF	*n*-BuLi	-40	**BrDTAP** detected by MS analysis with presence of debrominated products and poly x5
5	Et_2O/THF 2:1	*n*-BuLi	r.t	**BrDTAP** detected by MS analysis with presence of debrominated products and poly x5
6	Et_2O/THF 1:1	*n*-BuLi	r.t	**BrDTAP** detected by MS analysis with presence of debrominated products and poly x5
7	Et_2O/THF 1:2	*n*-BuLi	r.t	Poor formation of porphyrin, major presence of starting material in UV-Vis
8	Benzene	*n*-BuLi	r.t	no formation of porphyrin
9	Benzene / Et_2O 1:1	*n*-BuLi	r.t	Poor formation of porphyrin and major presence of poly x5 on MS spectrum
10	Benzene / Et_2O 9:1	*n*-BuLi	r.t	**BrDTAP** detected by MS analysis with presence of debrominated products and poly x5

Table II-1 Summary of the conditions tested to optimise the synthetic protocol of **BrDTAP.**

We decided to replace *n*-BuLi (pK_a 50) by *t*-BuLi (pK_a 53) and tried the lithiation of **DBBA** in Et_2O (entry 1) and in Et_2O/THF (1:1) to improve the solubility of **DBBA** (entry 2). No signal of porphyrin was detected at the end of the reaction by UV-Visible spectroscopy for both tested conditions and we concluded that the use of a stronger base was not required. Subsequently, we investigated the effect of solvents. When the reaction was performed in anhydrous THF (entry 3), a yellow solution was observed with complete dissolution of **DBBA**. The yellow solution turned red by addition of *n*-BuLi at r.t. Unfortunately, no porphyrin was detected at the end of the reaction and we concluded that the red solution was not due to the formation of the organolithium species. It is known that *n*-BuLi strongly reacts with THF at r.t that could be in the origin of the red solution.[19] Thus, the reaction was performed at -40°C to reduce the reactivity with THF (entry 4). By cooling the yellow solution of **DBBA** to -40°C, a precipitation occurred and no change was observed upon introduction of *n*-BuLi. After 30 min, pyrrole-2-carboxaldehyde was added to form **16** and the cooling bath was removed. The formation of a red solution was observed during stirring at r.t and the presence of a porphyrin was detected by UV-Vis spectroscopy after the reaction in propionic acid. After purification, the target porphyrin **BrDTAP** was identified (*m/z* 2031.43 $M^{+\cdot}$) by MALDI-TOF MS analysis. However, **BrDTAP** was obtained in a complex mixture that was difficult to separate and contained mono-, bis-, and tris-debrominated species (isotopic peak at *m/z* 1953.49, 1875.57, 1797.64) as well as pentamers by-products (isotopic signature at *m/z* 2557.43, 2478.64, 2401.52) (**Fig. II-19**). We attributed the presence of brominated by-products to a double lithiation of a small amount of **DBBA** in solution due to the poor dissolution of compounds. Unfortunately, the mixture was afforded in less than 1% and we were unable to further purify such small amount of porphyrin by chromatography techniques. However, the successful formation of **BrDTAP** was encouraging and we chose to improve the synthetic protocol.

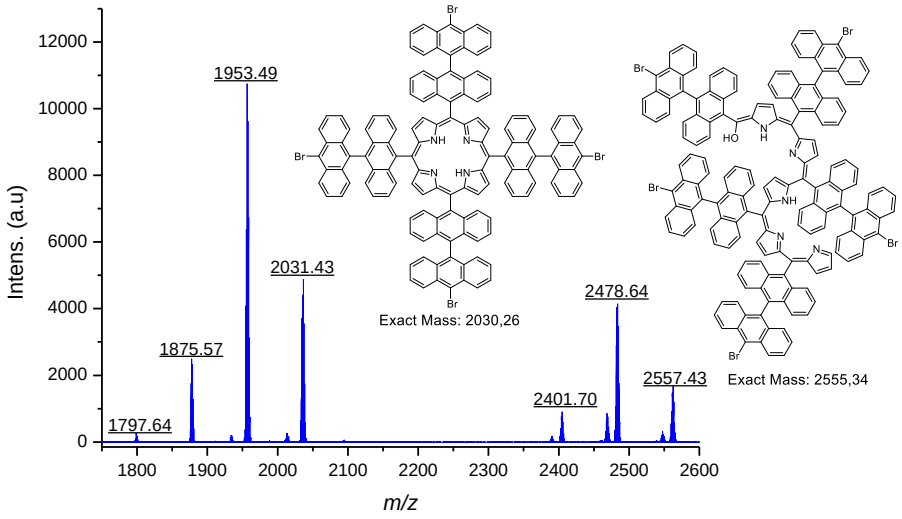

Fig. II-19 MS spectrum and chemical structures of **BrDTAP** the corresponding pentamer.

From the synthesis of **BrTAP**, we knew that the lithiation at low temperature in THF led to a limited formation of anthracenylporphyrins. We thus decided to pursue the development of the synthesis of **BrDTAP** in a mixture of THF/Et_2O at r.t. With a 2:1 ratio of THF/Et_2O (entry 5), only a yellow-orange suspension was observed by addition of *n*-BuLi and only traces of **BrDTAP** were detected by UV-Vis spectroscopy with a major absorption of starting **DBBA** and its corresponding debrominated by-products. By adjusting the ratio of THF/Et_2O to 1:1 and 1:2 (entries 6 and 7), **BrDTAP** was detected in the same complex mixture already afforded by the reaction at -40°C in THF (entry 4). In comparison to the experiments in THF and Et_2O alone, it seemed that the presence of Et_2O was important to form **BrDTAP** and could be possibly related to a stabilization of organolithium species. We used benzene instead of THF to avoid the issue of reactivity with *n*-BuLi at r.t. No porphyrin was isolated for the reaction in benzene alone (entry 8). This result tends to confirm the importance of Et_2O in the synthesis. By using a mixture of benzene/Et_2O with a ratio of 1:1 (entry 9), a clear yellow suspension was observed upon addition of *n*-BuLi and although the presence of **BrDTAP** was detected by UV-Vis spectroscopy, a major formation of pentamer was detected by MS analysis. Finally, by adjusting the ratio of benzene/Et_2O to 9:1 (entry 10), the same changes of colour and precipitation as in the synthesis of **BrTAP** occurred. An orange-red solution was observed by addition of *n*-BuLi to the initial yellow suspension that quickly reprecipitated. Upon addition of pyrrole-2-carboxaldehyde, the precipitate disappeared and this solution turned deep red after 1h of stirring. **BrDTAP** was again detected in addition to debrominated by-products and pentamers. In comparison to the other experiments, a larger amount of products was collected thus allowing purifications. The porphyrin was purified by silica column using CS_2/DCM (9:1) and the first green fraction was collected corresponded to **BrDTAP**. After recrystallisation from DCM/MeOH, 2 mg of a green powder was obtained that did not allow the record of a comprehensive NMR spectrum. Therefore, the purity of **BrDTAP** has not been proved yet and further analysis by MS has to be done to detect the presence of by-products. Despites the number of synthetic parameters explored, the formation of **BrDTAP** remained very limited and we found that the synthetic conditions with benzene/Et_2O to 9:1 (entry 10) were the most promising. **BrDTAP** was characterized by absorption spectroscopy and HRMS and its full characterization by NMR is still in progress in our group (see Experimental part).

b) Absorption spectroscopy

The optical signature of **BrDTAP** (solid blue line) is composed by a Soret band at 430 nm and four Q bands at 524, 567, 613, 648 nm **(Fig. II-20).** The three bands in the UV region at 343, 345 and 406 nm were attributed to the absorption of the anthracenes at the periphery of the molecule in comparison to the absorption spectrum of **DBBA** (dash black line).

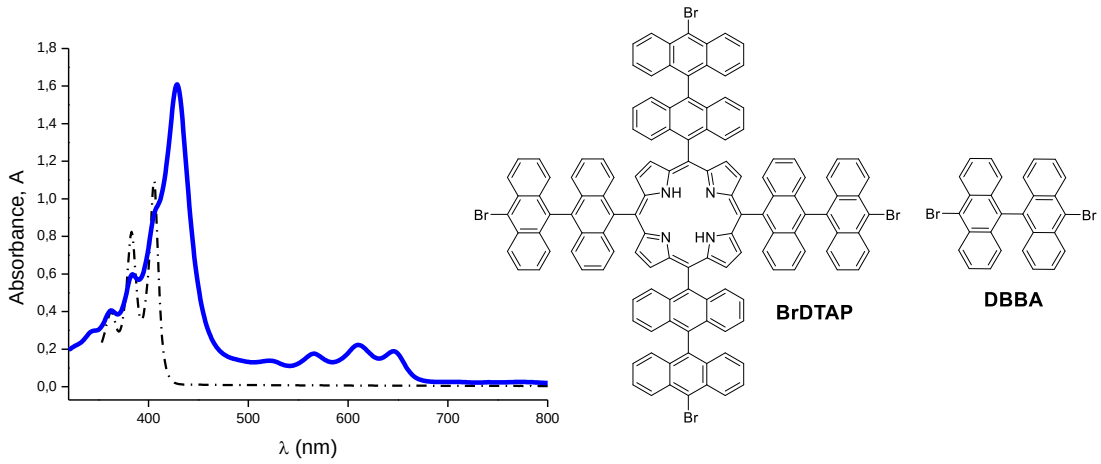

Fig. II-20 Absorption spectra in DCM of **BrDTAP** (solid blue line) and **DBBA** (dash black line).

II. 2.4. Bis-bromoanthracenyl porphyrin

II. 2.4.1. Bis-anthracenylporphyrin in the literature

Only a few papers have reported the synthesis of bis-anthracenyl porphyrin derivatives. This type of porphyrin is usually prepared by a Suzuki-Miyaura cross coupling reaction either from diiododiphenylporphyrins coupled with 9-boronic anthracene[1] or by reversing these functional groups with boronic acids on porphyrins and halogens on anthracene.[2] Based on these reports, it seems that the coupling reaction between the porphyrin and the anthracene moieties is limited by steric hindrance and a yield of 10% is usually obtained. To enhance the yield of bis-anthracenylporphyrins, Davis *et al.*[3] reported a screening of the conditions of the Suzuki-Miyaura coupling reaction. The best conditions were determined to be $PdCl_2(PPh_3)_2$ and $AsPh_3$ in the presence of CS_2CO_3 in THF at 67°C. After 72h of reaction, [5,15-bis(anthracen-9-yl)-10,20-diphenylporphyrinato]Ni(II) was afforded in 84% yield and the authors mentioned that a longer reaction time was required to afford the free-base porphyrin with a lower yield of 35%. This result indicated that the nature of the chelated metal plays a role in the reactivity of the porphyrin. Finally, Suzuki and Osuka reported that the condensation of pentafluorophenyldipyrromethane and anthracenecarboxaldehyde following the 2+2 method of MacDonald did not lead to the formation of bis-anthracenyl porphyrin.[20]

Our objective was to develop the synthesis of 5,15-bis(10-bromoanthracen-9-yl)-10,20-diphenylporphyrin (**BrBAP**), to trigger on surface a linear polymerisation leading to the formation of nitrogen doped **GNR-1 (Fig. II-21)**.

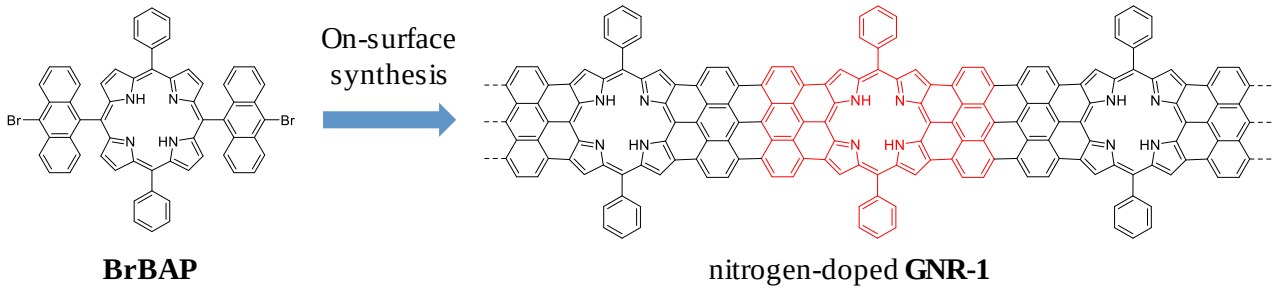

Fig. II-21 Target structure of nitrogen-doped **GNR-1** (right) from on-surface synthesis of 5,15-bis(10-bromoanthracen-9-yl)-10,20-diphenylporphyrin (**BrBAP**, left).

a) Synthesis

We first considered preparing **BrBAP** *via* a Suzuki-Miyaura cross coupling reaction between 5,15-diiodo-10,20-diphenylporphyrin and (10-bromoanthracen-9-yl)boronic acid. As it will be discussed in the next chapter, we applied this coupling reaction to form 5,15-di(anthracen-9-yl)-10,20-diphenylporphyrin (**BAP**) in 22% yield. Considering several factors based on the yield, the possible side reaction of (10-bromoanthracen-9-yl)boronic acid on itself and the long reaction time required, we finally chose to test the preparation of **BrBAP** *via* the 2+2 MacDonald method from the anthracenyldipyrromethane derivative **17** (**Fig. II-22**).

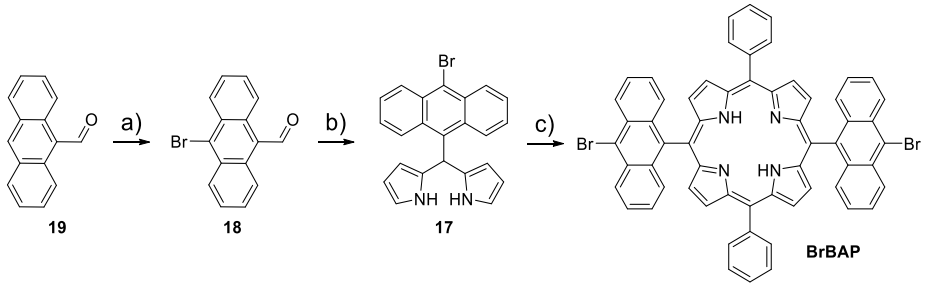

Fig. II-22 Synthetic route for **BrBAP**, a) Br_2, dry DCM, 8h, r.t, 65%; b) pyrrole (excess), TFA (cat), dry DCM, 15 min, r.t; c) benzaldehyde (1 eq), TFA, 2.5h, r.t then DDQ, 1h, at reflux, 6%

We prepared the 10-bromoanthracene-9-carboxaldehyde (**18**) by bromination of anthracene-9-carbaldehyde (**19**) (**Fig. II-22**, a). Recrystallisation from toluene/cyclohexane (3:1) yielded yellow needles corresponding to **18** in 65% yield as confirmed by both MS and ^{1}H NMR (see Experimental section). We synthetised the bromoanthracenedipyrromethane **17** by condensation of **18** in the presence of excess pyrrole with a catalytic amount of trifluoroacetic acid (TFA) (**Fig. II-22**, b). After treatments, the resulting residue was partially purified by filtration over a silica plug eluted with DCM/Et_3N (99:1); the first orange-red fraction containing the crude dipyrromethane **17** was collected. Because of its limited stability, **17** was used without further purification in the next step. Finally, **19** was condensed with benzaldehyde in the presence of TFA (**Fig. II-22**, c) following the optimized conditions described by Lindsey.[21] After 2.5h, 2,3-dichloro-5,6-dicyano-1,4-benzoquinone (DDQ)

was added to oxidise the porphyrinogen. Precipitation in MeOH yielded violet crystals of **BrBAP** in 6% yield (for both steps). **BrBAP** was characterized by absorption spectroscopy, HRMS and ^{1}H NMR. Additional ^{1}H 2D-COSY NMR and ^{13}C NMR have yet to be recorded to achieve the full characterization of the compound and correctly assign each signal of the ^{1}H NMR spectrum.

b) Absorption spectrum

The UV-Visible absorption spectrum of **BrBAP** was composed of a Soret band at 426 nm and four Q bands at 518, 550, 596, 656 nm **(Fig. II-23**). The absorption signals of anthracene in the UV region were difficult to observe and only a band at 366 nm was discernible.

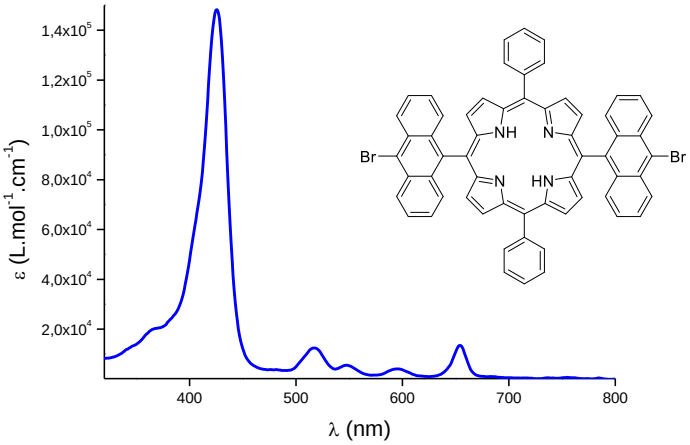

Fig. II-23 Absorption spectrum of **BrBAP** recorded in DCM.

II. 3. Anthracenylporphyrins on-surface

We now turn to the study of deposition of anthracenylporphyrins on a surface and to the investigation of their reactivity and assemblies with direct visualization using STM.

II. 3.1. Notions of crystallography

The periodic atomic arrangement of a crystallographic system is described by an unit cell composed of a crystalline structure (defined by 3 segments a, b, c with three angles α, β, γ) associated with one of the four crystallographic modes (P, F, C, I). For example, the face centred cubic structure (FCC) is described by a cubic system defined with a=b=c and α=β=γ= 90° and associated with the mode F (**Fig. II-24**, a). The FCC structure is the crystallization system of many metals like Au, Ag, Cu and Pd. In addition, crystallographic planes are expressed with Miller indices (*hlk*) that determine three points A, B, C contained in the same plane and defined by OA=a/*h*, OB=b/*k*, OC=c/*l*. For example, the plane (111) in a cubic system corresponded to *h*=*k*=*l*=1 and defined the three points A, B, C such as OA=OB=OC=a that defined the plane shown in blue in **Fig. II-24**, b.

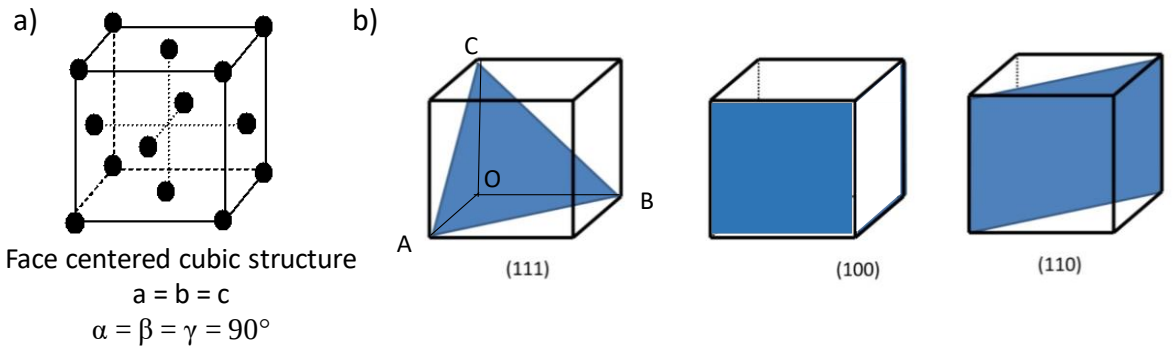

Fig. II-24 a) Representation of the face centered cubic (FCC) structure with crystallographic parameters; b) crystallographic planes with corresponding Miller indices (*hkl*).

The definition of planes in crystallographic systems directly reflect of the atomic arrangement and the symmetry of oriented surfaces. The unit cells of orientated surfaces are described with two unitary vectors $\overrightarrow{a1}$, $\overrightarrow{a2}$ and an angle between. The oriented surfaces (111), (100) and (110) of the FCC structure are shown in **Fig. II-25**. The unit cell of (111) is hexagonal and is defined by a1=a2=$a\sqrt{3}/2$ with an angle of 60°, the unit cell of (100) is hexagonal and is defined by a1=a, a2=$a\sqrt{2}/2$ with an angle of 60° and the unit cell of (110) is rectangular and is defined by a1=$a\sqrt{2}$, a2=a, with an angle of 90°.

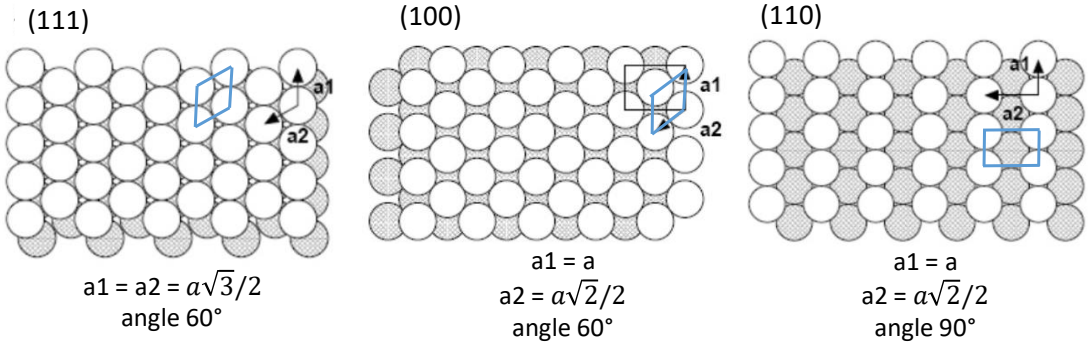

Fig. II-25 Atomic arrangements and parameters of crystallography of oriented surfaces (111), (100) and (110) of the FCC structure.

It was found in literature that depending on the nature of the metal and the crystallographic orientation of surfaces, different factors influencing the execution of the on-surface synthesis can be modulated. Notably, the catalytic activity and the adsorption force of a surface could be related to the nature and the density of atoms at the surface. A general tendency found in the literature indicates that, (111) is denser and should exhibit a less catalytic activity and a lower molecule/substrate interaction than a surface of (100) than (110), and depending of the nature of the metal, a surface composed of Cu should be more active than a surface of Ag, than a surface of Au.[22,23] In addition, it was found that the nature and the orientation of the surfaces are parameters able to modify the diffusion of species,

the configuration of the precursors and the reaction pathway that could lead to the formation of structures of varying topologies, sizes and qualities.[24,25] Accordingly, we chose to investigate the organization of **BrTAP** and **BrBAP** on different natures of surface of Au, Ag, Cu and Pd with different orientations of (100), (110) and (111). The STM studies were conducted by the groups of Sylvain Clair (IM2NP, Aix-Marseille University) and Laurence Masson (CINaM, Aix-Marseille University).

II. 3.2. Assemblies of tetra-bromoanthracenylporphyrin

BrTAP was evaporated on a surface of Au (111) held at r.t. No stable supramolecular phase was observed at r.t or after annealing at 100°C and 250°C and desorption occurred above 320°C. Likewise, no stable phase was observed on Ag (100) even after annealing the surface at 220°C. We assumed that the behaviour could be related to low interaction and high mobility of the physisorbed species on Au (111) or Ag (100). By deposition of **BrTAP** on Ag (111) at r.t, we observed the formation of short and packed chains of about 5-10 nm long, aligned along the [100] direction and regularly distributed with a distance of 1.4 nm along the [1-10] direction (**Fig. II-26**, a). After annealing the surface at 200°C, we observed the formation of a regular assembly with molecular rows of up to 100 nm long, aligned along the [1-10] direction and laterally distributed with a distance of 1.4 nm along the [100] direction (**Fig. II-26**, b). Different contrasts were observed and because we found that the distance between bright spots along the rows remained constant with a value of 0.7 nm, we assigned the central bright spots surrounded by the less intense lobes to the molecular units. We observed that the location of the bright spots were slightly off-center from the main row axis and we defined the unit cell with two molecular units expressed with the two unitary vectors $\overrightarrow{a1}$, $\overrightarrow{a2}$ corresponding to the distances between two bright spots along and between the molecular rows (**Fig. II-26**, c).

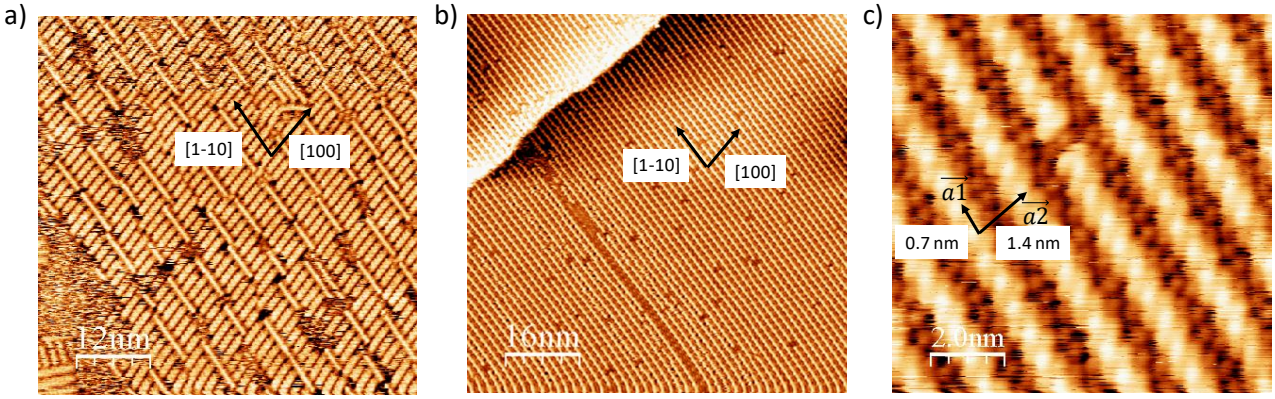

Fig. II-26 STM image of the deposition of **BrTAP** on Ag (111), a) supramolecular phase by deposition at r.t; b) assembly observed after annealing the surface at 200°C; c) close-up of the annealed sample with the unit cell expressed with vectors $\overrightarrow{a1}$, $\overrightarrow{a2}$ corresponding to the distances along and between molecular rows.

Gas-phase molecular dynamics simulations of **BrTAP** were conducted to better understand the assembly on surface to determine theoretical molecular distances (**Fig. II-27**, a). According to the theoretical model, **BrTAP** exhibited a square shape with a distance of 1.35 nm between bromines of two adjacent anthracenes and a distance of 1.92 nm for the diagonal. None of the theoretical distances matched with the distance of 0.7 nm experimentally determined along $\overrightarrow{a1}$. The intermolecular distance of 0.7 nm was previously found in the literature in studies of edge-on adsorption of porphyrins on a surface and similar STM images were observed for the deposition of **BrTAP** on Ag (111) (**Fig. II-27**, b).[26–28] We thus came to think that the assembly of **BrTAP** was incompatible with a flat-lying adsorption and the hypothesis of an edge-on adsorption was considered.

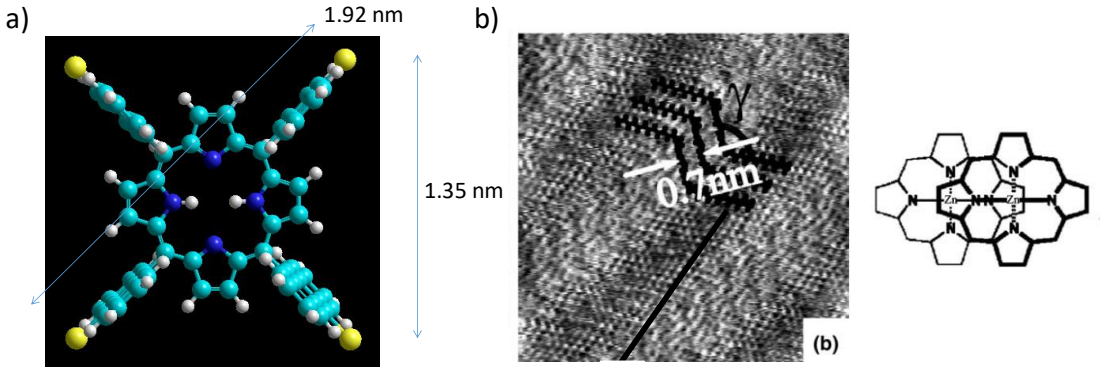

Fig. II-27 a) Gas-phase molecular dynamics simulations of **BrTAP** with molecular distances; b) close-up STM images of a packed assembly of edge-on adsorbed porphyrins on surface with a measure of the intermolecular distance of 0.7 nm.[26]

A better agreement was found in STM images when porphyrins were perpendicular to the plane of the surface (**Fig. II-28**). We assumed that π-stacking interactions between twisted anthracenyl moieties led to a stacked arrangement of macrocycles perpendicular to the row direction and the assembly better corresponded to aligned rows of edge-on porphyrins with the less intense lobes corresponding to 10-anthracenyl bromines.

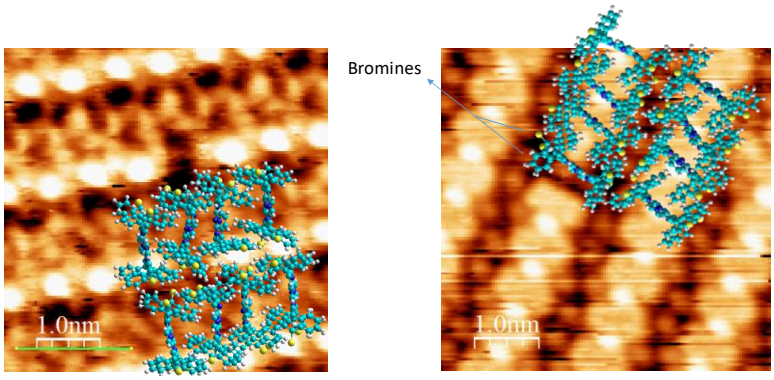

Fig. II-28 STM images of the annealed sample of **BrTAP** on Ag (111) superimposed with the model of aligned rows of edge-on porphyrins.

The latter observation suggested that the intermolecular interaction was stronger than the interactions with the Ag (111) surface that prevented the formation of 2D networks *via* polymerisation and thus the formation of GNM. In order to increase the interaction with the surface and force the molecule to lay down parallel to the surface, similar deposition and STM experiments were performed on more active surfaces like Ag (110), Cu (111) and Pd (111).

The deposition at r.t of **BrTAP** on Ag (110) and Cu (111) led to the formation of similar short chains of about 3 to 5 nm long as observed on Ag (111) (**Fig. II-29**, a-b). Disordered orientations were observed on Cu (111) whereas a regular distribution was seen on Ag (110) with a distance of 1.1 nm separating two adjacent chains along the [001] direction. Such a difference of orientations can be explained by the variety of adsorption sites characteristic of each surface. A difference of contrast with bright and less intense central spots was observed in STM images and we assigned the central spots to a single molecular unit. The intermolecular distance was measured to 0.75 nm. From the STM image of Ag (110) (**Fig. II-29**, c), we noticed that every second molecule was systematically observed as a brighter central lobe. A constant distance of 1.5 nm corresponding to five silver atoms of the surface was measured between two brights spots along the molecular rows. Because two molecules seemed to share an asymmetric environment with atoms from the surface, we attributed the difference of contrast to an epitaxial effect.

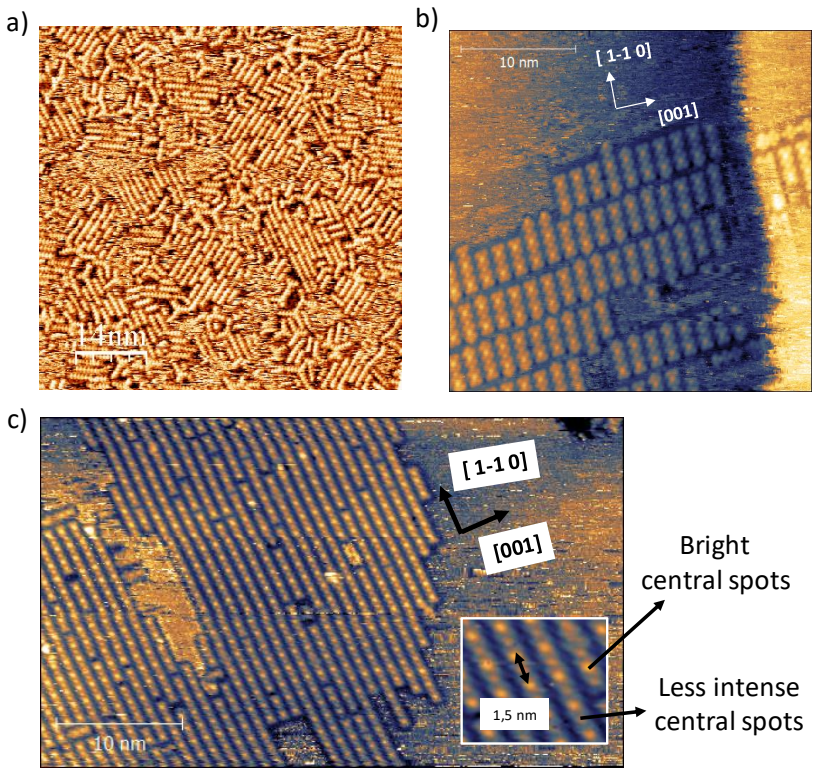

Fig. II-29 STM images of **BrTAP** after deposition at r.t a) on Cu (111); b-c) on Ag (110).

After deposition of **BrTAP** on Ag (110) at 300°C, we again observed the formation of molecular rows of up to 100 nm long, aligned along the [1-10] direction and laterally distributed with a distance of 1.1 nm (**Fig. II-30**, a). Similar assemblies were formed on Cu (111) after annealing the surface at 150°C (**Fig. II-30**, b). The latter results again ruled out a flat-lying adsorption of the porphyrins and again suggested an edge-on configuration. Therefore, the π-stacking interactions seemed to remain stronger than the adsorption with the surfaces of Ag (110) and Cu (111).

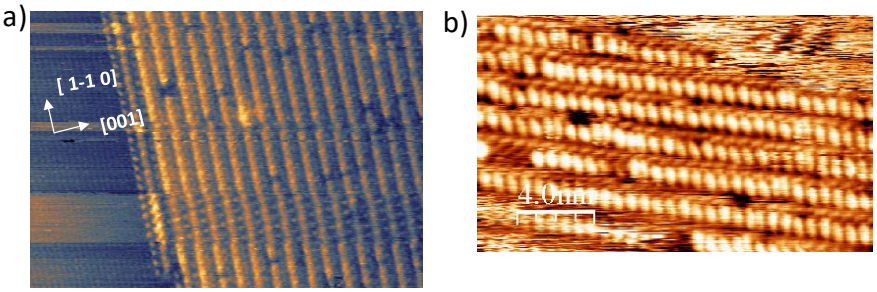

Fig. II-30 a) STM images of **BrTAP** a) after deposition on Ag (110) at 300°C; b) after annealing Cu (111) at 150°C.

Finally, the deposition at r.t of **BrTAP** on Pd (111) at coverage inferior to the monolayer led to highly diffusive species that were difficult to image on the surface and the deposition at full coverage of the surface led to the formation of a 2D monolayer with quasi-hexagonal order (**Fig. II-31**). Single molecular units were assigned to grey spots and an average intermolecular distance of 2.2 nm was determined. The latter experimental distance was in better agreement with the calculated distance in the theoretical model (**Fig. II-27**, a) and suggested a flat-lying adsorption of porphyrins. Hence, the molecule-substrate interactions on Pd (111) should be stronger than the intermolecular π-stacking.

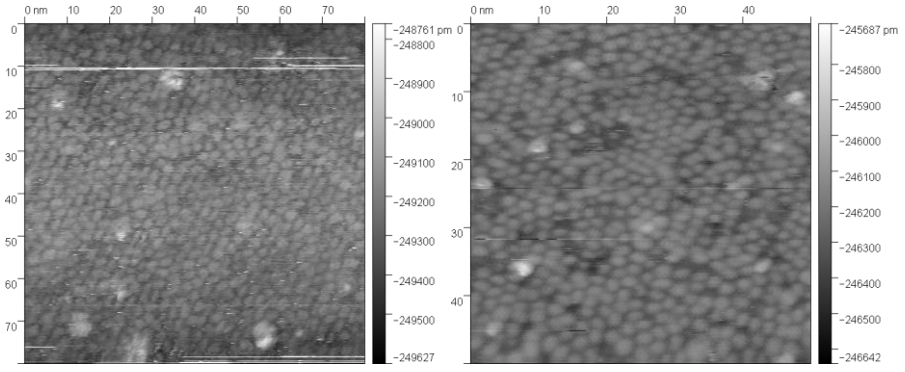

Fig. II-31 STM images of the deposition of **BrTAP** on Pd (111) at r.t at full coverage of the surface.

After annealing the surface at 300°C, the formation of molecular chains of about 5 nm and hexagonal structures were observed (**Fig. II-32**). The intermolecular distances along the bright chains decreased to 0.7 nm and the hexagonal structures were attributed to bromine domains. Consequently, the debromination of **BrTAP** was suspected and a return to the edge-on

configuration of porphyrins probably occurred. The presence of bromines on anthracenes was suspected to play an important role in the interactions on Pd (111) that allowed a flat-lying adsorption of porphyrins after deposition at r.t. In this scenario, we attributed the modification of the intermolecular interactions and the return to the edge-on configuration of porphyrins after annealing to debromination process. Because of the presumed edge-on adsorption, no polymerisation could be induced after the deposition of **BrTAP** on the surface and unfortunately the desired formation of **GNM-1** has not been achieved to date.

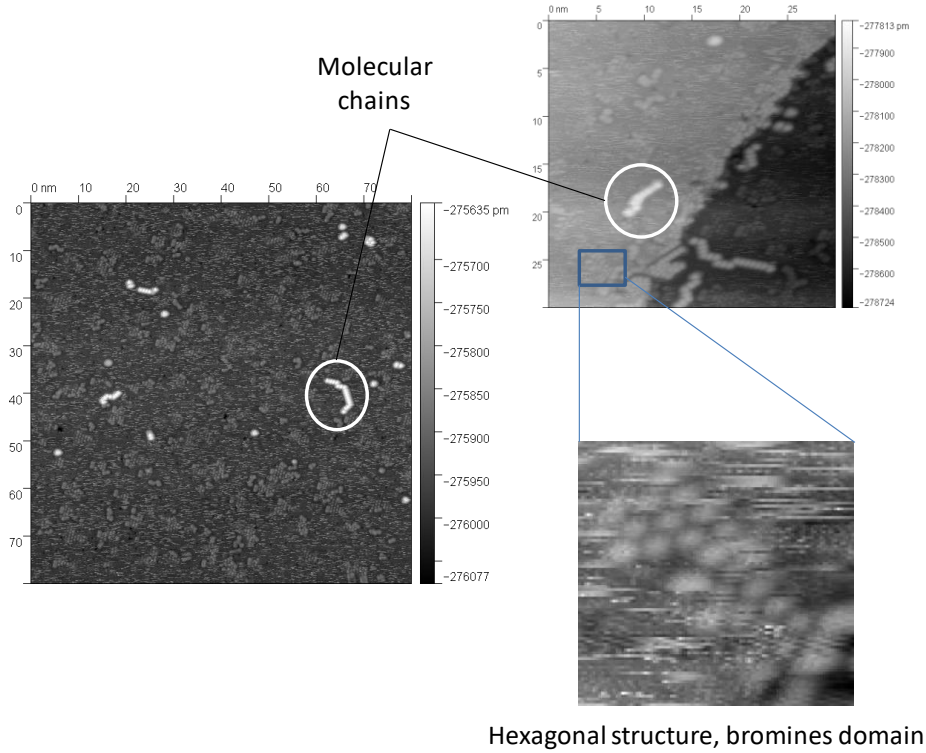

Fig. II-32 STM images of **BrTAP** on Pd (111) after annealing the surface at 300°C with marked molecular chains (white circles) and hexagonal structures assigned to bromines domains (blue square).

II. 3.3. Bis-bromoanthracenylporphyrin on surface

The organization of **BrBAP** on surface was investigated by deposition of the precursors on Cu (110) and Cu (111) at different temperatures. No stable adsorption was observed by deposition of **BrBAP** on Cu (110) at r.t even after annealing the surface at 160°C and 350°C (**Fig. II-33**, a-b). Nevertheless, the deposition of **BrBAP** at 250°C led to the formation of chains with multiple orientations on Cu (110) (**Fig. II-33**, c-d).

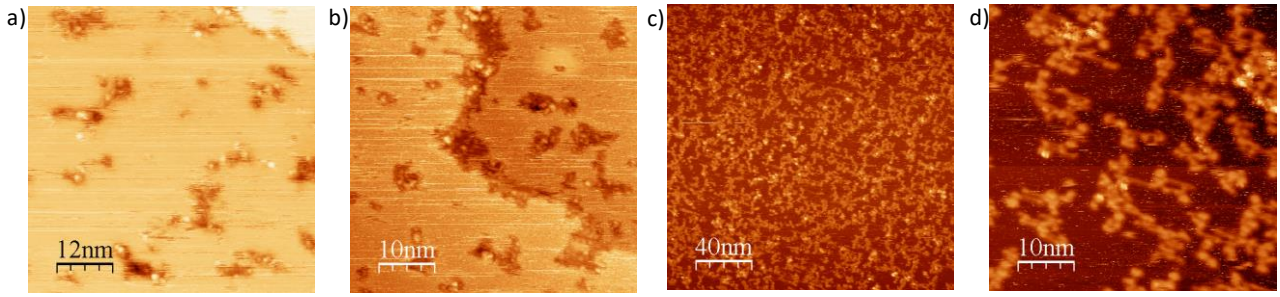

Fig. II-33 STM images of the deposition of **BrBAP** on Cu (110) a) at r.t; b) at r.t followed by annealing at 160°C; c-d) at 250°C.

By superimposition of the theoretical model of the fused **BrBAP** on the STM images, we found that the size of the single spots and of the spots in the assembly were compatible with individual precursors with a flat-lying adsorption (**Fig. II-34**, a). However, the molecular orientations were difficult to identify and we assumed that at the temperature of deposition, both cyclodehydrogenation and dehalogenative coupling occurred that led to the formation of uncontrolled assemblies. Similar results were found on Cu (111); no stable adsorption was observed upon deposition below 400°C and the deposition of **BrBAP** at 400°C led to the formation of assemblies with undefined orientations (**Fig. II-34**, b).

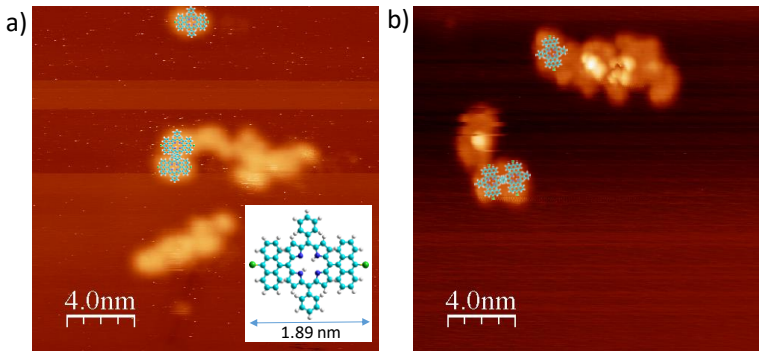

Fig. II-34 STM images with superimposition of the theoretical model of fused **BrBAP**, a) on Cu (110) after deposition at 250°C ; b) on Cu (111) after deposition at 400°C.

We concluded that the reactivity of Cu was too high at the temperature of deposition and did not allow the sequential control of the surface-assisted reactions of **BrBAP** that thus prevented the formation of **GNR-1**. The control of the temperature of deposition seemed to be crucial for the formation of nanostructures and it should be interesting to investigate the deposition of **BrBAP** either at r.t on a more reactive surface like Pd (111) or in temperature on a substrate like Ag (111) with a less catalytic activity.

II. 4. Conclusion and perspectives

To sum-up, several halogenated anthracenylporphyrin-based building blocks with different geometry, nature and number of halogens have been synthetised. The tetra-halogenated compounds **BrTAP**, **ClTAP** and **ITAP** were designed for the target on-surface formation of **GNM-1** whereas the bis-halogenated porphyrin **BrBAP** was designed to afford the structure of **GNR-1**. Although **BrTAP**, **ClTAP** and **BrBAP** were successfully isolated and characterized with common analytical tools, we found that **ITAP** was unstable under ambient conditions and dehalogenation was assumed based on the duplication of signals in the NMR spectra. Consequently, we found that **ITAP** was not suitable for on-surface deposition due to its incompatibility with thermal treatments. Thereafter, we imagined the structure of **BrDTAP** with an additional row of anthracenes along the periphery of the molecule. The objective of this extension was to achieve on a surface the formation of **GNM-2** with a decrease of nitrogen content, larger pores and longer necks compared with the structure of **GNM-1**. The synthesis of **BrDTAP** constituted an important challenge and a screening of the synthetic parameters were done to improve the synthetic protocol. We found that the most promising conditions for the decisive lithiation reaction was to perform the reaction in benzene/Et_2O with a ratio of 9:1 in the presence of *n*-BuLi. Despite the number of synthetic parameters explored, the formation of **BrDTAP** remained very limited and the characterization of **BrDTAP** by NMR is still in progress in the laboratory.

In a second part, the arrangement of **BrTAP** was investigated on a variety of surfaces in terms of nature and orientation to modulate the molecule-substrate interactions. In most cases, a strong intermolecular interaction due to π-stacking between twisted anthracenes was assumed that led to 1D organizations with edge-on configuration of porphyrins on the surface. Only the deposition of **BrTAP** on Pd (111) led to the formation of a 2D organization with flat-lying adsorption. After annealing the surface, debromination occured and the formation of short molecular 1D chains with a return to the edge-on configurations of porphyrins was observed. In order to prevent dehalogenation during annealing the surface and to investigate the cyclodehydrogenation reaction between anthracenes and porphyrins, it would be interesting to study the deposition of **ClTAP** on Pd (111). According to the works of Jacobse *et al.*[29] and Shu *et al.*[30], the cyclodehydrogenation reaction is expected to occur prior to the polymerisation reaction and the formation of a controlled network of porphyrins *via* subsequent dehalogenative polymerisation is not considered due to the possible formation of assemblies with undefined orientations. The strong intermolecular interaction between the anthracenes constitutes a serious limitation that has to be tackled to finally favor the interaction of species with substrates. To significantly affect the intermolecular interaction, our first

idea is to introduce an additional row of anthracenes on porphyrins. According to the calculated structure of **BrDTAP**, the first row of anthracene is twisted and nearly perpendicular to the macrocycle and the second row is parallel to the macrocycle due to the steric hindrance with the first row. Therefore, the two rows of anthracene were almost perpendicular between each other (**Fig. II-35**, a). The groups of Mullen and Fasel exploited such a perpendicular arrangement between the two adjacent anthracenes of **DBBA** to achieve a desired adsorption of the molecular precursor on a surface in 2010.[31] Inspired by this work, we strongly believe that the deposition of **BrDTAP** on a surface would lead to a completely different assembly with an important perturbation of the intermolecular π-stacking. The study of **BrDTAP** on a surface for the fabrication of **GNM-2** constitutes the next step of this work.

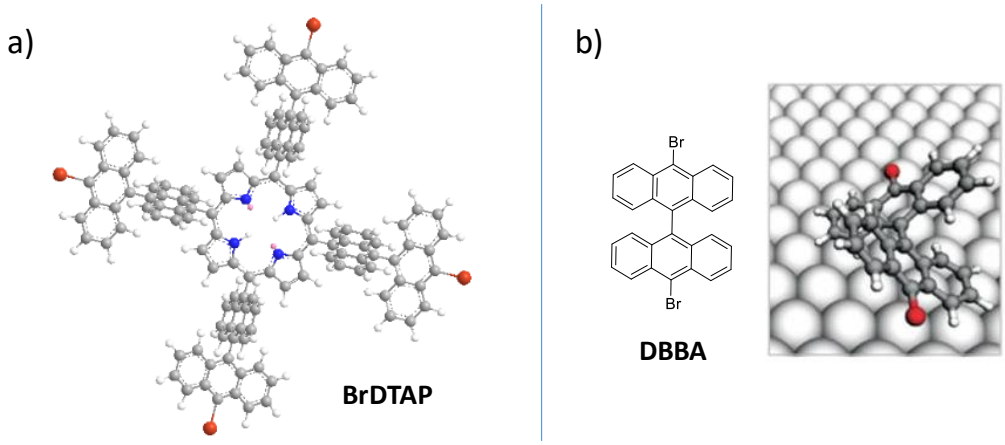

Fig. II-35 a) Calculated 3D model of **BrDTAP**; b) chemical structure and illustration of the perpendicular arrangement the two adjacent anthracenes of **DBBA** on a surface.[31]

Finally, the study of deposition of **BrBAP** on Cu (110) and Cu (111) at r.t did not lead to the stable adsorption of precursors and the deposition at 250°C and 400°C led to the formation of assemblies with undefined orientations. We explained the results by a low molecule-substrate interaction of the surfaces of Cu at r.t and to the strong reactivity at high temperatures that did not allow a sequential control of the surface-assisted reactions, thus preventing the desired formation of **GNR-1**. Consequently, we recommend pursuing the investigation of deposition of **BrBAP** either at r.t on a more reactive surface like Pd (111) to afford a stable adsorption of precursors followed by annealing the surface to sequentially activate the surface-assisted reaction; or in temperature on a substrate like Ag (111) with a less catalytic activity to avoid the multiple activation of surface-assisted reactions at a same temperature.

II. 5. References

(1) Sooambar, C.; Troiani, V.; Bruno, C.; Marcaccio, M.; Paolucci, F.; Listorti, A.; Belbakra, A.; Armaroli, N.; Magistrato, A.; De Zorzi, R.; et al. Synthesis, Photophysical, Electrochemical, and Electrochemiluminescent Properties of 5,15-Bis(9-Anthracenyl)Porphyrin Derivatives. *Org. Biomol. Chem.* **2009**, *7*, 2402–2413.

(2) Davis, N. K. S.; Thompson, A. L.; Anderson, H. L. Bis-Anthracene Fused Porphyrins : Synthesis , Crystal Structure , and Near-IR Absorption. *Org. Lett.* **2010**, *12*, 2124–2127.

(3) Davis, M.; Senge, M. O.; Locos, O. B. Anthracenylporphyrins. *Z. Naturforsch, B* **2010**, *65*, 1472–1484.

(4) Cense, J. M.; Lequan, R. M. Oxygenation d'une Ferroporphyrine Encombree Sur Ses Deux Faces, La Ferromeso-Tetra-Anthracenyl Porphine. *Tetrahedron Lett.* **1979**, *20*, 3725–3728.

(5) Harden, G. J.; Coombs, M. M. Biomimetic Iron Porphyrin-Catalysed Oxidation of Cyclopenta [a] Phenanthrenones. *J. Chem. Soc. Perkin Trans. 1* **1995**, 3037–3042.

(6) Vzorov, A. N.; Dixon, D. W.; Trommel, J. S.; Marzilli, L. G.; Compans, R. W. Inactivation of Human Immunodeficiency Virus Type 1 by Porphyrins. *Antimicrob. Agents Chemother* **2002**, *46*, 3917–3925.

(7) Adler, A. D.; Longo, F. R.; Shergalis, W. Mechanistic Investigations of Porphyrin Syntheses. I. Preliminary Studies on Ms-Tetraphenylporphin. *J. Am. Chem. Soc.* **1964**, *86*, 3145–3149.

(8) Tohara, A.; Sato, M. An Improved Synthesis of Meso -Tetraanthrylporphyrin by a Kinetically Controlled Lindsey Reaction. *J. Porphyr. Phthalocyanines* **2007**, *11*, 513–518.

(9) Kumar, A.; Maji, S.; Dubey, P.; Abhilash, G. J.; Pandey, S.; Sarkar, S. One-Pot General Synthesis of Metalloporphyrins. *Tetrahedron Lett.* **2007**, *48*, 7287–7290.

(10) Lindsey, J. S.; Wagner, R. W. Investigation of the Synthesis of Ortho-Substituted Tetraphenylporphyrins. *J. Org. Chem.* **1989**, *54*, 828–836.

(11) Volz, H.; Schaeffer, H. Mesosubstituted Porphyrins. III. 5,10,15,20-Tetraanthracenylporphyrin. *Chemiker-Zeitung* **1985**, *109*, 308–309.

(12) Filatov, M. A.; Heinrich, E.; Busko, D.; Ilieva, I. Z.; Landfester, K.; Baluschev, S. Reversible Oxygen Addition on a Triplet Sensitizer Molecule: Protection from Excited State Depopulation. *Phys. Chem. Chem. Phys.* **2015**, *17*, 6501–6510.

(13) Davis, N. K. S.; Thompson, A. L.; Anderson, H. L. A Porphyrin Fused to Four Anthracenes. *J. Am. Chem. Soc.* **2011**, *133*, 30–31.

(14) Pijeat, J.; Dappe, Y. J.; Thuéry, P.; Campidelli, S. Synthesis and Suzuki–Miyaura Cross Coupling Reactions for Post-Synthetic Modification of a Tetrabromo-Anthracenyl Porphyrin. *Org. Biomol. Chem.* **2018**, *16*, 8106–8114.

(15) Plater, M. J.; Aiken, S.; Bourhill, G. A New Synthetic Route to Donor- Acceptor Porphyrins. *Tetrahedron* **2002**, *58*, 2405–2413.

(16) Groom, C. R.; Bruno, I. J.; Lightfoot, M. P.; Ward, S. C. The Cambridge Structural Database. *Acta Crystallogr. Sect. B Struct. Sci. Cryst. Eng. Mater.* **2016**, *72*, 171–179.

(17) Duerr, B. F.; Chung, Y. S.; Czarnik, A. W. Syntheses of 9,10-Disubstituted Anthracenes Derived from 9,10-Dilithioanthracene. *J. Org. Chem.* **1988**, *53*, 2120–2122.

(18) Stern, D.; Finkelmeier, N.; Meindl, K.; Henn, J.; Stalke, D. Consecutive Donor-Base Exchange in Anthracenyllithium Compounds. *Angew. Chem. Int. Ed.* **2010**, *49*, 6869–6872.

(19) Bailey, W. F.; Luderer, M. R.; Uccello, D. P.; Bartelson, A. L. Effect of Solvent and Temperature on the Lithium−Bromine Exchange of Vinyl Bromides: Reactions of n -Butyllithium and t -Butyllithium with (E)-5-Bromo-5-Decene. *J. Org. Chem.* **2010**, *75*, 2661–2666.

(20) Suzuki, M.; Osuka, A. Improved Synthesis of Meso -Aryl-Substituted [26]Hexaphyrins. *Org. Lett.* **2003**, *5*, 3943–3946.

(21) Littler, B. J.; Ciringh, Y.; Lindsey, J. S. Investigation of Conditions Giving Minimal Scrambling in the Synthesis of Trans -Porphyrins from Dipyrromethanes and Aldehydes. *J. Org. Chem.* **1999**, *64*, 2864–2872.

(22) Tautz, F. S. Structure and Bonding of Large Aromatic Molecules on Noble Metal Surfaces: The Example of PTCDA. *Prog. Surf. Sci.* **2007**, *82*, 479–520.

(23) Hammer, B.; Norskov, J. K. Why Gold Is the Noblest of All the Metals. *Nature* **1995**, *376*, 238–240.

(24) Gao, H.-Y.; Franke, J.-H.; Wagner, H.; Zhong, D.; Held, P.-A.; Studer, A.; Fuchs, H. Effect of Metal Surfaces in On-Surface Glaser Coupling. *J. Phys. Chem. C* **2013**, *117*, 18595–18602.

(25) Dong, L.; Liu, P. N.; Lin, N. Surface-Activated Coupling Reactions Confined on a Surface. *Acc. Chem. Res.* **2015**, *48*, 2765–2774.

(26) Zhou, Y.; Wang, B.; Zhu, M.; Hou, J. G. Observation of Co-Existence of 'Face-on' and 'Edge-on' Stacking Styles in a Porphyrin Monolayer. *Chem. Phys. Lett.* **2005**, *403*, 140–145.

(27) Trelka, M.; Urban, C.; Rogero, C.; de Mendoza, P.; Mateo-Marti, E.; Wang, Y.; Silanes, I.; Écija, D.; Alcamí, M.; Yndurain, F.; et al. Surface Assembly of Porphyrin Nanorods with One-Dimensional Zinc–Oxygen Spinal Cords. *CrystEngComm* **2011**, *13*, 5591.

(28) Sakano, T.; Hasegawa, J.; Higashiguchi, K.; Matsuda, K. Chronological Change from Face-On to Edge-On Ordering of Zinc-Tetraphenylporphyrin at the Phenyloctane-Highly Oriented Pyrolytic Graphite Interface. *Chem. Asian. J.* **2012**, *7*, 394–399.

(29) Jacobse, P. H.; van den Hoogenband, A.; Moret, M. E.; Klein Gebbink, R. J. M.; Swart, I. Aryl Radical Geometry Determines Nanographene Formation on Au(111). *Angew. Chem. Int. Ed.* **2016**, *55*, 13052–13055.

(30) Shu, C.-H.; Xie, Y.-L.; Wang, A.; Shi, K.-J.; Zhang, W.-F.; Li, D.-Y.; Liu, P.-N. On-Surface Reactions of Aryl Chloride and Porphyrin Macrocycles via Merging Two Reactive Sites into a Single Precursor. *Chem. Commun.* **2018**, *54*, 12626–12629.

(31) Cai, J.; Ruffieux, P.; Jaafar, R.; Bieri, M.; Braun, T.; Blankenburg, S.; Muoth, M.; Seitsonen, A. P.; Saleh, M.; Feng, X.; et al. Atomically Precise Bottom-up Fabrication of Graphene Nanoribbons. *Nature* **2010**, *466*, 470–473.

Chapter III. Pyrolysis of *meso*-substituted porphyrins

Chapter III. Pyrolysis of meso-substituted porphyrins

This chapter is dedicated to the study of formation of π-extended porphyrins *via* the method of pyrolysis to perform the reaction of fusion of *meso*-substituted porphyrins with PAHs.

The first part of this chapter consists in a concise review of the literature on the formation of π-extended porphyrins and the characterization of their optical properties.

In a second part is presented the synthesis of precursors of π-extended porphyrins based on *meso*-substituted PAH-porphyrins. For this study, we synthetised mono-, bis- and tetra-substituted porphyrins containing pyrene, napthalene or anthracene moieties.

In the last part, the experimental setup of the pyrolysis will be presented and the results of thermal fusion of precursors will be discussed.

III. 1. Fusion of PAHs on porphyrins in the literature

The fusion of PAHs located on the *meso*-positions of porphyrins is a popular strategy to afford π-extended porphyrins. Red-shifts of the optical absorption and emission properties of porphyrins are observed after the fusion of PAHs on the β-pyrrole position of porphyrins. The extension of the π-system depends on the choice of the PAH and its aromaticity and allow the modulation of the visible/IR or NIR properties of the π-extended porphyrin. The following examples from the literature illustrate this point.

The fusion of phenyls on porphyrins has been reported in the literature since 2004 and was performed in solution *via* cycloaddition or coupling reactions.[1–3] The group of Kojima reported the fusion of multiple phenyls on a porphyrin *via* direct CH activation with Pd catalyst and although a mixture of isomers was formed, singly-, doubly-, triply- and quadruply ring-fused phenylporphyrins were successfully isolated and their adsorption spectra were reported (**Fig. III-1**).[4,5] The singly-, doubly-, triply- and quadruply ring-fused phenyl porphyrins exhibited maximal absorption bands at λ_{max} = 471 nm; 532 nm; 580 nm; and 592 nm respectively.

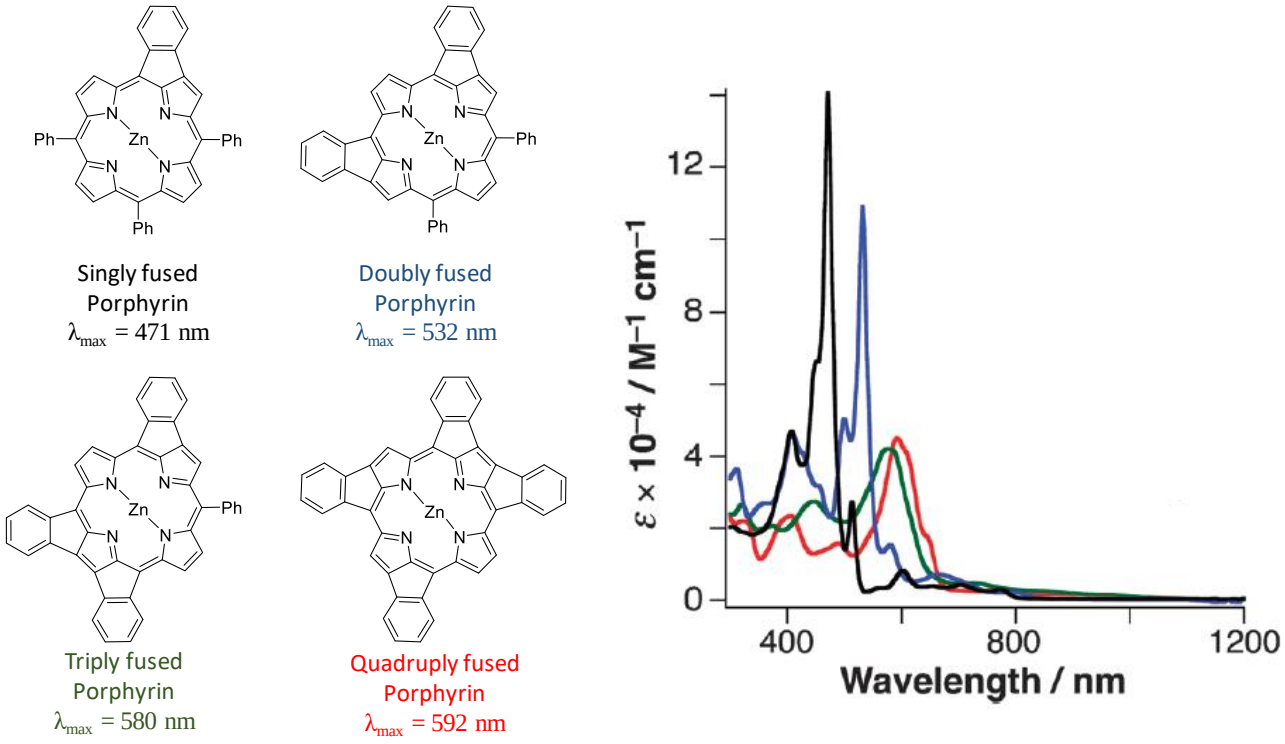

Fig. III-1 Chemical structures and absorption spectra of singly-(black), doubly-(blue), triply-(green) and quadruply-(red) ring fused phenylporphyrins.[4]

The fusion of PAHs on porphyrins is generally achieved by the oxidative cyclodehydrogenation with oxidants like $FeCl_3$, $Fe(ClO_4)_3$, DDQ/$Sc(OTf)_3$. In 2004, Yamane *et al.*[6] reported the fusion of pyrene derivatives on porphyrins *via* oxidative cyclodehydrogenation and mentionned that the fusion of large

PAHs occurred only when the porphyrins were metallated with nickel and when the PAHs contained activating groups like ether or ester. Although no spectrum was presented, the authors indicated that the absorption signature of the product of fusion from monopyrenylporphyrin was composed of optical bands at 724, 519, 430 and 420 nm.

Several examples of fusion of naphthalene bearing ether or ester groups on porphyrin cores were reported *via* chemical oxidations since 2007.[7–9] In particular, the group of Gryko investigated the fusion of 4,7-dimethoxynaphthylporphyrin depending on the inserted metal and found that although the presence of Cu and Ni in the porphyrin enhanced the yield of the reaction (83% and 60% yields respectively), the fusion of naphthalene with the free base porphyrin was possible.[9] In comparison to the optical signature of the starting Ni-porphyrin, the spectrum of the fused porphyrin exhibited two new absorption bands at 585 and 648 nm (**Fig. III-2**, a). According to the studies of Cammidge *et al.*,[10] Tanaka *et al.*,[7] and Hayashi *et al.*,[8] the presence of an additional "pseudo Soret band" was observed in the absorption signature of the naphthalene-fused porphyrin with Zn (**Fig. III-2**, b). Because no additional band was observed in the absorption spectra of the fused porphyrins containing Ni, Cu or with the free base product,[9] we wonder if the origin of this band could be due to the presence of Zn in the structure. It is worth mentioning that the fusion of naphthalene derivatives was also achieved by electrochemistry[11,12] or by Heck-type coupling reaction.[10]

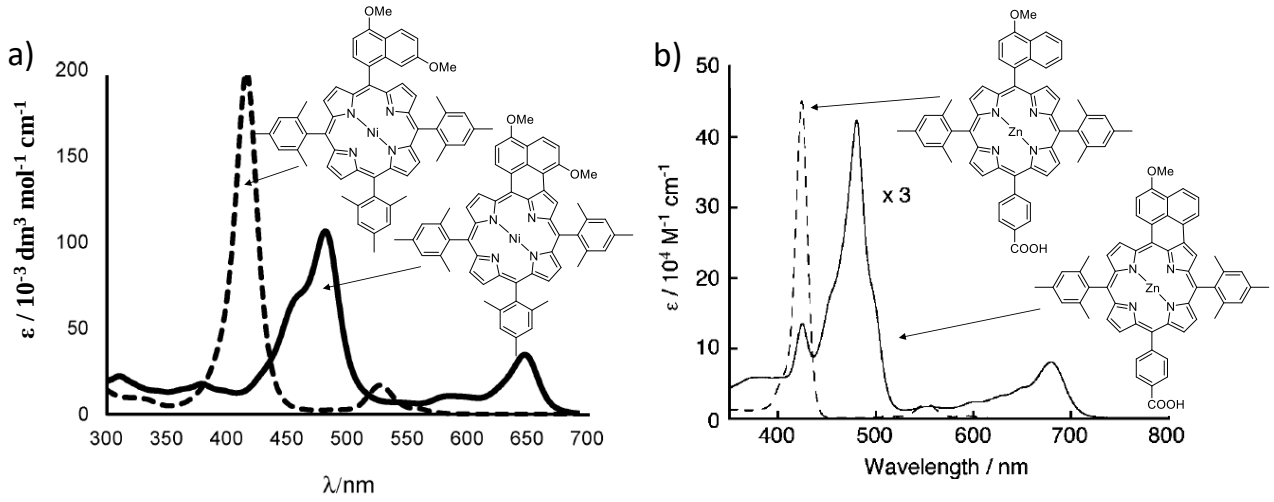

Fig. III-2 Chemical structures and absorption spectra of a) [4,7-dimethoxynaphtylporphyrinato]Ni(II) (grey) and its corresponding product of fusion (black);[9] b) [methyl 4-(10,15,20-tris(3,5-dimethylphenyl)porphyrinato-5-yl)-1-naphthoate]Zn(II) (dash line) and its corresponding product of fusion (solid line).[7,8]

The fusion of anthracene derivatives on porphyrins was studied by the group of Anderson and the fusion of mono-,[13,14] bis-,[15] and tetra-anthracenylporphyrins[16] achieved by chemical oxidation with $FeCl_3$ or DDQ/$Sc(OTf)_3$ were reported. Importantly, the authors mentioned that the fusion of multiple anthracenes occurred sequentially and successive oxidation reactions were required to afford the

desired products of fusion. The absorption spectra of the fused monoanthracenylporphyrin, bisanthracenylporphyrin and tetra-anthracenylporphyrin exhibited particular absorption bands at λ= 773 and 855 nm (**Fig. III-3**, a); λ= 973 nm (**Fig. III-3**, b); and λ= 1417 nm (see chapter I, **Fig I-13**) respectively that illustrated that the larger the π-system, the greater the red-shift.

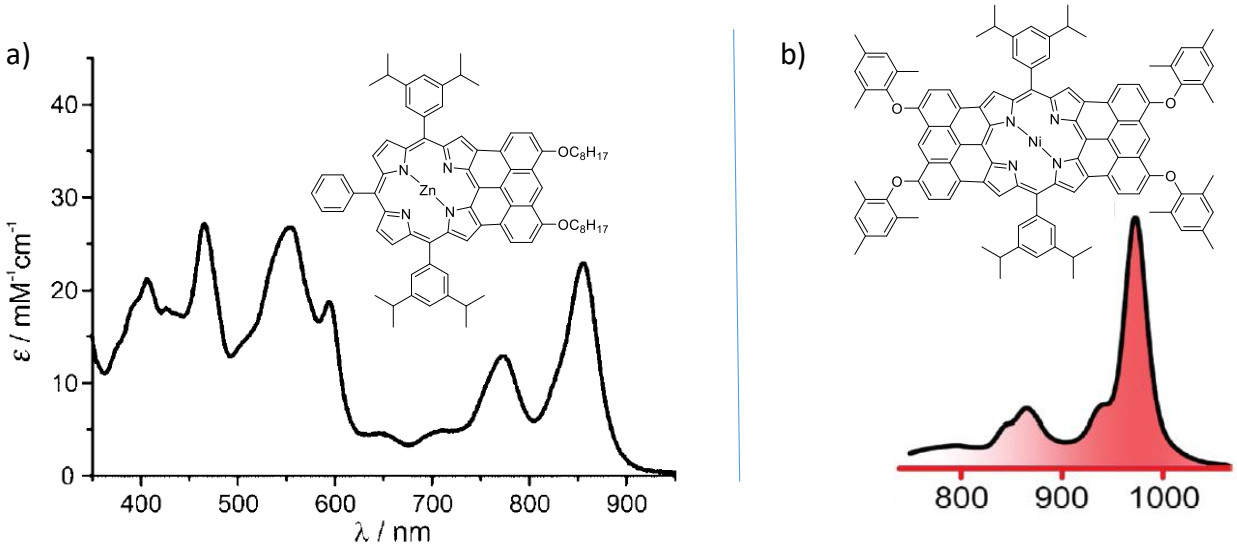

Fig. III-3 Chemical structures and absorption spectra of a) the fused monoanthracenylporphyrin; b) the fused bisanthracenylporphyrin.[13,15]

Other π-extended systems containing azulene,[17] perylene,[18] corannulene[19] and nanographene[20] derivatives have been described in the literature and exhibited absorption bands between 700-1150 nm. These examples illustrated the effect of the extension of the π-system on the absorption properties and a greater red-shift was generally observed by the multiple fusion of PAHs on the porphyrin core. The method of pyrolysis proposed by Thompson *et al.*[21,22] could represent an alternative strategy to form π-extended porphyrins *via* the thermal fusion of PAHs located on the *meso*-positions of porphyrins. This method neither requires the presence of Ni in the porphyrin nor the presence of donor groups on PAHs that respectively causes fast deactivation of the porphyrin excited states and drastically limits the choice of PAHs. The pyrolysis method consists in heating the porphyrin precursor at high temperatures, about 500-600°C, for a short period of typically 3-10 min under an argon flow. The efficiency of the method was demonstrated on several bis-substituted porphyrins with a variety of PAHs from naphthalene, pyrene, coronene derivatives and an example of fusion of tetra-substituted pyrenylporphyrin was reported (**Fig. III-4**).[21] However, mixtures of syn/anti isomers were afforded due to the use of asymmetric PAHs and the fusion of symmetric PAHs like anthracene on a porphyrin has not been reported so far.

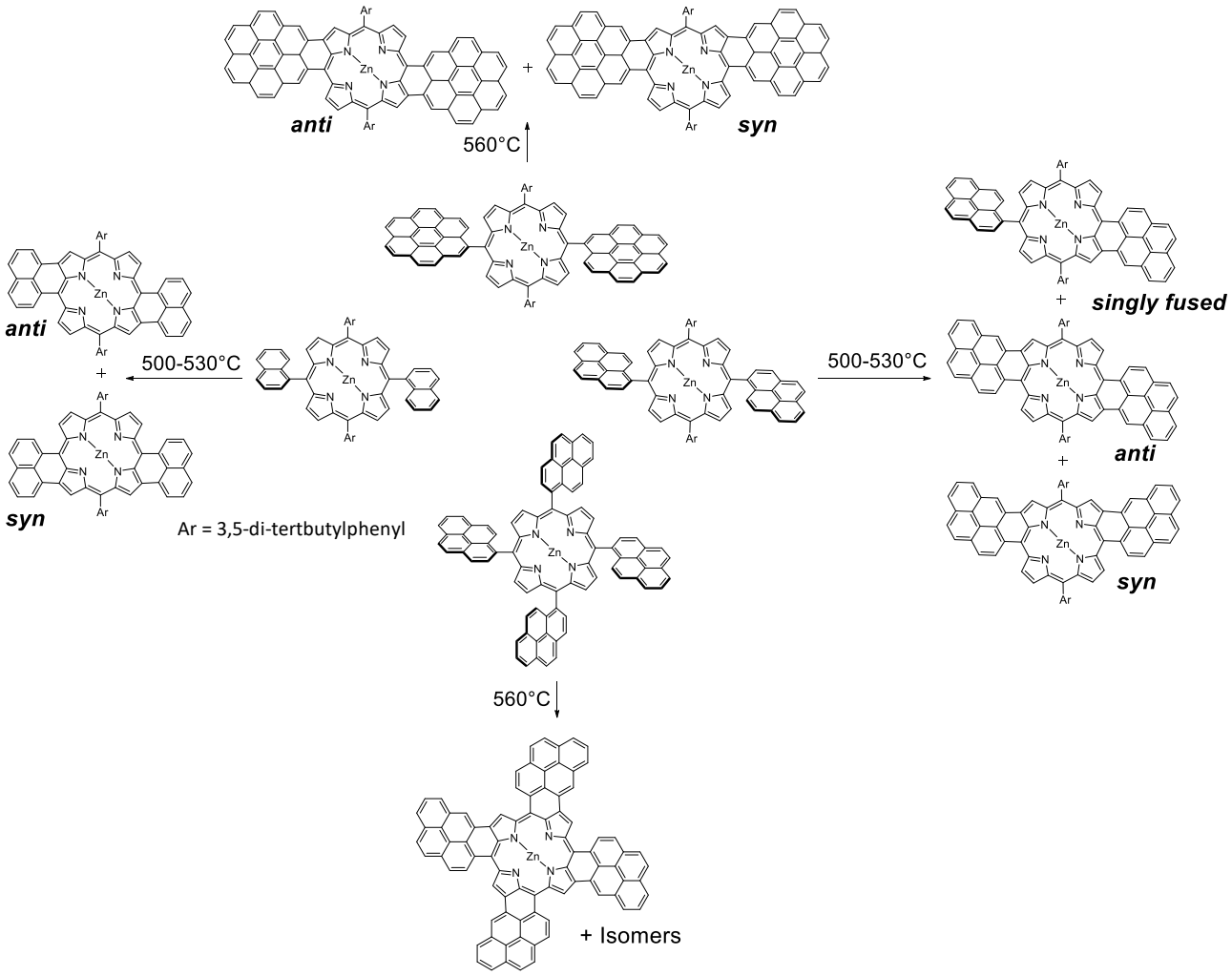

Fig. III-4 Examples of formation of π-extended porphyrins by the thermal fusion with variety of PAH-porphyrin derivatives.[21]

During this Ph. D., our objective was to investigate the thermal fusion of tetra-anthracenylporphyrin without the presence of activating groups *via* the pyrolysis technique. In addition, we proposed to investigate the thermal fusion of bis-anthracenylporphyrin and mono-substituted porphyrins containing anthracene, naphthalene and pyrene derivatives. In order to test our setup of pyrolysis, we also decided to reproduce the formation of the fused tetrapyrenylporphyrin reported in the work of Thompson. The next section is dedicated to the synthesis of the porphyrin precursors.

III. 2. Synthesis of porphyrin precursors

III. 2.1. Tetra-pyrenylporphyrin

5,10,15,20-tetra(pyren-1-yl)porphyrin (**TPyP)** was synthetised by the method of Adler and Longo.[23] After the condensation reaction of pyrrole and pyrene-1-carboxaldehyde in propionic acid, the resulting mixture was filtered on paper, washed with a large amount of MeOH and purified by chromatography techniques. Recrystallisation from DCM/MeOH afforded **TPyP** as violet crystals in 12% yield. Zn insertion was achieved by modification of literature procedure with $Zn(OAc)_2$ and yielded **ZnTPyP** 76% after recrystallisation from DCM/MeOH (**Fig. III-5**).[24]

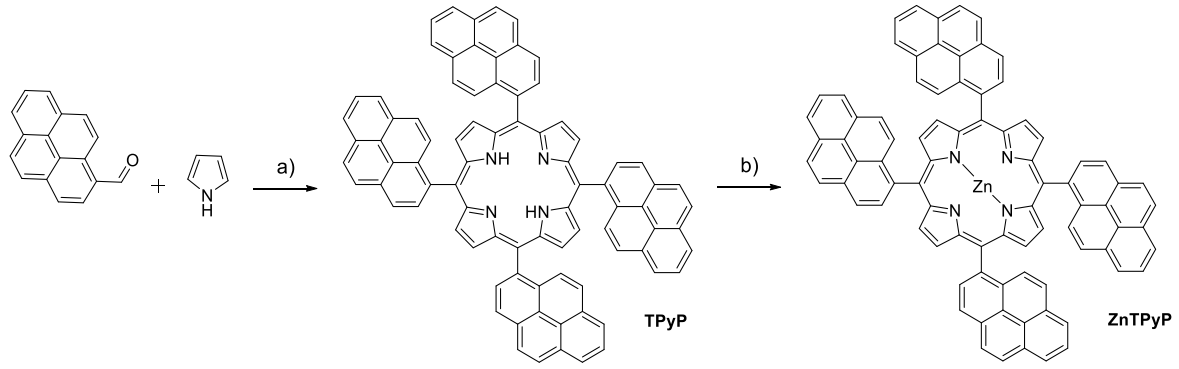

Fig. III-5 Synthetic route of **ZnTPyP**; a) propionic acid, 1h, 140°C, 12%; b) $Zn(OAc)_2.2H_2O$ (3eq), DCM, at reflux, 1h, 76%.

TPyP and **ZnTPyP** were characterized by ^{1}H NMR, MS, UV-Vis spectroscopy and the analytical data agreed with the ones reported in the literature (see Experimental part).[21]

III. 2.2. Tetra-anthracenylporphyrin

a) Synthesis

The synthesis of **TAP** was achieved following the strategy of Volz and Schaeffer from 9-bromoanthracene (**Fig. III-6**).[25] The lithiation step was performed in Et_2O with *n*-BuLi (2 mol/L, 2.04 eq) at r.t and although the mixture turned slightly orange upon addition of the lithium reagent, an important amount of insoluble material remained. After purification by chromatography techniques and precipitation from DCM/MeOH, **TAP** was isolated in 4% yield with respect to pyrrole-2-carboxaldehyde. In comparison to the yield afforded in the synthesis of **BrTAP**, we assume that the yield of synthesis of **TAP** was limited by the formation of the organolithium compound **2** and the partial solubility of 9-bromoanthracene in the solvent of reaction. Zinc insertion was achieved by modification of literature procedure with $Zn(acac)_2$ and afforded **ZnTAP** in 81% yield after purification.[24]

TAP and **ZnTAP** were successfully characterized by ^{1}H NMR, MS, UV-Vis spectroscopy and the analytical characterizations of **TAP** agreed with data from the literature (see Experimental part).[25]

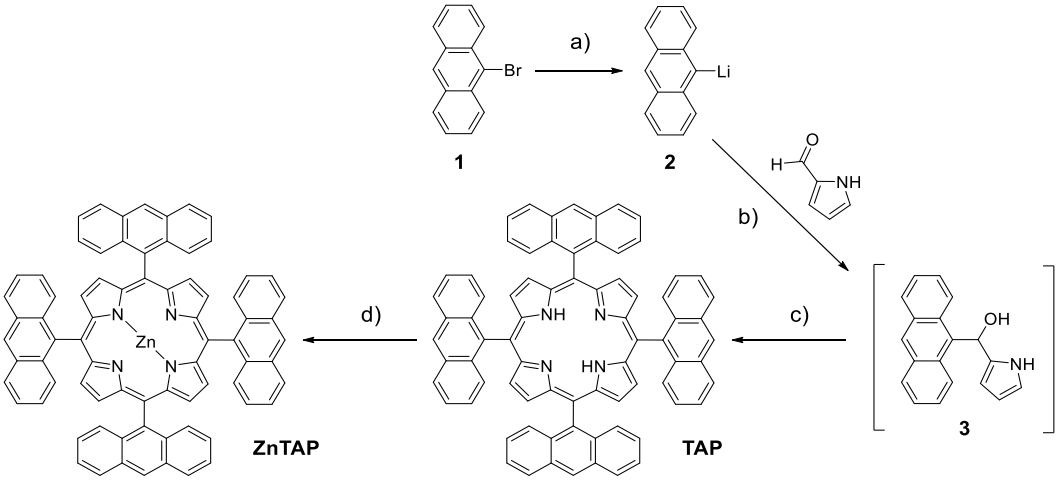

Fig. III-6 Synthetic route of **TAP**; a) *n*-BuLi (2 mol/L in hexane, 2.04 eq), diethylether, 30 min, r.t.; b) 1h, r.t (**3** was not isolated); c) propionic acid, 3h, 140°C, 4%; d) $Zn(acac)_2$ (3 eq) in DCM, 2h, at reflux, 81%

b) Characterizations

The ^{1}H NMR spectrum of **ZnTAP** was recorded in $C_2D_2Cl_4$ at 400MHz and the aromatic region of the spectrum is shown in **Fig. III-7.** The signal at δ 8.17 ppm was attributed to the eight hydrogens at β-pyrrolic positions and the other signals at δ (ppm): 8.87 (s, 4H, 10-anthracenyls), 8.28-8.23 (m, 8H, 4,5-anthracenyls), 7.48-7.41 (m, 8H, 3,6-anthracenyls), 7.26-7.20 (m, 8H, 1,8-anthracenyls), 7.02-7.02 (m, 8H, 2,7-anthracenyls) were attributed to the hydrogens of the anthracene moieties from the literature.[25]

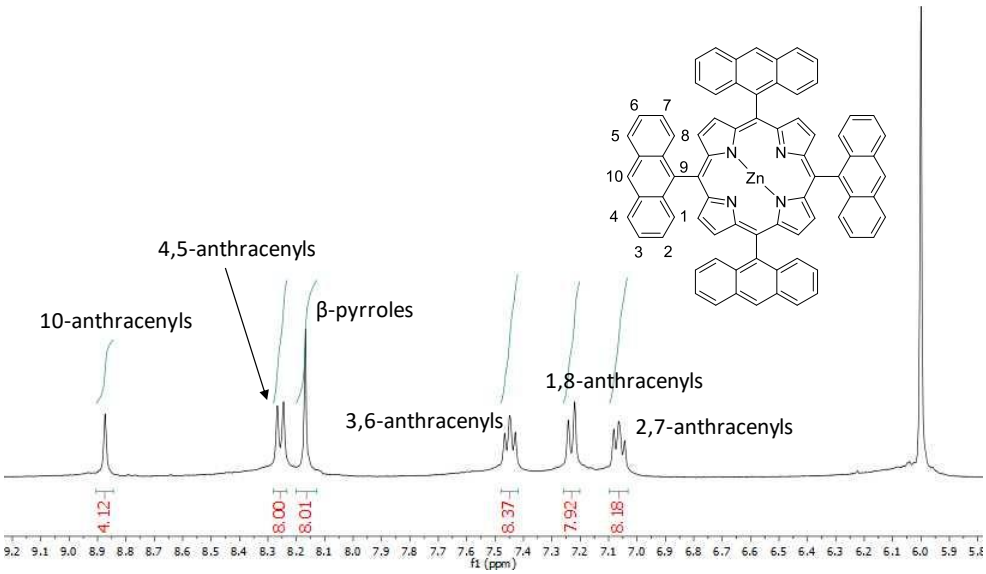

Fig. III-7 Aromatic region of the ^{1}H NMR spectrum of **ZnTAP** (400MHz, $C_2D_2Cl_4$, 298K).

The absorption spectrum of **ZnTAP** showed a Soret band at 429 nm followed by two Q-bands at 516 and 552 nm and the additional bands at 248, 352 nm were attributed to the absorption of the anthracene units (**Fig. III-8**).

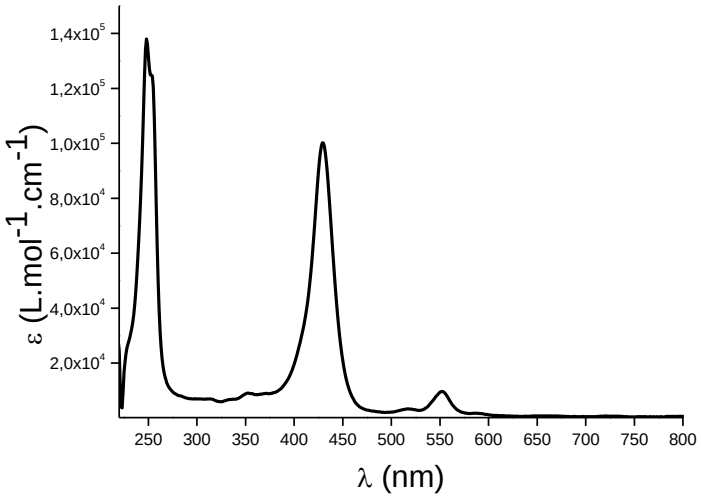

Fig. III-8 Absorption spectrum of **ZnTAP** in DCM.

III. 2.3. Bis-anthracenylporphyrin

a) **Synthesis**

Two synthetic strategies can be considered to form the 5,15-di(anthracen-9-yl)-10,20-diphenylporphyrin (**BAP**): the 2+2 method of MacDonald or the Suzuki-Miyaura cross-coupling reaction. Based on the previous synthesis of **BrBAP**, a yield of about 5% was expected for the 2+2 method and because higher yields were reported in the literature for Suzuki-Miyaura coupling, we opted for the coupling strategy to prepare **BAP**. The synthetic route of **BAP** is shown in **Fig. III-9**.

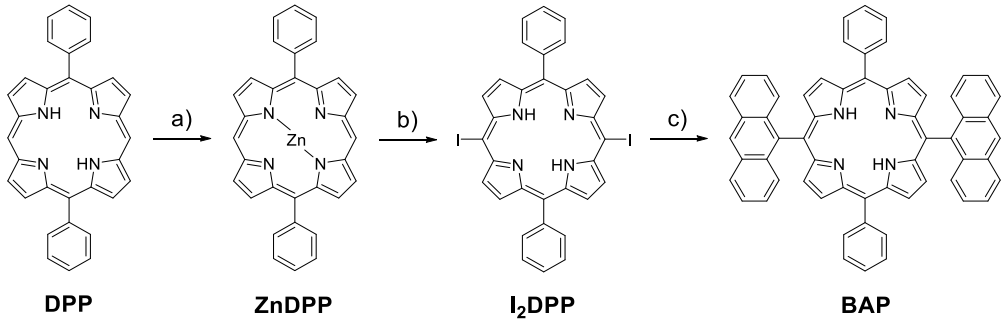

Fig. III-9 Synthetic route of **ZnBAP**; a) $Zn(OAc)_2.2H_2O$ (3 eq), DCM, at reflux for 1h, 96%; b) I_2 (4 eq) in $CHCl_3$/pyridine (9:1), $AgPF_6$ (2.1 eq) in acetonitrile, 15 min, r.t, 60%; c) Pd_2dba_3 (0.5 eq), SPhos (1 eq), K_3PO_4 (8 eq), anthracen-9-boronic acid (4 eq) in toluene, 85°C, 48h, 22%.

Zinc was inserted by modification of literature procedure[24] into 5,15-diphenylporphyrin (**DPP**) to prevent the insertion of Ag in the next step and yielded 96% of **ZnDPP** (**Fig. III-9**, a). Iodination of **ZnDPP** was achieved by treatment with I_2 in the presence of $AgPF_6$ following literature procedure[26,27] and led to the bis-iodinated porphyrin with a small amount of mono-iodinated species. After

demetallation with HCl (6 mol/L), the crude mixture was purified by silica chromatography eluted with $CHCl_3$/cyclohexane (1:2) and with 1% of Et_3N to neutralize silica. After evaporation of solvents, **I_2DPP** was isolated in 60% yield (**Fig. III-9**, b). **BAP** was synthetised *via* Suzuki-Miyaura cross-coupling reaction from **I_2DPP** and anthracen-9-boronic acid (6 eq) and different conditions were tested. With $Pd(OAc)_2$, SPhos and K_3PO_4 in toluene at 80°C for 72h, a complex mixture containing dehalogenated, coupling species and the starting material was afforded and was difficult to separate. With $PdCl_2(PPh_3)_2$, $AsPh_3$ and Cs_2CO_3 in THF at 67°C for 72h, starting **I_2DPP** with traces of dehalogenated species were detected by TLC and MS analysis that indicated a lack of reactivity at such temperature. Under the same conditions at higher temperature (75°C), the formation of the complex mixture of products was observed. Finally, we found that the most efficient conditions were in toluene at 85°C for 24h with Pd_2dba_3 and SPhos in the presence of K_3PO_4. The reaction led to the major production of **BAP** (**Fig. III-9**, c). The separation of the mono-and bis-anthracenyl porphyrins required two silica columns with toluene/heptane (1:1), CH_2Cl_2/cyclohexane (1:1) and a Size exclusion Chromatography using THF (SEC). After evaporation of solvents, a violet powder corresponding to target **BAP** was afforded in 22% yield. Finally, zinc insertion was achieved by modification of literature procedure[24] and afforded **ZnBAP** in 90% yield after purification (**Fig. III-10**).

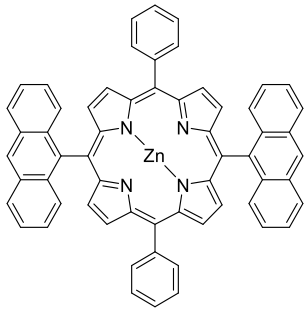

ZnBAP

Fig. III-10 Chemical structure of **ZnBAP**.

ZnDPP, **I_2DPP**, **BAP** and **ZnBAP** were characterized by ^{1}H NMR, MS and UV-Vis spectroscopy and the analytical data agreed with the ones reported in the literature (see Experimental part).[27,28]

b) **Characterization**

The ^{1}H NMR spectrum of **BAP** was recorded in $C_2D_2Cl_4$ at 400MHz and the aromatic region of the spectrum is shown in **Fig. III-11.** Two signals of hydrogens at β-pyrrolic positions were observed at 8.71 ppm (β1) and 8.34 ppm (β2) due to the asymmetry of the A_2B_2 porphyrin. The multiplet signals between 8.22-8.17 and 7.72-7.67 were respectively attributed to the four hydrogens in *ortho*-positions of the phenyls and to the six hydrogens in *meta*- and *para*-positions of the phenyls. The other signals at δ (ppm): 8.98 (s, 2H, 10-anthracenyls), 8.32-8.28 (m, 4H, 4,5-anthracenyls), 7.54-7.48 (m, 4H, 3,6-anthracenyls), 7.19-7.14 (m, 4H, 1,8-anthracenyls), 7.10-7.05 (m, 4H, 2,7-anthracenyls) were attributed to the hydrogens of the anthracene moieties in comparison to the spectral signatures of porphyrins developed in this thesis and from the literature.[25,28]

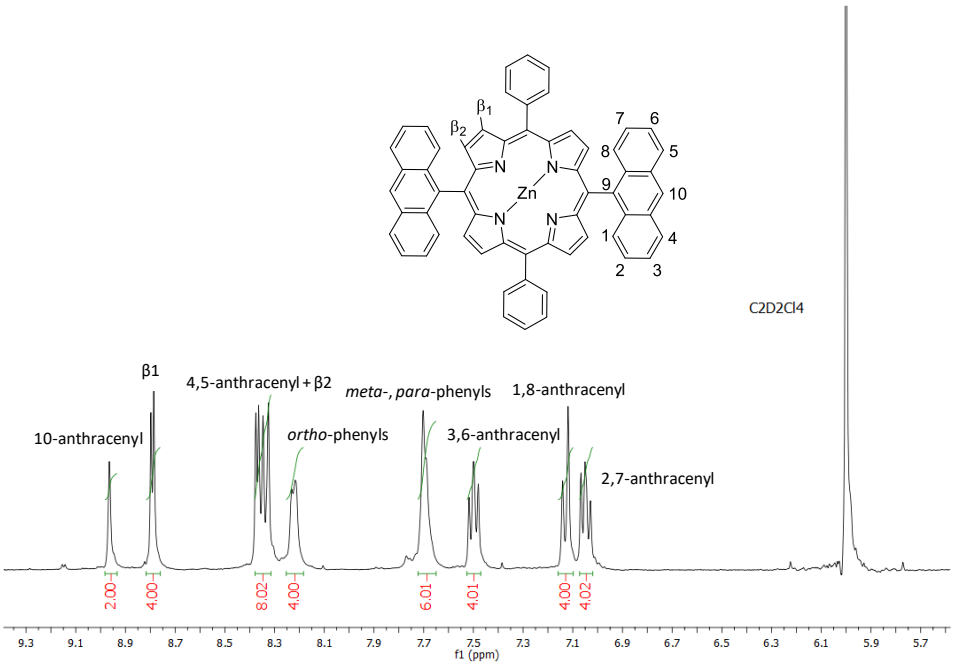

Fig. III-11 ^{1}H NMR spectrum of **BAP** (400MHz, $C_2D_2Cl_4$, 298K).

III. 2.4. Mononaphthyl-, pyrenyl- and anthracenylporphyrins

a) **Synthesis**

5-(naphthalen-1-yl)-10,15,20-triphenylporphyrin (**SNP**), 5-(pyren-1-yl)-10,15,20-triphenylporphyrin (**SPP**) and 5-(anthracen-9-yl)-10,15,20-triphenylporphyrin (**SAP**) were synthesised *via* Suzuki-Miyaura cross coupling reactions from 5-bromo-10,15,20-triphenylporphyrin with the corresponding PAH-boronic acid (**Fig. III-12**). We applied the same coupling conditions as in the synthesis of **BAP** with Pd_2dba_3, SPhos and K_3PO_4 in toluene at 85°C for 48h. After purification by chromatography techniques and recrystallisation from DCM/MeOH, **SNP**, **SPP** and **SAP** were isolated in 98%, 96% and 51% yields respectively.

The reaction of zinc insertion was achieved by modification of literature procedure and afforded **ZnSNP, ZnSPP** and **ZnSAP** in 93%, 87% and 87% yields respectively after purification.[24] **SNP, SPP, SAP, ZnSNP, ZnSPP and ZnSAP** were successfully characterized by ^{1}H and ^{13}C NMRs, HRMS and UV-Vis spectroscopy (see Experimental part).

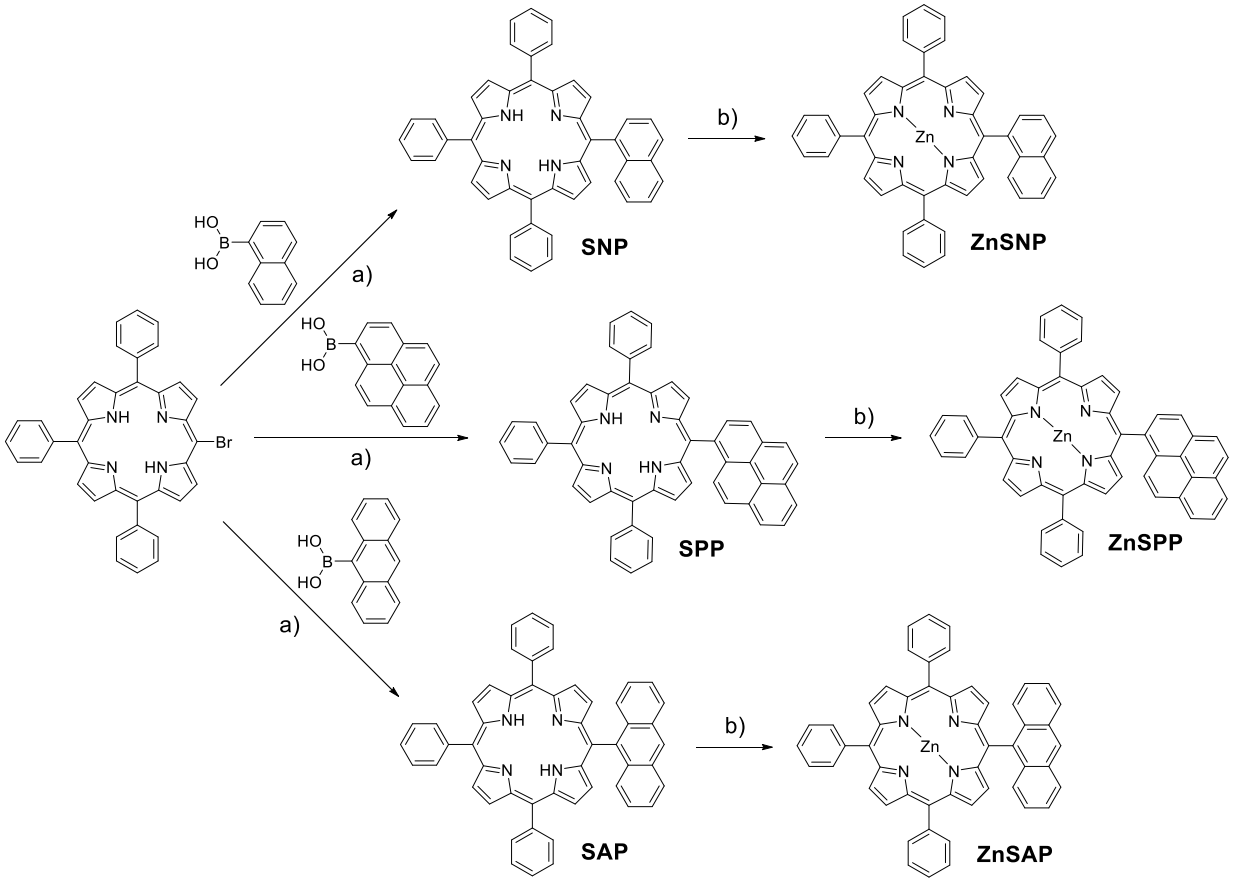

Fig. III-12 Synthetic routes of **ZnSNP**, **ZnSPP** and **ZnSAP**; a) Pd_2dba_3 (0.5 eq), SPhos (1 eq), K_3PO_4 (6 eq) in toluene, 48h, 85°C, 98% (**SNP**), 96% (**SPP**), 52% (**SAP**); b) $Zn(acac)_2$ (3 eq) in DCM, 2h, at reflux, 93% (**ZnSNP**), 87% (**ZnSPP**) and 87% (**ZnSAP**).

b) **Characterizations**

The 2D-cosy NMR map of **ZnSNP** recorded in $C_2D_2Cl_4$ at 400MHz is shown in **Fig. III-13**. Due to the asymmetry of the A_3B porphyrin, three signals of hydrogens at β-pyrrolic positions were observed at 9.01 ppm (β1, s), 8.89 ppm (β2, d, J = 4.64 Hz) and 8.71 (β3, d, J = 4.64 Hz). The multiplets between 8.38-8.22 and 7.84-7.73 were respectively attributed to the six hydrogens in *ortho*-positions of the phenyls superimposed with the two hydrogens in positions 2-, 4- of the naphthalene moiety and to the nine hydrogens in *meta*- and *para*-positions of the phenyls. The other signals at δ (ppm) 8.20-8.15 (m, 1H, 8-naphthyl), 7.96-7.88 (m, 1H, 3-naphthyl), 7.56-7.46 (m, 1H, 7-naphthyl), 7.14-7.06 (m, 2H, 5- and 6-naphthyl) were attributed to the hydrogens of the naphthalene moiety in comparison to the literature.[7–10]

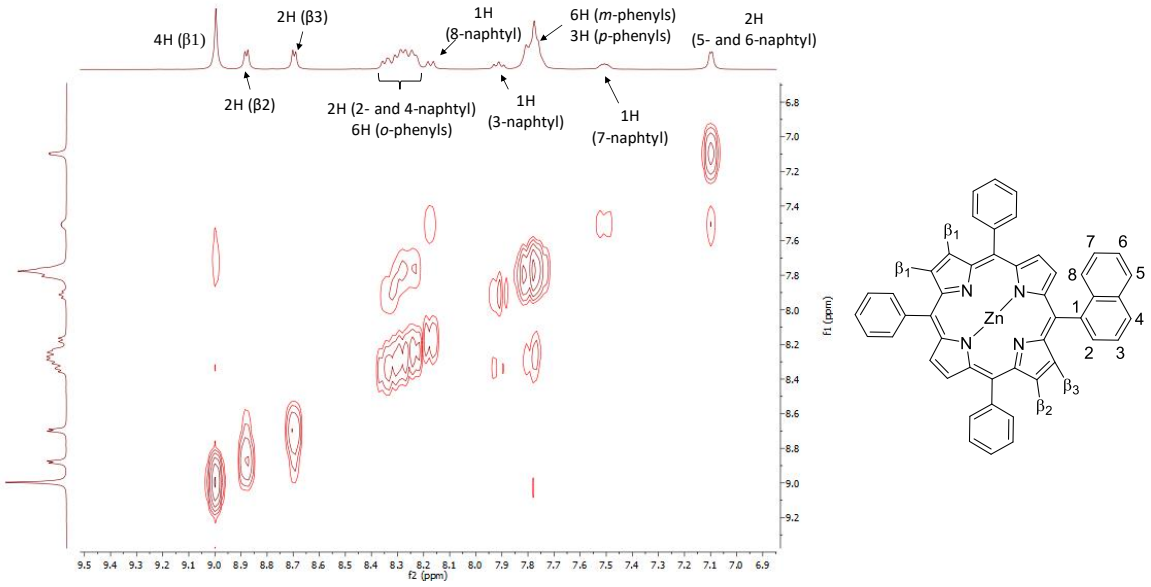

Fig. III-13 2D-cosy map and chemical structure of **ZnSNP** (400MHz, $C_2D_2Cl_4$, 298K).

The 2D-cosy NMR map of **ZnSPP** recorded in $C_2D_2Cl_4$ at 400MHz is shown in **Fig. III-14**. Three signals of hydrogens at β-pyrrolic positions were observed at 9.01 ppm (β1, s), between 8.92-8.83 ppm (β2, m) and at 8.61 (β3, d, J = 4.68 Hz). The multiplets between 8.38-8.23, 7.86-7.79 and 7.79-7.73 were respectively attributed to the six hydrogens in *ortho*-positions of the phenyls superimposed with two hydrogens of the pyrene moiety, to the six hydrogens in *meta*-positions of the phenyls and to the three hydrogens in *para*-positions of the phenyls. The other signals between δ (ppm) 8.92-8.83 (m, 1H) and at 8.57 (d, 1H, J = 7.80 Hz), 8.45 (d, 1H, J = 9.08 Hz), 7.71 (d, 1H, J = 9.40 Hz), 7.51 (d, 1H, J = 9.32 Hz) corresponded to the hydrogens of the pyrene moiety without specifying their positions.

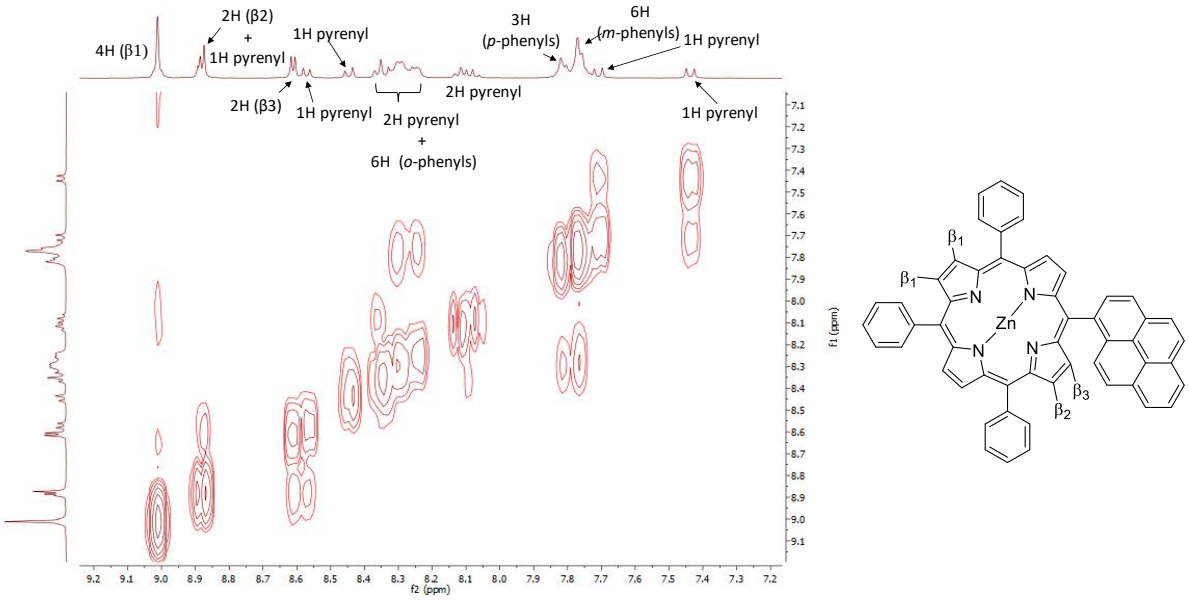

Fig. III-14 2D-cosy map and chemical structure of **ZnSPP** (400MHz, $C_2D_2Cl_4$, 298K).

The 2D-cosy NMR map of **ZnSAP** recorded in $C_2D_2Cl_4$ at 400MHz is shown in **Fig. III-15**. Three signals of hydrogens at β-pyrrolic positions were observed between 9.06-8.97 ppm (β1, m), 8.80 ppm (β2, d, J =4.4 Hz) and 8.36 (β3, d, J =4.8 Hz). The multiplets between 8.34-8.20, 7.87-7.79 and 7.78-7.69 were respectively attributed to the six hydrogens in *ortho*-positions of the phenyls (superimposed with the two hydrogens in positions 4-, 5- of the anthracene moiety), to the six hydrogens in *meta*-positions of the phenyls and to the three hydrogens in *para*-positions of the phenyls. The other signals at δ (ppm): 8.94 (s, 1H, 10-anthracenyl), 7.52-7.43 (m, 2H, 3,6-anthracenyl), 7.11-6.97 (m, 4H, 2,7- and 1,8-anthracenyl) were attributed to the hydrogens of the anthracene moiety in comparison to the literature.[7–10]

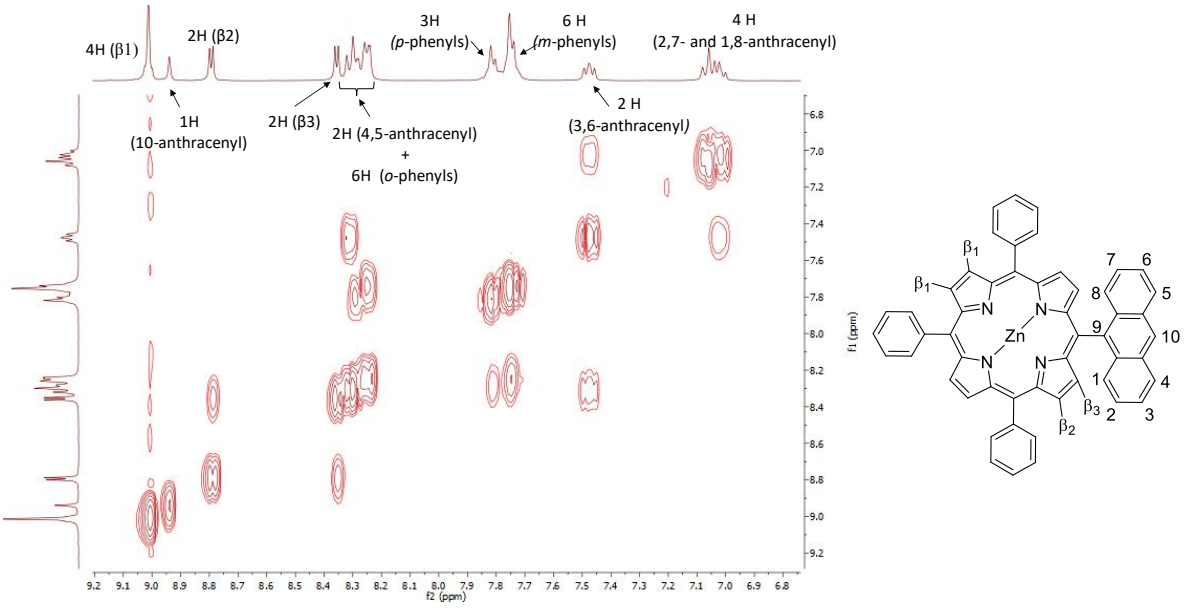

Fig. III-15 2D-cosy map and chemical structure of **ZnSAP** (400MHz, $C_2D_2Cl_4$, 298K).

III. 3. Pyrolysis of *meso*-substituted PAH-porphyrins

III. 3.1. Setup

Inspired from the experimental protocol described by the group of Thompson, we designed the setup illustrated in **Fig. III-16** and applied the following protocol for the pyrolysis experiment.

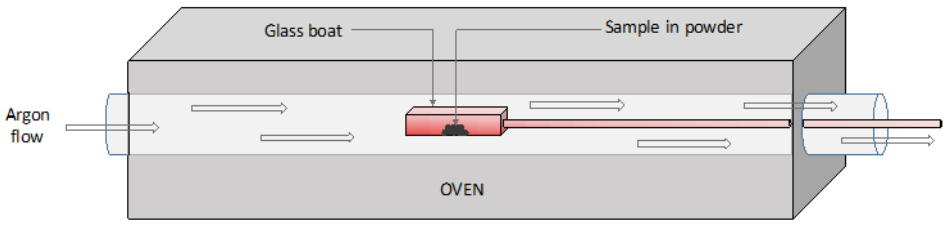

Fig. III-16 Illustration of the setup we used for the pyrolysis experiments.

A glass tube was preliminary heated at the reaction temperature and continuously flushed with an

argon flow. The temperature in the glass tube was monitored preliminary to the pyrolysis reaction with a thermocouple sensor placed under the argon flow at the future location of the glass boat. The glass boat containing the porphyrin precursor in powder was placed at the entrance of the glass tube under the argon flow for 10 min. Pyrolysis reaction started by inserting the glass boat into the furnace and evolution of the reaction was controlled with time monitoring by looking at the aspect of the sample after taking the glass boat out of the furnace. At the end of the reaction, the glass boat was taken out from the furnace, cooled down under the argon flow for 10 min and the crude mixture was collected with dichloromethane for purification.

III. 3.2. Pyrolysis of **ZnTPyP**

In order to validate our setup, we first reproduced the experiment of thermal fusion of **ZnTPyP**. After pyrolysis, the crude mixture was dissolved in DCM/pyridine (95:5) and passed through a silica pad to remove insoluble products. The resulting mixture was pure enough to detect the presence of products of fusion by MS and UV-visible spectroscopy that allowed the adjustment of the parameters of the reaction. The thermal fusion of **ZnTPyP** was investigated as a function of the temperature and the reaction time. A summary of the tests is presented in **Table III-1**.

Entry	Temperature (°C)	Time (sec)	Observation
1	550	60 and 90	Crystalline pink powder in glass boat, starting material on UV-Visible and MS
2	550	120	Molten product, mixture of doubly and triply fused products on MS
3	550	150 and 180	Molten product, mixture of triply and tetra fused products on MS
4	585	120	Molten product, mixture of triply and tetra fused products on MS
5	550	210	Molten product, tetrafused product on MS and UV-visible
6	585	150	Molten product, tetrafused product on MS and UV-visible
7	615	150 and 180	Few amount of molten product and intense white smoke release, sublimation and mixture of tetrafused and hyperfused products on MS

Table III-1 Summary of the tests of pyrolysis for the thermal fusion of **ZnTPyP**.

By heating **ZnTPyP** at 550°C for 60 and 90 sec, a crystalline pink powder was collected from the glass boat and only starting material was observed by MS and UV-visible spectroscopy (entry 1). For the reaction time of 120 sec at 550°C, the initial powder started to melt in the glass boat and a molten mixture was collected from the glass tube (entry 2). The resulting mixture contained doubly- and triply-fused products that were detected with isotopic signatures (MH^+) at *m/z* 1169.64 and 1167.63 respectively on the mass spectrum (**Fig. III-17**).

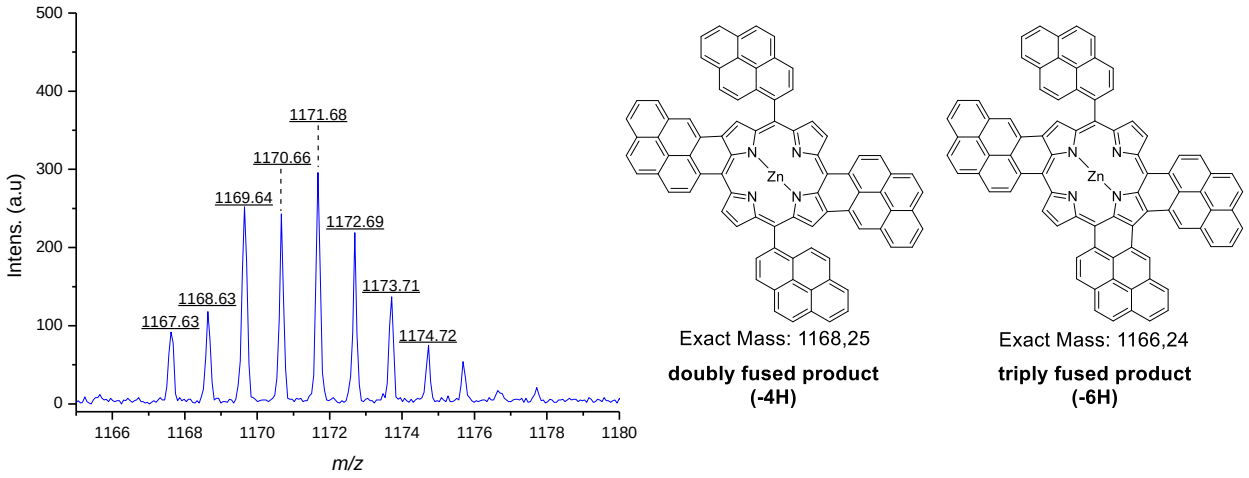

Fig. III-17 Mass spectrum and chemical structures of the doubly- and triply-fused products of fusion after the pyrolysis of **ZnTPyP** at 550°C for 120 sec.

A molten mixture was collected from the glass boat after pyrolysis of **ZnTPyP** at 550°C for 150 and 180 sec (entry 3) and at 585°C for 120 sec (entry 4). The solution of the resulting mixture in DCM was blue in comparison to the initial pink solution of **ZnTPyP**. The resulting mixture contained triply- and tetra-fused products that were detected with isotopic signatures (MH^+) *m/z* 1167.80 and 1165.77 respectively on the mass spectrum (**Fig. III-18**).

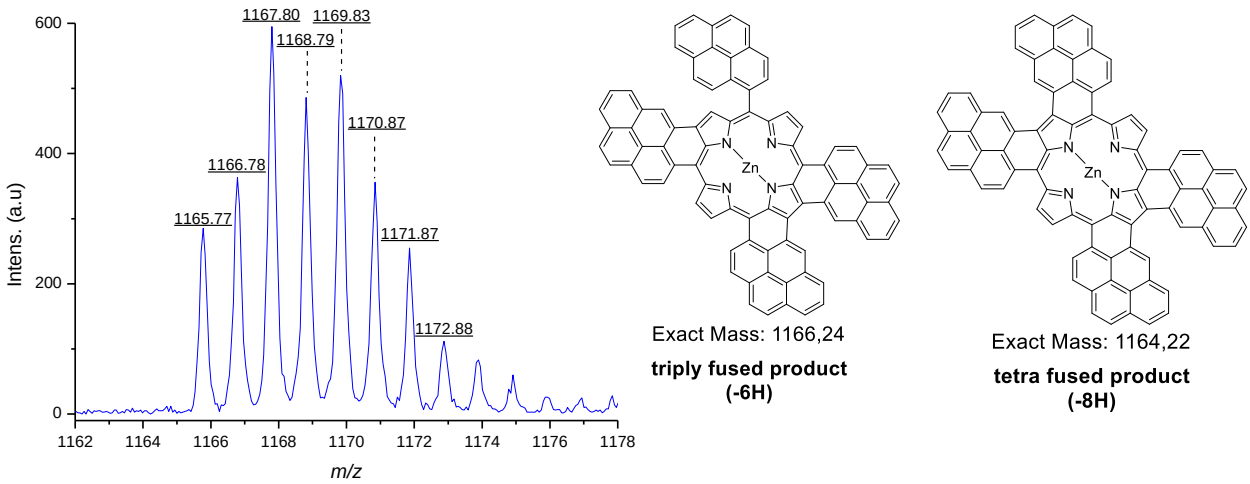

Fig. III-18 Mass spectrum and chemical structures of the triply- and tetra-fused products of fusion after the pyrolysis of **ZnTPyP** at 550°C for 150 sec.

According to MS analysis, the pyrolysis of **ZnTPyP** either at 550°C for 210 sec (entry 5) or at 585°C for 150 sec (entry 6) led to the unique formation of the target tetra-fused porphyrin that was observed on mass spectrum with isotopic signatures at *m/z* 1165.74 (MH^+, **Fig. III-19**).

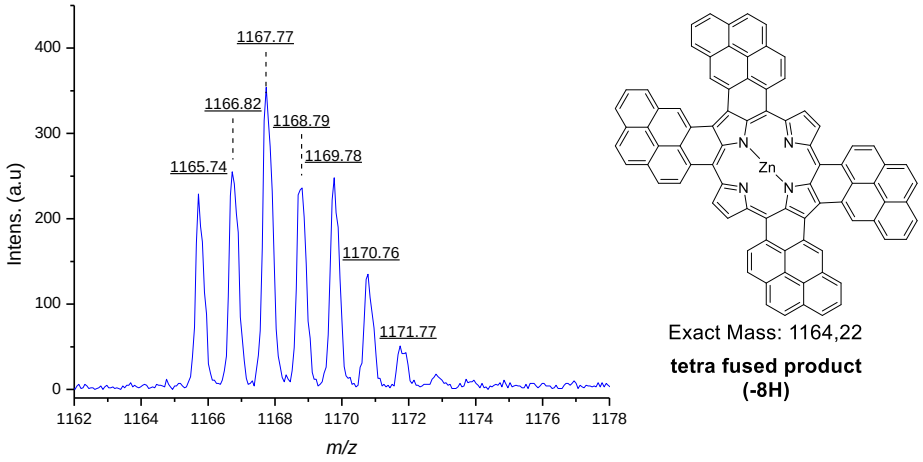

Fig. III-19 Mass spectrum and chemical structure of the target tetra-fused products of fusion after the pyrolysis of **ZnTPyP** either at 550°C for 210 sec or at 585°C for 150 sec.

By heating **ZnTPyP** at 615°C for 150 and 180 sec, the powder melted and an intense release of white smoke was observed (entry 7). The presence of the tetra-fused product was detected by MS analysis in addition to isotopic signals at *m/z* 1163.97 and 1161.97 corresponding to hyperfused-products (MH^+) with the additional loss of -2H and -4H (**Fig. III-20**).

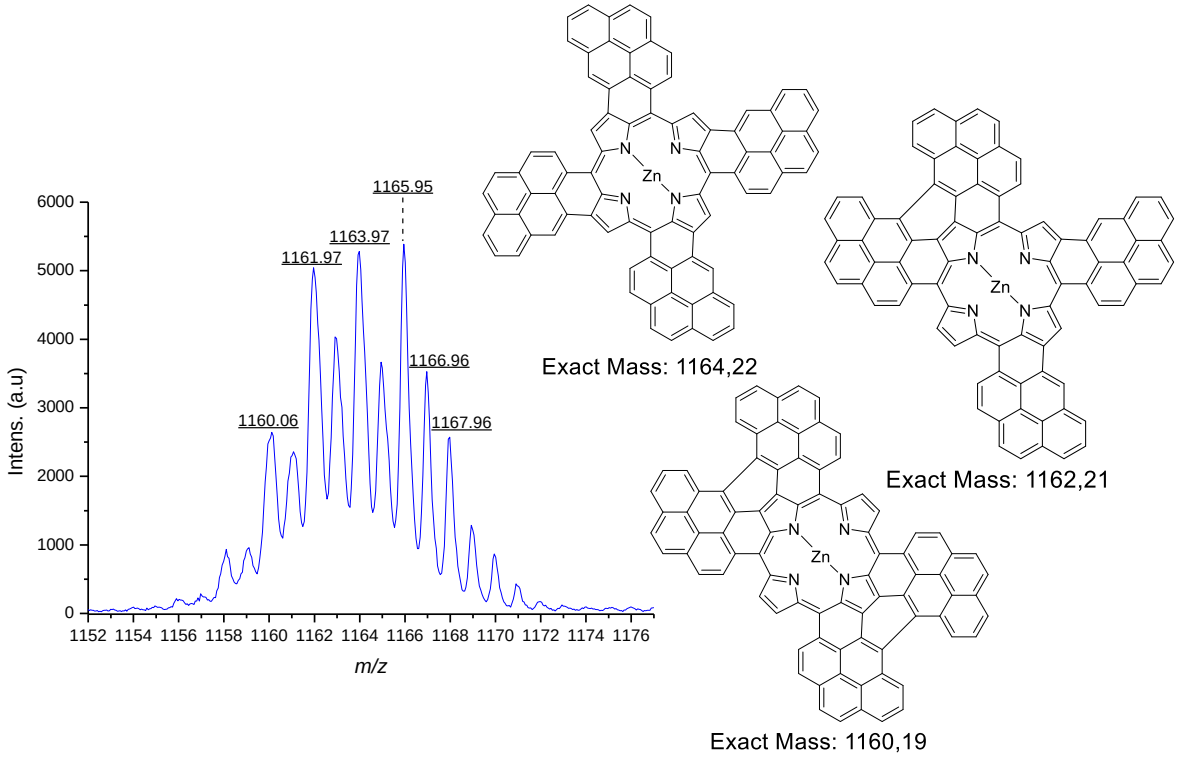

Fig. III-20 Mass spectrum and chemical structures of the tetra-fused- and the hyperfused products after the pyrolysis of **ZnTPyP** at 615°C for 180 sec.

The latter results suggested that the thermal fusion of the pyrene moiety on the porphyrin core was able to start at 550°C and approximately 120 sec were required to reach the temperature of reaction in the glass boat. However, a longer time or a higher temperature was needed to reach the target tetra-fused product. The pyrolysis conditions in entries 5 and 6 were found to be the most promising to achieve the thermal fusion of the four pyrenyl moieties and form an unique product. It appeared that the reaction started when the material melted and sublimation of compounds was observed by the release of a white smoke. Moreover, we found that the temperature required for the activation of the thermal fusion was relatively close to the temperature of degradation of **ZnTPyP** at 480°C determined by thermogravimetric analysis (TGA). Consequently, products of degradation with loss of one or two pyrenes were detected by MS analysis with increased intensities by prolonging the time of heating or by increasing the temperature. Increasing the temperature above 585°C led to formation of new species we called hyperfused products, with additional cyclodehydrogenation between the pyrene subunits out of the porphyrin core. The proportion of the hyperfused products was supposed to be statistic because of the preliminary formation of isomers that randomly settled the spatial arrangement of the pyrenyl groups. We supposed that the cyclodehydrogenation occurred only between pyrene derivatives with a particular spatial arrangement that made the moieties sufficiently close and thus variety of hyperfused products can form with different proportions. Although several mix of solvents were tested, we were not able to characterize the absorption properties of the hyperfused-products.

In addition, we performed a test of pyrolysis with the free base precursor (**TPyP**) that led to the formation of an insoluble mixture that could not be characterized. It is likely due to an important degradation of the starting material. Therefore, it appeared that the role of zinc in the cavity of porphyrin precursors was important for the reaction. The absorption spectra of the tetra-fused **ZnTPyP** (solid line) and starting **ZnTPyP** (dash line) are shown in **Fig. III-21**.

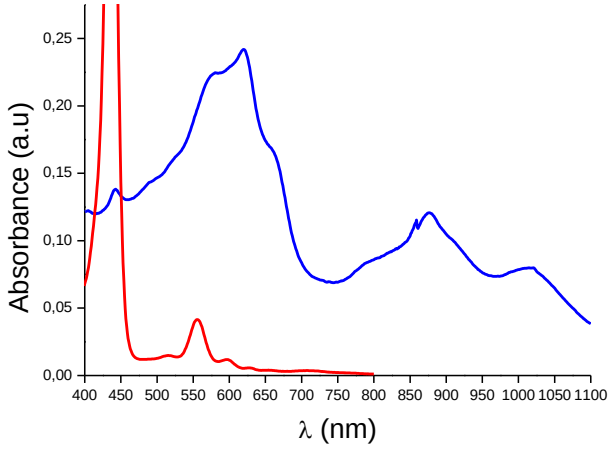

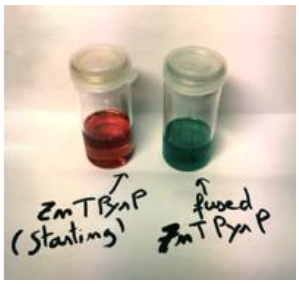

Fig. III-21 Absorption spectra of tetra-fused **ZnTPyP** (blue line) and starting **ZnTPyP** (red line). Insert caption showed the change of colour of the solutions of the starting material and of the fused product.

In comparison between the absorption spectra of the starting material and the fused products, we observed that the initial Soret band located at 434 nm disappeared during the fusion process and new bands in the visible region at λ = 445, 576, 629, 670 nm and in the NIR region at 881, 1022 nm appeared. Moreover, the change of the absorption properties with the reaction of fusion was marked by a visible change of colour from red to blue in solution (**Fig. III-21**). The absorption spectrum of the tetra-fused **ZnTPyP** corresponded to the optical signature of the tetra-fused porphyrin reported by the group of Thompson and confirmed that both the protocol and the setup we designed were correct.[21]

III. 3.3. Pyrolysis of **ZnTAP**

The thermal fusion of **ZnTAP** was investigated as a function of the temperature and the reaction time. After pyrolysis, the crude mixtures were dissolved in DCM/pyridine (95:5) and passed through a silica pad to remove insoluble products. The resulting mixtures were analysed by UV-visible spectroscopy and their absorption spectra were compared to literature to detect the presence of products of fusion.[13,15,16] The summary of the tests of pyrolysis of **ZnTAP** is presented in **Table III-2**.

Entry	Temperature (°C)	Time (sec)	Observation
1	515	180	crystalline powder in glass boat, starting material on UV-Visible
2	550	180	crystalline powder in glass boat, starting material on UV-Visible
3	585	180, 240, 300	calcined products stacked and crystalline pink powder in glass boat,starting material with new absorption bands at 848, 1024 and 1162 nm on the absorption spectrum
4	605	180, 210	calcined products and presence of starting material with new absorption bands at 848, 1024 and 1162 nm on absorption spectrum
5	640	180, 210	calcined products and pink smoke release, sublimation of **ZnTAP**

Table III-2 Summary of the tests of pyrolysis for the thermal fusion of **ZnTAP.**

We started to investigate the pyrolysis of **ZnTAP** at 515°C and 550°C both for 180 sec, a crystalline pink powder was collected from the glass boat that was identified to the starting **ZnTAP** by UV-Visible spectroscopy (entries 1 and 2). By heating **ZnTAP** at temperatures above 585°C and inferiors to 640°C, a calcined solid stacked at the bottom of the glass boat and a crystalline pink powder were

collected (entries 3 and 4). The analysis by MALDI-TOF mass spectrometry of the resulting powder dissolved in DCM only revealed the presence of the starting material with the isotopic signature at *m/z* 1177.81 but in addition to the signature of the starting material, absorption bands at 848, 1024 and 1162 nm were observed on the absorption spectrum (**Fig. III-22**).

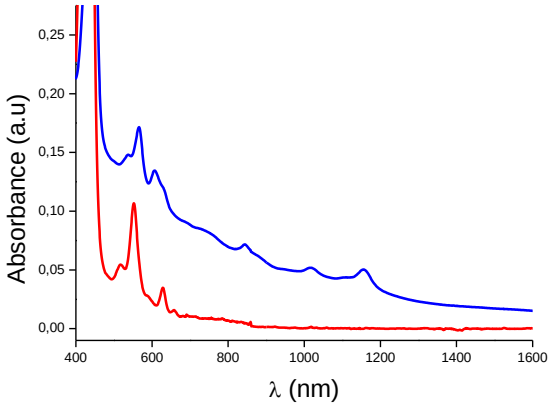

Fig. III-22 Absorption spectra in DCM/pyridine of the mixture after pyrolysis of **ZnTAP** at T = 585°C for 300 sec (blue), superimposed with the absorption of the starting material (red).

By heating **ZnTAP** at 640°C, a pink smoke released intensively from the glass tube after 90 sec of heating and only a calcined solid stacked on the glass boat was collected after pyrolysis (entry 5). Although several mix of solvents were tested, no discernible bands could be observed on the absorption spectrum of the calcined product. Consequently, it appeared that no reaction occurred for the temperatures of pyrolysis inferior to 550°C, and only the starting material was recovered. By increasing the temperature of reaction of up to 640°C, new bands located in the NIR region of the absorption spectrum of the mixture of pyrolysis were observed. The position of these bands were closed to the ones reported in the literature in the absorption spectra of the fused anthracenylporhyrins and suggested the initiation of the reaction of fusion in our system.[13,15,16] However, amongst all the conditions tested, **ZnTAP** did not melt and heating the precursor above 640°C induced an important sublimation of the starting material as identified by absorption spectroscopy. In addition, we analysed by MS the calcined solid stacked on the glass boat following a protocol reported by the group of Müllen and developed to analyse insoluble compounds.[29] Briefly, about 0.5 mg of sample was crushed with an excess amount of tetracyanoquinodimethane (TCNQ) in a crucible, dispersed in cyclohexane and deposited on the conductive plate of the MALDI-TOF device for analysis. Although the calcined solid was probably composed of degraded products, we were able to detect isotopic distributions at *m/z* 1077.71, 1057.68 and 887.47 (MH^+) that were respectively identified to **ZnTAP**, the product of hyperfusion with the loss of 20H and to the product of degradation with the loss of one anthracene (**Fig. III-23**).

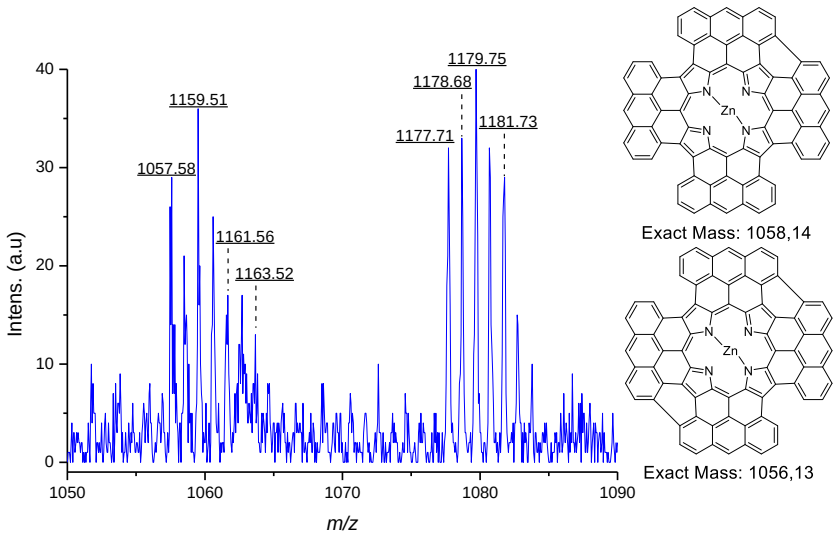

Fig. III-23 Mass spectrum and chemical structures of the starting material and the corresponding hyperfused products of fusion in the calcined mixture after the pyrolysis of **ZnTAP** at 605°C for 180 sec.

The latter results were encouraging because it indicated that the fusion of **ZnTAP** could be thermally activated. However **ZnTAP** did not melt and a gradient of temperature in the glass boat was suspected that would explain the inhomogeneous reactivity observed and the scattered results. In the present case, the precursor either degraded or probably hyperfused due to the high temperatures at the bottom of the glass boat or did not or barely reacted for the major part of the sample. Therefore, we suppose that the fusion of **ZnTAP** could be better achieved if we could homogeneously heat **ZnTAP**.

III. 3.4. Pyrolysis of **ZnBAP**

The thermal fusion of **ZnBAP** was investigated as a function of the temperature and the reaction time. The summary of the tests of pyrolysis of **ZnBAP** is presented in **Table III-3**.

By heating **ZnBAP** at 500°C for 180 sec, a pink powder was collected from the glass boat that was identified to **ZnBAP** by absorption spectroscopy (entry 1). By heating **ZnBAP** at 540°C and 570°C for 180 sec, molten mixtures were collected from the glass boat (entries 2 and 3). The solution of the resulting mixtures in DCM appeared more reddish than the initial pink solution of **ZnBAP** and an important amount of insoluble solid remained in suspension. The absorption spectra of these mixtures presented a similar aspect to the optical signature of the starting material with the appearance of less intense bands at 627, 796 and 883 nm (blue line, **Fig. III-24**).

Entry	Temperature (°C)	Time (sec)	Observation
1	500	180	pink powder in glass boat, starting material on UV-Visible
2	540	180	molten mixture collected from the glass boat, starting material and new absorption bands at 796, 883 nm observed on the absorption spectrum
3	570	180	molten mixture collected from the glass boat, starting material and new absorption bands at 796, 883 nm observed on the absorption spectrum
4	585	180	calcined products, no signal on UV-Visible spectroscopy
5	620	210	calcined products, no signal on UV-Visible spectroscopy

Table III-3 Summary of the tests of pyrolysis for the thermal fusion of **ZnBAP.**

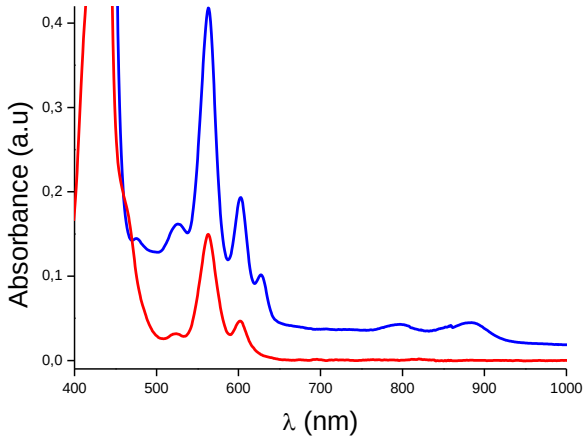

Fig. III-24 Absorption spectra in DCM/pyridine of the mixture after pyrolysis of **ZnBAP** at T = 570°C for 180 sec (blue), superimposed with the absorption of the starting material (red).

By heating **ZnBAP** either at 585°C for 180 sec (entry 4) or at 620°C for 210 sec (entry 5), a calcined solid stacked on the glass boat was collected. Although several mix of solvents were tested, no discernible bands could be observed on the absorption spectrum of the calcined product. Consequently, we observed that the powder did not melt for T < 550°C and only a crystalline powder corresponding to the stating material **ZnBAP** was collected from the glass boat. For T > 540°C, the powder melted and an important degradation was suspected according to the amount of the insoluble solid in suspension. It is worth mentioning that the temperature of degradation of **ZnBAP** has been determined to 515°C by TGA. We attributed the appearance of the absorption bands at 627, 796 and 883 nm to the presence of the product of fusion with one anthracene moiety in comparison to the literature.[13] Because a beginning of reaction occurred, we increased the temperature to 585°C and 620°C that drastically increased the degradation of **ZnBAP** and the resulting calcined solid was

characterized by MALDI-TOF mass spectrometry following the solid-state protocol. Three isotopic distributions at *m/z* 791.33, 865.24 and 939.52 were detected on the mass spectrum. The distribution at *m/z* 865.24 revealed a loss of 12H from the starting **ZnBAP** that corresponded to the product of fusion with the two anthracene moieties and the two phenyl rings fused on the porphyrin core. The other distributions at *m/z* 791.33 and 939.52 would correspond to products of fusion with respectively the loss and the addition of a phenyl ring as already observed in the synthesis of PAHs *via* pyrolysis technique in the literature.[30] The characterization of the optical properties of these compounds was compromised due to the high presence of degraded products masking the absorption signatures.

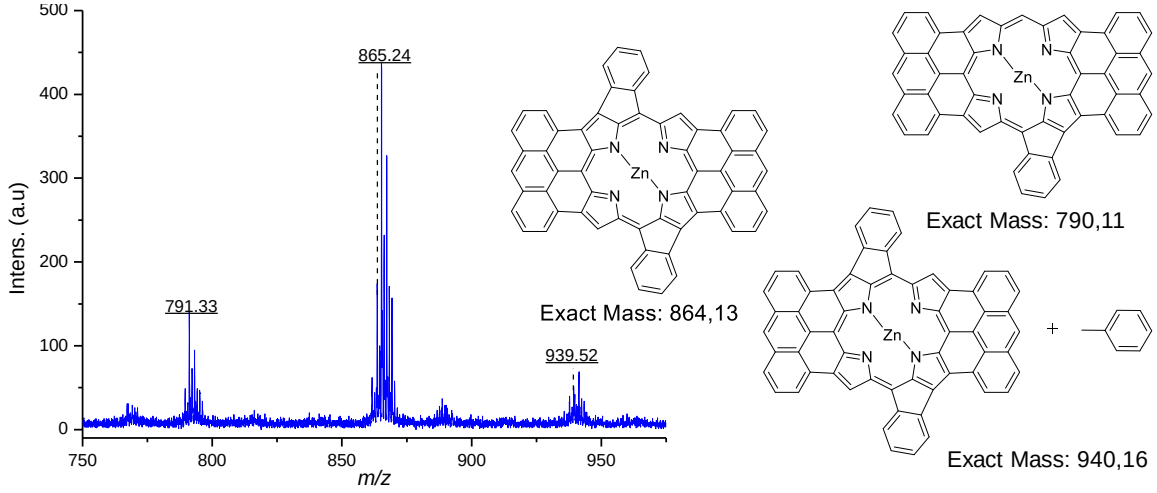

Fig. III-25 Mass spectrum and chemical structures of fused **ZnBAP** with extra fusion of phenyl rings and fused and of fused derivatives contained in the calcined solid after the pyrolysis of **ZnBAP** either 585°C for 180 sec or at 620°C for 210 sec.

According to MS and absorption spectroscopy, we deduced that the reaction of fusion of multiple anthracene moieties can be thermally activated but seemed to be sequential. The fusion of one anthracene by pyrolysis was accompanied by an important degradation that prevented a second pyrolysis with a risk of total destruction of compounds. Inspired from the results, we imagined that the technique would be efficient to fuse an unique anthracene derivative on porphyrins.

III. 3.5. Pyrolysis of **ZnSAP**, **ZnSNP** and **ZnSPP**

In order to prevent the formation of isomers, the objective of the pyrolysis of **ZnSAP**, **ZnSNP** and **ZnSPP** is to achieve only the fusion of one PAH moiety to the porphyrin core and lead to the formation [3,5,7-(10,15,20-triphenyl)anthraceneporphyrinato]zinc(II) (**fused ZnSAP)**, [3,5-(10,15,20-triphenyl)naphthaleneporphyrinato]zinc(II) (**fused ZnSNP)** and [3,5-(10,15,20-triphenyl)pyreneporphyrinato]zinc(II) (**fused ZnSPP**) (**Fig. III-26**).

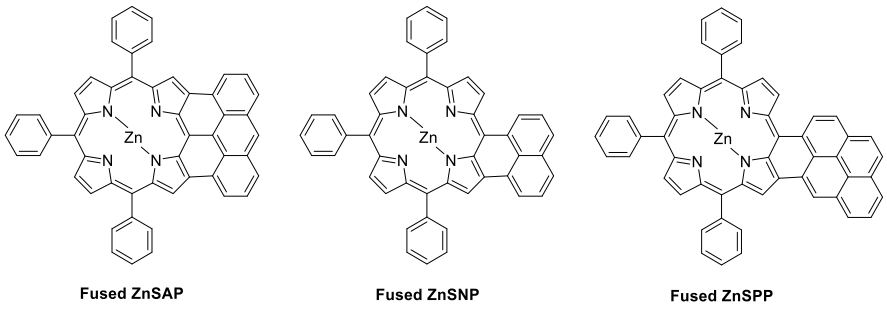

Fig. III-26 Chemical structures of target **fused ZnSAP**, **fused ZnSNP** and **ZnSPP**.

a) Experiments

By heating **ZnSAP**, **ZnSNP** and **ZnSPP** in powders at T<500°C, the liquefactions of the starting materials were not observed and we deduced that the thermal fusion of the compounds could not be achieved with a temperature of pyrolysis inferior to 500°C. We tested the pyrolysis of **ZnSAP**, **ZnSNP** and **ZnSPP** at 510-515°C and observed the liquefaction of the powders after 180 sec of heating. At such temperature, the sublimations of **ZnSAP** and **ZnSNP** were also observed with an important release of pink smoke from the glass tube after 120-150 sec of heating. Because no release of smoke was observed during the pyrolysis of **ZnSPP** at 510-515°C, we deduced that the sublimation of starting material did not occur. The molten mixtures of **ZnSAP**, **ZnSNP** and **ZnSPP** were collected from the glass boat respectively after 225 sec, 330 sec and 210 sec of pyrolysis. The crude mixtures were passed through a silica pad to remove insoluble products and separate the fused derivatives from the unreacted products.

The absorption spectra of the fused products of **ZnSAP**, **ZnSNP**, **ZnSPP** exhibited new absorption bands compared to the parent porphyrins. In comparison to the absorption spectra of the fused porphyrins reported in the literature,[6–8,10,13] we concluded that the thermal fusions of **ZnSAP**, **ZnSNP** and **ZnSPP** were successfully achieved after the pyrolysis at 510-515°C for 225 sec, 330 sec and 210 sec respectively and led to the formation of our target **fused ZnSAP**, **fused ZnSNP** and **fused ZnSPP**. The crude mixtures were purified on silica column eluted with DCM/cyclohexane (1:1, v/v) and a red, a brown-green and a brown fractions that respectively contained **fused ZnSAP**, **fused ZnSNP**, **fused ZnSPP** were collected. The mass spectra of the fractions are presented in **Fig. III-27**.

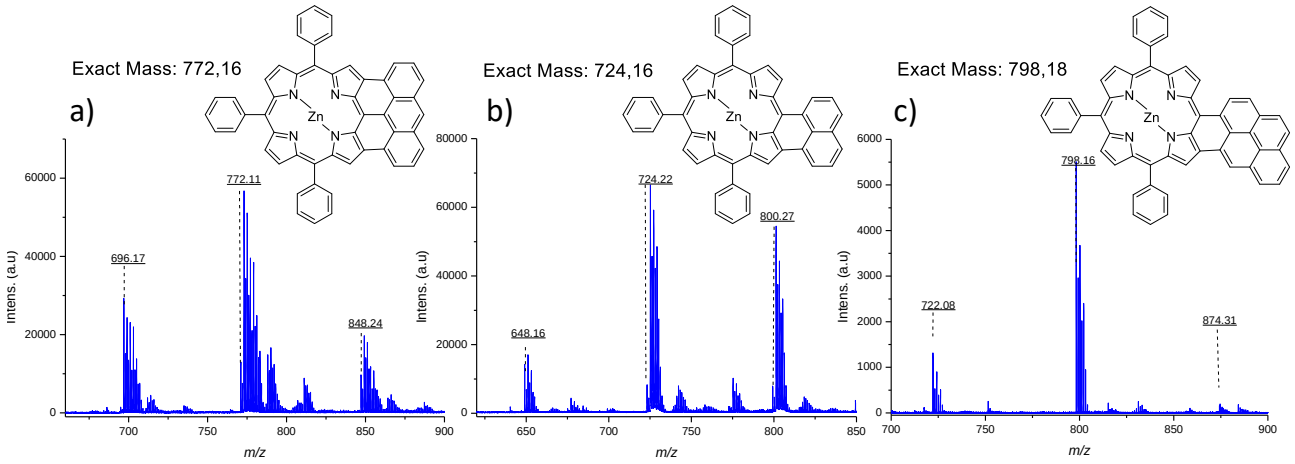

Fig. III-27 Mass spectra of the products of pyrolysis at 510-515°C of a) **ZnSAP** for 225 sec; b) **ZnSNP** for 330 sec; c) **ZnSPP** for 210 sec.

The isotopic distribution at *m/z* 772.11 revealed a loss of 4H from the starting **ZnSAP** (exact mass 776.16) corresponding to fused **ZnSAP** (exact mass 772.16) (**Fig. III-27**, a). The isotopic signals at *m/z* 724.22 and 798.16 revealed a loss of 2H from the starting materials **ZnSNP** (exact mass 726.16) and **ZnSPP** (exact mass 800.18) respectively corresponding to fused **ZnSNP** (exact mass 724.16) and fused **ZnSPP** (exact mass 798.18) (**Fig. III-27**, b and c). In addition, other isotopic distributions at *m/z* +76 and -76 surrounding the signals of the fused compounds were systematically observed and corresponded to the fused derivatives with the addition and the loss of a phenyl ring.

We tried to optimize the pyrolysis conditions to reduce the formation of by-products and the residual presence of starting materials. We found that increasing the reactions times or the temperature reduced the presence of starting materials but increased the decomposition of compounds and enhanced the formation of undesired fused by-products with addition and loss of phenyls at the periphery of the porphyrins. The very close physicochemical properties of these compounds made difficult their separations on silica columns. Indeed, we tested the separation of the compounds *via* preparative HPLC or with the use of thinner kind of silica (0.015-0.040 mm) that were unfortunately incomplete for a large number of eluent ratios and gradients tested. We finally found that better separations can be achieved by SEC using THF and three partly superimposed fractions were observed. According to MS analysis, the first fractions corresponded to the isotopic signals of the fused products with the additional phenyl at *m/z* +76; the second fractions corresponded to the signals of the target fused compounds and the last fractions corresponded to the signals of the fused products with the loss of one phenyl ring at *m/z* -76. Several SEC were performed to afford sufficient separations of the mixtures and **fused ZnSPP**, **fused ZnSAP** were successfully isolated and characterized by HRMS and UV-Visible-NIR spectroscopy. **Fused ZnSPP** was isolated with an appreciable amount that allowed the record of a comprehensive ^{1}H NMR spectrum and the fusion of

ZnSAP has to be repeated to record a comprehensive ^{1}H NMR spectrum. The purification of **fused ZnSNP** was found to be more complicated because of the small differences between the fused naphthylporphyrin and its derivatives, and is still in progress in our group. Nevertheless, the identity of **fused ZnSNP** was confirmed by HRMS analysis.

b) Absorption spectroscopy

The absorption spectra of **fused ZnSAP**, **fused ZnSPP** and of the mixture containing **fused ZnSNP** and the products of addition and loss of a phenyl ring are shown **Fig. III-28** (blue). In comparison to the absorption signatures of starting materials (red), the Soret bands initially located at 421 nm were absent and new optical bands were observed at:

- 408, 526, 593, 769 and 851 nm in the absorption spectrum of **fused ZnSAP** (**Fig. III-28**, a)
- 413, 492, 665 and 703 nm in the absorption spectrum of **fused ZnSPP** (**Fig. III-28,** b)
- 411, 472, 647 and 667 nm in the absorption spectrum of **fused ZnSNP** (**Fig. III-28,** c).

Different red-shifts of the optical absorption properties of porphyrins were experimentally observed by the β-fusion with anthracene, pyrene and naphthalene moieties to the porphyrin cores.

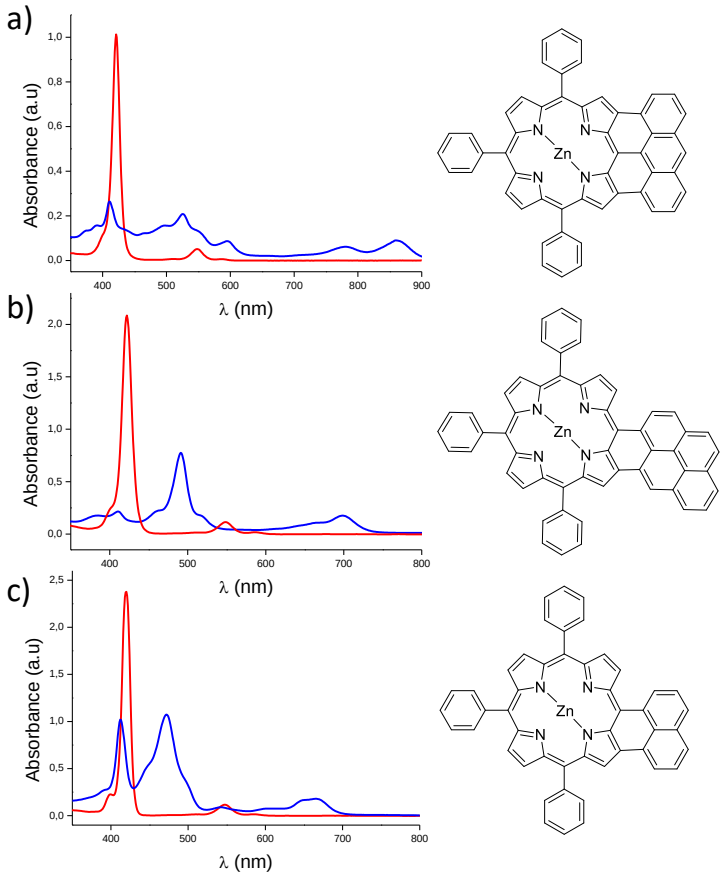

Fig. III-28 Absorption spectra (blue) and chemical structures of a) **fused ZnSAP**; b) **fused ZnSPP**; c) mixture containing **fused ZnSNP** and products of addition and loss of a phenyl ring; superimposed with the absorption signatures of the starting materials (red).

c) HRMS

The formation of the desired **fused ZnSAP, fused ZnSPP** and **fused ZnSNP** were confirmed by HRMS. For **fused ZnSAP**, an exact mass of 772.1605 was calculated from $C_{52}H_{28}N_4Zn$ and an exact mass of 772.1607 was experimentally determined for M^+ (**Fig. III-29**, a). Likewise for **fused ZnSPP** and **fused ZnSNP**, exact masses of 798.1762 and 724.1605 were respectively calculated from $C_{54}H_{30}N_4Zn$ and $C_{48}H_{28}N_4Zn$ and exact masses of 798.1778 and 724.1610 were experimentally determined for M^+ respectively (**Fig. III-29**, b and c).

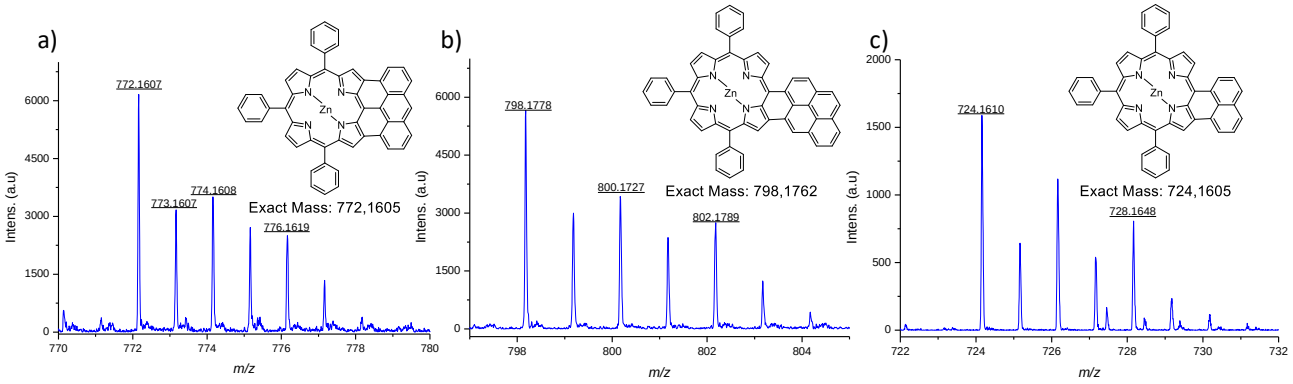

Fig. III-29 HRMS spectra of a) **fused ZnSAP**; b) **fused ZnSPP**; c) **fused ZnSNP.**

d) 1H NMR

The ^1H NMR spectrum of **fused ZnSPP** was recorded in $C_2D_2Cl_4$ at 400MHz and the aromatic region of the spectrum is shown in **Fig. III-30**. In comparison to the spectrum of the starting **ZnSPP**, we observed that the chemicals shifts in the spectra of the **fused ZnSPP** were deshielded up to 9.55 ppm and the signals of the hydrogens at β-pyrrolic positions were considerably affected by the β-fusion with the pyrene moiety. We attributed the chemical shifts on the NMR spectrum of **fused ZnSPP** from the spectral signatures of starting **ZnSPP** and anthracenylporphyrins reported in the literature.[6,13] Based on the important deshielding and the multiplicity, we found that the signals at 9.58 and 9.47 (s, 1H) could be attributed either to the hydrogen β1 of pyrrole or to the hydrogen in position 9 of the pyrene moiety. According to the arguments of multiplicity and coupling constant, the signals at 9.54 (d, 1H, J = 4.8 Hz), 8.97 (d, 1H, J = 4.8 Hz) and between 8.86-8.77 (m, 3H) were respectively attributed to the two hydrogens β2, β3 and the group of the three hydrogens β4, β5, β6. Likewise, the signals at 9.38 (d, 1H, J = 8.0 Hz) and 8.71 (d, 1H, J = 8.4 Hz) were respectively attributed to the hydrogens in positions 2 and 3 of the pyrene moiety. In comparison to the spectrum of the starting **ZnSPP**, the signals between 8.35-8.27, 7.93-7.87, 7.86-7.72 were not impacted by the β-fusion and were respectively attributed to the hydrogens in *ortho*-, *para*-, *meta*-positions of the phenyls. The signals at 8.46 (d, 1H, J = 7.2 Hz), 8.25-8.19 (m, 3H), 8.11 (t, 1H, J = 7.6 Hz), 7.86-7.72 (m, 2H) ppm corresponded to the hydrogens of the pyrenyl without specifying their positions.

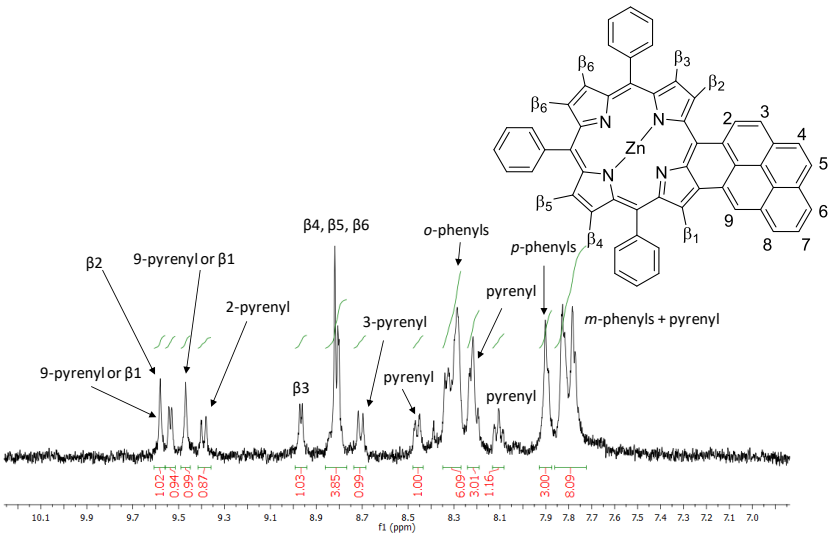

Fig. III-30 Aromatic region of the ^{1}H NMR spectrum of **fused ZnSPP** (400MHz, $C_2D_2Cl_4$, 298K).

III. 3.6. Metal-free π-extended porphyrin

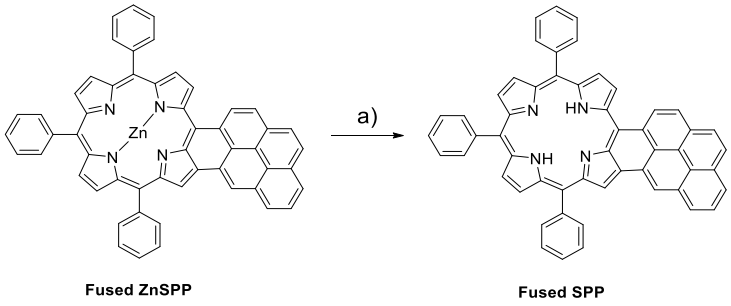

Fig. III-31 Acid treatment to remove zinc from the cavity of **fused ZnSPP** and afford the metal-free π-extended porphyrin **fused SPP**; a) HCl (6 mol/L), in DCM, 10 min, r.t.

Finally, zinc was removed from the cavity of **fused ZnSPP** under acidic conditions to form 3,5-(10,15,20-triphenyl)pyreneporphyrin (**fused SPP**) following literature procedure.[27] **Fused SPP** was detected by MALDI-TOF analysis with the isotopic signature at *m/z* 737.32 corresponding to MH^+(**Fig. III-32**, a). In comparison to the optical spectra of **fused ZnSPP**, the absorption spectrum of **fused SPP** (**Fig. III-32**, b) exhibited the same band at 410 nm, new blue shifted bands at 482, 584, 632, 658 nm and a new red shifted band at 733 nm. Both analysis confirmed that zinc was completely removed from the cavity of the porphyrin leading to **fused ZnSPP**. Because the reaction was performed on a very small amount of product, the ^{1}H NMR spectrum was not recorded. Finally, we proved that the formation of π-extended porphyrin without the presence of any metal or activating group on the PAH can be successfully achieved by the method of pyrolysis followed by acid treatment.

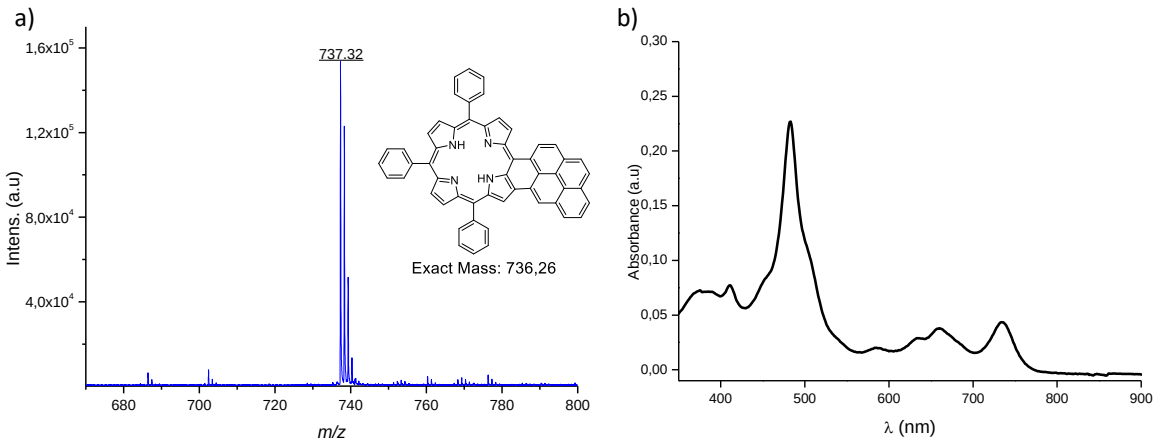

Fig. III-32 a) MS; and b) absorption spectra in $CHCl_3$ of **fused SPP**.

III. 4. Conclusion and perspectives

To conclude, a series of PAHs *meso*-substituted porphyrins containing naphthalene (**ZnSNP**), pyrene (**ZnSPP** and **ZnTPyP**) and anthracene (**ZnSAP**, **ZnBAP** and **ZnTAP**) derivatives were synthetised and used as precursors to investigate the formation of π-extended porphyrin *via* pyrolysis. An experimental setup for the pyrolysis was designed and validated by reproduction of the fusion of **ZnTPyP**. Amongst all the conditions of pyrolysis tested, we found that 120 sec of heating was necessary to reach the working temperature in the glass boat and succeeded in the thermal fusion of the four pyrenyl moieties of **ZnTPyP** at 550-585°C from 150 to 210 sec. According to MS analysis, hyperfused compounds were presumed to form under pyrolysis conditions above 585°C and suggested that the pyrolysis technique would form species that are inaccessible *via* solution synthesis. Beyond the fusion of **ZnTPyP**, we concluded from the pyrolysis of **ZnTAP** and **ZnBAP** that the thermal fusion of multiple anthracenes was difficult to achieve and faced with issues of non-liquefaction, sublimation and severe degradation of precursors. Finally, we succeeded in the thermal fusion of the mono anthracene, naphthalene and pyrene moieties of **ZnSAP**, **ZnSNP**, **ZnSPP**. Although the formation of by-products with addition and loss of a phenyl ring on the target product of fusion was observed by MS analysis, **fused ZnSPP** and **fused ZnSAP** were successfully isolated by SEC and characterized by HRMS and UV-Visible-NIR spectroscopy. **Fused** ZnSPP was characterized by ^{1}H NMR spectrum and the fusion of ZnSAP has to be repeated to record a comprehensive ^{1}H NMR spectrum. The purification of **fused ZnSNP** is still in progress in the group and its identity was confirmed by HRMS analysis. Finally, we removed zinc from the cavity of **fused ZnSPP** that led to the formation of the **fused SPP** which was characterized by absorption spectroscopy and MS spectrometry. Therefore, we demonstrated that after pyrolysis, an acid treatment can be used to successfully remove zinc from the cavity of porphyrins leading to π-extended

porphyrin without any metal or activating group on the PAH.

An alternative strategy to afford π-extended porphyrins would be to perform the pyrolysis of precursors in gas phase *via* a technique called Flash Vacuum Pyrolysis (FVP).[31,32] FVP operates under vacuum between 10^{-7}-10^{-8} mbar and the apparatus is generally composed of a first oven used to sublime the precursors and a second in series to induce the thermal fusion. In comparison to the setup of pyrolysis developed in this study, the apparatus of the FVP technique allows an independent control of the two temperatures of sublimation and pyrolysis as well as the flow of precursors that are important assets to properly achieve the reaction of fusion. The thermal fusion of our precursors *via* FVP is currently under investigation in the group of the Professor Anna Chrostowska (IPREM) from the University of Pau and the first challenge is the control of sublimation of precursors.

III. 5. References

(1) Fox, S.; Boyle, R. W. First Examples of Intramolecular Pd(0) Catalysed Couplings on Ortho-Iodinated Meso-Phenyl Porphyrins. *Chem. Commun.* **2004**, 1322–1323.

(2) Shen, D.-M.; Liu, C.; Chen, Q.-Y. A General and Efficient Palladium-Catalyzed Intramolecular Cyclization Reaction of β-Brominated Porphyrins. *J. Org. Chem.* **2006**, *71*, 6508–6511.

(3) Fox, S.; Boyle, R. W. Synthetic Routes to Porphyrins Bearing Fused Rings. *Tetrahedron* **2006**, *62*, 10039–10054.

(4) Ishizuka, T.; Saegusa, Y.; Shiota, Y.; Ohtake, K.; Yoshizawa, K.; Kojima, T. Multiply-Fused Porphyrins—Effects of Extended π-Conjugation on the Optical and Electrochemical Properties. *Chem. Commun.* **2013**, *49*, 5939.

(5) Saegusa, Y.; Ishizuka, T.; Komamura, K.; Shimizu, S.; Kotani, H.; Kobayashi, N.; Kojima, T. Ring-Fused Porphyrins: Extension of π-Conjugation Significantly Affects the Aromaticity and Optical Properties of the Porphyrin π-Systems and the Lewis Acidity of the Central Metal Ions. *Phys. Chem. Chem. Phys.* **2015**, *17*, 15001–15011.

(6) Yamane, O.; Sugiura, K.; Miyasaka, H.; Nakamura, K.; Fujimoto, T.; Nakamura, K.; Kaneda, T.; Sakata, Y.; Yamashita, M. Pyrene-Fused Porphyrins: Annulation Reactions of Meso-Pyrenylporphyrins. *Chem. Lett.* **2004**, *33*, 40–41.

(7) Tanaka, M.; Hayashi, S.; Eu, S.; Umeyama, T.; Matano, Y.; Imahori, H. Novel Unsymmetrically π-Elongated Porphyrin for Dye-Sensitized TiO2 Cells. *Chem. Commun.* **2007**, 2069–2071.

(8) Hayashi, S.; Tanaka, M.; Hayashi, H.; Eu, S.; Umeyama, T.; Matano, Y.; Araki, Y.; Imahori, H. Naphthyl-Fused π-Elongated Porphyrins for Dye-Sensitized TiO2 Cells. *J. Phys. Chem. C* **2008**, *112*, 15576–15585.

(9) Lewtak, J. P.; Gryko, D.; Bao, D.; Sebai, E.; Vakuliuk, O.; Ścigaj, M.; Gryko, D. T. Naphthalene-Fused Metallo-Porphyrins–Synthesis and Spectroscopy. *Org. Biomol. Chem.* **2011**, *9*, 8178.

(10) Cammidge, A. N.; Scaife, P. J.; Berber, G.; Hughes, D. L. Cofacial Porphyrin−Ferrocene Dyads and a New Class of Conjugated Porphyrin. *Org. Lett.* **2005**, *7*, 3413–3416.

(11) Chen, P.; Fang, Y.; Kadish, K. M.; Lewtak, J. P.; Koszelewski, D.; Janiga, A.; Gryko, D. T. Electrochemically Driven Intramolecular Oxidative Aromatic Coupling as a Pathway toward π-Extended Porphyrins. *Inorg. Chem.* **2013**, *52*, 9532–9538.

(12) Fang, Y.; Koszelewski, D.; Kadish, K. M.; Gryko, D. T. Facile Electrosynthesis of π-Extended Porphyrins. *Chem. Commun.* **2014**, *50*, 8864–8867.

(13) Davis, N. K. S.; Pawlicki, M.; Anderson, H. L. Expanding the Porphyrin π-System by Fusion with Anthracene. *Org. Lett.* **2008**, *10*, 3945–3947.

(14) Ball, J. M.; Davis, N. K. S.; Wilkinson, J. D.; Kirkpatrick, J.; Teuscher, J.; Gunning, R.; Anderson, H. L.; Snaith, H. J. A Panchromatic Anthracene-Fused Porphyrin Sensitizer for Dye-Sensitized Solar Cells. *RSC Adv.* **2012**, *2*, 6846.

(15) Davis, N. K. S.; Thompson, A. L.; Anderson, H. L. Bis-Anthracene Fused Porphyrins : Synthesis , Crystal Structure , and Near-IR Absorption. *Org. Lett.* **2010**, *12*, 2124–2127.

(16) Davis, N. K. S.; Thompson, A. L.; Anderson, H. L. A Porphyrin Fused to Four Anthracenes. *J. Am. Chem. Soc.* **2011**, *133*, 30–31.

(17) Kurotobi, K.; Kim, K. S.; Noh, S. B.; Kim, D.; Osuka, A. A Quadruply Azulene-Fused Porphyrin with Intense near-IR Absorption and a Large Two-Photon Absorption Cross Section. *Angew. Chem. Int. Ed.* **2006**, *45*, 3944–3947.

(18) Jiao, C.; Huang, K.-W.; Guan, Z.; Xu, Q.-H.; Wu, J. N -Annulated Perylene Fused Porphyrins with Enhanced Near-IR Absorption and Emission. *Org. Lett.* **2010**, *12*, 4046–4049.

(19) Ota, K.; Tanaka, T.; Osuka, A. Meso-β Dibenzo[a,g]Corannulene-Fused Porphyrins. *Org. Lett.* **2014**, *16*, 2974–2977.

(20) Chen, Q.; Brambilla, L.; Daukiya, L.; Mali, K. S.; De Feyter, S.; Tommasini, M.; Müllen, K.; Narita, A. Synthesis of Triply Fused Porphyrin-Nanographene Conjugates. *Angew. Chem. Int. Ed.* **2018**, *57*, 11233–11237.

(21) Diev, V. V.; Schlenker, C. W.; Hanson, K.; Zhong, Q.; Zimmerman, J. D.; Forrest, S. R.; Thompson, M. E. Porphyrins Fused with Unactivated Polycyclic Aromatic Hydrocarbons. *J. Org. Chem.* **2012**, *77*, 143–159.

(22) Diev, V. V.; Femia, D.; Zhong, Q.; Djurovich, P. I.; Haiges, R.; Thompson, M. E. A Quinoidal Bis-Phenalenyl-Fused Porphyrin with Supramolecular Organization and Broad near-Infrared Absorption. *Chem. Commun.* **2016**, *52*, 1949–1952.

(23) Adler, A. D.; Longo, F. R.; Shergalis, W. Mechanistic Investigations of Porphyrin Syntheses. I. Preliminary Studies on Ms-Tetraphenylporphin. *J. Am. Chem. Soc.* **1964**, *86*, 3145–3149.

(24) Plater, M. J.; Aiken, S.; Bourhill, G. A New Synthetic Route to Donor- Acceptor Porphyrins. *Tetrahedron* **2002**, *58*, 2405–2413.

(25) Volz, H.; Schaeffer, H. Mesosubstituted Porphyrins. III. 5,10,15,20-Tetraanthracenylporphyrin. *Chemiker-Zeitung* **1985**, *109*, 308–309.

(26) Bonifazi, D.; Accorsi, G.; Armaroli, N.; Song, F.; Palkar, A.; Echegoyen, L.; Scholl, M.; Seiler, P.; Jaun, B.; Diederich, F. Oligoporphyrin Arrays Conjugated to [60]Fullerene: Preparation, NMR Analysis, and Photophysical and Electrochemical Properties. *Helv. Chim. Acta* **2005**, *88*, 1839–1884.

(27) Hirata, O.; Yamamoto, M.; Sugiyasu, K.; Kubo, Y.; Ikeda, M.; Takeuchi, M.; Shinkai, S. Allosteric Saccharide Sensing by a Phenylboronic-Acids-Appended 5,15-Bis(Triarylethynyl)Porphyrin. *J. Supramol. Chem.* **2002**, *2*, 133–142.

(28) Davis, M.; Senge, M. O.; Locos, O. B. Anthracenylporphyrins. *Z. Naturforsch, B* **2010**, *65*, 1472–1484.

(29) Przybilla, L.; Brand, J.-D.; Yoshimura, K.; Räder, H. J.; Müllen, K. MALDI-TOF Mass Spectrometry of Insoluble Giant Polycyclic Aromatic Hydrocarbons by a New Method of Sample Preparation. *Anal. Chem.* **2000**, *72*, 4591–4597.

(30) Shukla, B.; Koshi, M. A Highly Efficient Growth Mechanism of Polycyclic Aromatic Hydrocarbons. *Phys. Chem. Chem. Phys.* **2010**, *12*, 2427.

(31) Wentrup, C. Flash Vacuum Pyrolysis: Techniques and Reactions. *Angew. Chem. Int. Ed.* **2017**, *56*, 14808–14835.

(32) Chrostowska, A.; Leśniak, S. Recent Studies on Flash Vacuum Thermolysis in Tandem with UV-Photoelectron Spectroscopy and Quantum Calculations. *Aust. J. Chem.* **2014**, *67*, 1166.

Chapter IV. Suzuki-Miyaura coupling reaction on the tetra-bromoanthracenylporphyrin

Chapter IV. Suzuki-Miyaura coupling reaction on the tetra-bromoanthracenylporphyrin

This chapter is dedicated to the post-synthetic modification *via* Suzuki-Miyaura cross coupling reaction of the 5,10,15,20-tetrakis(10-bromoanthracen-9-yl)porphyrin (**BrTAP**) with additional substituted-phenyl and PAH moieties.

In the first part, the reactivity of **BrTAP** was explored *via* Suzuki-Miyaura cross coupling reaction with PAH-boronic acids (anthracene, pyrene, naphthalene) and substituted-phenyl boronic acids (phenyl, *p*-nitrophenyl, *p*-tolyl and *p*-methoxyphenyl) in order to generate a series of original tetra-anthracenylporphyrin-based molecules.
In the second part, absorption, fluorescence and PLE measurements were conducted to characterize the optical properties of these original tetra-anthracenylporphyrin derivatives.

IV. 1. Synthesis of anthracenylporphyrin derivatives

Among the large collection of porphyrinic structures, only a few reports can be found in the literature about the synthesis of anthracenylporphyrin derivatives that can be related to an important synthetic challenge (see chapter II).[1–4] TAP-containing reactive functions on the anthracenes were not reported so far and we decided to explore the reactivity of **BrTAP** *via* Suzuki-Miyaura cross coupling to generate a series of original tetra-anthracenyl porphyrin derivatives (**Fig. IV-1**).

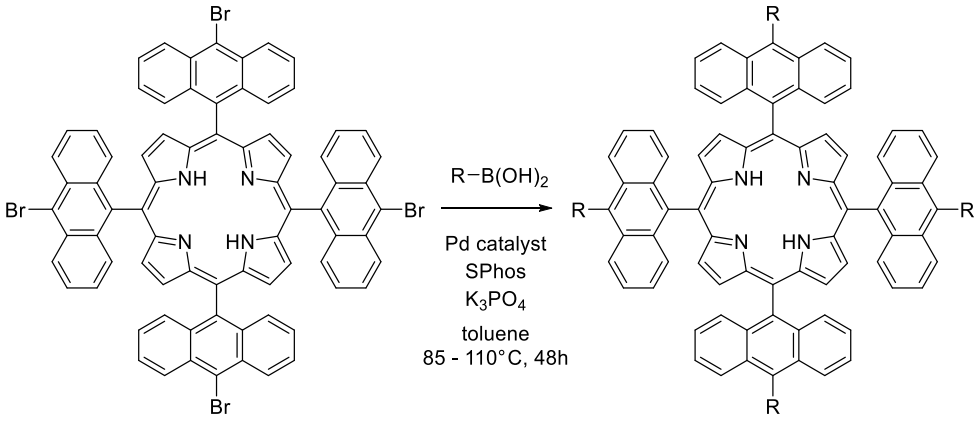

Fig. IV-1 General representation of the Suzuki-Miyaura cross coupling reaction on **BrTAP**.

Amongst the variety of coupling reactions developed on porphyrins,[5–7] we chose to apply Suzuki-Miyaura coupling for three reasons:

- to achieve exclusively heterocoupling reactions
- because the reaction has been successfully applied to functionalize anthracene derivatives with phenyl and a variety of PAHs[8–10]
- because a large number of aryl boronic acids are commercially available.

The Suzuki-Miyaura coupling reactions on **BrTAP** were investigated with a series of boronic acids ranging from sterically bulky PAHs, 9-anthracenyl-, 1-pyrenyl-, 1-naphthylboronic acid and electronically rich *vs* poor phenyl derivatives, phenyl-, *p*-methoxyphenyl-, *p*-tolyl-, *p*-nitrophenylboronic acids. The summary of the coupling reactions is presented in **Table IV-1**.

Entry	R -	Pd catalyst / T	Yield (%)	Label
1		Pd_2dba_3 / 85°C	69	**TPAP**
2	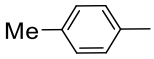	Pd_2dba_3 / 85°C	56	**TMPAP**
3	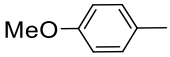	Pd_2dba_3 / 85°C	35	**TMPAP**
4	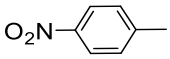	Pd_2dba_3 / 85°C	*a*	**TNPAP**
5	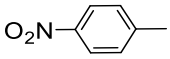	$Pd(OAc)_2$ / 110°C	*b*	**TNPAP**
6	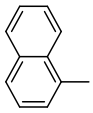	Pd_2dba_3 / 85°C	36	**TNAP**
7	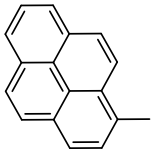	Pd_2dba_3 / 85°C	28	**TPyAP**
8	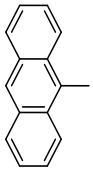	Pd_2dba_3 / 85°C	*b*	**TAAP**
9	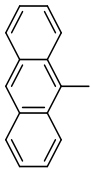	$Pd(OAc)_2$ / 110°C	*c*	**TAAP**

Table IV-1 Summary of the Suzuki-Miyaura coupling reactions performed on **BrTAP** with substituted-phenyl- and PAH-boronic acids; [a] starting material, [b] complex mixture of partially coupled and debrominated products, [c] successive debromination of the starting material with no evidence of coupling products.

We used as standard conditions, the conditions reported by the group of Schoefberger for the Suzuki-Miyaura coupling on corrole derivatives with Pd_2dba_3 in the presence of SPhos and K_3PO_4 in degassed toluene at 85°C (condition 1).[11] As suggested in the literature, multiple cross coupling reactions on porphyrins required longer reaction time than mono- or di-coupling reactions.[12] We decided to perform the reactions under standard conditions for 48h because the progress of the reactions was monitored by TLC and showed no further advancement after this reaction time. When no coupling

products were detected by MS analysis after this period under condition 1, we changed the palladium catalyst for $Pd(OAc)_2$ and increased the temperature up to 110°C (condition 2).

Under condition 1, reactions with phenyl-, *p*-tolyl- and *p*-methoxyphenylboronic acids succeeded in coupling four times with **BrTAP** and reached the target formations of 5,10,15,20-tetrakis(10-phenylanthracen-9-yl)porphyrin (**TPAP,** entry 1), 5,10,15,20-tetrakis(10-(p-tolyl)anthracen-9-yl)porphyrin (**TTAP,** entry 2) and 5,10,15,20-tetrakis(10-(4-methoxyphenyl)anthracen-9-yl)porphyrin (**TMPAP,** entry 3) as confirmed by HRMS analysis with the observation of isotopic signals at *m/z* 1318.5000, 1374.5577 and 1438.5428 respectively (**Fig. IV-2**). **TPAP**, **TTAP** and **TMPAP** were purified by chromatography column on silica gel using toluene/heptane with different ratios of solvents and recrystallisation from DCM/MeOH allowed the isolation of **TPAP**, **TTAP** and **TMPAP** respectively in 69%, 56% and 35% yields. In order to improve the yield, we increased the temperature of the reaction with *p*-methoxyphenylboronic acid to 110°C under condition 1 that led to the formation of a complex mixture, which was complicated to purify, of mono, bis, tris and tetracoupling products also containing debrominated species.

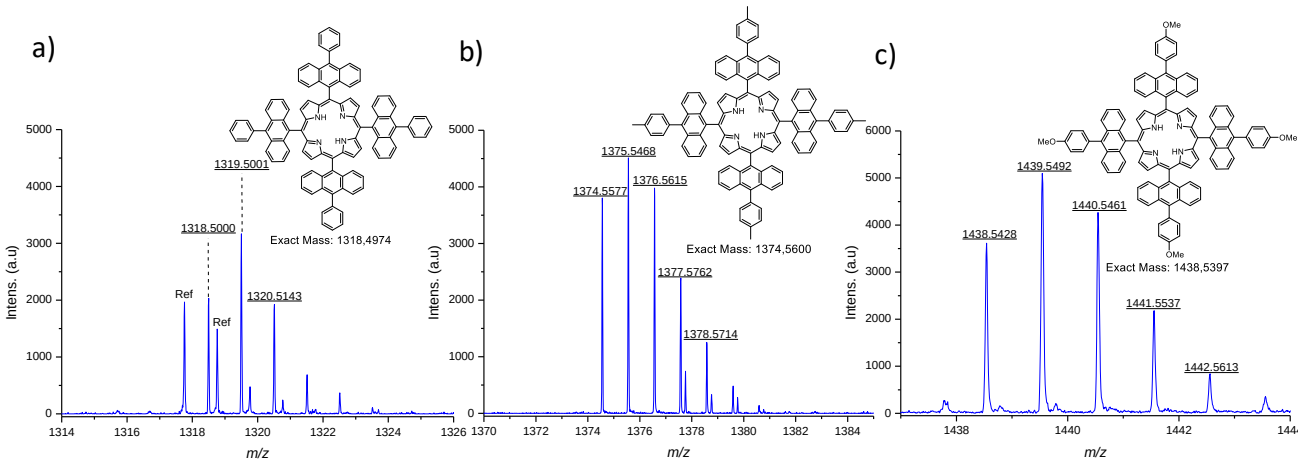

Fig. IV-2 HRMS spectra of compounds a) **TPAP**; b) **TTAP** and; c) **TMPAP**.

The reactions with *p*-nitrophenyl boronic acid under condition 1 led only to the detection by mass spectrometry of starting material with traces of debrominated derivatives (entry 4). Under condition 2, the formation of a mixture of partially coupled and debrominated porphyrins also containing the target 5,10,15,20-tetrakis(10-(4-nitrophenyl)anthracen-9-yl)porphyrin **TNPAP** was observed by MS analysis (entry 5). Because of the formation of a complex mixture of porphyrins that was difficult to separate, **TNPAP** was not isolated.

Concerning the coupling reactions with PAHs, 1-naphthalene- and 1-pyreneboronic acids were successfully coupled on **BrTAP** under condition 1 and the formation of 5,10,15,20-tetrakis(10-(naphthalen-1-yl)anthracen-9-yl)porphyrin (**TNAP,** entry 6) and 5,10,15,20-tetrakis(10-(pyren-1-

yl)anthracen-9-yl)porphyrin (**TPyAP,** entry 7) were confirmed by HRMS analysis with the observation of isotopic signatures at *m/z* 1518.5589 and 1814.6197 respectively (**Fig. IV-3**). After purifications with chromatography techniques and precipitation in MeOH, **TNAP** and **TPyAP** were respectively isolated in 36% and 28% yields.

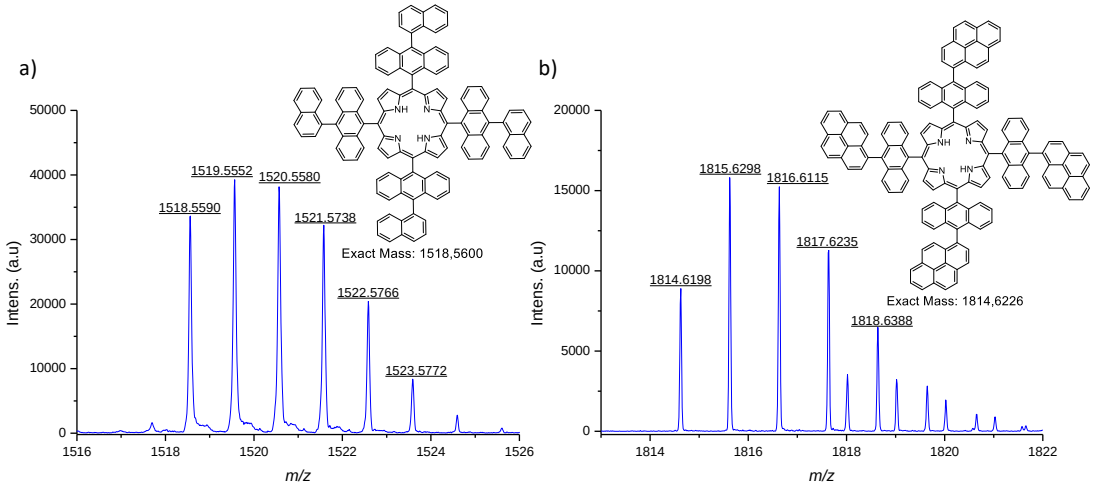

Fig. IV-3 HRMS spectra of compounds a) **TNAP** and; b) **TPyAP**.

Under condition 1, the reaction between **BrTAP** and 9-anthracene boronic acid led to the formation of the tetra-coupled target compound 5,10,15,20-tetra([9,9'-bianthracen]-10-yl)porphyrin (**TAAP)** in a complex mixture of partially coupled and debrominated porphyrins (entry 8) detected by MS analysis (**Fig. IV-4**). Because of the complexity of the mixture, the target **TAAP** could not be isolated. When the reaction was performed at 110°C (condition 2), only debromination of the starting material with no evidences of coupling products were observed by MS analysis (entry 9).

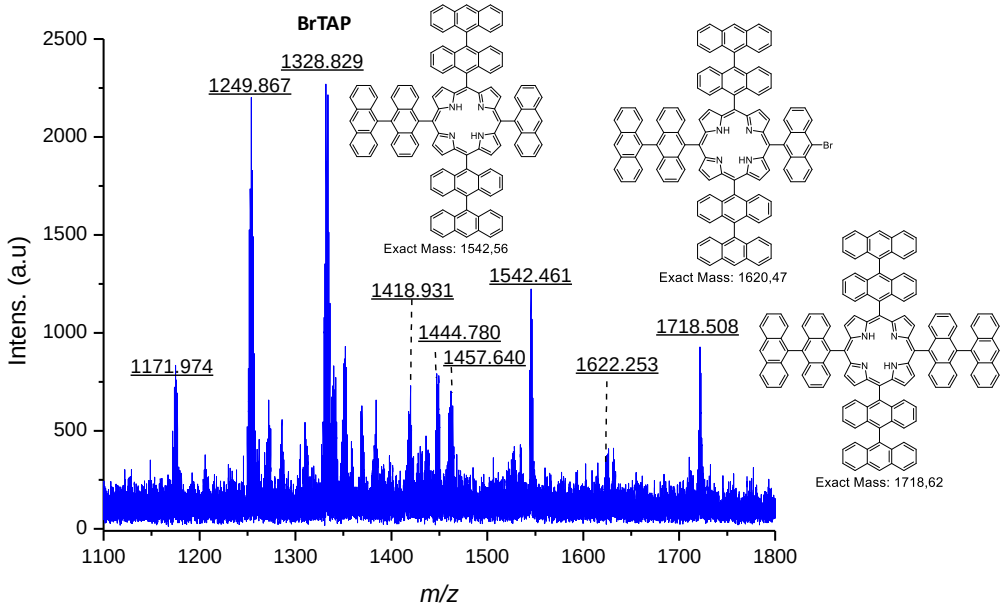

Fig. IV-4 MS spectrum of the product of reaction between **BrTAP** and 9-anthracene boronic acid under condition 1.

As mentioned in the literature, the efficiency of the Suzuki-Miyaura coupling reaction depends on the electron donating/withdrawing behaviours of the aryl boronic acids.[13,14] Generally, the presence of electron donating groups have a limited impact on the reactions; it was confirmed for **TPAP** and **TTAP** for which the yields are of *ca.* 69 and 56%, respectively. However, for **TMPAP**, the yield dropped to 35% yield and we noticed that **TMPAP** exhibited a very low solubility in all common solvents. We might think that the completion of the reaction was limited by the decrease of solubility during the formation of the polyadducts, which affected the yield of the reaction. This assumption was also supported by the fact that the reaction with *p*-methoxyphenylboronic acid gave higher amounts of bis- and tris-functionalised by-products compared to the other reactions. Increasing the reaction time and/or the temperature enhanced the dehalogenation process, recognized as a side reaction, and the formation of a complex mixture of partially coupled and debrominated porphyrins was observed. In addition, the presence of a strong electron withdrawing group (*p*-nitro) also induced a competition between the coupling reaction and the debromination process (entries 4 and 5).

In the literature, it was reported that the yields of Suzuki-Miyaura coupling reactions between bromoanthracene and phenyl or more sterically hindered PAHs decreased with the steric hindrance. Indeed, the yield of the mono-coupling on bromoanthracene with phenylboronic acid reached 50-80% yield[10,15] whereas it dropped to 65-75% for pyrenyl-,[10,16] 55% for naphthyl-,[10] and to 20% for anthracenylboronic acids.[9] We believe that the reactivity of the 9 position of the anthracene moiety would perturb the efficiency of the coupling reaction. In addition, the important steric hindrance in PAHs might limit the efficiency of the oxidative addition and/or the transmetallation and might thus lower the yield of the reaction. Finally, it appears that the process of dehalogenation limits the Suzuki-Miyaura couplings on **BrTAP**. This side reaction is well-known in Suzuki-Miyaura coupling reported in the literature and depends to some extent on the substrates and the conditions used.[17] In particular, it was suggested that the rate of the dehalogenation depended on the oxidative addition step of arylhalide.[18] Considering the yields reported for mono-coupling reactions with bromoanthracene in the literature, the tetra-coupling on **BrTAP** with phenyl, pyrene and naphthalene derivatives gave reasonable yields (entries 1, 6, 7).

TPAP, **TTAP**, **TMPAP**, **TNAP** and **TPyAP** were found to be slightly soluble in common solvents and were characterized by HRMS, UV-visible spectroscopy and ^{1}H NMR in $C_2D_2Cl_4$ at 333K (see Experimental part). However, we were not able to record comprehensive ^{13}C NMR spectra. The following section is dedicated to the optical characterization of the compounds.

IV. 2. Optical characterisation

The optical properties of the porphyrin derivatives containing phenyl, naphthyl, anthracenyl moieties (**TPAP**, **TNAP** and **TPyAP** respectively) were studied by absorption and fluorescence spectroscopies (**Fig. IV-5**).

IV. 2.1. Absorption

The absorption spectra of **TPAP**, **TNAP** and **TPyAP** exhibited the typical features of the free-base porphyrin (*i.e.* a Soret and four Q bands) and the anthracene moieties. In the spectra of **TNAP** and **TPyAP**, new absorption bands arising from the naphthalene and the pyrene moieties were discernible on the UV-Vis spectra (**Fig. IV-5**, b-c). The spectra of **TPAP**, **TNAP** and **TPyAP** did not present significant shifts of the absorption peaks compared to the free PAH and starting **BrTAP** and indicating that attaching the PAHs to the anthracenes did not affect the Franck-Condon states of these compounds and suggesting no significant charge transfer between subunits in the ground state.

IV. 2.2. Fluorescence

The photoexcitation of **TPAP** and **TNAP** at either the maximum absorption of the external aromatic moieties, respectively phenyl (λ_{max} = 250 nm) and naphthalene (λ_{max} = 329 nm) or at the Soret of the porphyrin (λ_{max} = 429 nm) led only to the observation of the fluorescence signals of the porphyrin at 650 and 720 nm without the observation of the fluorescence of PAHs in the UV or near visible region (**Fig. IV-5**, a-b). In contrast, the photoexcitation of the pyrenyl units (λ_{max} = 342 nm) of **TPyAP** led to the fluorescence of the porphyrin subunit and to a broad signal of fluorescence centred at 484 nm that was attributed to pyrene excimers as reported in the literature (**Fig. IV-5**, c).[19,20] This pyrene excimer signal was likely due to interactions between pyrenes of neighbouring molecules in solution.

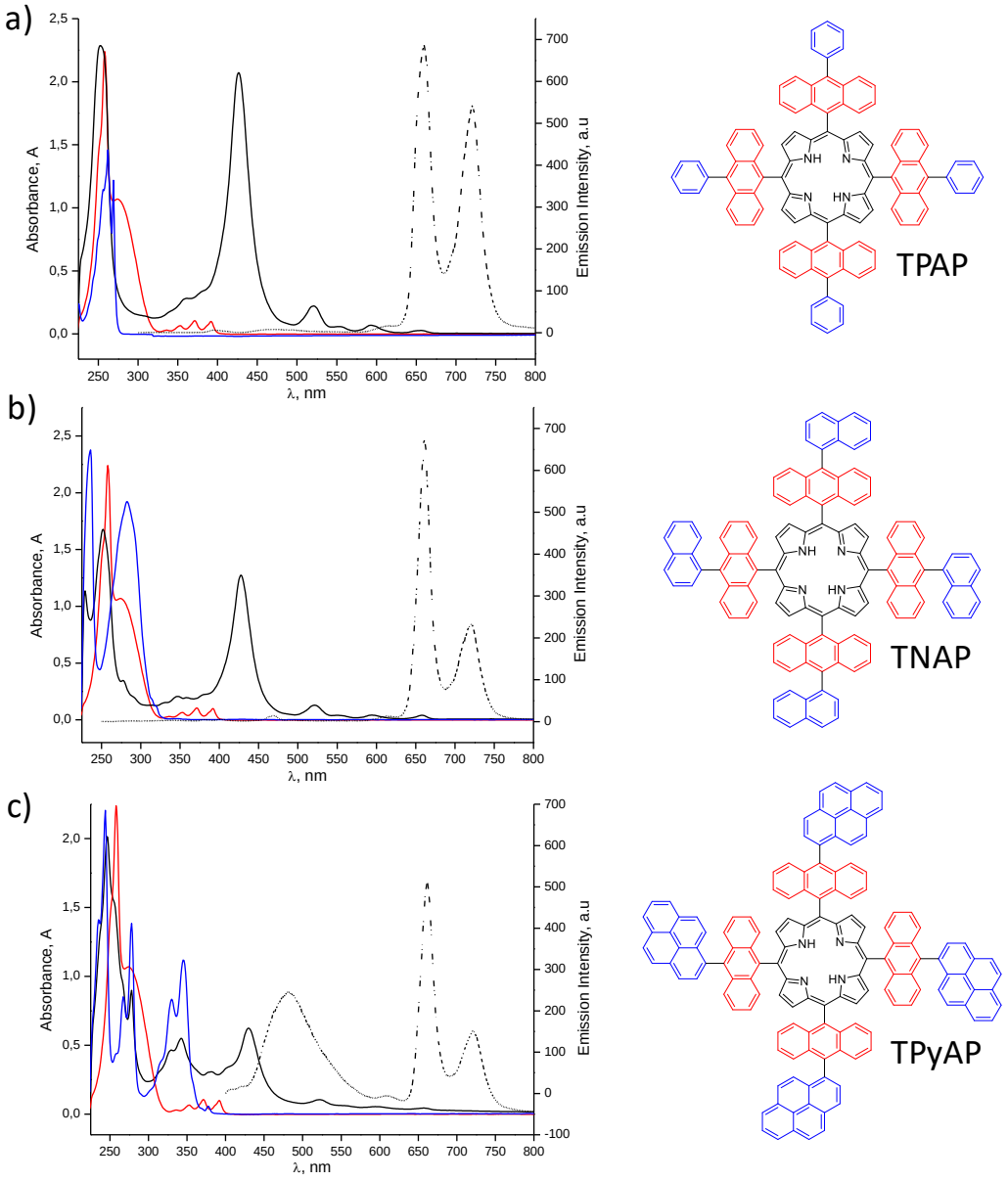

Fig. IV-5 Absorption and fluorescence spectra (respectively solid and dash lines) in DCM of a) **TPAP** (λ_{exc} = 250 nm); b) **TNAP** (λ_{exc} = 329 nm); c) **TPyAP** (λ_{exc} = 342 nm) superimposed with absorption of reference 9-bromoanthracene (red solid lines) and references pyrene, naphthalene and toluene (blue solid lines).

IV. 2.3. Spectral overlaps and photoluminescence excitation

The extinction of the luminescence of the photoexcited PAHs led us to consider the possibility of energy transfers between each moiety. Indeed, the energy transfer between anthracene moieties and the core of a porphyrin was observed by Sudha *et al.*[21] and energy transfers in phenyl-anthracene (PA) or diphenyl-anthracene (DPA) systems were also reported in the literature.[11,22,23]

In order to investigate the transition responsible for the emission at 720 nm, we first examined the spectral overlap of the absorption and emission signals of each subunits of the molecules and we observed that appreciable overlaps existed between each moiety (**Fig. IV-6**).

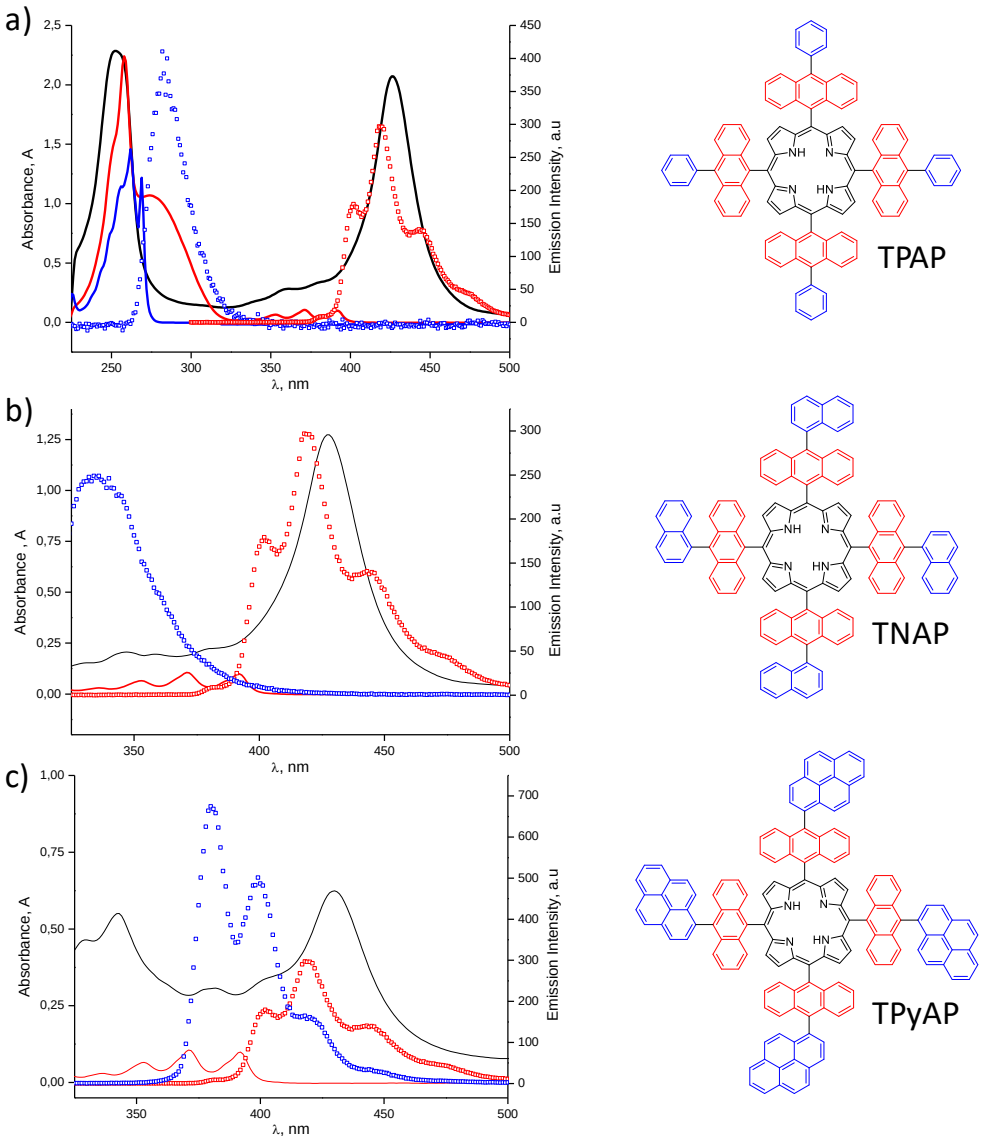

Fig. IV-6 Spectral overlap in DCM of the emission spectra (dash lines) of free external PAHs (toluene/naphthalene/pyrene, (blue) and anthracene (red)) and absorption spectrum (solid lines) of anthracene (red) and a) **TPAP**; b) **TNAP** and; c) **TPyAP** (black).

We recorded the photoluminescence excitation (PLE) spectra of **TPAP**, **TNAP** and **TPyAP** for the emission at 720 nm (**Fig. IV-7**). Similar spectra were found when the emission at 660 nm was monitored. The superimposition of PLE with the absorption spectra of each subunit (blue for the external PAH, red for the anthracene moiety and black for the porphyrin core), allowed the identification of the fingerprints of each molecule substituents with different intensities according to the different participations to the luminescence and confirmed the connection of intrinsic energy levels between the moieties.

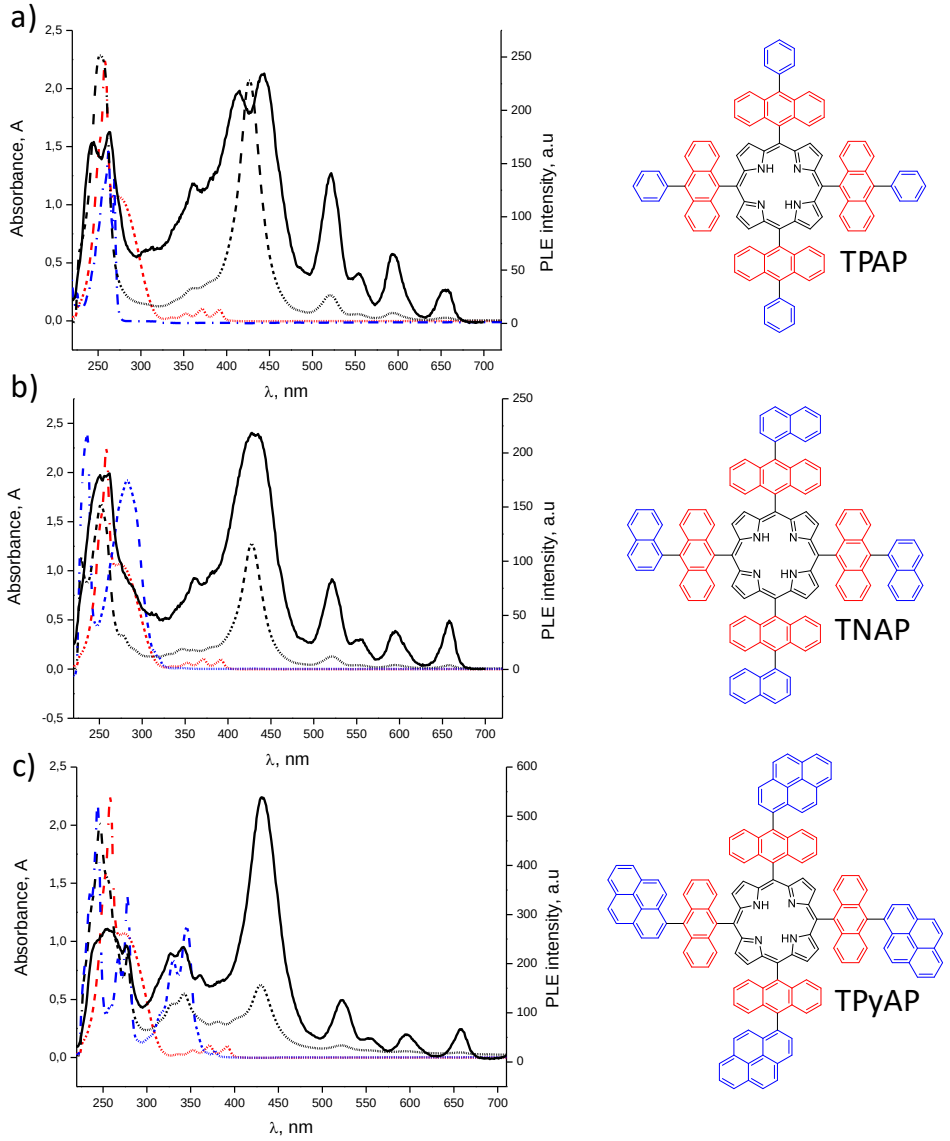

Fig. IV-7 PLE spectra (black solid lines, λ_{exc} = 720 nm) in DCM of a) **TPAP**; b) **TNAP**; c) **TPyAP**; superimposed with the absorption spectra (dash lines) of reference external PAHs (toluene/naphthalene/pyrene, blue), 9-bromoanthracene (red) and corresponding **TPAP**, **TNAP**, **TPyAP** (black).

IV. 2.4. Density Functional Therory calculations

Density Functional Theory (DFT) calculations were performed on **TPAP**, **TNAP** and **TPyAP** to visualize the localization of the electronic density and get insight on the possible energy transfers. The DFT calculations were carried out by Yannick. J. Dappe (SPEC) from the CEA-Saclay. For each molecule, the geometry was optimized at 0 K until the forces went below 0.1 eV/Å and the isoelectronic density of states (isodos) were calculated at energies corresponding to HOMO-1, HOMO, LUMO and LUMO+1. These isodos are presented in **Fig. IV-8** with the corresponding

atomic structure for each molecule. The atomic structures clearly showed a perpendicular geometry between the external PAHs and the anthracene subunits and between the anthracene subunits and the porphyrin core with angles close to 90°. Consequently, one can observe in the isodos an important localization of the electronic density in the porphyrin core only. Hence, the perpendicular geometry suggested that there was no electronic delocalization between each part of the molecules, making those independent constituents, which is in agreement with the definition of supramolecular entities proposed by Balzani.[24]

All of these arguments regarding the quenching of PAH luminescence, overlapping, PLE and DFT calculations suggested independent behaviors of subunits making possible an energy transfer from the external PAH moieties to the porphyrin core of **TPAP**, **TNAP** and **TPyAP**. However, only transient absorption/emission spectroscopy would definitely confirm this hypothesis.

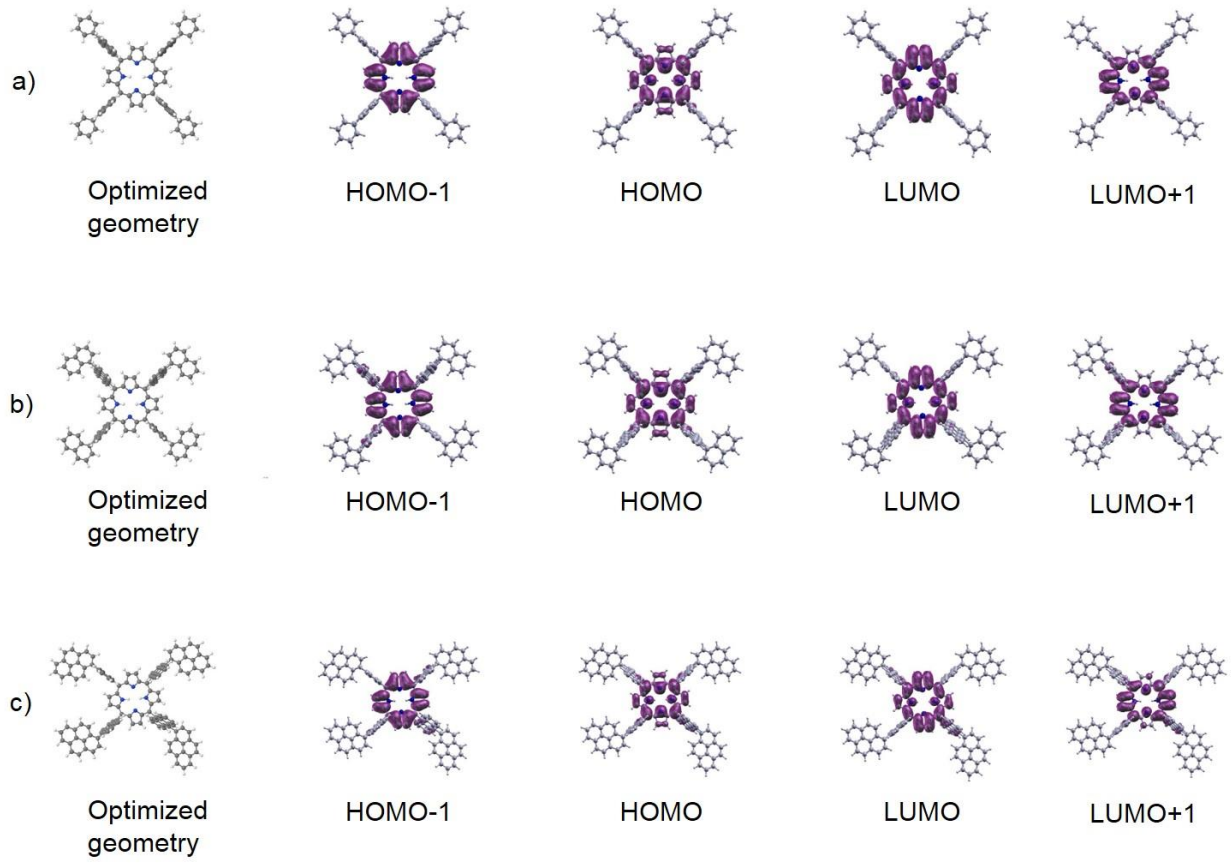

Fig. IV-8 Optimized geometry and HOMOs and LUMOs of compounds a) **TPAP**; b) **TNAP** and; c) **TPyAP**.

IV. 3. Conclusion and perspectives

To conclude, we demonstrated that the four anthracenes at the periphery of **BrTAP** can be successfully functionalized *via* Suzuki-Miyaura cross coupling reactions with phenyl-, tolyl-, p-methoxyphenyl-, napthyl- and pyrenyl boronic acids to generate a series of original tetra-anthracenyl porphyrin-based molecules respectively called **TPAP**, **TTAP**, **TMPAP**, **TNAP**, **TPyAP**. The coupling reactions with *p*-nitrophenyl- and anthracenyl boronic acids formed tetranitrophenylanthracenylporphyrin (**TNPAP**) and tetrabisanthracenylporphyrin (**TAAP**) that were detected by mass spectrometry in mixtures containing a variety of coupling products and debrominated species. Because of the complexity of the mixtures, **TNPAP** and **TAAP** could not be separated. The optical properties of the tetra-anthracenyl porphyrin derivatives with phenyls (**TPAP**), napthyls (**TNAP**) and pyrenyl subunits (**TPyAP**) were investigated. The emission spectra of **TPAP**, **TNAP** and **TPyAP** showed almost exclusively the fluorescence of the porphyrin core in the visible region with the extinction of the fluorescence of the PAHs in the UV or near visible regions, except for **TPyAP**, in which the emission of a pyrene exciplex was discernable. Arguments regarding the quenching of the luminescence of PAHs, the absorption and emission overlaps, the PLE and DFT calculations are in agreement with the hypothesis of energy transfer from the external PAHs to the porphyrin core. However, only transient absorption/emission spectroscopy would definitely confirm this hypothesis.

Finally, we showed that **BrTAP** constitutes a valuable scaffold for the fabrication of functional derivatives that may open the way toward the use of tetra-anthracenyl porphyrins as a versatile building block for the construction of more complex structures. We can imagine testing the reactivity of **BrTAP** *via* other types of coupling reactions and we tried to form a MOF by the polymerisation of **BrTAP** *via* a Yamamoto-type Ullmann coupling reaction. Unfortunately, we only observed the debromination of the starting material in the mass spectrum and we supposed that the size of anthracene moieties prevented the coupling reaction between each other. As an alternative, we can imagine that a Sonogashira coupling reaction would convert the bromine atoms of **BrTAP** into alkynes to allow the use of chemical reactions developed on triple bonds and generate other supramolecular species containing **TAP** derivatives.

IV. 4. References

(1) Volz, H.; Schaeffer, H. Mesosubstituted Porphyrins. III. 5,10,15,20-Tetraanthracenylporphyrin. *Chemiker-Zeitung* **1985**, *109*, 308–309.

(2) Sooambar, C.; Troiani, V.; Bruno, C.; Marcaccio, M.; Paolucci, F.; Listorti, A.; Belbakra, A.; Armaroli, N.; Magistrato, A.; De Zorzi, R.; et al. Synthesis, Photophysical, Electrochemical, and Electrochemiluminescent Properties of 5,15-Bis(9-Anthracenyl)Porphyrin Derivatives. *Org. Biomol. Chem.* **2009**, *7*, 2402–2413.

(3) Davis, N. K. S.; Thompson, A. L.; Anderson, H. L. Bis-Anthracene Fused Porphyrins : Synthesis , Crystal Structure , and Near-IR Absorption. *Org. Lett.* **2010**, *12*, 2124–2127.

(4) Davis, M.; Senge, M. O.; Locos, O. B. Anthracenylporphyrins. *Z. Naturforsch, B* **2010**, *65*, 1472–1484.

(5) Aratani, N.; Osuka, A. Exploration of Giant Functional Porphyrin Arrays. *Bull. Chem. Soc. Jpn.* **2015**, *88*, 1–27.

(6) Setsune, J. Palladium Chemistry in Recent Porphyrin Research. *J. Porphyr. Phthalocyanines* **2004**, *8*, 93–102.

(7) Cavaleiro, J. A. S.; Tomé, A. C.; Neves, M. G. P. M. S. 9 Meso -Tetraarylporphyrin Derivatives: New Synthetic Methodologies. In *Handbook of Porphyrin Science*; Kadish, K. M., Smith, K. M., Guilard, R., Eds.; World Scientific: Singapore, 2010; pp 193–294.

(8) Kim, S. K.; Yang, B.; Ma, Y.; Lee, J. H.; Park, J. W. Exceedingly Efficient Deep-Blue Electroluminescence from New Anthracenes Obtained Using Rational Molecular Design. *J. Mater. Chem.* **2008**, *18*, 3376–3384.

(9) Jacobse, P. H.; van den Hoogenband, A.; Moret, M. E.; Klein Gebbink, R. J. M.; Swart, I. Aryl Radical Geometry Determines Nanographene Formation on Au(111). *Angew. Chem. Int. Ed.* **2016**, *55*, 13052–13055.

(10) Tao, S.; Zhou, Y.; Lee, C.-S.; Lee, S.-T.; Huang, D.; Zhang, X. Highly Efficient Nondoped Blue Organic Light-Emitting Diodes Based on Anthracene-Triphenylamine Derivatives. *J. Phys. Chem. C* **2008**, *112*, 14603–14606.

(11) König, M.; Reith, L. M.; Monkowius, U.; Knör, G.; Bretterbauer, K.; Schoefberger, W. Suzuki-Miyaura Cross-Coupling Reaction on Copper-Trans-A2B Corroles with Excellent Functional Group Tolerance. *Tetrahedron* **2011**, *67*, 4243–4252.

(12) Zhou, X.; Tse, M. K.; Wan, T. S. M.; Chan, K. S. Synthesis of Beta-Mono-, Tetra-, and Octasubstituted Sterically Bulky Porphyrins via Suzuki Cross Coupling. *J. Org. Chem.* **1996**, *61*, 3590–3593.

(13) Venkata Rao, K.; Haldar, R.; Maji, T. K.; George, S. J. Dynamic, Conjugated Microporous Polymers: Visible Light Harvesting via Guest-Responsive Reversible Swelling. *Phys. Chem. Chem. Phys.* **2016**, *18*, 156–163.

(14) Yuan, Y.; Sun, F.; Ren, H.; Jing, X.; Wang, W.; Ma, H.; Zhao, H.; Zhu, G. Targeted Synthesis of a Porous Aromatic Framework with a High Adsorption Capacity for Organic Molecules. *J. Mater. Chem.* **2011**, *21*, 13498–13502.

(15) Lee, H.; Kim, B.; Kim, S.; Kim, J.; Lee, J.; Shin, H.; Lee, J. H.; Park, J. Synthesis and Electroluminescence Properties of Highly Efficient Dual Core Chromophores with Side Groups for Blue Emission. *J. Mater. Chem. C* **2014**, *2*, 4737–4747.

(16) Baumgarten, M.; Gherghel, L.; Friedrich, J.; Jurczok, M.; Rettig, W. Electronic Decoupling in Ground and Excited States of Asymmetric Biaryls. *J. Phys. Chem. A* **2000**, *104*, 1130–1140.

(17) Navarro, O.; Kaur, H.; Mahjoor, P.; Nolan, S. P. Cross-Coupling and Dehalogenation Reactions Catalyzed by (N-Heterocyclic Carbene)Pd(Allyl)Cl Complexes. *J. Org. Chem.* **2004**, *69*, 3173–3180.

(18) Jedinák, L.; Zátopková, R.; Zemánková, H.; Šustková, A.; Cankař, P. The Suzuki-Miyaura Cross-Coupling Reaction of Halogenated Aminopyrazoles: Method Development, Scope, and Mechanism of Dehalogenation

Side Reaction. *J. Org. Chem.* **2017**, *82*, 157–169.

(19) Xu, Z.; Singh, N. J.; Lim, J.; Pan, J.; Ha, N. K.; Park, S.; Kim, K. S.; Yoon, J. Unique Sandwich Stacking of Pyrene-Adenine-Pyrene for Selective and Ratiometric Fluorescent Sensing of ATP at Physiological PH. *J. Am. Chem. Soc.* **2009**, *131*, 15528–15533.

(20) Huang, J.; Wu, Y.; Chen, Y.; Zhu, Z.; Yang, X.; Yang, C. J.; Wang, K.; Tan, W. Pyrene-Excimer Probes Based on the Hybridization Chain Reaction for the Detection of Nucleic Acids in Complex Biological Fluids. *Angew. Chem. Int. Ed.* **2011**, *50*, 401–404.

(21) Sudha, K.; Sundharamurthi, S.; Karthikaikumar, S.; Abinaya, K.; Kalimuthu, P. Switching of Förster to Dexter Mechanism of Short-Range Energy Transfer in *Meso* -Anthrylporphyrin. *J. Phys. Chem. C* **2017**, *121*, 5941–5948.

(22) Iida, A.; Yamaguchi, S. Intense Solid-State Blue Emission with a Small Stokes' Shift: π-Stacking Protection of the Diphenylanthracene Skeleton. *Chem. Commun.* **2009**, 3002–3004.

(23) Xu, K.; Zhao, J.; Escudero, D.; Mahmood, Z.; Jacquemin, D. Controlling Triplet-Triplet Annihilation Upconversion by Tuning the PET in Aminomethyleneanthracene Derivatives. *J. Phys. Chem. C* **2015**, *119*, 23801–23812.

(24) Sauvage, J.; Collin, J.; Chambron, J.; Guillerez, S.; Coudret, C.; Balzani, V.; Barigelletti, F.; Cola, L. De; Flamigni, L. Ruthenlum (II) and Osmium (II) Bis (Terpyridine) Complexes in Covalently-Linked Multicomponent Systems : Synthesis , Electrochemical Behavior , Absorption Spectra , and Photochemical and Photophysical Properties. *Chem. Rev.* **1994**, *94*, 993–1019.

Chapter V. Conclusion and perspectives

Chapter V. Conclusion and perspectives

In this manuscript, we showed that porphyrins are a class of compounds particularly suitable as molecular building blocks for the fabrication of supramolecular assemblies. On the other hand, the modification of the optical properties of porphyrins was also presented by the formation of π-extended porphyrins with exceptional optical properties in NIR region. These π-extended porphyrins are formed in literature by the fusion of PAHs substituted on their *meso*-positions *via* the Scholl reaction. The fabrication and control of dopant in atomically precise nanostructures of graphene like GQDs, GNRs and GNMs is a hot topic of research that aims to control the optoelectronic properties and particularly the bandgap opening of the nanomaterials. In this context, porphyrin derivatives with a controlled content of nitrogen are attractive compounds that can be used either as building blocks for the bottom-up fabrication of nitrogen-doped GNRs and GNMs or as nitrogen-doped GQDs by the formation of π-extended porphyrins. Considering that a variety of metals can be inserted into the cavity of porphyrins, metallo-porphyrins are also appealing compounds to form graphene-like nanostructures and can potentially introduce new redox, magnetic and optoelectronic properties. During this Ph.D., we developed a series of halogenated anthracenylporphyrin-based building blocks and investigated their assemblies on surface. We also studied the fusion of *meso*-substituted anthracenyl-, pyrenyl- and naphthylporphyrins *via* pyrolysis to achieve the formation of π-extended porphyrin by a method other than the restrictive Scholl reaction in solution.

In chapter II, we reported on the synthesis of halogenated anthracenylporphyrin-based building blocks we called **BrTAP**, **ClTAP, ITAP, BrDTAP** and **BrBAP.** Although **BrTAP**, **ClTAP** and **BrBAP** were successfully isolated and characterized with common analytical tools and we found that **ITAP** was unfortunately unstable at ambient conditions. We also succeeded in the synthesis of **BrDTAP** and its characterization by ^{1}H NMR is still in progress in our group to confirm the structure of the product. We investigated the deposition of **BrTAP** on different surfaces with direct visualization of assemblies using STM. In most cases, a strong intermolecular interaction due to π-stacking between twisted anthracenes led to 1D organizations with edge-on configuration of porphyrins on the surface. Only the deposition of **BrTAP** on Pd (111) led to the formation of a 2D organization with flat-lying adsorption; however, during annealing and debromination, the phase was modified and the edge-on configuration was restored. The study of deposition of **BrBAP** on Cu (110) and Cu (111) at r.t did not lead to stable adsorption of precursors and the deposition at 250°C and 400°C led to the formation of assemblies with undefined orientations. We explained the results by a low molecule-substrate interaction of the surfaces of Cu at r.t and to the strong reactivity at high temperatures that did not allowed a sequential control of the surface-assisted reactions.

In chapter III, a series of porphyrins substituted in *meso*-position with naphthalene (**ZnSNP**), pyrene (**ZnSPP** and **ZnTPyP**) and anthracene (**ZnSAP**, **ZnBAP** and **ZnTAP**) were synthetised and used as

precursors to investigate the formation of π-extended porphyrin *via* the method of pyrolysis. An experimental setup for the pyrolysis was designed and validated by reproduction of the fusion of **ZnTPyP**. We concluded from the pyrolysis of **ZnTAP** and **ZnBAP** that the multiple fusion of anthracenes was difficult to achieve and faced with issues of non-liquefaction, sublimation and severe degradation of the precursors. We succeeded in the thermal fusions at 510-515°C of the mono-anthracene, naphthalene and pyrene moieties of **ZnSAP**, **ZnSNP**, **ZnSPP**. **Fused ZnSPP** and **fused ZnSAP** were successfully isolated and the purification of **fused ZnSNP** was found to be more complicated because of the small differences between the fused naphthylporphyrin and its derivatives. In addition, we were able to remove zinc from the cavity of **fused ZnSPP** using an acid treatment and afforded **fused SPP** as π-extended porphyrin without the presence of any metals or activating groups on the PAH moiety. As an alternative, we believe that the formation of π-extended porphyrins could be achieved by the thermal fusion of precursors in gas phase *via* the method of Flash Vacuum Pyrolysis (FVP) with the control of the two temperatures of sublimation and pyrolysis independently, and of the flow of precursors in the apparatus.

In chapter IV, we demonstrated that the four anthracenes at the periphery of **BrTAP** can be successfully functionalized *via* Suzuki-Miyaura cross coupling reactions with phenyl-, tolyl-, p-methoxyphenyl-, napthyl- and pyrenyl boronic acids to generate a series of original tetra-anthracenyl porphyrin-based molecules respectively called **TPAP**, **TTAP**, **TMPAP**, **TNAP**, **TPyAP**. The coupling-reactions with *p*-nitrophenyl- and anthracenyl boronic acids formed tetranitrophenylanthracenylporphyrin (**TNPAP**) and tetrabisanthracenylporphyrin (**TAAP**) that were detected by mass spectrometry in mixtures containing variety of coupling products and debrominated species. Because of the complexity of the mixtures, **TNPAP** and **TAAP** could not be separated. The optical characterizations of the tetra-anthracenyl porphyrin derivatives with phenyls (**TPAP**), napthyls (**TNAP**) and pyrenyl subunits (**TPyAP**) were investigated. We noticed that the emission spectra of **TPAP**, **TNAP** and **TPyAP** showed almost exclusively the fluorescence of the porphyrin core in the visible region with the extinction of the fluorescence of the PAHs in the UV or near visible regions, excepted for **TPyAP** in which the emission of a pyrene exciplex was discernable. Arguments regarding the quenching of the luminescence of PAHs, the absorption and emission overlaps, the PLE and DFT calculations are in agreement with the hypothesis of energy transfer from the external PAHs to the porphyrin core. However, only transient absorption/emission spectroscopy would definitely confirm this hypothesis. Finally, we showed that **BrTAP** constitutes a valuable scaffold for the fabrication of functional derivatives that may open the way toward the use of tetra-anthracenyl porphyrins as a versatile building block for the construction of more complex structures. We can imagine testing the reactivity of **BrTAP** *via* other types of coupling reactions. We tested the

polymerisation of **BrTAP** *via* Yamamoto-type Ullmann coupling that only led to the debromination of the starting material detected on the mass spectrum. The large size of the anthracene moiety and its low reactivity were supposed to limit the coupling reaction. As an alternative, we can imagine that Sonogashira coupling reaction would convert the bromine atoms of **BrTAP** into alkynes to allow the use of chemical reactions developed on triple bonds and generate other supramolecular species containing **TAP** derivatives.

For the future, we strongly believe that the study of deposition of **BrDTAP** on a surface would lead to a completely different assembly because of the perturbation of the intermolecular interactions due to the additional row of anthracenes on the porphyrin-based building block. Indeed, according to the calculated structure of **BrDTAP** (**Fig. II-35**, a), the two rows of anthracene were almost perpendicular to each other. This orientation could severely perturb the π-stacking interaction. On the other hand, the second row of anthracene was nearly parallel to the macrocyclic plane of the porphyrin and could favour a flat-lying absorption with substrates. This perpendicular arrangement between two bonded anthracenes was exploited by the groups of Mullen and Fasel to afford the desired adsorption of **DBBA** on Au (111) and to successfully form the first GNR synthesised *via* a bottom-up approach on a surface (see ref 31, chapter II).

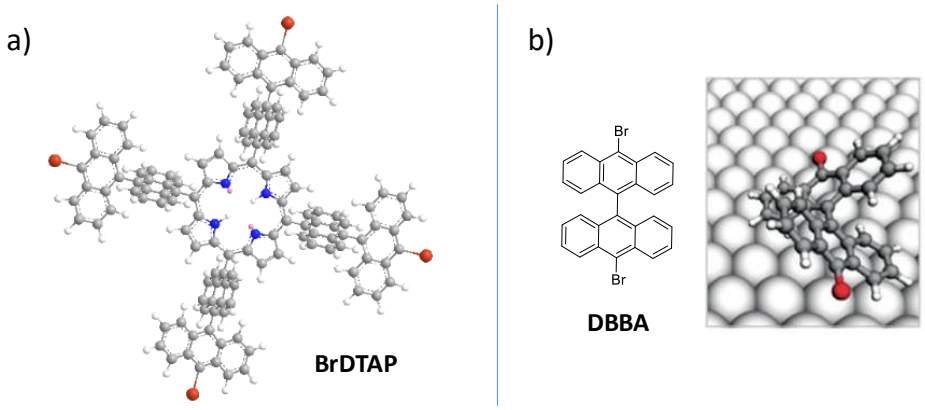

Fig. V-1 a) Calculated 3D model of **BrDTAP**; b) chemical structure and illustration of the perpendicular arrangement the two adjacent anthracenes of **DBBA** on surface.

Considering that no study related to the cyclodehydrogenation on surface of PAHs on porphyrins have been reported so far, it would be interesting to study the deposition of **ClTAP** on Pd (111) to investigate the cyclodehydrogenation reaction between anthracenes and porphyrins by reversing the sequential dehalogenation and cyclodehydrogenation temperatures. By replacing bromines by chlorines, Jacobse *et al.* (see ref 29, chapter II) found that the intramolecular cyclodehydrogenation of 10,10'-dichloro-9,9'-bianthryl (**DCBA**) occurred at a lower temperature than that required for the dehalogenative polymerisation and led to disordered polybisanthracene (**Fig. V-2**). Because we observed a flat-lying adsorption of **BrTAP** on Pd (111), we strongly think that **ClTAP** will be

adsorbed in a similar way on Pd (111) and the study of its deposition may allow the investigation of the cyclodehydrogenation between anthracenes and porphyrins if the cyclodehydrogenation occurs prior to the polymerisation on the surface.

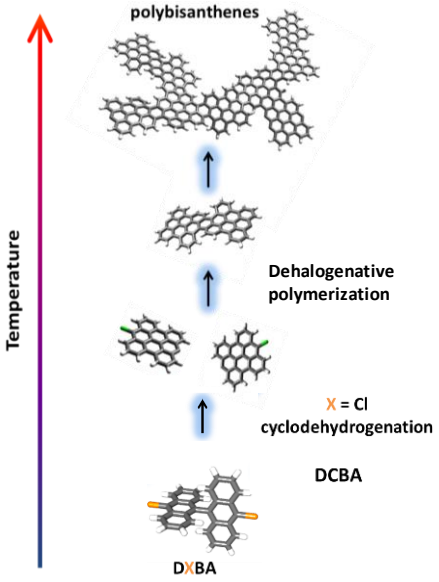

Fig. V-2 Illustration of the formation of polybisanthracenes achieved by "on-surface" synthesis of 10,10'-dichloro-9,9'-bianthryl (**DCBA**) on Au (111). The resulting polymer was disordered because of the inversion of the activation temperature of dehalogenation and cyclodehydrogenation reactions.

In addition, it would be interesting to investigate the deposition of **BrBAP** at r.t on Pd (111) to achieve the formation of **GNR-1** on the surface. The high reactivity of the surface of Pd (111) is expected to enhance the interaction between **BrBAP** and the substrate, and could potentially lead to a stable adsorption of precursors at r.t. Subsequent annealing the surface would allow the sequential activation of surface-assisted reactions leading to the formation of controlled structures on the surface. To expand the concept of the additional row of anthracenes on porphyrin-based building blocks, we can also imagine using the structure of 5,15-bis(10'-bromo-[9,9'-bianthracen]-10-yl)-10,20-diphenylporphyrin (**BrDBAP**), which can be seen as an extended version of **BrBAP**, to achieve the formation of **GNR-2** on surface with a decrease of nitrogen content (**Fig. V-3**). A comparative study of the electronic properties of **GNR-1** and **GNR-2** would provide a reliable comprehension of the impact of nitrogen doping.

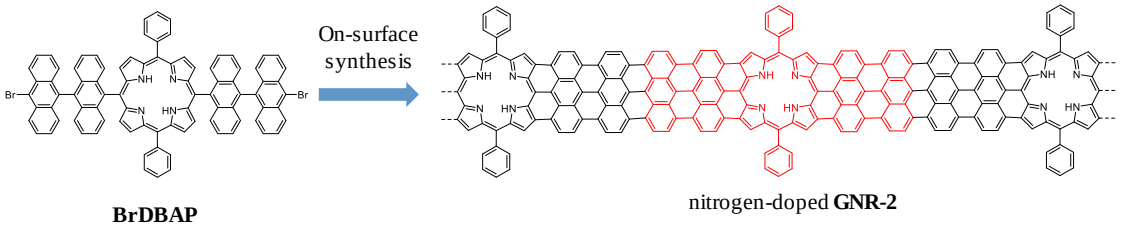

Fig. V-3 Structure of nitrogen-doped **GNR-2** (right) from the on-surface synthesis of 5,15-bis(10'-bromo-[9,9'-bianthracen]-10-yl)-10,20-diphenylporphyrin (**BrDBAP**, left).

Finally, apart from porphyrins, we imagined the structures of the polyphenylene derivatives **P1** and **P2** that could be used as symmetric building blocks to form on surface **GNM-3** and its structurally analogue nitrogen-doped **GNM-4** (**Fig. V-4**). The study of these two GNMs that only differ from the presence of nitrogen in structures would provide a reliable comprehension of the impact of the chemical variation on the electronic properties of GNMs.

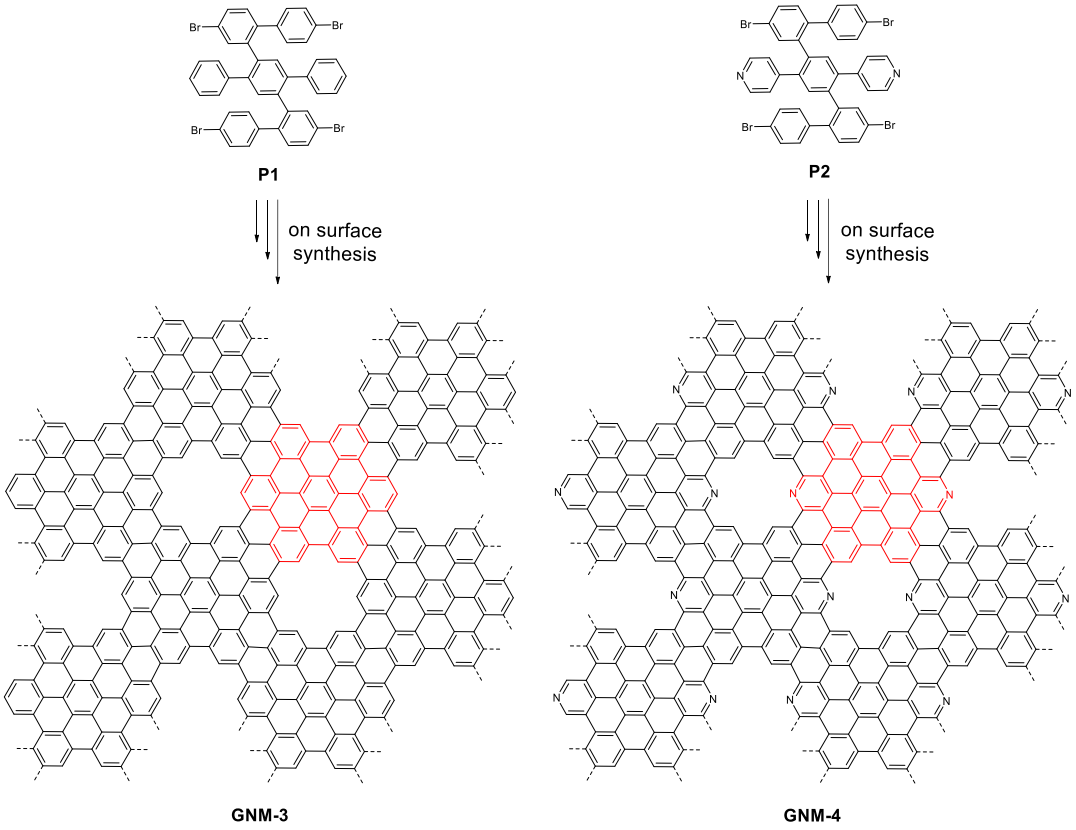

Fig. V-4 Structures of purely carbon based doped **GNM-3** and nitrogen-doped **GNM-4** formed by on-surface synthesis from precursors **P1** and **P2** respectively.

Chapter VI. Experimental part

VI. 1. Material and methods

NMR spectra of synthetic products below were recorded on a Bruker Ascend 400'54 with the exception of **BrTAP**, **TPAP**, **TPyAP**, **TNAP**, **TTAP** for which spectra were recorded on a Bruker Avance 400 and **ZnBrTAP** and **TMPAP** which were recorded on a Bruker Avance 500. HRMS and MS, MALDI-TOF spectra were recorded on a Bruker Ultraflextreme. Only HRMS of **ZnBrTAP**, ESI-QTOF was recorded on a Bruker maXis. UV/Vis measurements were performed using a Perkin Elmer Lambda 900 spectrometer. HPLC chromatograms were recorded on Thermo Fisher Spectra System P4000 with Thermo Scientific column Hypersil Gold Silica (100 x 4.6 mm). ThermoGravimetric Analysis (TGA) were performed on TA Instrument TGA Q50. Thin layer chromatography (TLC) was performed on silica gel 60 F254 (Merck) precoated aluminium sheets. Column chromatography was performed on Merck silica gel 60 (0.063-0.200 mm). Solvents and chemicals were purchased from Carlo Erba and Sigma-Aldrich or TCI-Europe. 5,15-Diphenylporphyrin and 5-bromo-10,15,20-triphenylporphyrin were purchased from Porphychem and unless stated otherwise, used without further purification. Diethyl ether and $CHCl_3$ were dried over CaH_2 and P_2O_5 respectively and distilled under argon. Unless stated otherwise, reactions were performed under an atmosphere of dry argon.

VI. 2. Anthracenylporphyrins based building blocks

5,10,15,20-tetrakis(10-bromoanthracen-9-yl)porphyrin (BrTAP)

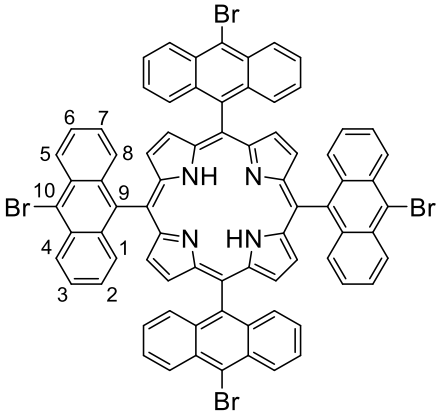

BrTAP was prepared by modification of literature procedure.[1] To a solution of 9,10-dibromoanthracene (6.0 g, 17.85 mmol) in dry diethyl ether (28 mL) was added *n*-butyllithium (2 M in hexane, 9 mL, 18 mmol) and the mixture was stirred at room temperature for 30 min. Then, a solution of pyrrole-2-carboxaldehyde (846 mg, 8.59 mmol) in diethyl ether (7 mL) was added and the mixture was stirred at r.t for 1 h. The deep red mixture was poured into a cold and saturated solution of NH_4Cl (60 mL). The organic phase was separated, washed with water (3 x 30 mL) and dried over Na_2SO_4 before the solvent was removed under vacuum. The intermediary crude product was directly introduced into a boiling solution of propionic acid (50 mL), stirred for 3h at 140°C and allowed to cool overnight. At the end of the reaction, the thick black mixture was filtered over paper filter and washed with MeOH until the elution of a clear solution. The collected precipitate was poured into MeOH (500 mL), sonicated for 2 min and filtered again. This process was repeated twice to remove the major part of polymeric side products. Then the latter precipitate was purified on a large silica column eluted with CH_2Cl_2 to collect the very first orange-red fraction. The solvent was removed and final product was recrystallised from CH_2Cl_2/MeOH to afford violet crystals as pure compound **(BrTAP)** (430 mg, 15% with respect to pyrrole-2-carboxaldehyde). ^{1}H NMR (400 MHz, $(CDCl_2)_2$): δ 8.80-8.77 (m, 8H, 4,5-anthracenyls), 8.11 (s, 8H, β-pyrroles), 7.60-7.57 (m, 8H, 3,6-anthracenyls), 7.30-7.28 (m, 8H, 1,8-anthracenyls), 7.12-7.08 (m, 8H, 2,7-anthracenyls), -1.77 (s, 2H, H_{NH}). ^{13}C NMR (125 MHz, $(CDCl_2)_2$): δ 156.85, 135.85, 135.65, 134.97, 131.54, 131.5, 129.67, 129.14, 127.58, 126.74, 125.89, 125.20, 124.64, 124.28, 115.64. UV/Vis (CH_2Cl_2): λ_{max} (log ϵ_{max}) = 252 (5.47), 258 (5.45), 355 (4.56), 382 (4.67), 429 (5.33), 519 (4.41), 549 (3.99), 591 (4.01), 658 nm (3.96). HRMS (MALDI - TOF) *m/z* $[M]^+$ calcd for $C_{76}H_{42}Br_4N_4$ 1326.0137, found: 1326.0136.

[5,10,15,20-tetrakis(10-bromoanthracen-9-yl)porphyrinato]zinc(II) (ZnBrTAP)

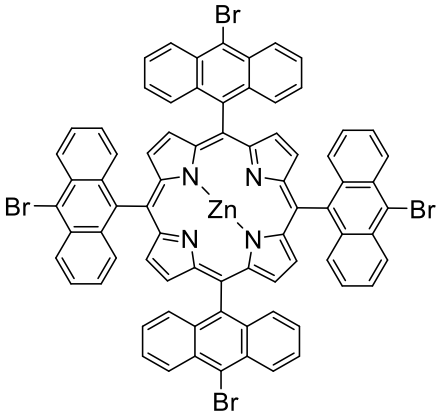

Zinc insertion reaction was achieved by modification of a literature procedure[2] with **BrTAP** (20 mg, 0.01 mmol, 1 eq) in non-distilled toluene (50 mL), $Zn(acac)_2.x\ H_2O$ (12 mg, 0.04 mmol, 4 eq), at reflux overnight. Recrystallisation from CH_2Cl_2/MeOH afforded violet-pink powder as pure target **ZnBrTAP** (16 mg, 76%). ^{1}H NMR (500 MHz, $(CDCl_2)_2$): δ 8.80-8.77 (m, 8H, anthracenyls), 8.15 (s, 8H, β-pyrroles), 7.99-7.96 (m, 8H, anthracenyls), 7.30-7.20 (m, 8H, anthracenyls), 7.10-7.07 (m, 8H, anthracenyls). ^{13}C NMR (125 MHz, $(CDCl_2)_2$): δ 151.25, 136.86, 135.67, 132.26, 131.08, 129.64, 129.20, 127.55, 126.65, 125.72, 123.86, 120.58, 120.48, 116.25, 113.07. UV/Vis (CH_2Cl_2): λ_{max} (log ϵ_{max}) = 252 (5.56), 345 (4.46), 364 (4.39), 435 (5.48), 554 (4.43), 629 nm (3.64). HRMS (MALDI-TOF) *m/z* $[M]^+$ calcd for $C_{76}H_{40}Br_4N_4Zn$ 1388.9351, found: 1388.9331.

9,10-diiodoanthracene

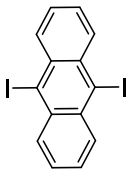

9,10-Diiodoanthracene was prepared following the literature procedure.[3] 9,10-dibromoanthracene (3.0 g, 8.9 mmol, 1 eq) in dry Et_2O (30 mL), *n*-BuLi (9.25 mL, 23.14 mmol, 2 M, 2.6 eq), I_2 (7.5 g, 29.5 mmol, 3.37 eq). Recrystallisation from CCl_4 afforded yellow needles as target product (1.8 g, 47%). ^{1}H NMR (400 MHz, $(CDCl_3)$): δ 11.49 (s, 1H), 8.59-8.52 (m, 4H), 7.65-7.58 (m, 4H). MS (MALDI - TOF) *m/z* $[M]^+$ calcd for $C_{14}H_8I_2$ 429.87, found: 429.87.

5,10,15,20-tetrakis(10-iodoanthracen-9-yl)porphyrin (ITAP)

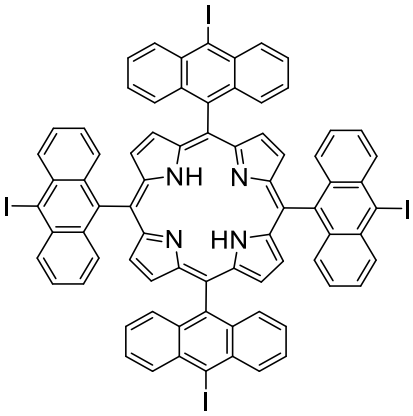

ITAP was prepared following the protocol developed for the preparation of **BrTAP**[4] from 9,10-diiodoanthracene (2.0 g, 4.65 mmol, 2 eq), pyrrole-2-carboxaldehyde (221 mg, 2.32 mmol, 1 eq), *n*-BuLi (2.4 mL, 4.74 mmol, 2 M, 2.04 eq) in Et_2O (13 mL). The mixture was in addition purified on silica column with toluene/heptane (1:1, v/v) and violet crystals corresponding to **ITAP** (5 mg, 0.6%) were afforded after precipitation in MeOH. Unfortunately after only one night of drying under vacuum, degradation of the molecule by successive deiodination was observed by ^{1}H NMR. This degradation was confirmed by the multiplication of signals in the ^{1}H NMR spectrum after forcing the degradation by heating the molecule at 50°C under vacuum for 2h. This degradation was confirmed by MS with observation of peaks corresponded to the loss of one and two iodines. UV/Vis (CH_2Cl_2): λ_{max} (log ϵ_{max}) = 252 (5.26), 367(4.28), 386 (4.39), 428 (4.98), 518 (4.12), 551 (3.75), 591 (3.73), 648 nm (3.43). HRMS (MALDI - TOF) *m/z* $[M]^+$ calcd for $C_{76}H_{42}I_4N_4$ 1517.9583, found: 1517.9583.

9-bromo-10-chloroanthracene

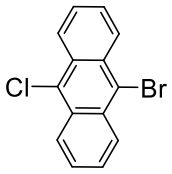

Bromination of 9-chloroanthracene was achieved by following the literature procedure.[5] 9-chloroanthracene (4.0 g, 18.8 mmol, 1 eq) in CH_2Cl_2 (60 mL), Br_2 (1.55 mL, 30.1 mmol, 1.6 eq) in CH_2Cl_2 (20 mL). Recrystallisation from CH_2Cl_2 afforded yellow needles as target product after filtration (1.84 g, 33%). ^{1}H NMR (400 MHz, ($CDCl_3$)): δ 8.65-8.51 (m, 4H), 7.69-7.60 (m, 4H). MS (MALDI - TOF) *m/z* $[M]^+$ calcd for $C_{14}H_8BrCl$ 289.95, found: 289.95.

5,10,15,20-tetrakis(10-chloroanthracen-9-yl)porphyrin (ClTAP)

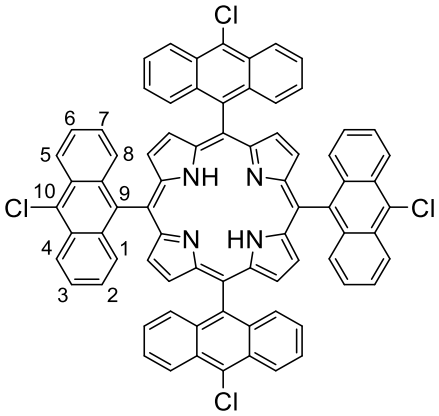

ClTAP was prepared following the protocol developed for the preparation of **BrTAP**,[4] from 9-bromo-10-chloroanthracene (800 mg, 2.74 mmol, 2 eq), pyrrole-2-carboxaldehyde (131 mg, 1.37 mmol, 1 eq), *n*-BuLi (1.4 mL, 2.80 mmol, 2 M, 2.04 eq) in Et_2O (12 mL). The mixture was in addition purified on a silica column with toluene/heptane (1:1, v/v) and violet crystals corresponding to **ClTAP** (30 mg, 8%) were afforded after precipitation in MeOH. ^{1}H NMR (400 MHz, $(CDCl_2)_2$): δ 8.84-8.70 (m, 8H, 4,5-anthracenyls), 8.11 (s, 8H, β-pyrroles), 7.64-7.54 (m, 8H, 3,6-anthracenyls), 7.35-7.25 (m, 8H, 1,8-anthracenyls), 7.16-7.06 (m, 8H, 2,7-anthracenyls), -1.77 (s, 2H, H_{NH}). ^{13}C NMR (100 MHz, $(CDCl_2)_2$, 553K): δ 135.40, 130.12, 129.51, 129.00, 128.90, 128.07, 127.98, 126.30, 125.86, 124.58, 115.55. UV/Vis (CH_2Cl_2): λ_{max} (log ϵ_{max}) = 251 (5.17), 313 (3.71), 363 (4.11), 428 (5.03), 519 (4.00), 551 (3.28), 592 (3.48), 648 nm (2.73). HRMS (MALDI - TOF) *m/z* $[M]^+$ calcd for $C_{76}H_{42}Cl_4N_4$ 1150.2158, found: 1150.2159.

5,10,15,20-tetrakis(10'-bromo-[9,9'-bianthracen]-10-yl)porphyrin (BrDTAP)

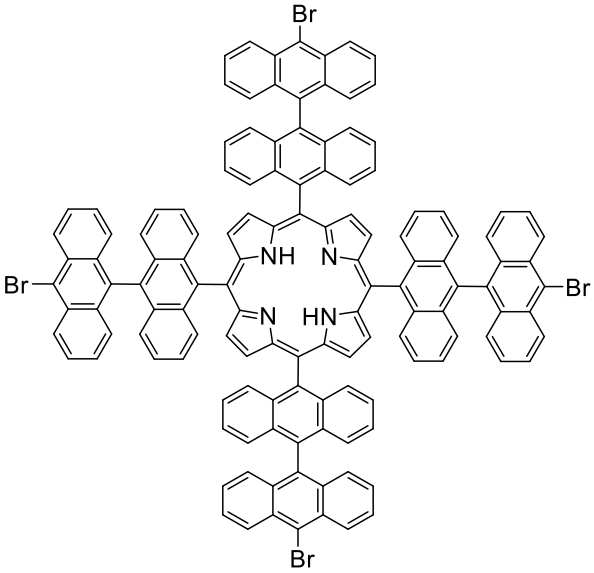

To an orange suspension of 10,10'-dibromo-9,9'-bianthracene (**DBBA**) (3.0 g, 17.85 mmol) in a mixture of anhydrous THF (30 mL) and dry Et_2O (30mL) was added *n*-butyllithium (2 M in hexane, 9 mL, 18 mmol) and the mixture was stirred at r.t for 30 min. Then, a solution of pyrrole-2-carboxaldehyde (846 mg, 8.59 mmol) in dry Et_2O (3 mL) was added and a red solution quickly formed and was stirred at r.t for 1 h. The resulting brown mixture was poured into a cold, saturated solution of NH_4Cl (50 mL). The organic phase was separated, washed with water (3 x 30 mL) and dried over Na_2SO_4 before the solvent was removed under vacuum. The intermediary crude product was directly introduced into a boiling solution of propionic acid (50 mL), stirred for 3h at 140°C and allowed to cool overnight. At the end of the reaction, the black thick mixture was filtered over filter paper and washed with MeOH until the filtrate was a clear solution. The collected precipitate was poured into MeOH (500 mL), sonicated for 2 min and filtered again. This process was repeated twice to remove the major part of polymeric side products. Then the precipitate was purified on large silica column eluted with CH_2Cl_2 and the first fraction was collected. DBBA and derivatives were removed using silica column eluted with toluene/heptane (1:1, v/v) or SEC in toluene. The red dark fraction collected contained a mixture of target **BrDTAP**, its corresponding pentamer and debrominated by-products. The crude mixture was purified by a silica column using CS_2/CH_2Cl_2 (9:1) to collect the first green fraction. The solvent was removed and final product was recrystallised from CH_2Cl_2/MeOH to afford a green powder as target compound **(BrDTAP)** (2 mg, traces). UV/Vis (CH_2Cl_2): λ_{max} = 343, 345, 406, 430, 524, 567, 613, 648 nm. HRMS (MALDI - TOF) *m/z* $[M]^+$ calcd for $C_{132}H_{74}Br_4N_4$ 2030.2641, found: 2030.2616.

10-bromoanthracene-9-carbaldehyde

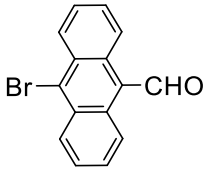

Bromination of 9-anthracenecarbaldehyde was achieved by modification of a literature procedure.[6] To a yellow solution of 9-anthracenecarbaldehyde (4.0 g, 19.36 mmol, 1 eq) in CH_2Cl_2 was added dropwise a solution of Br_2 (1.6 mL, 31.12 mmol, 1.6 eq) in CH_2Cl_2. The resulted brown mixture was stirred at r.t for 8 h and finally quenched by addition of a saturated solution of $Na_2S_2O_3$ (50 mL). The yellow organic phase was separated, treated with aqueous solution of 1 M Na_2CO_3 (50 mL), washed with water (3 x 30 mL) and dried over Na_2SO_4 before the solvent was removed under vacuum. The yellow paste was recrystallised from toluene/cyclohexane (3:1) to give the target product as yellow needles after filtration (3.58 g, 65%). ^{1}H NMR (400 MHz, ($CDCl_3$)): δ 11.49 (s, 1H), 8.90-8.87 (m, 4H), 8.69-8.66 (m, 4H). MS (MALDI - TOF) *m/z* $[M]^+$ calcd for $C_{15}H_9BrO$ 283.98, found: 283.96.

5,15-bis(10-bromoanthracen-9-yl)-10,20-diphenylporphyrin (BrBAP)

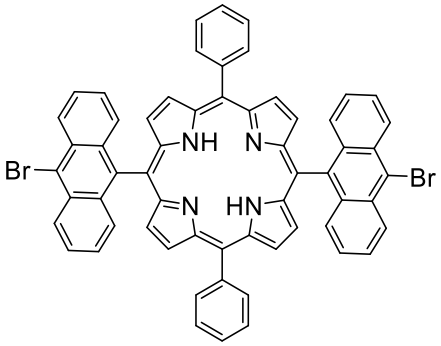

To a stirred, degassed mixture of 10-bromoanthracene-6-carbaldehyde (1.0 g, 3.51 mmol, 1 eq) in distilled pyrrole (40 mL) and non-stabilized CH_2Cl_2 (20 mL), was added at r.t a catalytic amount of trifluoroacetic acid (30 µL, 0.4 mmol, 0.1 eq). The initial yellow solution turned quickly green then dark-red over the reaction time. After 15 min, CH_2Cl_2 was added to dilute the dark red mixture, which was further treated with an aqueous solution of 0.1 M NaOH (50 mL). The organic phase was separated, washed with water (3 x 30 mL) and dried over Na_2SO_4 before CH_2Cl_2 and excess pyrrole were removed under vacuum. The resulting residue was partially purified by loading onto a silica plug eluted with CH_2Cl_2/Et_3N (99:1) to give a crude dipyrromethane after evaporation of solvents of the first orange-red fraction. To a stirred and preliminary degassed solution of crude dipyrromethane and formaldehyde (0.25 mL, 2.49 mmol) in non-stabilized CH_2Cl_2 (280 mL), was added trifluoroacetic acid (0.38 mL, 4.98 mmol). After 2.5h, DDQ (700 mg, 3.08 mmol) was added and the mixture was refluxed for an additional hour. At the end of the reaction, the entire mixture was passed through a pad of alumina eluted with CH_2Cl_2 until the complete collection of the first dark-orange fraction. The solvent was removed under vacuum and the crude mixture was purified by silica chromatography with toluene/heptane (1:1 to 2:1). After evaporation of solvents from the green-violet fraction, violet crystals were afforded after recrystallisation from CH_2Cl_2/MeOH (105 mg, 0.11 mmol, 6% for the both steps). ^{1}H NMR (400 MHz, $(CDCl_2)_2$): δ 8.96-8.66 (m, 8H), 8.49 (d, 2H, J=4.76 Hz), 8.28 (d, 2H, J=4.88 Hz), 8.19 (d, 4H, J=4.8Hz), 8.07 (d, 2H, J=4.2 Hz), 7.75-7.58 (m, 8H), 7.33 (d, 2H, J=8.56 Hz), 7.19 (d, 2H, J=8.92 Hz), 7.15-.7.05 (m, 4H), -2.27 (s, 2H). UV/Vis (CH_2Cl_2): λ_{max} (log ϵ_{max}) = 366 (4.30), 426 (5.17), 518 (4.09), 550 (3.72), 596 (3.60), 656 nm (4.10). HRMS (MALDI - TOF) *m/z* $[M]^+$ calcd for $C_{60}H_{36}Br_2N_4$ 970.1301, found: 970.1297.

VI. 3. Precursors of pyrolysis experiments

5,10,15,20-tetra(anthracen-9-yl)porphyrin (TAP)

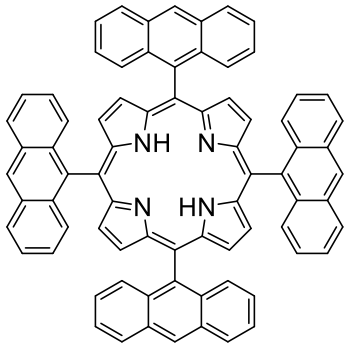

TAP was prepared by following the literature procedure,[1] starting from 9-bromoanthracene (5.0 g, 19.46 mmol, 1 eq), pyrrole-2-carboxaldehyde (925 mg, 9.7 mmol, 1 eq) and *n*-BuLi (10 mL, 20.0 mmol, 2 M, 2.04 eq), Et_2O (12 mL). Cyclotetramerized in propionic acid (50 mL) at 140°C for 3h and allowed to cool overnight. After purification, violet crystals of **TAP** were afforded (95 mg, 4% with respect to pyrrole-2-carboxaldehyde). ^{1}H NMR (400 MHz, $(CDCl_2)_2$): δ 8.89 (s, 4H, anthracenyl), 8.34-8.18 (m, 8H, anthracenyl), 8.12 (s, 8H, β-pyrroles), 7.51-7.40 (m, 8H, anthracenyl), 7.32-7.24 (m, 8H, anthracenyl), 7.15-7.02 (m, 8H, anthracenyl), -1.74 (s, 2H, H_{NH}). UV/Vis (CH_2Cl_2): λ_{max} (log ϵ_{max}) = 255 (5.54), 258 (5.45), 354 (4.49), 375 (4.57), 426 (5.22), 519 (4.32), 548 (3.91), 592 (3.89), 657 nm (3.76). MS (MALDI - TOF) *m/z* $[M]^+$ calcd for $C_{76}H_{46}N_4$ 1014.37, found: 1014.34.

[5,10,15,20-tetra(anthracen-9-yl)porphyrinato]zinc(II) (ZnTAP)

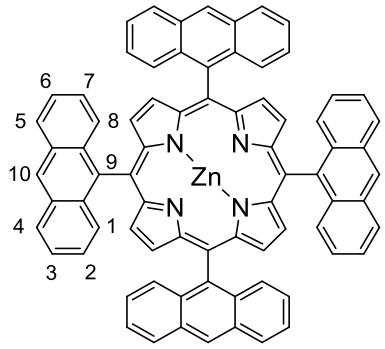

Zinc insertion was achieved by modification of literature procedure[2] with **TAP** (30 mg, 0.03 mmol, 1 eq) in CH_2Cl_2 (100 mL), $Zn(acac)_2.x\ H_2O$ (23 mg, 0.09 mmol, 3 eq), at reflux overnight. Recrystallisation from CH_2Cl_2/MeOH afforded pink powder as pure target **ZnTAP** (26 mg, 81%). ^{1}H NMR (400 MHz, $(CDCl_2)_2$): δ 8.87 (s, 4H, 10-anthracenyls), 8.28-8.23 (m, 8H, 4,5-anthracenyls), 8.17 (s, 8H, β-pyrroles), 7.48-7.41 (m, 8H, 3,6-anthracenyl H), 7.26-7.20 (m, 8H, 1,8-anthracenyls), 7.02-7.02 (m, 8H, 2,7-anthracenyls). λ_{max} (log ϵ_{max}) = 248 (5.14), 352 (3.95), 429 (5.00), 516 nm (3.52), 552 (3.98). MS (MALDI-TOF) *m/z* $[M]^+$ calcd for $C_{76}H_{44}N_4Zn$ 1076.29, found: 1076.28.

5,10,15,20-tetra(pyren-1-yl)porphyrin (TPyP)

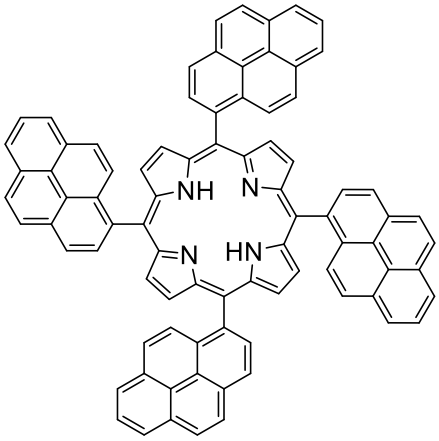

TPyP was prepared following the literature procedure.[7] Starting from pyren-1-carboxaldehyde (4.0 g, 17.37 mmol, 1 eq), distilled pyrrole (1.20 mL, 17.37 mmol, 1 eq), propionic acid (100 mL). Recrystallisation from CH_2Cl_2/MeOH afforded **TPyP** as violet crystals (581 mg, 12%). ^{1}H NMR (400 MHz, ($CDCl_3$)): δ 8.87-8.71 (m, 4H), 8.49-8.34 (m, 12H), 8.34-8.20 (m, 12H), 8.09-7.96 (m, 8H), 7.73-7.46 (m, 8H), -1.92 (s, 2H, H_{NH}). UV/Vis (CH_2Cl_2): λ_{max} (log ϵ_{max}) = 236 (5.06), 243 (5.20), 265 (4.85), 275 (4.98), 326 (4.75), 338 (4.8), 432 (5.26), 520 (4.23), 555 (3.89), 593 (3.79), 652 nm (3.59). MS (MALDI - TOF) *m/z* $[M]^+$ calcd for $C_{84}H_{46}N_4$ 1010.37, found: 1010.37.

[5,10,15,20-tetra(pyren-1-yl)porphyrinato]zinc (II) (ZnTPyP)

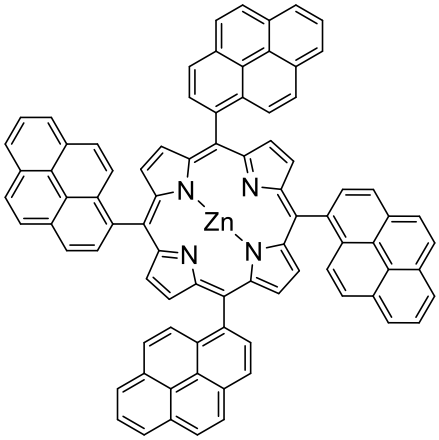

Zinc insertion reaction was achieved by modification of literature procedure[2] with **TPyP** (150 mg, 0.15 mmol, 1 eq) in non-distilled CH_2Cl_2 (100 mL), $Zn(OAc)_2.2\ H_2O$ (82 mg, 0.45 mmol, 3 eq), at reflux for 1h. Recrystallisation from CH_2Cl_2/MeOH afforded violet-pink powder as pure target **ZnTPyP** (120 mg, 76%). ^{1}H NMR (400 MHz, ($CDCl_2)_2$): δ 9.01-8.81 (m, 4H), 8.58-8.48 (m, 12H), 8.42-8.26 (m, 12H), 8.16-8.02 (m, 8H), 7.82-7.70 m, 4H), 7.69-7.45 (m, 4H). UV/Vis (CH_2Cl_2): λ_{max} (log ϵ_{max}) = 236 (5.01), 243 (5.16), 264 (4.74), 275 (4.90), 323 (4.70), 337 (4.75), 434 (5.39), 553 (4.29), 589 nm (3.54). MS (MALDI - TOF) *m/z* $[M]^+$ calcd for $C_{84}H_{44}N_4Zn$ 1172.29, found: 1172.40.

[5,15-diphenylporphyrinato]zinc(II) (ZnDPP)

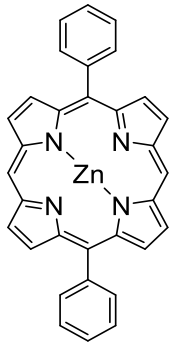

Zinc insertion reaction was achieved by modification of literature procedure[2] with 5,15-diphenylporphyrin (100 mg, 0.22 mmol, 1 eq) in $CHCl_3$ (100 mL), $Zn(OAc)_2.2\ H_2O$ (142 mg, 0.65 mmol, 3 eq) at reflux for 1h. Recrystallisation from CH_2Cl_2/MeOH afforded violet-pink powder as pure target **ZnDPP** (109 mg, 96% yield). ^{1}H NMR (400 MHz, $CDCl_3$): δ 10.34 (s, 2H, meso), 9.45 (d, J = 4.4 Hz, 4H, β pyrroles), 9.15 (d, J = 4.4 Hz, 4H, β pyrroles), 8.32-8.22 (m, 4H, *m*-phenyls), 7.85-7.76 (m, 6H, *o*-phenyls + *p*-phenyls). UV/Vis (CH_2Cl_2): λ_{max} (log ε_{max}) = 412 (5.39), 541 (4.10). MS (MALDI-TOF) m/z $[M]^+$ calcd for $C_{32}H_{20}N_4Zn$: 524.10, found: 524.91.

5,15-diiodo-10,20-diphenylporphyrin (I_2DPP)

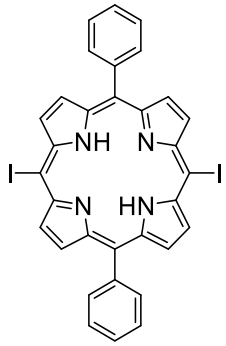

Iodination of **ZnDPP** was achieved by modification of literature procedure.[8] To a solution of **ZnDPP** (50 mg, 0.19 mmol) and I_2 (194 mg, 0.76 mmol, 4 eq) in $CHCl_3$ (10 mL) and pyridine (300 µL) was added dropwise a solution of $AgPF_6$ (101 mg, 0.40 mmol, 2.1 eq) in MeCN (2 mL) and the mixture was stirred at room temperature for 15 min. The reaction was quenched by addition of water (10 mL) and the organic phase was extracted with $CHCl_3$ (3 x 30 mL), washed with water (3 x 30 mL) and dried over Na_2SO_4 before the solvent was removed under vacuum. The crude product was dissolved in $CHCl_3$ and a solution of HCl (6 mol/L, 100 mL) was added to remove zinc. After 3h of stirring at r.t., HCl was quenched by addition of a saturated solution of $NaHCO_3$ (2 x100 mL) and the combined organic phase were extracted with water (3 x 30 mL) and dried over Na_2SO_4 before the solvent was removed under vacuum. The crude product was purified by silica chromatography with $CHCl_3$/cyclohexane (1:2) with 1% Et_3N. After evaporation of solvents, a violet powder corresponding to target **I_2DPP** was afforded (41 mg, 60%). ^{1}H NMR (400 MHz, $CDCl_3$): δ 9.62 (d, J= 4.8 Hz, 4H, β pyrroles), 8.80 (d, J=4.8 Hz, 4H, β pyrroles), 8.18-8.13 (m, 4H, *m*-phenyls), 7.83-7.74 (m, 6H, *o*-phenyls + *p*-phenyls), -2.62 (s, 2H, H_{NH}). UV/Vis (CH_2Cl_2): λ_{max} (log ε_{max}) = 425 (5.48), 525 (4.14), 561 (4.09), 603 (3.65), 660 (3.77). MS (MALDI-TOF) *m/z* $[M + H]^+$ calcd for $C_{32}H_{21}I_2N_4$ 714.99, found: 715.02.

5,15-di(anthracen-9-yl)-10,20-diphenylporphyrin (BAP)

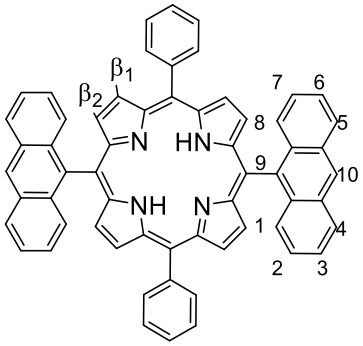

BAP was prepared *via* Suzuki-Miyaura cross coupling reaction by modification of literature procedures.[9,10] Palladium catalyst Pd_2dba_3 (39.5 mg, 0.04 mmol, 0.5 eq) with SPhos (35.4 mg, 0.09 mmol, 1 eq), K_3PO_4 (143.5 mg, 0.7 mmol, 8 eq), **I_2DPP** (62 mg, 0.09 mmol, 1 eq) and anthracen-9-boronic acid (77 mg, 0.34 mmol, 4 eq) were dissolved in 30 mL of a degassed solution of toluene and water (1 mL), shielded from ambient light and stirred at 85°C for 24h. At the end of the reaction, the mixture was washed with water (3 x 40mL), dried over Na_2SO_4 and the organic solvent was evaporated. The crude mixture was purified by two silica chromatography columns eluted with toluene/heptane (1:1), CH_2Cl_2/cyclohexane (1:1) and a SEC in distilled THF. After evaporation of solvents, a violet powder corresponding to target **BAP** was afforded (16 mg, 22%). ^{1}H NMR (400 MHz, $CDCl_2)_2$): δ 8.98 (s, 2H, 10-anthracenyls), 8.71 (d, 4H, J = 4.8 Hz, β1), 8.34 (d, 4H, J =4.8 Hz, β2), 8.32-8.28 (m, 4H, 4,5-anthracenyls), 8.22-8.17 (m, 4H, *o*-phenyls), 7.72-7.67 (m, 6H, *m*-phenyls + *p*-phenyls), 7.54-7.48 (m, 4H, 3,6-anthracenyls), 7.19-7.14 (m, 4H, 1,8-anthracenyls), 7.10-7.05 (m, 4H, 2,7-anthracenyls), -2.25 (s, 2H, H_{NH}). UV/Vis (CH_2Cl_2): λ_{max} (log ε_{max}) = 422 (5.40), 517 (4.35), 550 (3.85), 591 (3.84), 647 (3.45). MS (MALDI-TOF) *m/z* $[M + H]^+$ calcd for $C_{60}H_{39}N_4$ 815.31, found: 815.34.

[5,15-di(anthracen-9-yl)-10,20-diphenylporphyrinato]zinc(II) (ZnBAP)

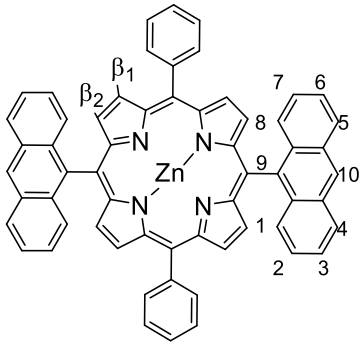

Zinc insertion reaction was achieved by modification of literature procedure[2] with **BAP** (15.7 mg, 0.02 mmol, 1 eq) in toluene (100 mL), $Zn(OAc)_2.2\ H_2O$ (10.3 mg, 0.06 mmol, 3 eq), at 85°C for 1h. Recrystallisation from CH_2Cl_2/MeOH afforded violet-pink powder as pure target **ZnTAP** (15 mg, 90%). ^{1}H NMR (400 MHz, $(CDCl_2)_2$): δ 8.97 (s, 2H, 10-anthracenyls), 8.80 (d, 4H, J = 4.8 Hz, β1), 8.38 (d, 4H, J =4.8 Hz, β2), 8.36-8.31 (m, 4H, 4,5-anthracenyls), 8.24-8.20 (m, 4H, *o*-phenyls), 7.72-7.65 (m, 6H, *m*-phenyls + *p*-phenyls), 7.53-7.47 (m, 4H, 3,6-anthracenyls), 7.15-7.09 (m, 4H, 1,8-anthracenyls), 7.08-7.01 (m, 4H, 2,7-anthracenyls). λ_{max} (log ϵ_{max}) = 255 (5.21), 422 (5.37), 516 nm (3.52), 552 (4.18). HRMS (MALDI-TOF) *m/z* $[M]^+$ calcd for $C_{60}H_{36}N_4Zn$ 876.2226, found: 876.2237.

5-(anthracen-9-yl)-10,15,20-triphenylporphyrin (SAP)

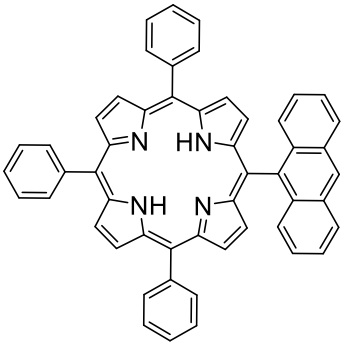

SAP was prepared by Suzuki-Miyaura cross coupling reaction, modification of literature procedure.[10] Palladium catalyst Pd_2dba_3 (9.1 mg, 0.01 mmol, 0.5 eq) with SPhos (16.4 mg, 0.04 mmol, 1 eq), K_3PO_4 (51.5 mg, 0.54 mmol, 6 eq), 5-bromo-10,15,20-triphenylporphyrin (25 mg, 0.04 mmol, 1 eq) and anthracen-9-boronic acid (27 mg, 0.12 mmol, 3 eq) were dissolved in 30 mL of preliminary degassed solution of toluene and water (1 mL), shielded from ambient light and stirred at 85°C for 48 h. At the end of the reaction, the mixture was washed with water (3 x 40mL), dried over Na_2SO_4 and the organic solvent was evaporated. The crude mixture was purified by silica column using toluene/heptane (1:1) to collect the second red fraction. Solvents were removed and final product was recrystallised from CH_2Cl_2/MeOH to afford **SAP** (15 mg, 51%). ^{1}H NMR (400 MHz, $(CDCl_2)_2$): δ 8.96 (s, 1H, anthracenyl), 8.93-8.88 (m, 4H, β pyrroles), 8.69 (d, 2H, J =4.4 Hz, β pyrroles), 8.32 (d, 2H, J =4.8 Hz, β pyrroles), 8.29-8.20 (m, 8H, 2H anthracenyl + 6H *o*-phenyls), 7.85-7.79 (m, 3H, *p*-phenyls), 7.78-7.71 (m, 6H, *m*-phenyls), 7.52-7.46 (m, 2H, anthracenyl), 7.13-7.07 (m, 2H, anthracenyl), 7.07-7.01 (m, 2H, anthracenyl), -2.55 (s, 2H, H_{NH}). ^{13}C NMR (125 MHz, $(CDCl_2)_2$, 333K): δ 141.85, 141.55, 135.60, 135.02, 134.48, 134.25, 130.64, 128.46, 128.21, 128.02, 127.76, 127.68, 126.68, 126.68, 125.70, 124.95, 120.63, 120.07, 114.98. UV/Vis (CH_2Cl_2): λ_{max} (log ϵ_{max}) = 231 (4.19), 257 (4.95), 352 (4.11), 373 (4.20), 419 (5.34), 515 (4.06), 550 (3.61), 589 (3.53), 647 nm (3.24). HRMS (MALDI - TOF) *m/z* $[M]^+$ calcd for $C_{52}H_{34}N_4$ 714.2778, found: 714.2775.

[5-(anthracen-9-yl)-10,15,20-triphenylporphyrinato]zinc(II) (ZnSAP)

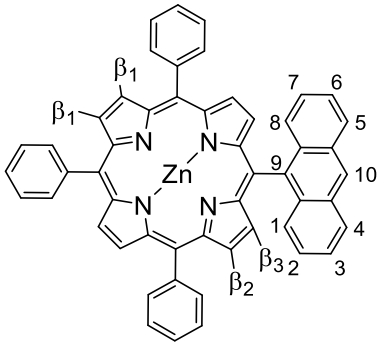

Zinc insertion reaction was achieved by modification of literature procedure.[2] **SAP** (10 mg, 0.01 mmol, 1 eq) in non-distilled toluene (100 mL), $Zn(acac)_2.x\ H_2O$ (8 mg, 0.03 mmol, 3 eq), at reflux overnight. Recrystallisation from CH_2Cl_2/MeOH afforded violet-pink powder as pure target **ZnSAP** (7 mg, 87%). ^{1}H NMR (400 MHz, $(CDCl_2)_2$): δ 9.06-8.97 (m, 4H, β1 pyrroles), 8.94 (s, 1H, 10-anthracenyl), 8.80 (d, 2H, J =4.4 Hz, β2 pyrroles), 8.36 (d, 2H, J =4.8 Hz, β3 pyrroles), 8.34-8.20 (m, 8H, 4,5-anthracenyl + *o*-phenyls), 7.87-7.79 (m, 3H, *p*-phenyls), 7.78-7.69 (m, 6H, *m*-phenyls), 7.52-7.43 (m, 2H, 3,6-anthracenyl), 7.11-6.97 (m, 4H, 2,7- and 1,8-anthracenyl). ^{13}C NMR (125 MHz, $(CDCl_2)_2$, 333K): δ 151.12, 150.09, 149.90, 149.81, 142.41, 142.19, 136.37, 134.98, 134.46, 132.57, 132.16, 132.01, 131.71, 130.58, 128.56, 128.20, 127.78, 127.52, 127.45, 126.59, 126.56, 125.59, 124.91, 121.58, 120.95, 115.93. UV/Vis (CH_2Cl_2): λ_{max} (log ϵ_{max}) = 257 (4.75), 352 (3.71), 421 (5.20), 548 (3.90), 586 (3.00). HRMS (MALDI - TOF) *m/z* $[M]^+$ calcd for $C_{52}H_{34}N_4Zn$ 776.1913, found: 776.1926.

5,10,15-triphenyl-20-(naphthalen-1-yl)porphyrin (SNP)

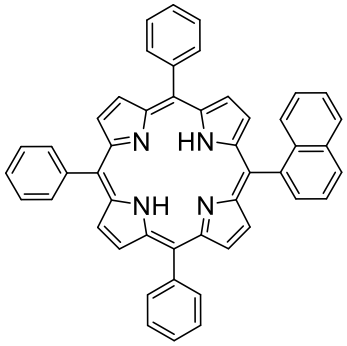

SNP was prepared by Suzuki-Miyaura cross coupling reaction, modification of literature procedure.[10] Palladium catalyst Pd_2dba_3 (37 mg, 0.04 mmol, 0.5 eq) with SPhos (66 mg, 0.16 mmol, 1 eq), K_3PO_4 (205 mg, 0.97 mmol, 6 eq), 5-bromo-10,15,20-triphenylporphyrin (100 mg, 0.16 mmol, 1 eq) and naphthalen-1-boronic acid (83.5 mg, 0.48 mmol, 3 eq) were dissolved in 80 mL of a degassed solution of toluene and water (1 mL), shielded from ambient light and stirred at 85°C for 48 h. At the end of the reaction, the mixture was washed with water (3 x 40 mL), dried over Na_2SO_4 and the organic solvent was evaporated. The crude mixture was purified by silica column using toluene/heptane (1:1) and the second red fraction was collected. Solvents were removed and final product was recrystallised from CH_2Cl_2/MeOH to afford **SNP** (105 mg, 98%). ^{1}H NMR (400 MHz, $(CDCl_2)_2$): δ 8.91 (m, 4H, β-H pyrroles), 8.80 (d, 2H, J = 4.72 Hz, β-H pyrroles), 8.61 (d, 2H, J = 4.72 Hz, β-H pyrroles), 8.36-8.30 (m, 2H, napthyl), 8.30-8.21 (m, 6H, *o*-phenyls), 8.21-8.17 (m, 1H, naphtyl), 7.96-7.88 (m, 1H, napthyl), 7.87-7.72 (m, 9H, *m*-phenyls + *p*-phenyls), 7.57-7.49 (m, 1H, napthyl), 7.24-7.10 (m, 2H, napthyl), -2.65 (s, 2H, H_{NH}). ^{13}C NMR (100 MHz, $(CDCl_2)_2$): δ 141.84, 141.67, 139.04, 136.59, 134.48, 132.76, 132.65, 128.60, 128.50, 127.80, 127.66, 126.66, 126.08, 125.55, 124.24, 120.40, 120.06, 117.17. UV/Vis (CH_2Cl_2): λ_{max} (log ϵ_{max}) = 419 (5.47), 520 (4.04), 554 (3.58), 594 (3.56), 647 nm (3.33). HRMS (MALDI - TOF) *m/z* $[M]^+$ calcd for $C_{48}H_{24}N_4$ 664.2621, found: 664.2649.

[5,10,15-triphenyl-20-(naphthalen-1-yl)porphyrinato]zinc(II) (ZnSNP)

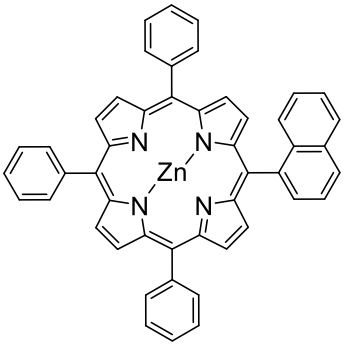

Zinc insertion reaction was achieved by modification of literature procedure.[2] **SNP** (90 mg, 0.13 mmol, 1 eq) in non-distilled toluene (150 mL), $Zn(acac)_2.x\ H_2O$ (106 mg, 0.40 mmol, 3 eq), at reflux for 2h. Recrystallisation from CH_2Cl_2/MeOH afforded violet-pink powder as pure target **ZnSNP** (92 mg, 93%). ^{1}H NMR (400 MHz, $(CDCl_2)_2$): δ 9.01 (m, 4H, β1 pyrroles), 8.89 (d, 2H, J = 4.64 Hz, β2 pyrroles), 8.71 (d, 2H, J = 4.64 Hz, β3 pyrroles), 8.38-8.22 (m, 8H, 2- and 4-napthyl + *o*-phenyls), 8.20-8.15 (m, 1H, 8-naphtyl), 7.96-7.88 (m, 1H, 3-napthyl), 7.84-7.73 (m, 9H, *m*-phenyls + *p*-phenyls), 7.56-7.46 (m, 1H, 7-napthyl), 7.14-7.06 (m, 2H, 5- and 6-napthyl). ^{13}C NMR (100 MHz, $(CDCl_2)_2$): δ 150.62, 150.03, 149.93, 149.88, 142.46, 142.35, 139.71, 136.68, 134.43, 134.38, 132.60, 132.56, 132.13, 132.00, 131.90, 131.80, 128.55, 128.36, 127.77, 127.41, 126.50, 125.93, 125.45, 124.19, 121.31, 120.96, 118.11. UV/Vis (CH_2Cl_2): λ_{max} (log ϵ_{max}) = 421 (5.54), 552 (4.12). HRMS (MALDI - TOF) *m/z* $[M]^+$ calcd for $C_{48}H_{30}N_4Zn$ 726.1756, found: 726.1767.

5,10,15-triphenyl-20-(pyren-1-yl)porphyrin (SPP)

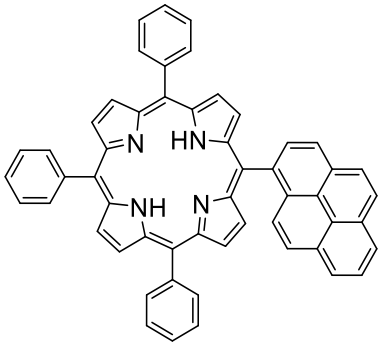

SPP was prepared by Suzuki-Miyaura cross coupling reaction, modification of literature procedure.[10] Palladium catalyst Pd_2dba_3 (37 mg, 0.04 mmol, 0.5 eq), SPhos (66 mg, 0.16 mmol, 1 eq), K_3PO_4 (205 mg, 0.97 mmol, 6 eq), 5-bromo-10,15,20-triphenylporphyrin (100 mg, 0.16 mmol, 1 eq) and pyren-1-boronic acid (119.6 mg, 0.48 mmol, 3 eq) were dissolved in mixture of toluene (80 mL) and water (1 mL), shielded from ambient light and stirred at 85°C for 48 h. At the end of the reaction, the mixture was washed with water (3 x 40mL), dried over Na_2SO_4 and the organic solvent was evaporated. The crude mixture was purified by silica column using toluene/heptane (1:1) to collect the second red fraction. Solvents were removed and final product was recrystallised from CH_2Cl_2/MeOH to afford **SPP** (116 mg, 96%). ^{1}H NMR (400 MHz, $(CDCl_2)_2$): δ 8.94 (m, 4H, β-H pyrroles), 8.86 (d, 1H, J = 7.72 Hz, pyrenyl), 8.81 (d, 2H, J = 4.76 Hz, β-H pyrroles), 8.57 (d, 1H, J = 7.84 Hz, pyrenyl), 8.54 (d, 2H, J= 4.80 Hz, β-H pyrroles), 8.45 (d, 1H, J = 9.08 Hz, pyrenyl), 8.40-8.34 (m, 2H, pyrenyl), 8.33-8.24 (m, 6H, *o*-phenyls), 8.18-8.08 (m, 2H, pyrenyl), 7.87-7.81 (m, 3H, *p*-phenyls), 7.81-7.74 (m, 6H, *m*-phenyls),7.51 (d, 1H, J = 9.28 Hz, pyrenyl), -2.58 (s, 2H, H_{NH}). ^{13}C NMR (100 MHz, $(CDCl_2)_2$): δ 141.84, 141.65, 136.78, 134.48, 133.25, 132.70, 131.41, 131.18, 130.53, 128.00, 127.72, 127.67, 127.48, 127.12, 126.67, 126.37, 125.63, 125.27, 124.31, 123.90, 122.84, 120.44, 120.20, 117.54. UV/Vis (CH_2Cl_2): λ_{max} (log ϵ_{max}) = 244 (4.65), 268 (4.36), 276 (4.47), 327 (4.29), 340 (4.36), 421 (5.43), 519 (4.14), 555 (3.74), 595 (3.60), 648 nm (3.44). HRMS (MALDI - TOF) *m/z* $[M]^+$ calcd for $C_{54}H_{34}N_4$ 738.2778, found: 738.2787.

[5,10,15-triphenyl-20-(pyren-1-yl)porphyrinato]zinc(II) (ZnSPP)

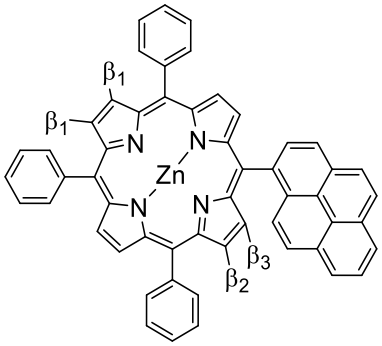

Zinc insertion reaction was achieved by modification of a literature procedure.[2] **SPP** (85 mg, 0.11 mmol, 1 eq) in non-distilled toluene (150 mL), $Zn(acac)_2.x\ H_2O$ (91 mg, 0.34 mmol, 3 eq), at reflux for 2h. Recrystallisation from CH_2Cl_2/MeOH afforded violet-pink powder as pure target **ZnSPP** (80 mg, 87%). ^{1}H NMR (400 MHz, $(CDCl_2)_2$): δ 9.01 (m, 4H, β1 pyrroles), 8.92-8.83 (m, 3H, 1H pyrenyl + 2H β2 pyrroles), 8.61 (d, 2H, J = 4.68 Hz, β3 pyrroles), 8.57 (d, 1H, J = 7.80 Hz, pyrenyl), 8.45 (d, 1H, J = 9.08 Hz, pyrenyl), 8.38-8.23 (m, 8H, 2H pyrenyl + *o*-phenyls), 8.14-8.05 (m, 2H, pyrenyl), 7.86-7.79 (m, 3H, *p*-phenyls), 7.79-7.73 (m, 6H, *m*-phenyls), 7.71 (d, 1H, J = 9.40 Hz, pyrenyl), 7.51 (d, 1H, J = 9.32 Hz, pyrenyl). ^{13}C NMR (100 MHz, $(CDCl_2)_2$): δ 150.83, 150.11, 149.95, 149.91, 142.51, 142.39, 137.61, 134.47, 134.45, 134.39, 133.23, 132.66, 132.22, 132.02, 131.94, 131.44, 131.01, 130.54, 127.78, 127.75, 127.44, 127.40, 127.29, 127.25, 126.49, 126.28, 125.52, 125.17, 124.35, 123.87, 122.71, 121.33, 121.06, 118.42. UV/Vis (CH_2Cl_2): λ_{max} (log ϵ_{max}) = 244 (4.71), 268 (4.37), 276 (4.49), 327 (4.33), 341 (4.34), 422 (5.56), 552 (4.27). HRMS (MALDI - TOF) *m/z* $[M]^+$ calcd for $C_{54}H_{32}N_4Zn$ 800.1913, found: 800.1921.

VI. 4. Π-extended porphyrins

General procedure for Pyrolysis reactions

Procedure adapted from the literature.[11] A glass tube was first heated at the reaction temperature and continually flushed with an argon flow. The temperature in the glass tube was monitored prior to the pyrolysis reaction with a thermocouple sensor placed under the argon flow at the location of the glass boat. A glass boat containing the porphyrin precursor in powder was placed at the entrance of the glass tube under the argon flow for 10 min. The pyrolysis reaction started by inserting the glass boat into the furnace. The progress of the reaction was controlled by time monitoring by looking at the aspect of the sample by removing the glass boat from the furnace. At the end of the reaction, the glass boat was removed from the furnace, cooled under the argon flow for 10 min and the crude mixture was collected with CH_2Cl_2 for purification.

[2,3,5,10,12,13,15,20-pyreneporphyrinato]zinc(II) (fused ZnTPyP)

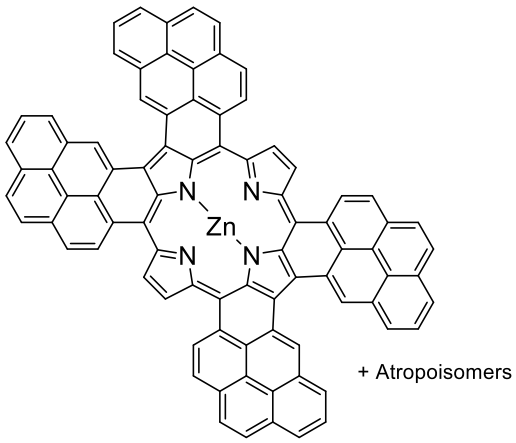

ZnTPyP in powder was subjected to pyrolysis at 550°C for 210 sec or at 585°C for 150 sec. The crude mixture was dissolved in CH_2Cl_2/pyridine (95:5) and passed through a silica pad to remove insoluble products. The resulting mixture was pure enough to detect the presence of products of fusion by MS and UV-visible spectroscopy. UV/Vis (CH_2Cl_2/pyridine): λ_{max} (nm) = 445, 576, 629, 670, 881, 1022. MS (MALDI - TOF) *m/z* $[M+H]^+$ calcd for $C_{84}H_{37}N_4Zn$ 11165.2, found: 1165.7.

[3,5,7-(10,15,20-triphenyl)anthraceneporphyrinato]zinc(II) (fused ZnSAP)

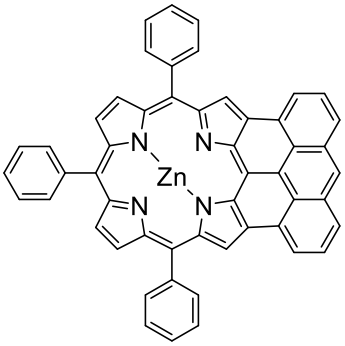

ZnSAP in powder (17 mg) was subjected to pyrolysis at 500°C for 225 sec. The resulting product was dissolved in CH_2Cl_2 and passed through a silica pad to remove insoluble products. The crude mixture was purified by silica column eluted with CH_2Cl_2/cyclohexane(1:1, v/v) and two successive SEC, in which the red fraction was collected. After precipitation in CH_2Cl_2/MeOH, a deep red powder (4 mg) was afforded as pure target fused **ZnSAP**. UV/Vis (CH_2Cl_2): λ_{max} (log ϵ_{max}) = 408 (4.45), 526 (4.32), 593 (3.93), 769 (3.80), 851 (3.97). HRMS (MALDI - TOF) *m/z* $[M]^+$ calcd for $C_{52}H_{28}N_4Zn$ 772.1605 found: 772.1607.

[3,5-(10,15,20-triphenyl)pyreneporphyrinato]zinc(II) (fused ZnSPP)

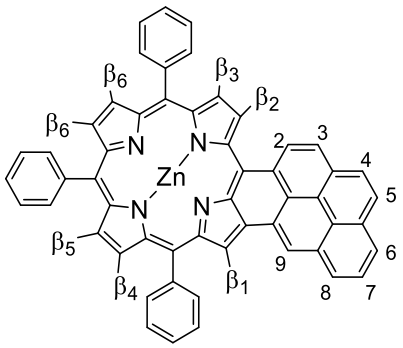

ZnSPP in powder (15 mg) was subjected to pyrolysis at 500°C for 210 sec. The resulting product was dissolved in CH_2Cl_2 and filtared through a silica pad to remove insoluble products. The crude mixture was purified by silica column eluted with CH_2Cl_2/cyclohexane(1:1, v/v) and two SECs in THF. After precipitation in CH_2Cl_2/MeOH, a deep brown powder was afforded as pure target fused **ZnSPP** (4.4 mg, 29%). ^{1}H NMR (400 MHz, $(CDCl_2)_2$): δ 9.58 (s, 1H, β1 pyrrole or 9-pyrenyl), 9.54 (d, 1H, J = 4.8 Hz, β2 pyrrole), 9.47 (s, 1H, β1 pyrrole or 9-pyrenyl), 9.38 (d, 1H, J = 8.0 Hz, 2-pyrenyl), 8.97 (d, 1H, J = 4.8 Hz, β3 pyrrole), 8.86-8.77 (m, 3H, β4, β5, β6 pyrrole), 8.71 (d, 1H, J = 8.4 Hz, 3-pyrenyl), 8.46 (d, 1H, J = 7.2 Hz, pyrenyl), 8.35-8.27 (m, 6H, *o*-phenyls), 8.25-8.19 (m, 3H, pyrenyl), 8.11 (t, 1H, J = 7.6 Hz, pyrenyl), 7.93-7.87 (m, 3H, *p*-phenyls), 7.86-7.72 (m, 8H, 6H *m*-phenyls + 2H pyrenyl). UV/Vis (CH_2Cl_2): λ_{max} (log ϵ_{max}) = 389 (3.50), 413 (3.57), 492 (4.14), 665 (3.29), 703 (3.48). HRMS (MALDI - TOF) *m/z* $[M]^+$ calcd for $C_{48}H_{28}N_4Zn$ 724.1605 found: 724.1610.

3,5-(10,15,20-triphenyl)pyreneporphyrin (fused SPP)

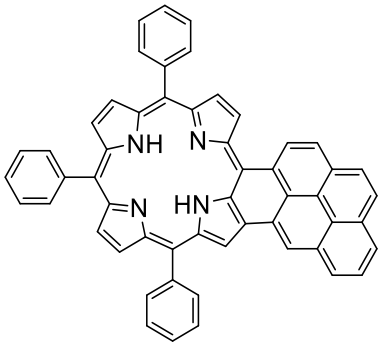

Zinc was removed from the cavity of **fused ZnSPP** (about 1 mg) following a literature procedure[27] with HCl (6 mol/L, 5 mL) in CH_2Cl_2 (5 mL). After 10 min of stirring at r.t, HCl was neutralized by addition of a saturated solution of $NaHCO_3$ (2 x10 mL) and the combined organic phase were extracted with water (2 x 10 mL) and dried over Na_2SO_4 before the solvent was removed under vacuum. UV/Vis ($CHCl_3$): λ_{max} = 385, 410, 482, 584, 632, 658, 733 nm. MS (MALDI - TOF) *m/z* $[MH]^+$ calcd for $C_{54}H_{33}N_4$ 737.27 found: 737.32.

VI. 5. Anthracenylporphyrin-based molecules

General procedure for Suzuki-Miyaura modification of BrTAP

Procedure adapted from the literature.[8] Palladium catalyst Pd_2dba_3 (5 mg, 0.005 mmol, 0.25 eq) or $PdOAc_2$ (2.5 mg, 0.011 mmol, 0.5 eq), SPhos (9 mg, 0.022 mmol, 1 eq), K_3PO_4 (0.54 mmol, 24 eq), **BrTAP** (30 mg, 0.022 mmol, 1 eq) and corresponded boronic acid (0.27 mmol, 12 eq) were dissolved in 20 mL of preliminary degassed solution of toluene and water, shielded from ambient light and stirred at 85°C for 48 h. At the end of the reaction, the mixture was washed with water (3 x 40mL), dried over Na_2SO_4 and the organic solvent was evaporated. The crude mixture was purified on silica column using toluene/heptane (from 1:1 to 2:1, v/v) (compounds **TPAP, TTAP)**, toluene/heptane (80:20 with 0.25 MeOH to 80:20 with 2%MeOH, v/v) or SEC eluted with THF (compounds **TNAP, TPyAP**) to collect the red fraction. Solvents were removed and final product was recrystallised from CH_2Cl_2/MeOH to afford the target pure compound.

5,10,15,20-tetrakis(10-phenylanthracen-9-yl)porphyrin (TPAP)

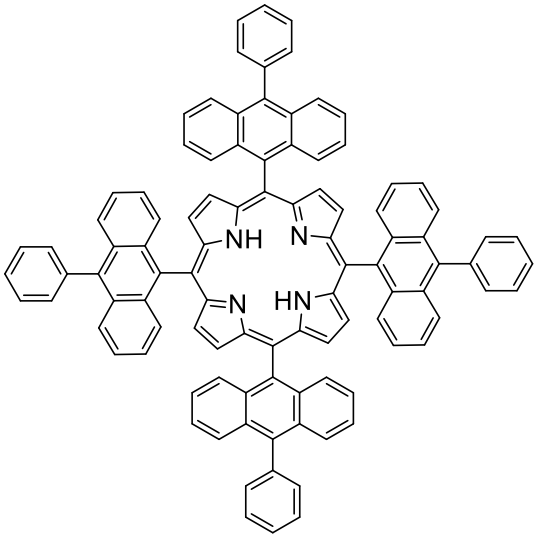

Prepared via Suzuki-Miyaura cross coupling approach under condition 1 to yield 20 mg (0.015 mmol, 69%). ^{1}H NMR (400 MHz, $(CDCl_2)_2$): δ 8.20-8.17 (m, 8H), 7.84-7.82 (m, 8H), 7.66-7.54 (m, 20H), 7.38-7.22 (m, 16H), 7.00-6.97 (m, 8H), -1.73 (s, $2H_{NH}$). ^{13}C NMR not recorded because of limited solubility resulting in a very weak signal. UV/Vis (CH_2Cl_2): λ_{max} (log ϵ_{max}) = 227 (4.75), 253 (5.39), 362 (4.48), 380 (4.56), 426 (5.34), 521 (4.37), 553 (3.80), 593 (3.87), 656 nm (3.46). HRMS (MALDI - TOF) *m/z* $[M]^+$ calcd for $C_{100}H_{62}N_4$ 1318.4969, found: 1318.5004.

5,10,15,20-tetrakis(10-(p-tolyl)anthracen-9-yl)porphyrin (TTAP)

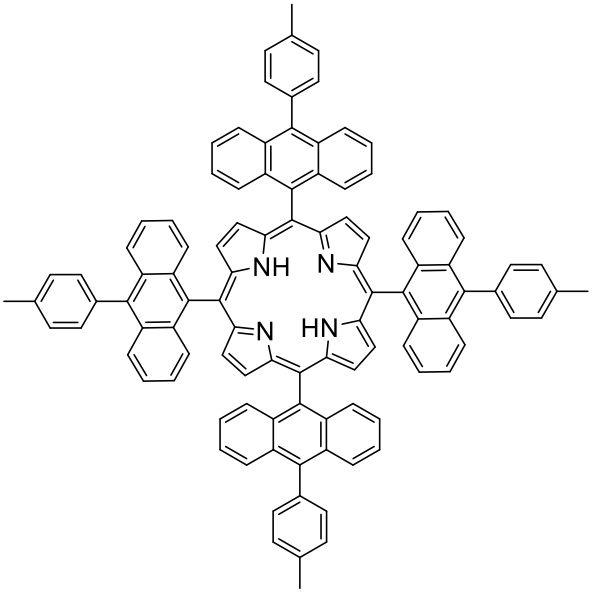

Prepared via Suzuki-Miyaura cross coupling approach under condition 1 to yield 17 mg (0.012 mmol, 56%). ^{1}H NMR (400 MHz, $(CDCl_2)_2$): δ 8.14-8.12 (m, 8H), 7.83-7.80 (m, 8H), 7.50-7.38 (m, 16H), 7.25-7.16 (m, 16H), 6.94-6.91 (m, 8H), 2.47 (s, 12H, CH_3), -1.76 (s, $2H_{NH}$). ^{13}C NMR not recorded because of limited solubility inducing very weak signal. UV/Vis (CH_2Cl_2): λ_{max} (log ϵ_{max}) = 227 (4.33), 253 (5.39), 363 (3.99), 380 (4.07), 426 (5.35), 521 (4.38), 553 (3.80), 593 (3.87), 656 nm (3.46). HRMS (MALDI - TOF) *m/z* $[M]^+$ calcd for $C_{104}H_{70}N_4$ 1374.5595, found: 1374.5577.

5,10,15,20-tetrakis(10-(4-methoxyphenyl)anthracen-9-yl)porphyrin (TMPAP)

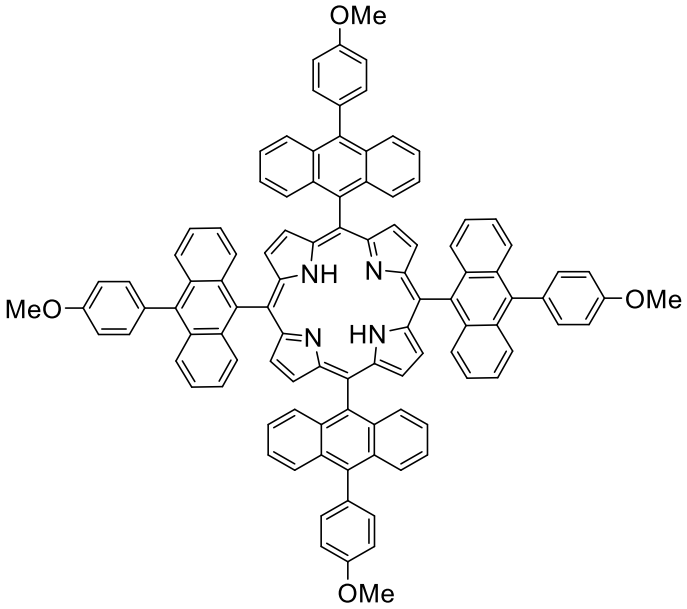

Prepared via Suzuki-Miyaura cross coupling approach under condition 1 to yield 11 mg (0.007 mmol, 35%). ^{1}H NMR (500 MHz, $(CDCl_2)_2$): δ 8.32-8.27 (m, 8H), 7.97-7.94 (m, 8H), 7.68-7.64 (m, 16H), 7.42-7.14 (m, 32H), 7.11-7.01 (m, 8H), 4.02 (s, 12H, O-CH_3), -1.62 (s, 2H_{NH}). ^{13}C NMR not recorded because of very weak solubility. UV/Vis (CH_2Cl_2): λ_{max} (log ϵ_{max}) = 233 (4.94), 255 (5.36), 258 (5.36), 361 (4.41), 427 (5.35), 523 (4.30), 555 (3.78), 596 (3.81), 656 nm (3.47). HRMS (MALDI - TOF) *m/z* $[M]^+$ calcd for $C_{104}H_{70}N_4O_4$ 1438.5392, found: 1438.5428.

5,10,15,20-tetrakis(10-(naphthalen-1-yl)anthracen-9-yl)porphyrin (TNAP)

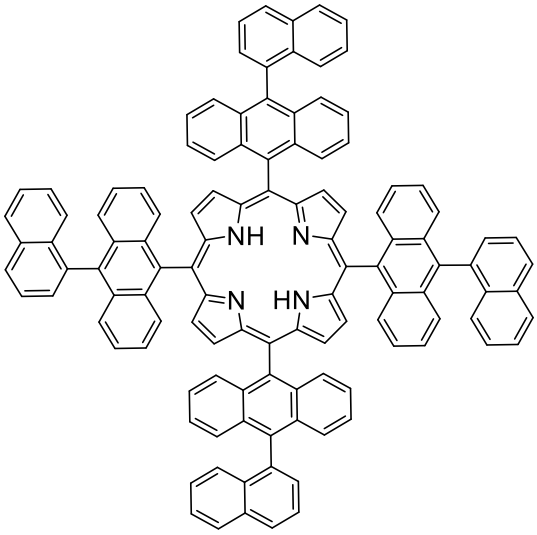

Prepared via Suzuki-Miyaura cross coupling approach under condition 1 to yield 12 mg (0.008 mmol, 36%). ^{1}H NMR (400 MHz, $(CDCl_2)_2$): δ 8.11-6.99 (m, 67H), -1.63 (s, $2H_{NH}$). ^{13}C NMR not recorded because of very weak solubility. UV/Vis (CH_2Cl_2): λ_{max} (log ϵ_{max}) = 229 (5.17), 252 (5.34), 277 (4.66), 331 (4.30), 347 (4.43), 358 (4.41), 427 (5.22), 521 (4.23), 550 (3.72), 594 (3.74), 658 nm (3.72). HRMS (MALDI - TOF) *m/z* $[M]^+$ calcd for $C_{116}H_{70}N_4$ 1518.5595, found: 1518.5589.

5,10,15,20-tetrakis(10-(pyren-1-yl)anthracen-9-yl)porphyrin (TPyAP)

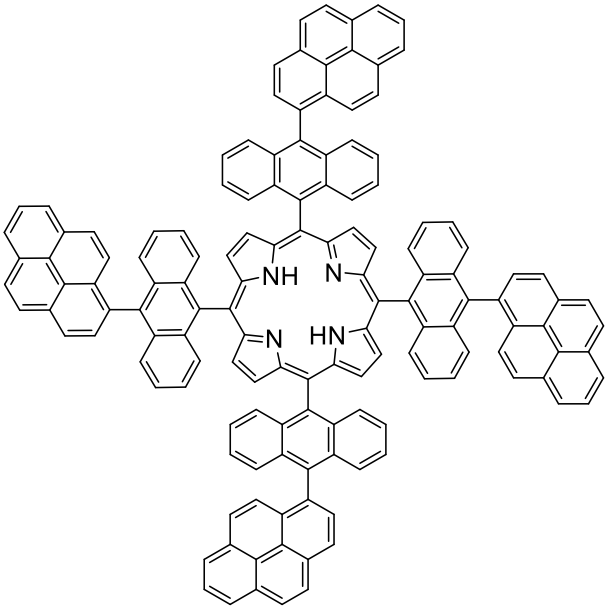

Prepared via Suzuki-Miyaura cross coupling approach under condition 1 to yield 11 mg (0.006 mmol, 28%). ^{1}H NMR (400 MHz, $(CDCl_2)_2$): δ 8.49-7.04 (m, 76H), -1.59 (s, $2H_{NH}$). ^{13}C NMR not recorded because of very weak solubility. UV/Vis (CH_2Cl_2): λ_{max} (log ϵ_{max}) = 246 (5.56), 256 (5.44), 278 (5.21), 329 (4.93), 344 (4.99), 382 (4.74), 430 (5.05), 522 (4.28), 553 (4.04), 594 (3.99), 658 nm (3.90). HRMS (MALDI - TOF) *m/z* $[M]^+$ calcd for $C_{140}H_{78}N_4$ 1814.6221, found: 1814.6198.

VI. 6. References

(1) Volz, H.; Schaeffer, H. Mesosubstituted Porphyrins. III. 5,10,15,20-Tetraanthracenylporphyrin. *Chemiker-Zeitung* **1985**, *109*, 308–309.

(2) Plater, M. J.; Aiken, S.; Bourhill, G. A New Synthetic Route to Donor- Acceptor Porphyrins. *Tetrahedron* **2002**, *58*, 2405–2413.

(3) Duerr, B. F.; Chung, Y. S.; Czarnik, A. W. Syntheses of 9,10-Disubstituted Anthracenes Derived from 9,10-Dilithioanthracene. *J. Org. Chem.* **1988**, *53*, 2120–2122.

(4) Pijeat, J.; Dappe, Y. J.; Thuéry, P.; Campidelli, S. Synthesis and Suzuki–Miyaura Cross Coupling Reactions for Post-Synthetic Modification of a Tetrabromo-Anthracenyl Porphyrin. *Org. Biomol. Chem.* **2018**, *16*, 8106–8114.

(5) Stern, D.; Finkelmeier, N.; Meindl, K.; Henn, J.; Stalke, D. Consecutive Donor-Base Exchange in Anthracenyllithium Compounds. *Angew. Chem. Int. Ed.* **2010**, *49*, 6869–6872.

(6) Xu, K.; Zhao, J.; Escudero, D.; Mahmood, Z.; Jacquemin, D. Controlling Triplet-Triplet Annihilation Upconversion by Tuning the PET in Aminomethyleneanthracene Derivatives. *J. Phys. Chem. C* **2015**, *119*, 23801–23812.

(7) Adler, A. D.; Longo, F. R.; Shergalis, W. Mechanistic Investigations of Porphyrin Syntheses. I. Preliminary Studies on Ms-Tetraphenylporphin. *J. Am. Chem. Soc.* **1964**, *86*, 3145–3149.

(8) Bonifazi, D.; Accorsi, G.; Armaroli, N.; Song, F.; Palkar, A.; Echegoyen, L.; Scholl, M.; Seiler, P.; Jaun, B.; Diederich, F. Oligoporphyrin Arrays Conjugated to [60]Fullerene: Preparation, NMR Analysis, and Photophysical and Electrochemical Properties. *Helv. Chim. Acta* **2005**, *88*, 1839–1884.

(9) Davis, M.; Senge, M. O.; Locos, O. B. Anthracenylporphyrins. *Z. Naturforsch, B* **2010**, *65*, 1472–1484.

(10) König, M.; Reith, L. M.; Monkowius, U.; Knör, G.; Bretterbauer, K.; Schoefberger, W. Suzuki-Miyaura Cross-Coupling Reaction on Copper-Trans-A2B Corroles with Excellent Functional Group Tolerance. *Tetrahedron* **2011**, *67*, 4243–4252.

(11) Diev, V. V.; Schlenker, C. W.; Hanson, K.; Zhong, Q.; Zimmerman, J. D.; Forrest, S. R.; Thompson, M. E. Porphyrins Fused with Unactivated Polycyclic Aromatic Hydrocarbons. *J. Org. Chem.* **2012**, *77*, 143–159.

Publications

Papers:

"Synthesis and Suzuki–Miyaura Cross Coupling Reactions for Post-Synthetic Modification of a Tetrabromo-Anthracenyl Porphyrin" J. Pijeat, Y. J. Dappe, P. Thuéry, S. Campidelli Organic & Biomolecular Chemistry **2018**, 16, 8106–8114

"Bottom-up Approach for the Synthesis of Graphene Nanoribbons" J. Pijeat, J. S. Lauret, S. Campidelli, in Graphene Nanoribbons, A. Tejeda, L. Brey, P. Seneor, Eds. IOP Publishing Ltd. **in press**

"Self-Assembly of a Tetra-anthracenylporphyrin on Silver Surfaces" N. Kalashnyk *et al*., **in preparation**

Oral presentation:

"Bottom-up synthesis of porphyrin based graphene nanoribbons and nanomeshes" J. Pijeat, N. Kalashnyk, R. Plamont, T. S. Balaban, S. Clair, P. Thuery, S. Campidelli, International conference of porphyrins and phthalocyanines (ICPP-10), Munich, July **2018**

Poster presentations:

"Toward π-extended porphyrin, alternative route to fused unactivated aromatic rings by thermal cyclodehydrogenation" J. Pijeat and S. Campidelli, Chem2DMat, Strasbourg, August **2017**

"Toward π-extended porphyrin, alternative route to fused unactivated aromatic rings by thermal cyclodehydrogenation" J. Pijeat and S. Campidelli, GDR graphene and Co, Aussois, October **2017**

"Bottom-up synthesis of porphyrin based graphene nanoribbons and nanomeshes" J. Pijeat, N. Kalashnyk, R. Plamont, T. S. Balaban, S. Clair, P. Thuery, S. Campidelli, International conference of porphyrins and phthalocyanines (ICPP-10), Munich, July **2018**

Titre : Briques de construction à base d'anthracénylporphyrines pour la fabrication bottom-up de nanostructures de graphène dopées à l'azote

Mots clés : anthracene, porphyrine, graphène, bottom-up

Résumé : La synthèse de graphène par approche « bottom-up » fait l'objet de nombreux travaux de recherche ayant pour but de contrôler les propriétés électroniques et optiques de ce matériau par la fabrication de nanostructures avec une précision atomique. D'autre part, le contrôle de dopant dans le graphène permettant d'en moduler les propriétés suscite un grand intérêt et dans ce contexte l'utilisation de porphyrines avec un taux d'azote contrôlé est attrayante. Par leurs ressemblances structurelles, les porphyrines π-étendues peuvent être considérées comme des nanoparticules de graphène dopées à l'azote (GQDs) présentant de fortes propriétés infrarouge tandis que les briques de construction à base de porphyrines peuvent être utilisées pour la synthèse sur surface de deux type de nanoarchitectures de graphene appélées nanorubans (GNRs) et nanomèches (GNMs). Cette thèse a pour objectif de développer la synthèse de porphyrines à base d'anthracenes et de les utiliser comme précurseurs pour la fabrication de nanostructures. La première partie de cette thèse est dédiée à la synthèse organique de différentes anthracénylporphyrines et à l'étude de leurs assemblages sur surface dans la chambre d'un microscope à effet tunnel. La seconde partie est dédiée à l'étude de formation de porphyrines π-étendues *via* une méthode pyrolyse flash pouvant activer thermiquement des réactions de couplage par déhydrogenation entre des hydrocarbures aromatiques polyycliques (PAHs) et des porphyrines. La dernière partie est dédiée à la modification post synthétique d'une tetrabromoanthracénylporphyrine par addition de PAHs *via* la réaction de couplage de Suzuki-Miyaura et à la caractérisation des propriétés optiques de ces porphyrines nouvellement formées.

Title : Anthracenylporphyrin-based building blocks for the bottom-up fabrication of nitrogen-doped graphene nanostructures

Keywords : anthracene, porphyrin, graphene, bottom-up

Abstract : The synthesis of graphene via bottom-up approach is a hot topic of research that aims to control the electronic and optical properties of this material by the fabrication of atomically precised nanostructures. Moreover, the control of dopant in graphene is of great interest to modulate the properties of the material. In this context, the contribution of porphyrins with a controlled content of nitrogen is attractive. Because of structural similarities with graphene quantum dots (GQDs), π-extented porphyrins can be regarded as nitrogen-doped GQD with promising NIR properties. Porphyrins are convenient building blocks for the on-surface synthesis of nanoarchitectures of graphene called nitrogen-doped Graphene Nanoribbons (GNRs) and Graphene NanoMeshes (GNMs). This thesis aims to develop the synthesis of symmetrical and robust porphyrins with anthracenes and to use them as precursors for the fabrication of nanostructures. The first part of this thesis is dedicated to the organic synthesis of variety of anthracenylporphyrins and the study of their assemblies on surface in a chamber of a Scanning Tunneling Microscope. The second part is dedicated to the study of formation of π-extended porphyrins via a method of pyrolysis able to thermally activate dehydrogenative coupling reactions between Polycyclic Aromatic Hydrocarbons (PAHs) and porphyrins. The last part is dedicated to the post synthetic modification of a tetrabromoanthracenylporphyrin with additional PAHs via Suzuki-Miyaura coupling and the characterization of the optical properties of the resulting porphyrins.